Studies of Two Dimensional Electron Systems via Surface Acoustic Waves and Nuclear Magnetic Resonance Techniques

A Thesis by

Lisa A. Tracy

In Partial Fulfillment of the Requirements

for the Degree of

Doctor of Philosophy

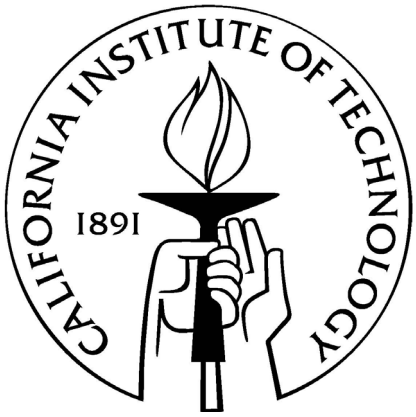

California Institute of Technology

Pasadena, CA

2007

(Defended September 10, 2007)

Acknowledgements

I first want to thank my thesis advisor, Jim Eisenstein, who made this research possible. I thank Jim for his abundance of ideas and general enthusiasm and also for being a good teacher who was willing to share his expertise and deep understanding of physics.

Thanks to my thesis committee, especially Gil Refael for helpful discussions early on and Greg Fiete for taking the time to meet and make comments.

Many thanks goes to all of the labmates over the years. I would like to thank Ken Cooper for generously taking the time to help with the bulk of my initial lab training. Thanks to Mindy Kellogg who was always wiling to lend a helping hand. Thanks to Ian Spielman, who was willing to listen to my questions (and give impressive answers) and play the role of lab helpdesk. Thanks to Tony Bonetti for all of his help and generosity. Xerxes Lopez-Yglesias deserves special thanks for a lot of help in the lab, friendship, and quick thinking. Thanks to Bart McGuyer, who was willing to get his hands dirty helping out in the sub-basement. Finally, I thank Ghislain Granger and Alex Champaign for their help, good physics discussions, and generally good company in lab.

Thanks to my collaborators, especially Loren Pfeiffer and Ken West, whose expertise was essential to this research. Thanks to Mike Lilly for his collaboration and also for my new job!

Thanks to Steve Stryker for all of his technical assistance and for keeping Sloan sub-basement running smoothly. Thanks to Terry, Armando, Rick and the rest of the physics shop for the training and all the help with my projects.

Thanks to many individuals from my undergrad days, especially Atul Konkar, Jure Demsar, Peter Bennett, Robert Culbertson, and Stuart Lindsay for their mentoring and help.

Thanks also goes to individuals outside of the lab. I would like to thank Ilya Mandel, Songye Chen, Ben Toner, Graeme Smith, Disa Eliasdottir**,** Donall O'Connell, Kris Sigurdson, Mihai Bondarescu, and Anura Abeyesinghe for their friendship early on at Caltech. Thanks to Mike Rubel for all of the Thursday lunches and many other good

times. Thanks to Liz Wood for chamber music, bicycle rides, and great friendship over the years.

Finally, thanks to my parents for their unwavering love and support.

Abstract

This thesis presents measurements investigating the spin degree of freedom in two dimensional electron systems (2DES's). The measurements use nuclear magnetic resonance (NMR) techniques to study the role of spin in several 2DES states.

We first examine the spin transition that occurs in a half-filled Landau level in a single layer 2DES and compare our measurements to expectations from a composite fermion (CF) model. We show the temperature and density dependence of the nuclear T_1 and resistively-detected NMR signal. The T_1 data can be roughly understood via a Korringa-like model of nuclear spin relaxation. However, the observed density dependence of both T_1 and the NMR signal is not explained by conventional CF theory.

We next consider a bilayer 2DES consisting of two closely spaced 2D electron layers, where each of the individual layers contains a half-filled Landau level. In this system, a transition occurs from a compressible single layer-like state to an incompressible correlated bilayer state as a function of the effective spacing between the two layers. When the effective spacing is made small enough, interactions between the two layers lead to the formation of a new state that can be viewed as a Bose condensate of excitons. Using NMR techniques we show that the spin degree of freedom is active during this transition.

In a single-layer 2DES with one completely filled Landau level ($\nu = 1$), charged spin-texture excitations called "skyrmions" are expected to exist. We probe the spin dynamics near this state using NMR. We find relatively fast nuclear relaxation rates that are consistent with a theory of spin excitations for a skyrmion solid. Our measurements also provide clues as to the origin of an "anomalous" NMR lineshape seen near $\nu=1$.

We also present surface acoustic wave (SAW) measurements in a low density 2DES at zero magnetic field, under conditions where a 2D metal-insulator transition may occur. We find that our SAW data are consistent with a disorder-driven, percolation-type transition.

Table of Contents

Introduction

Two-dimensional electron systems (2DES's) in semiconductors continue to provide experimental access to a wide range of phenomena in correlated electron physics. Two of the best known examples of exciting discoveries in 2DES's are the integer and fractional quantum Hall effects, which were first observed roughly 25 years ago [1-2]. However, 2DES research remains active, spanning a variety of topics including fractional statistics and charge, metal-insulator transitions, charge density waves, and Bose-Einstein condensation. New physics continues to emerge as sample quality improves, experimentally accessible temperatures decrease, and new experimental probes are developed.

This thesis starts with a discussion of surface acoustic wave (SAW) measurements that probe the frequency and length scale dependent conductivity of the 2DES at low densities. Several aspects of SAW's make them an interesting probe for low density 2DES's near the putative metal-insulator transition.

The second part of this thesis presents experiments that investigate the role of spin in several 2DES states. We use a resistively detected nuclear magnetic resonance (RDNMR) technique that is well-suited for studying 2DES's (and nanostructures in general). Due to the hyperfine interaction between nuclei and electrons in the 2DES host semiconductor, the electron spin polarization can be probed using NMR techniques. For typical 2DES's in GaAs/AlGaAs heterostructures, at moderate perpendicular magnetic fields the Coulomb interaction is large compared to the Zeeman energy and can play a significant role in determining the behavior of the electron spin. This leads to a variety of spin phenomena ranging from ground state spin transitions for fractional quantum Hall states to the existence of "skyrmion" spin excitations in the quantum Hall regime. This thesis describes several applications of RDNMR to the study of the electron spin degree of freedom in 2DES's. Recent work includes investigation of a spin transition in the half-filled Landau level, observation of a spin transition in a correlated bilayer 2DES, and measurements of electron spin dynamics near the lowest filled Landau level in a single layer 2DES.

Chapter 1 describes the samples and experimental techniques that are generic to all of the experiments described in this thesis. The chapter starts with an introduction to

GaAs/AlGaAs heterostructures and how they are used to create high mobility 2DES's. The chapter ends with a brief overview of basic experimental techniques typically employed, such as standard semiconductor processing, dc transport measurements, cryogenic refrigeration, and high magnetic fields.

Chapter 2 presents surface acoustic wave (SAW) measurements in low density 2DES's at zero magnetic field, under conditions where a 2D metal-insulator transition may occur. Controversy exists over whether this transition is better described as an exotic, interaction-driven phase transition or by more straightforward physics of disordered conductors. We compare our SAW data to standard dc resistivity measurements and show that our measurements are consistent with a disorder-driven, percolation-type transition [3].

Chapter 3 introduces the physics of 2D electrons in a perpendicular magnetic field, from a classical to quantum mechanical picture, and eventually, the fully interacting picture and the fractional quantum Hall effect (FQHE). The composite fermion picture of the FQHE is also introduced.

Chapter 4 gives an overview of spin in 2DES's and then an introduction to nuclear magnetic resonance (NMR) techniques that are used in the experiments described in the rest of the thesis. We introduce a resistively-detected NMR (RDNMR) technique used to probe the spin degree of freedom in 2DES's.

In **Chapter 5** we probe the transition from partial to complete electron spin polarization as a function of density in a single layer 2DES with a half-filled Landau level [4]. The fractional quantum Hall effect can be understood in an elegant way using a composite fermion (CF) picture. In this picture, a single layer 2DES at Landau level filling fraction $\nu = 1/2$ can be described as a Fermi liquid of CF's, where a CF is an electron with two magnetic flux quanta attached [5]. The CF picture has been very effective at describing a wide range of experiments, but the limit of its applicability is still an ongoing subject of interest. Both the nuclear spin-lattice relaxation time T_1 and the derivative of the resistivity with respect to the electronic Zeeman splitting $d\rho_{xx}/dE_Z$ reflect this transition. Our RDNMR measurements show that at $\nu = 1/2$, T_1 has a temperature dependence that is roughly described by a 2D version of Korringa nuclear spin relaxation. However, the density dependence of both T_1 and $d\rho_{xx}/dE_Z$ fail to agree with a simple composite fermion (CF) picture. T_1 is roughly density independent in the

partially polarized phase, in contrast to the variation expected from the dependence of the CF density of states on Coulomb energy. The sign of $d\rho_{xx}/dE_Z$ is not understood and an unexpected peak in $d\rho_{xx}/dE_Z$ develops at low temperatures near the critical density for the spin transition.

Chapter 6 describes RDNMR experiments in a bilayer 2DES consisting of two closely spaced single layer 2DES's. Interactions between the two layers can create new many body states in bilayers that have no single layer 2DES analog. At total Landau level filling factor ν_T = 1 and small effective interlayer spacing, a remarkable state emerges that can be viewed as a Bose condensate of excitons. There is a phase transition from a compressible state where the layers are weakly coupled to an incompressible excitonic condensate state as the coupling between the layers is increased by reducing the effective interlayer spacing [6-10]. This chapter discusses experiments which probe this phase transition. Specifically, we present RDNMR measurements probing the spin degree of freedom in a bilayer 2DES at total filling factor ν_T = 1, performed by Ian Spielman and myself [11]. Our data shows that the spin degree of freedom is active during this transition.

Chapter 7 discusses RDNMR measurements that probe the electron spin near the completely filled lowest Landau level (ν = 1) in a single layer 2DES [12]. Although the ν = 1 quantum Hall might at first glance appear to be easily described by a single-particle picture, upon greater scrutiny, one finds that Coulomb interactions actually play a large role in determining the behavior of this state. The lowest energy charged excitations at filling factors at and nearby ν = 1 are actually predicted to be skyrmions, excitations with a smooth spatial variation in spin which carry spin and charge. The presence of skyrmions is expected to have a large impact on nuclear spin dynamics for this state. Our data is consistent with a theory of the spin excitations due to formation of a skrymion solid. We also provide clues as to the origin of the "anomalous" RDNMR lineshape seen near ν = 1.

The thesis ends with a brief **Conclusions and Future Directions** section, which gives a final overview and possible future directions for related experiments.

References

[1] K. von Klitzing, G. Dorda, and M. Pepper, *Phys. Rev. Lett.* **45**, 494 (1980).

[2] D. C. Tsui, H. L. Stormer, and A. C. Gossard, *Phys. Rev. Lett.* **48**, 1559 (1982).

[3] L.A. Tracy, J.P. Eisenstein, M.P. Lilly, L.N. Pfeiffer, K.W. West, *Solid State Comm*. **137**, 150 (2006).

[4] L. A. Tracy, J. P. Eisenstein, L. N. Pfeiffer, and K. W. West. *Phys. Rev. Lett.* **98**, 086801 (2007).

[5] J. K. Jain. *Phys. Rev. Lett*. **63**, 199 (1989).

[6] J. P. Eisenstein, G. S. Boebinger, L. N. Pfeiffer, K. W. West, and S. He, *Phys. Rev. Lett*. **68**, 1383 (1992).

[7] S. Q. Murphy, J. P. Eisenstein, G. S. Boebinger, L. N. Pfeiffer, and K. W. West, *Phys. Rev. Lett*. **72**, 728 (1994).

[8] I. B. Spielman, J. P. Eisenstein, L. N. Pfeiffer, and K. W. West, *Phys. Rev. Lett*. **84**, 5808 (2000).

[9] M. Kellogg, I. B. Spielman, J. P. Eisenstein, L. N. Pfeiffer, and K. W. West, *Phys. Rev. Lett*. **88**, 126804 (2002).

[10] M. Kellogg, J. P. Eisenstein, L. N. Pfeiffer, and K. W. West, *Phys. Rev. Lett*. **93**, 036801 (2004).

[11] I. B. Spielman, L. A. Tracy, J. P. Eisenstein, L. N. Pfeiffer, and K. W. West, *Phys. Rev. Lett*. **94**, 076803 (2005).

[12] L. A. Tracy, J. P. Eisenstein, L. N. Pfeiffer, and K. W. West *Phys. Rev. B* **73**, 121306 (2006).

Chapter 1:
Samples and Experimental Techniques

Two-dimensional electron systems (2DES) are systems consisting of electrons confined to motion in a plane. High-mobility 2DES's are fascinating systems that give rise to a wide range of phenomena. This chapter presents an overview of 2DES samples and measurement techniques used to investigate their properties.

1.1 GaAs/AlGaAs Heterostructures

A variety of experimental systems exist for the creation of 2DES's, ranging from a Si MOSFET to electrons on the surface of ^{4}He. The measurements described in this thesis were performed using high electron mobility 2DES's in GaAs/AlGaAs heterostructures, where mobility μ is defined by $\sigma = ne\mu$, where σ is the conductivity and n is the electron density. Mobility is a measure of sample disorder. Using the Drude model (see Chapter 3, section 3.1), $\mu \sim \tau$, where τ is the transport lifetime, which is determined, in part, by the rate at which electrons collide with sample impurities. Thus, very pure samples tend to have high mobilities and allow better observation of delicate many-body electron states. The GaAs/AlGaAs heterostructures used for the measurements described in this thesis were kindly provided by our collaborators Loren Pfeiffer and Ken West at Bell Labs.

1.1.1 Overview

The highest electron mobility 2DES's are currently formed in GaAs/AlGaAs heterostructures (the alloy $Al_xGa_{1-x}As$ is abbreviated as AlGaAs). The GaAs/AlGaAs system has several key properties that allow for high mobilities. One of the most important of these properties is that the system is well lattice-matched; the lattice constant of AlAs is only 0.15% larger than that for GaAs. This leads to a minimum amount of strain, and thus defect formation, at interfaces between two alloys with different Al content. The highest mobility 2DES's in GaAs/AlGaAs are grown via molecular beam epitaxy (MBE). For a UHV environment at a pressure lower than 10^{-12} Torr, the mean free path of molecules is greater than size of the vacuum chamber. Under

these conditions, molecules emerging from heated sources do not diffuse – they form a molecular beam. MBE allows for controlled growth of individual atomic layers. The technique is precise but slow; a typical growth rate is approximately one monolayer/second. Several advances in MBE techniques, such as modulation [1] and delta doping [2], where the dopant atoms are placed remote from the active area of the device, have caused mobility to increase. The current record for high mobility is ~ 30 × 10^6 cm^2/Vs (~ 300 μm mean free path!) at low temperature (T < 0.3 K), achieved by Loren Pfeiffer and Ken West at Bell Labs.

1.1.2 GaAs crystal structure

The crystal structure of GaAs (or AlAs) is shown in Fig. 1.1. GaAs has a zincblende structure; it is comprised of two fcc (face centered cubic) sublattices, one for Ga and another for As, displaced from one another by (1/4, 1/4, 1/4)a, where a is the lattice constant ~ 5.66 A (see Fig. 1.1). In the alloy AlGaAs, Ga atoms are randomly replaced by Al atoms. The samples discussed in this thesis are oriented so that the [001] direction is perpendicular to the 2DES.

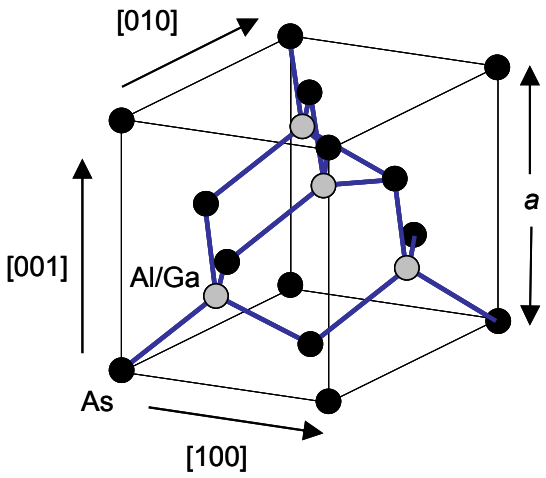

Fig. 1.1. GaAs (or AlAs) unit cell with crystalline directions denoted by Miller indices ([100], [010], and [001]).

1.1.3 GaAs/AlGaAs interface

The interface between two AlGaAs alloys of differing Al and Ga content can be used to confine electrons. A sketch of the band energies at this interface is shown in Fig. 1.2, where E_C and E_V are the conduction and valence band energies at the Γ point [3].

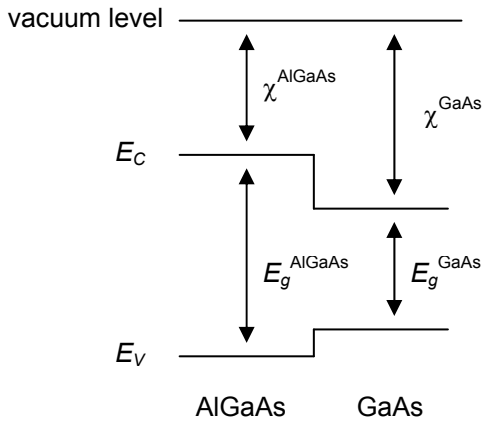

Fig. 1.2. Ideal alignment of bands at GaAs-AlGaAs interface. χ is the electron affinity.

The alignment of the conduction and valence bands is determined by the combination of the band gap E_g and electron affinity χ for each alloy. For reference, the difference between the conduction band energies at the interface between GaAs and the common alloy $Al_{0.3}Ga_{0.7}As$ is $\Delta E_C = 0.23$ eV [3].

Charge carriers can be introduced by doping. In (100) oriented AlGaAs, substituting Si impurities for Al or Ga in the lattice will introduce electrons into the conduction band. This addition of negative charge carriers by addition of impurities is called *n*-type doping. There are two main states for the Si donor in AlGaAs – the standard donor, which can be modeled as a hydrogen atom-like state, and the deep donor or DX center [3]. The standard donor state can be treated as a hydrogen atom with the vacuum permittivity replaced by the dielectric constant of AlGaAs and the bare electron mass replaced by an effective mass, which gives a binding energy of the electron to the donor of ~ 50 K. The DX center occurs when the replacement of the Al or Ga atom is accompanied by a distortion of the surrounding lattice. The binding energy of the DX

center donor is much larger than the hydrogenic type donor and is experimentally approximately $T \sim 150$ K.

Examples of *n*-type doped heterostructures are sketched in Fig. 3.1. These structures are modulation doped – the Si impurities are placed remote from the 2DES AlGaAs/GaAs interfaces. If these impurities were located in the region where conduction takes place they would contribute to electron scattering. Modulation doping [1] can lead to large improvements in 2DES mobility. In one specific type of modulation doping, referred to as delta doping [2], the dopants are placed in a thin monolayer sheet positioned a few tens of nanometers away from the 2DES region. This places the 2DES as far from the dopants as possible, leading to a reduction in the scattering rate.

Alternatively, undoped FET structures exist, where carriers are drawn in from Ohmic contacts into a GaAs/AlGaAs interface region by gating [4]. These structures can have very high mobilities at low densities due to the absence of disorder stemming from ionized donors near the 2DES.

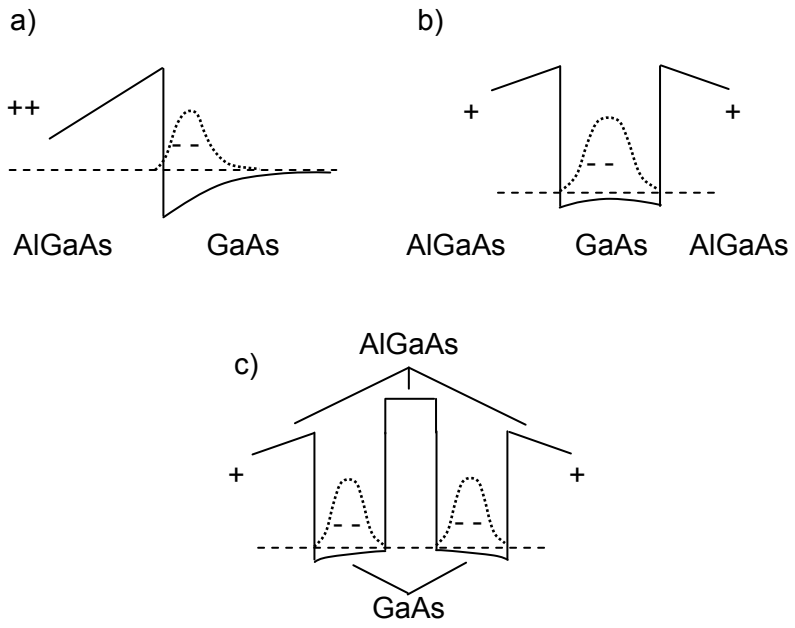

Fig. 1.3. Schematic band diagrams for a 2DEG confined in a) at a single interface and b) in a quantum well, and c) a bilayer 2DES confined in a double quantum well structure. Solid line: conduction band. Dashed line: chemical potential. Dotted line: electronic wavefunction. Symbol "+" denotes position of ionized Si dopants.

An actual MBE structure is typically much more complicated than just an interface or two and some dopants. An example of an actual single interface structure is shown in Fig. 1.4.

The MBE layers are grown on a single-crystal GaAs substrate wafer, typically ~ 0.5 mm thick. This substrate is a polished slice sawed from a large single-crystal boule of GaAs. First, a thick buffer layer of GaAs is grown to create a smooth surface and move the important layers away from the defects and impurities present on the wafer surface. Next, a cleaning superlattice is grown consisting of ~100 alternating AlGaAs, GaAs layers which getter and trap impurities at the GaAs/AlGaAs interfaces [5]. Another thick GaAs layer is grown and then the GaAs/AlGaAs interface for the 2DES. The Si dopants are placed remotely from this interface (modulation doped). A layer of AlGaAs separates the 2DES from the sample surface. A thin cap of GaAs is grown on the surface to prevent oxidation of the AlGaAs. The Fermi level is pinned mid-gap at the GaAs cap surface due to a large density of surface states in the middle of the band gap.

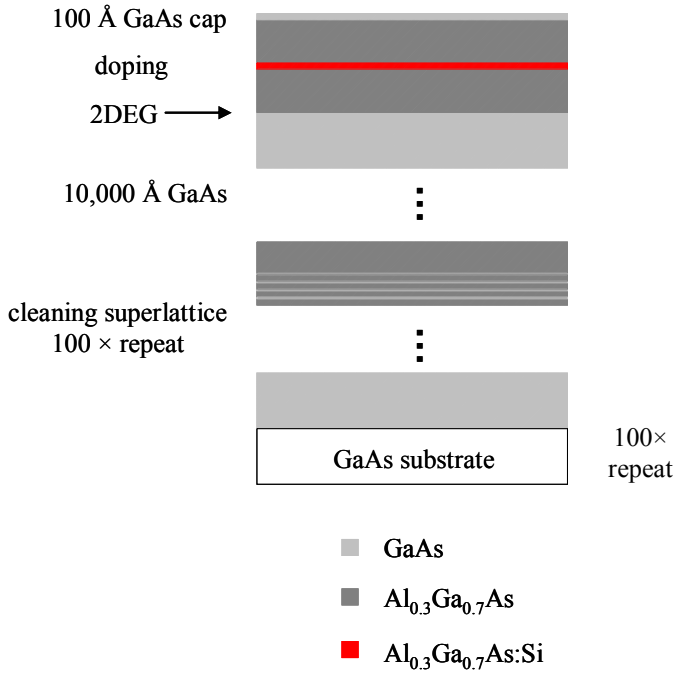

#	Material	Thickness (Å)
1	GaAs	100
2	$Al_{0.3}Ga_{0.7}As$	1,000
3	$Al_{0.3}Ga_{0.7}As$:Si	50
4	$Al_{0.3}Ga_{0.7}As$	800
5	GaAs	10,000
6	$Al_{0.3}Ga_{0.7}As$	500
7*	GaAs	30
8*	$Al_{0.3}Ga_{0.7}As$	100
206	GaAs	3,000
207	GaAs substrate	~ 0.5 mm

100× repeat

Fig. 1.4. Example sample structure for a 2DEG formed at a single interface with modulation doping.

1.1.4 Effective Mass and g-Factor

$Al_xGa_{1-x}As$ for $x < 0.4$ is a direct gap semiconductor with a spherically symmetric conduction band Fermi surface near the Γ point. A single effective mass, m^*, can be used to describe the kinetic energy of electrons near the bottom of the conduction band, where the band dispersion E vs. k is roughly parabolic. For GaAs $m^* = 0.067m_e$, where m_e is the electron mass in vacuum.

The Zeeman splitting E_Z in AlGaAs can be parameterized by an effective g-factor g^*, where $E_Z = g^*\mu B$. For GaAs, $g^* \approx -0.44$, whereas the g-factor of an electron in vacuum is $g_e = 2$. Due to spin-orbit coupling, g^* is not equal to g_e and even has the opposite sign!

1.1.5 2DES Wavefunction

It is useful to be able to estimate properties of the bound 2DES states, such as the shape of the electronic wavefunction in the direction of confinement, binding energies, etc. This requires a self-consistent solution of the Poisson and Schrodinger equations, which can be done numerically. An example of a Poisson-Schrodinger self-consistent calculation is shown in Fig. 1.5. The solution includes the exchange and correlation energies in the self-consistent potential, using the local density approximation (LDA) [6]. In the LDA approximation, the exchange-correlation energy at each z-coordinate (z is the direction normal to the 2DES) is set equal to the exchange-correlation energy of a homogeneous, three dimensional electron gas with a density proportional to the square of the modulus of the 2D subband wavefunction at that point. The calculation shown in Fig. 1.5 is for a 2DES formed at a single GaAs/AlGaAs interface. One unknown parameter that complicates the calculation of the exact wavefunction is the precise slope of the conduction band energy in the tail of the wavefunction, heading towards the substrate. In actual samples, impurities (bundled under the term "depletion charge") may tend to deplete carriers, causing the conduction band to rise towards the middle of the band gap away from the 2DES region. Also, as mentioned previously, the Fermi level will be pinned mid-gap at interfaces with a large number of surface states, such as at the surface of the GaAs substrate wafer. Thus, the Fermi level must eventually reach the middle of the band gap away from the 2DES region. The effect of depletion charge was ignored in the calculation of Fig. 1.5.

A convenient approximate solution for the 2DES wavefunction for the case of a single interface structure is the Fang-Howard wavefunction [7], a variational wavefunction of the form

$$\psi(z) \propto z \exp(-bz/2),$$

where the interface is located at $z = 0$, and b is a parameter that is used to minimize the energy, given a specific 2DES density n (the value of the barrier height at the interface is ignored since $\psi(0) = 0$). Using the Hartree approximation (i.e., ignoring the exchange and correlation energies) the solution with the minimum energy is given by

$$b = \left(\frac{33me^2 n}{8\hbar^2 \varepsilon} \right)^{1/3}.$$

A comparison of the Fang-Howard wavefunction and the Poisson-Schrodinger solution is shown in Fig. 1.5.

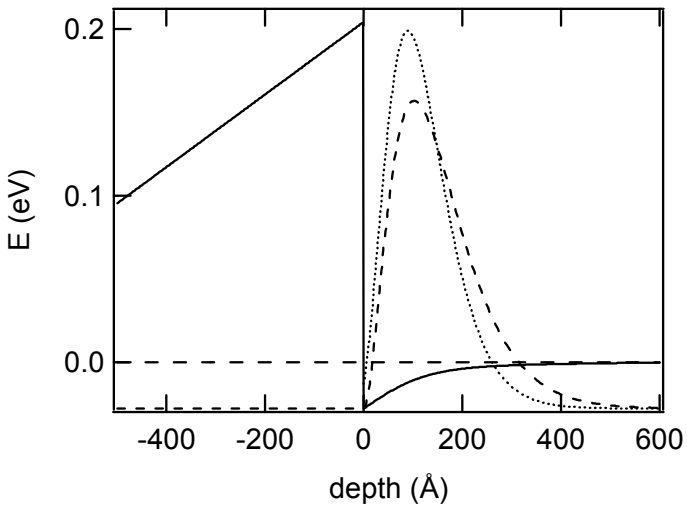

Fig. 1.5. Dotted line: Schrodinger-Poisson solution to wavefunction modulus squared for the single interface structure shown in Fig. 1.4. Solid line: conduction band energy. Dashed line: Fang-Howard wavefunction squared. The horizontal dashed line corresponds to the Fermi energy. The electron density is $n = 1.5 \times 10^{11}$ cm^{-2}.

1.2 Experimental Techniques

1.2.1 Sample Fabrication

In order to make measurements it is usually necessary to create a specialized sample from a piece of the parent GaAs/AlGaAs wafer. Fabricating a 2DES device can consist of simply cleaving a chip and adding ohmic contacts with a soldering iron or can be a multiple step process defining a patterned 2DES mesa region, metallic gates, and lithographically defined ohmic contacts. For completeness, a brief description of the processes used to fabricate the samples described in this thesis is included in Appendix A.

1.2.2 DC Transport Measurements

One of the most common techniques used to investigate 2DES's is via dc resistance measurements. The following is a description of the basic characterization of 2DES samples via low-frequency transport measurements.

1.2.2a Van der Pauw Method

The resistivity (at zero magnetic field) of any conducting sheet with four point contacts on the periphery, as shown in Fig. 6, can be obtained using the van der Pauw method [8].

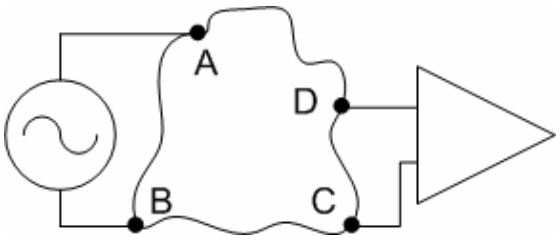

Fig. 1.6. Four point van der Pauw measurement setup.

The sheet resistivity per square is given by.

$$\rho_{\square} = \frac{\pi}{\ln(2)} \frac{R_{AB,CD} + R_{AD,CB}}{2} f(r),$$

$$r = \max\left\{R_{AB,CD} / R_{AD,CB}, R_{AD,CB} / R_{AB,CD}\right\},$$

where $R_{XY,WZ} = V_{WZ}/I_{XY}$ is the resistance measured by applying current I_{XY} between contacts X and Y and measuring the voltage V_{WZ} between contacts W and Z, and the factor f is given by

$$\cosh\left(\frac{\ln(2)}{f}\frac{r-1}{r+1}\right) = \frac{1}{2}\exp\left(\frac{\ln(2)}{f}\right).$$

A plot of f versus r is shown in Fig. 1.7.

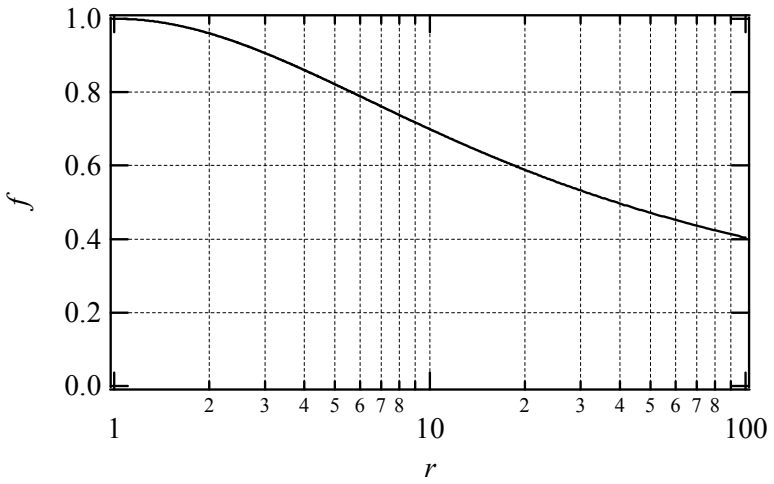

Fig. 1.7. Function f versus r for calculating resistivity (see text).

1.2.2b Hall Bar

Another common geometry used for determining sheet resistivity is the Hall bar, as shown in Fig. 1.8.

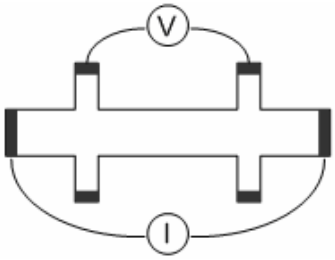

Fig. 1.8. Typical Hall bar geometry.

The bar is designed so that the current distribution is uniform along the width of the bar in the region of the side-arm contacts. The distance between the side arms should be greater than the arm width so that the voltage probes are point-like. Then, the sheet resistivity is given by the longitudinal resistance divided by the number of squares between the voltage probes:

$$\rho_{\square} = \left(\frac{V}{I}\right)\frac{1}{\#\text{ of squares}}.$$

1.2.2c Density and mobility

The 2DES density can be obtained by via Hall resistance measurements (see Chapter 3 for a discussion of transport in a magnetic field), where

$$\rho_H = B_{\perp} / ne,$$

where n is the electron density, $B_{\perp}$ is the magnetic field normal to the 2DES, and $\rho_H = V / I$ (see Fig. 1.9) is the Hall resistance.

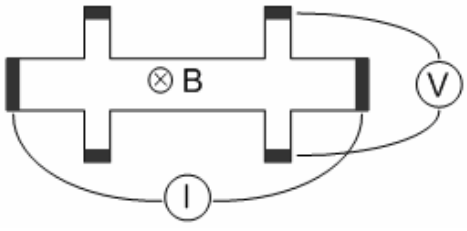

Fig. 1.9. Schematic for measurement of Hall resistance.

An alternative method of determining the density is to use the SdH oscillations of the longitudinal resistance versus magnetic field (see Chapter 3). The positions of the resistance minima are given by $B = hn/\nu e$, where ν is an integer. Then the slope of a plot of B versus $1/\nu$ is a convenient way to obtain the density that is insensitive to offsets in the measurement of the magnetic field. Finally, given the density and the sheet resistivity, the mobility is given by

$$\mu = \frac{1}{\rho_{\square} ne}.$$

1.2.2d Measurement Circuit

One very common measurement performed to obtain the data in this thesis is determination of the longitudinal resistivity of a 2DES in a perpendicular magnetic field. Figure 1.10 shows the typical circuit used for this measurement.

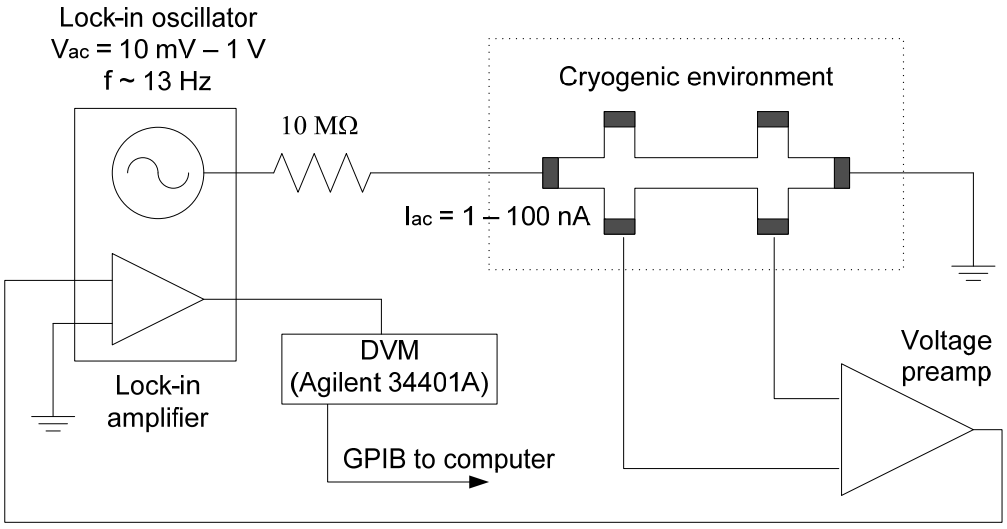

Fig. 1.10. Basic circuit for measurement of longitudinal resistivity.

The four-point measurement of the longitudinal resistivity is made by passing a fixed current through the sample, and measuring the voltage between two contacts on one side of the sample. The measurement is usually performed at low, but finite frequencies

(typically 13 Hz) using lock-in detection to avoid the 1/*f* noise which becomes a problem at very low frequencies in many electronic components such as resistors and transistors. Measurement currents range from I = 1 to 100 nA, depending on the sample geometry and temperature. Large currents can cause Joule self-heating of the 2DES. As shown in Fig. 1.10, a current source is created by placing a 10 MΩ resistor in series with the lock-in oscillator. A low-noise differential voltage amplifier, such as the Princeton Applied Research PAR116, Ithaco 1201, or Stanford Research Systems SR550 voltage preamp, measures across the two voltage probes. The output of this preamp is connected to the input of a lock-in amplifier, either a Princeton Applied Research PAR124A or Stanford Research Systems SRS830 lock-in amplifier. The lock-in output is digitized by a digital volt meter (DMM, Agilent 34401A) and sent to a computer via GPIB. Details about the wiring of the cryostat can be found in the next section.

1.2.3 Cryogenics

Low temperatures are required to see the delicate many-body physics of 2DES's. The majority of measurements discussed in this thesis were performed at low temperatures (down to ~ 15 mK) reached via dilution refrigeration. Some measurements were also performed in a ^{3}He immersion cryostat. The following is an overview of the Oxford 200TL dilution refrigerator, which was used for most of the measurements described in this thesis.

1.2.3a Dilution Unit

Dilution refrigeration can allow one to reach temperatures down to $T \sim 2$ mK. A description of the general principles behind dilution refrigeration, as well as other useful information about cryogenic techniques, can be found in Ref. [9].

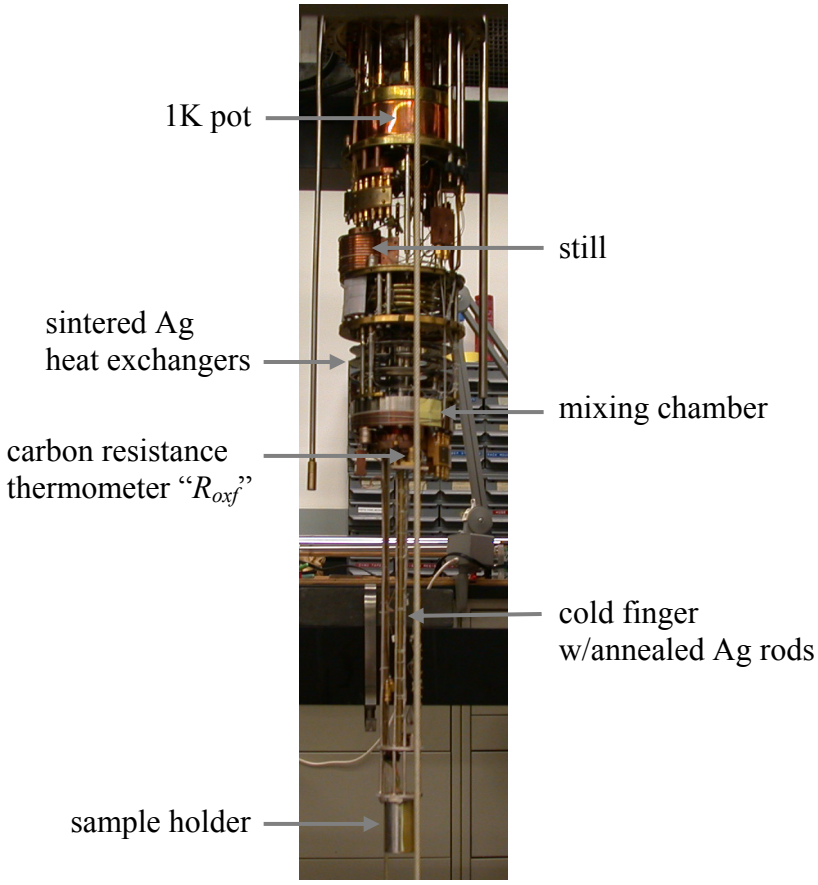

Fig. 1.11. TL 200 dilution unit.

At low temperatures (below 0.87 K) a mixture of ^{3}He and ^{4}He, for a ^{3}He concentration greater than 6%, will separate into two phases, a concentrated phase consisting mostly of ^{3}He and a dilute phase consisting mostly of ^{4}He. Roughly, dilution refrigeration "evaporates" ^{3}He in a ^{3}He - ^{4}He mixture, by passing ^{3}He from the concentrated phase to the dilute phase (~ 6% ^{3}He), where ^{3}He remains soluble in ^{4}He even as $T \rightarrow 0$. Figure 1.11 indicates a few of the main components of the dilution unit. ^{3}He is continuously circulated through the unit using hermetically sealed pumps. The ^{3}He is first condensed at the "1K pot", a reservoir of ^{4}He which is pumped to reach T ~ 1.5 K, a temperature at which the ^{3}He will liquefy (the condenser pressure is usually ~ 100 mBar). The ^{3}He is further cooled on its way to the mixing chamber by heat exchangers, where ^{3}He entering and exiting the mixing chamber is allowed to thermally equilibrate. The condensed liquid ^{3}He then flows into the mixing chamber, which

contains both the dilute and concentrated phase of the ^{3}He - ^{4}He mixture, where the less dense ^{3}He rich phase floats on top of the dilute phase. In the mixing chamber the ^{3}He is passed from the concentrated to dilute phase. The mixing chamber is where the fridge reaches the lowest temperatures. A cold finger, made of very pure, annealed high-thermal conductivity silver, connects the mixing chamber to the sample stage. After exiting the mixing chamber, the ^{3}He passes into the still, where it is evaporated and pumped back into the condenser. The still is heated to increase the ^{3}He circulation rate and is maintained a temperature of roughly $T \sim 0.7$ K. The sealed pumps pump directly on the still, which is connected to the pumps via very wide plumbing lines for maximum pumping speed.

The TL 200 fridge cooling power ($\sim T^2$) is 200 μW at a temperature of 100 mK and the fridge currently reaches a base temperature of ~ 15 mK. This is the cold finger temperature; cooling the electrons in a 2DES sample and determining the electron temperature is generally more challenging. It is difficult to directly determine the electron gas temperature. However, we know that the magnetotransport of 2DES samples continues to evolve down to the lowest fridge temperatures. For example, measurements of the activation energies of various quantum hall states continue to follow the expected Arrhenius trend at low temperatures.

1.2.3b Thermometry and Wiring

The main thermometer is a carbon resistor (R_{oxf}) mounted near the mixing chamber on a silver rod connected directly to the sample stage. The system is equipped with a solenoid magnet providing fields of up to B = 13.75 T at the sample stage (higher fields are available if the lambda fridge is used). The magnetic field at the mixing chamber is kept small via cancellation coils. The R_{oxf} thermometer is placed near the mixing chamber in order to avoid errors due to the magnetic field dependence of the resistivity.

The link between the mixing chamber and the sample is provided by a cold finger consisting of four silver rods (see Fig. 1.11). This silver contains very few impurities (99.999% pure), and has been annealed to reduce the number of grain boundaries, improving the thermal conductivity at low temperatures.

The cryostat wiring consists of semi-rigid coax, manganin wire twisted pairs, and stainless steel flexible coax. At T = 4 K and 1 K heat sinking of the manganin leads is achieved by wrapping the wires around OFHC copper spools. At the "50 mK plate", located below the still, and at the mixing chamber, the leads are heat sunk via Cu-Kapton-Cu laminate heat sinks, where the front-side Cu is patterned into leads that are placed in series with the fridge wiring, and the back-side Cu is clamped (good thermal joint) to the 50 mK plate or mixing chamber. An example of one of these laminate heat sinks is shown in Fig. 1.12.

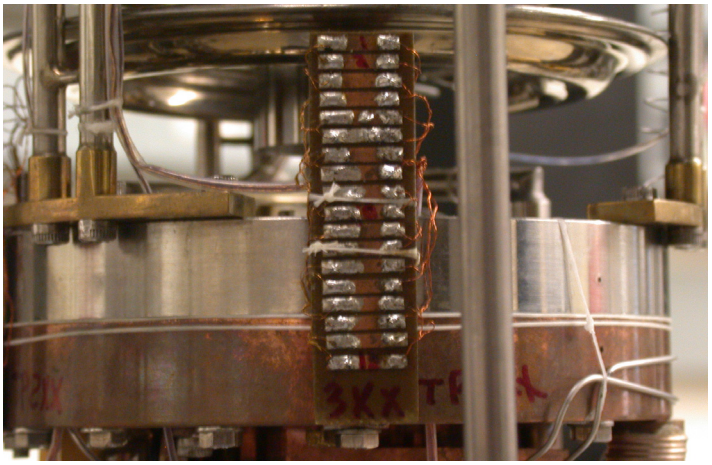

Fig. 1.12. Cu-kapton-Cu laminate heat sinking (center of photo, labeled "TP3XX") of the manganin leads at the mixing chamber.

Additional heat sinking is done for each wire at the sample holder with a series 10 kΩ metal-film resistor and a 500 pF polyester-foil capacitor in parallel to ground (configured like a low-pass *RC* filter).

1.2.3c RF Leads

A description of the RF leads installed in the lab cryostats can be found in Appendix B.

References

[1] H.L. Stormer, R. Dingle, A.C. Gossard, W. Wiegmann and M.D. Sturge, Solid State Commun. **29**, 705 (1979).

[2] E. F. Schubert, J. B. Stark, B. Ulrich, J. E. Cunningham, App. Phys. Lett. **52**, 1508 (1988).

[3] John H. Davies. *The Physics of Low-Dimensional Semiconductors*. Cambridge University Press, Cambridge 1998.

[4] B. E. Kane, L. N. Pfeiffer, and K. W. West, *Appl. Phys. Lett*. **67**, 1262 (1995).

[5] R. F. C. Farrow. Molecular Beam Epitaxy: Applications to Key Materials. Noyes, New Jersey 1995.

[6] Frank Stern and Sankar Das Sarma, *Phys. Rev. B* **30**, 840 (1984).

[7] F. F. Fang and W. E. Howard, *Phys. Rev. Lett.* **16**, 797 (1966).

[8] L.J. van der Pauw, *Philips Technical Review* **20**, 220-224 (1958).

[9] Pobell, F. *Matter and Methods at Low Temperatures*, *2nd ed*. Springer, 1996.

Chapter 2:
Surface Acoustic Wave Propagation in Low density 2DES's near the Metal-Insulator Transition

The apparent metal-insulator transition (MIT) in two-dimensions remains a subject of interest due to the fact that the basic physics of this fundamental topic – the exact nature of the ground state of a two dimensional electron system (2DES) – is still not well understood. Controversy exists over whether this transition is better described as an exotic, interaction-driven phase transition or by more straightforward physics of disordered conductors. This chapter discusses surface acoustic wave propagation in the presence of a 2DES at the low densities where this putative MIT should occur [1].

2.1 The 2D Metal-Insulator Transition

The ground state of a 2DES at zero magnetic field remains an enigma, due to the extreme difficulty of solving the many-body problem of interacting 2D electrons. This is especially true when one tries to incorporate disorder, which is necessary in order to describe actual experimental systems. One aspect of this problem many have focused on is the temperature dependence of the 2DES conductivity as a function of 2DES density. Varying the electron density changes the strength of electron-electron interactions relative to the kinetic energy and also varies both of these energy scales relative to the strength of the disorder. Experimentally and theoretically, there is some evidence suggesting a transition from metallic to insulating behavior upon varying the density.

The following is a brief overview of experimental data and theoretical arguments regarding the apparent MIT. The reader is referred to two review articles [2, 3] which take opposite viewpoints regarding the nature of this transition and review much of the experimental and theoretical literature relevant to this topic.

2.1.1 Previous Experiments

The definition of a metal versus an insulator is given by the temperature dependence of the resistivity. For a metal, the resistivity remains finite as the temperature goes to zero, and for an insulator the resistivity will diverge in the zero temperature limit. An apparent

MIT has been experimentally observed in some systems as the density of the 2DES is tuned. Previous experiments [2 - 5] have shown that at low densities the 2DES appears insulating – the resistivity increases with decreasing temperature at the lowest accessible temperatures, while at high densities resistivity continues to decrease with decreasing temperature, raising the possibility of a metallic phase at high densities. At some intermediate density, the resistivity looks temperature independent, and frequently this point is then identified as the critical density at which the MIT occurs. However, all data is taken at finite temperatures, so it is hard to say what will actually happen as the temperature is lowered further. This problem is further exacerbated by the fact that some predictions for the insulating behavior of the resistivity, such as contributions from weak localization, give a very weak, logarithmic temperature dependence, which will be difficult to observe and, at experimentally accessible temperatures, may be masked by other contributions from, for example, phonon scattering.

2.1.2 Theoretical Expectations

The apparent metal-insulator transition came as a surprise. The standard picture (somewhat controversial) is that a "metallic" state is not expected to exist in two dimensions, at least for non-interacting electrons.

Non-interacting picture

For high enough 2DES densities, the electron-electron interactions are relatively weak compared to the kinetic energy. This is due to the fact that the Fermi energy scales linearly with density, $E_F \propto n$, while for the Coulomb interaction $E_C \propto \sqrt{n}$. We first examine this high-density limit, ignoring the effect of electron-electron interactions.

Classical Drude conductivity

Within the Drude picture the 2DES resistivity is given by

$$\rho_{CL} = \frac{m}{ne^2\tau_m},$$

$$\frac{1}{\tau_m} = \frac{1}{\tau_i} + \frac{1}{\tau_{ie}},$$

where $1/\tau_m$ is the momentum relaxation rate (the rate at which the electron undergoes a collision that alters its initial momentum), $1/\tau_i$ is the impurity scattering rate, and $1/\tau_{ie}$ is the inelastic scattering rate. As the temperature is reduced, the inelastic relaxation rate vanishes and the resistivity should become a constant $\rho_0 = m/ne^2\tau_i$ as $T \to 0$, where ρ_0 is commonly referred to as the residual resistivity.

Weak localization

Next, including quantum corrections, for a non-interacting 2DES and a small amount of disorder the electron gas is expected to be weakly localized. More precisely, weak localization occurs when $l_\phi \gg l_m$, where l_m is the mean free path and l_ϕ is the phase-relaxation length. The mean free path is the distance an electron travels between collisions which alter its momentum. The phase-relaxation length is the distance an electron travels before its phase is destroyed due to inelastic collisions (typically due to phonon or electron-electron scattering – see [6] for further discussion of l_m and l_ϕ). In this regime, there is a small correction to the conductivity that one would have obtained by simple application of Ohm's law:

$$\sigma = \sigma_{CL} - \frac{2e^2}{\pi h}\ln(l_\phi / l_m), \tag{1}$$

where σ_{CL} is the classical prediction for the conductivity. This reduction in conductivity from the classical value is due the fact that it is more probable for phase-coherent electrons to backscatter. Performing a sum of the scattering amplitudes over all backscattering paths and the time-reversed versions of those paths leads to a factor of two increase in the total backscattering probability over the classical, non-coherent version of this sum, which would sum over the scattering probabilities, not the amplitudes.

Lowering the temperature tends to lengthen the phase-relaxation length. At low enough temperatures, electron-electron scattering will dominate over the effect of phonons. Electron-electron scattering increases as the temperature is raised and states k_BT above and below the Fermi level are filled and emptied. Thus, the weak localization

contribution causes a decrease in the conductivity as the temperature is lowered, giving rise to insulating behavior.

Electron-electron interactions

There is another correction to the temperature dependence of the conductivity due to electron-electron interactions. This term looks similar in form to the weak localization correction, having a logarithmic temperature dependence [7]:

$$\delta\sigma \approx -\frac{e^2}{\pi h}\ln\left[(v_F / l_m)(\hbar / k_B T)\right].$$

Thus, adding weak interactions strengthens the insulating temperature dependence of the weakly-localized state.

Strong localization

For large enough disorder such that $l_m k_F \sim 1$, the 2DES is strongly localized. The conductance in this regime is of order or less than e^2/h. Conduction occurs via variable range hopping from localized site to site. Efros and Shklovskii [8] argue that the temperature dependence of the conductivity is given by $\sigma \sim \left(T^{-1}\right)\exp(-\alpha / T^p)$, where p = 1/2.

Scaling theory

The scaling theory of localization [9] predicts how the conductance G of a square sample of size L^2 scales with system size at zero temperature. Based on various analytical arguments, the theory says that there is a scaling parameter β which is a function of only the dimensionless conductance $g \equiv G/(e^2/h)$, where

$$\beta\left[\ln(g)\right] = \frac{d\ln g}{d\ln L}.$$

The behavior of this scaling function can be determined by examining some limiting cases. For large, finite conductivities the 2DES is weakly localized and depends on sample size like

$$\sigma(L) = \sigma(l_m) - \frac{2e^2}{\pi h}\ln(L/l_m),$$

where L replaces l_ϕ in Eq. 1 in the zero temperature limit since $l_\phi \to \infty$. Then

$$\beta \propto \frac{1}{g}.$$

As a check, in the limit $g \to \infty$, the metallic limit, we obtain $\beta \to 0$ which gives Ohm's law. For small conductivities, strong localization requires that the conductance fall exponentially with length:

$$\sigma(L) \propto \exp(-\alpha L).$$

Then

$$\beta = \ln(g/g_0),$$

where g_0 is a constant of order unity. For intermediate conductivities, it is argued on physical grounds that the scaling parameter should be a smooth function of ln(g). The resulting prediction for β is shown in Fig. 2.1. For reference, Fig. 2.1 also shows the scaling for conductance in one and three dimensions as well. In general, in order to obtain Ohm's Law in the large conductivity limit, we require $\beta \to d-2$ as $g \to \infty$, where d is the dimensionality.

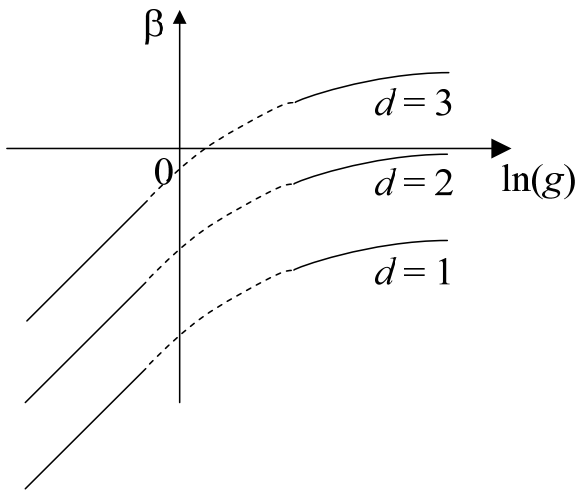

Fig. 2.1. Scaling of conductivity as proposed by Ref. [5], where d is the dimensionality.

For $d = 2$, at all finite conductivities, $\beta < 0$ implies that all states are localized. Thus, the prediction of scaling theory is that no metallic state should exist in two dimensions.

The case of strong interactions

On the other extreme, we can ignore disorder but consider the case of strong electron-electron interactions. Quantum Monte Carlo calculations predict that the two-dimensional electron gas should crystallize at large r_s, where $r_s = E_C / E_F \sim n^{-1/2}$ is a dimensionless parameter determining the relative importance of interactions, where E_C is the Coulomb energy and E_F is the Fermi energy. The most recent calculations of Attaccalite *et al.* [10] predict that the lowest energy ground state for $r_s > 35$ is a Wigner crystal. Any small amount of disorder should then pin this crystal, leading to insulating behavior at low temperatures.

Summary

In reality none of the above mentioned limiting cases completely describe actual experimental systems. When both disorder and strong interactions play a strong role the conclusions become less clear. Interpretation of both theory and experiment in the putative MIT regime remain difficult and controversial.

2.2 Introduction to Surface Acoustic Waves

We next discuss experiments involving surface acoustic wave (SAW) propagation near a 2DES in the MIT regime. Several aspects of SAW's make them an interesting probe of low-density 2DES's. We first introduce SAW's and their interaction with 2DES's.

2.2.1 Surface Acoustic Waves

SAW's can be used to study the frequency and length-scale dependent conductivity of two-dimensional electron systems. A SAW is an elastic wave that travels on the surface of an elastic body and whose energy is confined to a depth of about one wavelength below the surface. Because GaAs is piezoelectric, a SAW will interact with a 2DES located near (within one SAW wavelength) the sample surface.

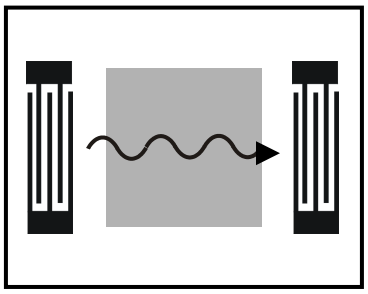

Fig. 2.2. Schematic of SAW propagation across a region containing a 2DES (shaded region), launched and detected by interdigitated transducers.

One can use the piezoelectricity of GaAs to launch and detect SAW's by placing interdigitated metallic transducers on either side of the region containing a 2DES (see Fig. 2.2). By applying a potential between the fingers at the resonant frequency of the transducer, which is where the wavelength of the SAW matches the period of the transducer, one can create an elastic distortion and launch a surface acoustic wave across the 2DES region, which is then received by a second transducer. The interdigitated transducers can be created with either optical or e-beam lithography, depending on the desired SAW wavelength. For further reading, see Appendix C, which describes SAW propagation in GaAs and details about SAW transducer operation.

2.2.2 SAW Interaction With a 2DES

The electric potential created by the SAW will be screened by a 2DES located near the sample surface. This screening will affect both the velocity and amplitude of the SAW. The resulting attenuation and velocity shift are given by [11]

$$\Gamma = k\frac{K_{eff}^2}{2}\frac{\sigma/\sigma_M}{1+(\sigma/\sigma_M)^2}, \tag{2}$$

$$\frac{\Delta v}{v} = \frac{K_{eff}^2}{2}\frac{1}{1+(\sigma/\sigma_M)^2}, \tag{3}$$

where Γ is the attenuation per unit length, v is the SAW velocity, k is the SAW wavevector, K_{eff}^2 is a piezoelectric coupling coefficient with a value of approximately 6.4 $\times 10^{-4}$, σ is the electron gas conductivity, and σ_M is a characteristic conductivity. K_{eff}^2 and σ_M vary with kd, where d is the 2DES depth (see Appendix C, section C.1.3). The velocity change $\Delta v \equiv v(\sigma) - (\sigma \gg \sigma_M)$ is referenced to the SAW velocity in the presence of a perfect conductor ($\Delta v \to 0$ as $\sigma \to \infty$).

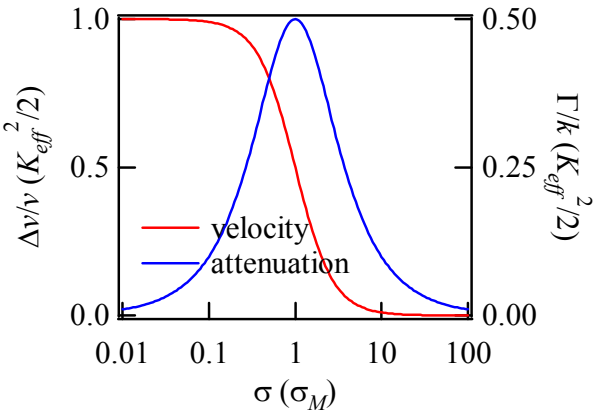

Fig. 2.3. Dependence of SAW attenuation and velocity shift on 2DES conductivity from Eq.'s (2) and (3).

For conductivities below σ_M, the amplitude and velocity of the SAW is unaffected by the 2DES and propagates as in bulk GaAs. As shown in Fig. 2.3, for conductivities comparable to or greater than σ_M, the screening of the piezoelectric potential causes

attenuation and a decrease in the SAW velocity. The value of σ_M can be crudely understood by considering the capacitive charging of the 2DES. Consider a square patch of 2DES of area λ^2, where λ is the SAW wavelength. To screen the piezoelectric potential, the charge on this patch must be rearranged to match the SAW potential. If we set the *RC* time constant for this charging equal to the SAW period, λ/v_s, we find that $R \sim 1/\varepsilon v_s \sim 1/\sigma_M$.

The above model has been successfully applied to SAW propagation in 2DES's in GaAs/AlGaAs heterostructures in the quantum Hall [12] and fractional quantum Hall [13] regimes. Interestingly, there are exceptions to the applicability of the above model when the SAW wavelength becomes comparable to some other 2DES length scale, as was seen near Landau level filling factor $\nu = 1/2$ where the SAW absorption by the 2DES was enhanced due to a geometric resonance effect for composite fermions [14].

2.3 Experiment

Because σ_M is a very low conductivity (for our experimental conditions $\sigma_M \sim 7 \times 10^{-7}\ \Omega^{-1}$), SAW's will be very sensitive to the 2DES conductivity at low 2DES densities, near the conditions required to observe the MIT. SAW's then allow investigation of the frequency or length scale dependence of the conductivity in this regime. Also, SAW's sample the 2DES conductivity in a different way than ordinary four-point resistance measurements; for example, a very inhomogeneous 2DES containing isolated patches with conductivity greater than σ_M separated by regions with zero conductivity will cause a non-zero SAW velocity shift, while the four-point resistance of the sample may appear infinite.

2.3.1 Overview

The samples used in this experiment are modulation doped GaAs/AlGaAs heterostructures. Most of the data is from a structure where a 2DEG is formed at a single GaAs/AlGaAs interface. The as-grown density of this 2DES is $n = 1.4 \times 10^{11}$ cm^{-2} with a corresponding mobility about 3×10^6 cm^2/Vs at low temperatures. The 2DES is confined to a 2 mm × 2 mm square mesa. A single ohmic contact and a top gate allow one to change the 2DES density and determine the 2DES conductivity via a low-frequency

admittance measurement. Interdigitated SAW transducers are placed on either side of the region containing the 2DES. The SAW fractional velocity shift is measured using standard homodyne techniques, using a phase-locked loop (PLL). Simultaneous SAW and admittance measurements were done in a ^{3}He immersion cryostat at a temperature of $T \sim 0.3$ K and additional admittance measurements were also performed at lower temperatures down to 50 mK in a dilution refrigerator.

2.3.2 Phase-Locked Loop (PLL)

The use of a phase-locked loop (PLL) provides a frequency and phase sensitive method of measuring SAW velocity shifts. The PLL measurement results in better noise rejection than simple rectification and amplitude detection.

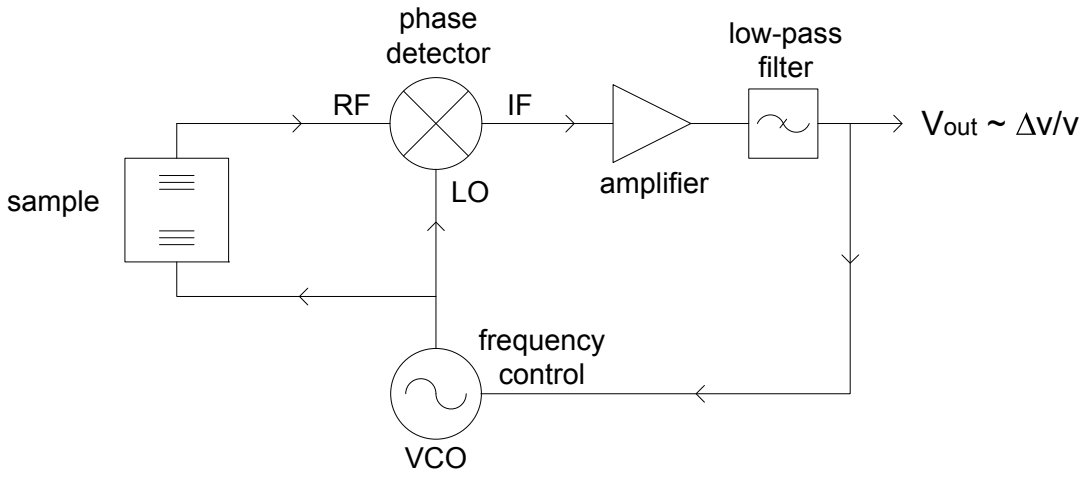

Fig. 2.4. Simplified PLL circuit for SAW $\Delta v/v$ measurements.

Figure 2.4 shows a simplified diagram of the PLL. The signal generator is a voltage-controlled oscillator (VCO) which drives the sample and the LO of the phase detector at a frequency $f = f_{\text{base}} + \mathrm{d}f/\mathrm{d}V \times V_{out}$. The phase detector in this loop is a mixer which multiplies the RF and LO signals. The voltage at the IF output is the result of this multiplication, *i.e.*

$$V_{IF} \propto V_{LO} \times V_{RF} = V_1 \sin(\omega t) V_2 \sin(\omega t + \phi) = \frac{V_1 V_2}{2}\left[\cos(2\omega t + \phi) - \cos(\phi)\right],$$

where $\omega = 2\pi f$, $V_{LO} = V_1 \sin(\omega t)$, and $V_{RF} = V_2 \sin(\omega t + \phi)$. Thus, the IF output consists of a dc component ~ cos(ϕ) plus a component at 2*f*. If the low-pass filter following the IF output has a passband much less than 2*f*, then only the cos(ϕ) term will determine V_{out}. To get a rough understanding of how the loop works, consider, for example, a situation where f_{base} is set to a value such that the initial phase difference ϕ_t between the RF and LO is $\phi_t = \pi/2 + \pi n$, where *n* is an integer. Then, we have V_{out} = 0, and the VCO frequency will remain at $f = f_{base}$. However, if $\phi_t \neq \pi/2 + \pi n$ and the sign of the amplifier gain at the phase detector IF output is set correctly (for negative feedback), then upon closing the loop, the circuit will attempt to minimize the frequency control voltage. It will do so by driving the VCO frequency to a value that brings ϕ to some new value ϕ_0 near $\pi/2 + \pi n$. After ϕ_0 is established, the loop will adjust the frequency in order to maintain a roughly constant $\phi = \phi_0$, for small SAW velocity changes.

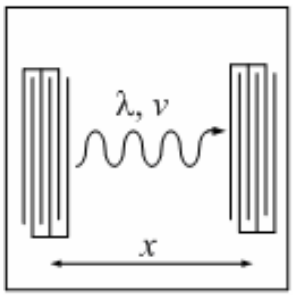

Fig. 2.5. Sample with SAW path length *x*.

To see roughly how this circuit allows measurement of SAW $\Delta v/v$, consider the loop in an initial condition where the SAW velocity and wavelength have initial values $v = v_0$ and $\lambda = \lambda_0$, respectively. Then, let the conductivity of the electron gas change so that the SAW velocity changes to some new value $v_0 + \Delta v$, and the SAW wavelength changes to $\lambda_0 + \Delta\lambda$. Because the majority of the time delay between the RF and LO occurs in the SAW sample, not the coaxial leads, the phase difference between the RF and LO at the phase detector is determined by $\phi = 2\pi x f / v$ (see Fig. 2.5). The PLL will try to maintain

a constant phase difference ϕ by adjusting the frequency f so that x/λ is held constant. Since $x/\lambda = xf/v$ is held constant, we have $\Delta f/f_0 = \Delta v/v_0$, where $\Delta f = f - f_0$ (f_0 is defined as the frequency when $\Delta v = 0$). Then, the SAW velocity shift is simply given by the VCO control voltage (plus an offset that depends on the choice of the base frequency of the VCO): $\Delta v / v_0 = \left(f_{base} - f_0 \right) / f_0 + df / dV \times V_{out} / f_0$.

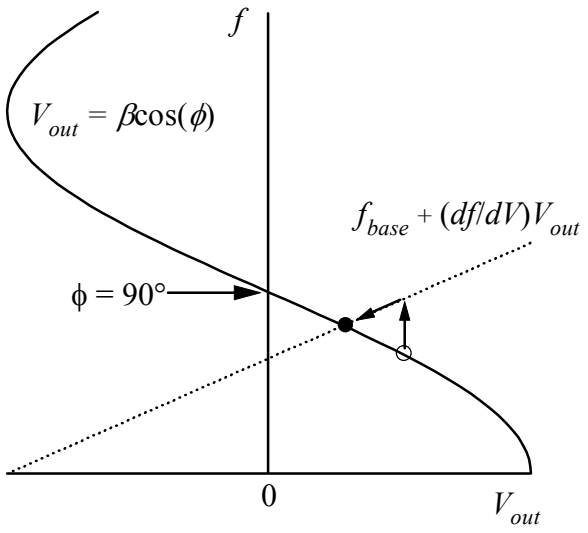

Fig. 2.6. Convergence of PLL. The solid trace shows the amplified and filtered mixer IF output, $V_{out} = \beta \cos(\phi)$, where $\phi = 2\pi xf / v$. The dotted line is the VCO frequency. The open circle represents the initial state of the PLL, prior to connecting V_{out} to the VCO frequency control input, where $f = f_{base}$ and $V_{out} = \cos\left(2\pi x f_{base} / v_0\right)$. The small arrows show the convergence of f and V_{out} to equilibrium after the loop is closed. The solid circle marks the equilibrium f and V_{out}.

Figure 2.6 sketches the initial behavior of the loop. The dotted line shows the VCO frequency and the solid line shows the amplified and filtered mixer IF output. Before the loop is closed (frequency control input disconnected), $f = f_{base}$ and $V_{out} = \cos\left(2\pi x f_{base} / v_0\right)$, as indicated by the open circle in Fig. 2.6. After the PLL is closed, the VCO moves to a new frequency, as determined by V_{out}. The sequence of arrows from the open to closed marker in Fig. 2.6 indicates how the loop converges to the equilibrium values of f and V_{out}. We have assumed that the VCO frequency responds quickly compared to the bandwidth of the low pass filter, which is the case for our actual measurement circuit. It is also visually clear from Fig. 2.6 that for large amplitude β, the

intersect of $f_{base}+(df/dV)V_{out}$ and $\beta\cos(\phi)$ will occur near where $\cos(\phi)=0$, *i.e.* $\phi\sim 90°$.

Writing down the voltages at various points in the loop, we have

$$V_{out} = gV_{IF}$$
$$V_{IF} = \alpha V_1 V_2 \cos(\phi)$$
$$\Delta f = (f_{base} - f_0) + (df/dV)\times V_{out},$$

where g is the gain of the amplifier, α is a constant determined by the mixer specifications, f_{base} is the frequency of the VCO when $V_{out} = 0$, f_0 is the frequency when the loop is initially closed and $\Delta v = 0$, and V_1 and V_2 are the magnitude of the voltages at the mixer LO and RF terminals. Now, ϕ is determined by f, v, and path length x, as shown in Fig. 2.5:

$$\phi = 2\pi xf/v.$$

Then,

$$(f - f_{base})/f_0 = \beta\cos(2\pi xf/v),$$

where $\beta \equiv (df/dV)g\alpha V_1 V_2/f_0$. For large loop gain β and choice of f_{base} such that $\left|(f-f_{base})/(\beta f_0)\right| \ll 1$, we can write

$$2\pi xf/v = \cos^{-1}\frac{(f-f_{base})}{\beta f_0}$$
$$\approx \phi_b \pm \frac{(f-f_{base})}{\beta f_0},$$

where $\phi_b = 3\pi/2 + 2\pi n$ or $\pi/2 + 2\pi n$, for some integer n. Then

$$v \approx (2\pi x/\phi_b)\left(1 \pm \frac{f-f_{base}}{f_0\beta\phi_b}\right)f \approx (2\pi x/\phi_b)f.$$

Thus, *v*/*f* is held approximately constant, which implies that $\Delta v / v_0 \approx \Delta f / f_0$.

2.3.2 Measurement Setup

Figure 2.7 shows a diagram of the actual SAW $\Delta v/v$ measurement circuit. This circuit is similar to that of the basic PLL loop shown in Fig. 2.5; however a few more components are needed in order to take care of technical details. In practice, the measurement is pulsed, rather than cw. The main reason for this is to avoid the signal due to capacitive coupling between the input and output SAW transducers. The measurement is pulsed at a repetition rate of about 10 kHz with a pulse length ranging from 0.1 to 1 μs. The pulsed measurement allows one to separate out the SAW signal (delayed in time by the sample size / speed of sound) from the nearly instantaneous signal due to capacitive coupling. Switch "C" pulses the input RF to the sample and switch "G" gates the RF output from the sample, rejecting the capacitively coupled signal and keeping only the SAW signal. The best pulse length to use is the longest pulse possible (to get the narrowest bandwidth to reject noise) without having any overlap between the capacitively coupled signal and the SAW signal. The SAW frequency typically ranges from about 100 MHz to 2 GHz.

Mixer "L" is a level 7 mixer, meaning that +7 dBm should be applied to the LO input. In order to avoid dc offsets at the mixer IF output, the RF level should be kept below 7 dBm. However, if the RF input voltage is too small, there may be insufficient gain and the mixer may add noise to the measurement. RF levels between 0 and 7 dBm are recommended. The attenuator "K" can be used to adjust the RF level.

The low-pass filter shown in Fig. 2.5 has been replaced in the circuit of Fig. 2.7 by a boxcar integrator. A boxcar integrator is a gated integrator, which accepts incoming signals during a user-defined period of time, and rejects signals for all other times. The boxcar integrates this accepted signal over the length of the gate and then averages this integrated signal for a desired number of repetitions. The gate length is set approximately equal to the length of the RF pulse sent to the sample. Typically, 1,000 – 10,000 cycles were averaged via the boxcar integrator in this experiment. At a repetition rate of 10 kHz, this gives a measurement time constant in the range of 0.1 to 1 sec

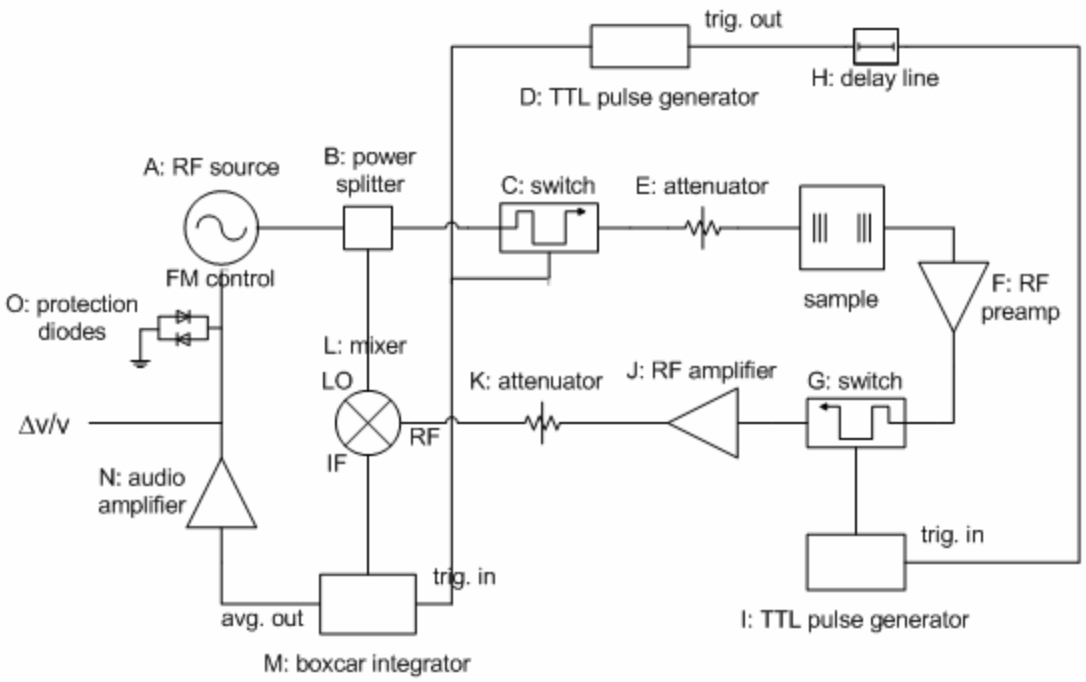

Parts list:

A. HP8648B RF signal generator, with frequency modulation (FM) control
B. MiniCircuits ZFSC-2-2500 power splitter, 0º phase shift.
C. MiniCircuits ZASW-2-50DR PIN diode switch.
D. HP8116A function generator
E. MiniCircuits VAT-X attenuator
F. Miteq JS2 low noise RF preamp
G. MiniCircuits ZASW-2-50DR PIN diode switch
H. Advance Electronics 605B variable delay line
I. Wavetek 183 XCG/Sweep generator
J. MiniCircuits ZKL-2 RF amplifier
K. MiniCircuits VAT-X attenuator
L. MiniCircuits ZFM-2000 mixer
M. SRS280 boxcar integrator
N. PAR113 audio amplifier
O. Overvoltage protection diodes (1N914) for FM input

Fig. 2.7. Complete SAW $\Delta v/v$ measurement circuit and parts list.

.

The protection diodes "O" protect the HP8648B RF signal generator FM input from excessive voltages (which could occur, for example, if one set the loop gain β to have the wrong sign). The instrument may be damaged for voltages $|V_{FM}| > 1$ V.

The initial RF preamp "F" (Miteq JS2 low-noise preamp) was the main source of noise in the $\Delta v/v$ measurement. This preamp has a gain of about 36 dB and noise figure NF ≈ 0.6 dB at frequencies ranging from 0.2 – 2 GHz. This translates to a voltage noise contributed by the amplifier alone (i.e., for a cold source resistance) of 0.35 nV/$\sqrt{\text{Hz}}$, referred to the amplifier input. If one were to look at the amplifier output over its entire bandwidth (~ 0.2 – 2 GHz), this would correspond to a total noise of about 15 μV rms, referred to the amplifier input. The PLL measurement, however, can use a narrower bandwidth. The SAW signal received by the high-frequency preamplifier is a 0.2 to 2 GHz signal lasting for a pulse length of τ = 0.1 to 1 μS. This signal is amplified and sent to the mixer. The mixer IF output has roughly the same shape as the pulse envelope function, which is a square pulse of length τ. The Fourier transform of this envelope has a width ~ $1/\tau$ ~ 1 – 10 MHz. This is the minimum bandwidth needed to measure the mixer IF signal. The boxcar integrator rejects frequencies below $1/\tau$ by gating the incoming signal and removes frequencies above $1/\tau$ via integration over the gate width. Now, with this reduced bandwidth, the total noise, referred to the preamplifier input is 0.4 – 1 μV rms.

Unwanted fluctuations in the PLL output voltage are mostly due to fluctuations in the RF preamp output. The amount of rms phase noise accepted by the PLL is $\delta\phi = (\delta V / V)/\sqrt{2} \times \sqrt{\text{BW}}$, where δV is the spectral rms voltage noise density of the preamp, V is the SAW signal rms voltage at the output transducer, and BW ~ $1/\tau$ is the bandwidth. For large loop gain, the phase ϕ between the mixer LO and RF inputs is held roughly constant. Then,

$$\phi = 2\pi x(f_0 + \Delta f + \delta f)/(v_0 + \Delta v) + \delta\phi$$

is held constant, where δf is the change in f induced by the phase noise (we define Δf as the ideal frequency shift one would measure with no preamp noise). Then, for $\Delta f / f_0,\ \Delta v / v_0 \ll 1$ and fixed Δv (and thus Δf), we have

$$\delta f / f_0 = \frac{v_0}{2\pi x f_0} \delta\phi .$$

Using the above expression for phase noise, the rms fluctuations in the frequency are

$$\delta f / f_0 = (\delta V / V) \frac{v_0}{2^{3/2} \pi x f_0} \times \sqrt{\mathrm{BW}} .$$

To compare with experiment, we next estimate the expected fluctuations in the measurement of $\Delta v/v$ due to the preamp phase noise for typical experimental conditions. For a pulse width of 1 μS, a rms voltage at the SAW output transducer V = 10 μV, and a SAW frequency of f_0 = 1 GHz, we find $\delta f/f_0 \sim 10^{-5}$. By averaging over N = 10,000 cycles, this error is reduced by another factor of $1/\sqrt{N}$ = 1/100, so that $\delta f/f_0 \sim 10^{-7}$. This estimate is in rough agreement with the fluctuations seen in $\Delta v/v$ in Fig. 2.8.

2.4 Data and Discussion

2.4.1 SAW $\Delta v/v$ Gate Voltage Dependence

Figure 2.8 shows SAW fractional velocity shift $\Delta v/v$ at 671 MHz as a function of top gate voltage V_g. The two curves correspond to data from two different devices: one where the surface acoustic waves travel along the [110] direction, and the other along the $[1\bar{1}0]$ direction. As a negative gate voltage is applied, the density of the 2DES is reduced. We first concentrate on the gate voltage dependence of $\Delta v/v$ at smaller gate voltages.

The linear dependence of $\Delta v/v$ on V_g for gate voltages V_g > -1.6 V was not initially expected and is actually due to the fact that the SAW $\Delta v/v$ measurement is a very sensitive method of detecting changes in sample strain. Applying a voltage between the gate and 2DES creates a strain in the GaAs through the piezoelectric effect (see Appendix C). An electric field in the [001] direction causes a shrinkage along the [110] direction and an expansion along the $[1\bar{1}0]$ direction, and vice-versa for an electric field of opposite sign. Using the piezoelectric coupling constant e_{14} and elastic moduli for GaAs, one can make a simple estimate of the strain and thus the slope of the $\Delta v/v$ versus V_g

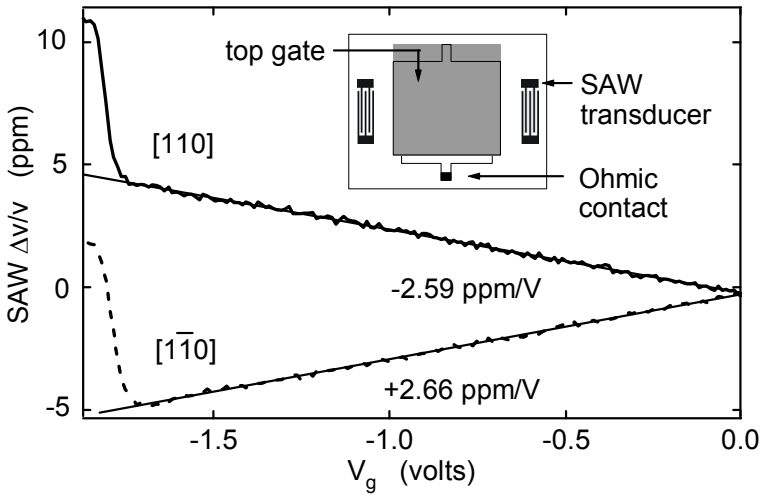

Fig. 2.8. SAW fractional velocity shift $\Delta v/v$ at 671 MHz as a function of top gate voltage in two 2DES samples cut from the same MBE wafer. The two traces correspond to SAW propagation in two orthogonal directions, along the [110] and [1 $\bar{1}$0] crystalline axes. The linear portion of the data for V_g > -1.6 V is due to a piezoelectric-induced strain, while the steep rise in $\Delta v/v$ near V_g = -1.7 V is due to the depletion of the 2DES.

curve: $S_4 = (e_{14}/c_{44})(V_g/d)$, where d is the 2DES depth. This yields a predicted velocity shift of ~ 5 ppm/V, which is similar in magnitude to the experimentally observed slope. This estimate assumes the strain is uniform throughout the region of SAW propagation, which will not be true for regions of the sample outside of the 2DES mesa region or for depths below the 2DES mesa (~ 1 μm tall). The data of Fig. 2.8 are an experimental demonstration of breaking the rotational symmetry of GaAs with a gate. This effect is usually ignored, but may have implications for some 2DES experiments, such as the density dependence of the anisotropic transport seen in high Landau levels [15].

2.4.2 Frequency Dependence

Next we focus on the step in the velocity shift seen at very low density, at the end of the linear strain-induced effect. This step in the velocity roughly corresponds to the conductivity of the electron gas passing through the value σ_M as the density is lowered. Fig. 2.9 shows this step for measurements taken at various frequencies, corresponding to harmonics of the interdigitated SAW transducers − the 1st harmonic up to the 11th. This corresponds to frequencies ranging from about 120 MHz to 1.3 GHz and wavelengths

ranging from approximately 24 to 2 microns. The difference in the size of the step for the various frequencies is due to fact that the top gate screens the interaction between the surface acoustic wave and the 2DES by different amounts depending on the SAW wavelength. The inset shows all of these curves normalized by the step size. The fact that all of these curves lie on top of one another demonstrates that there is no visible length scale or frequency dependence. We shall return to this point later.

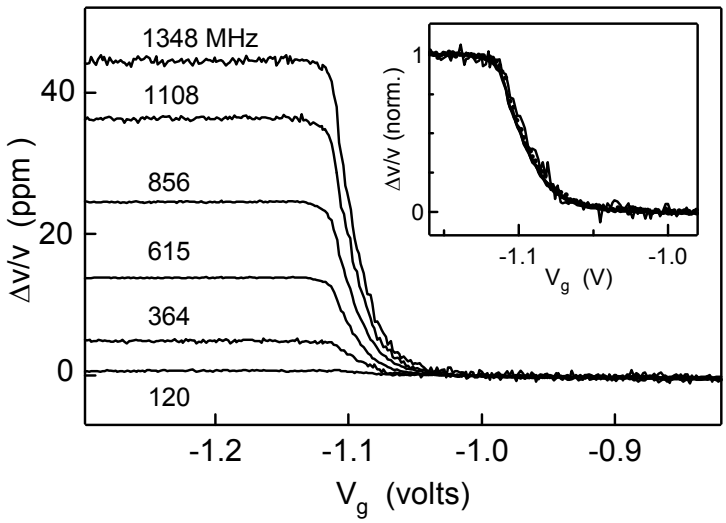

Fig. 2.9. Depletion-induced step in SAW velocity shift vs. gate voltage at several frequencies. Inset: collapse of same data sets onto a single curve after normalization by the total step in $\Delta v/v$ at each frequency. The 120 MHz data is not included due to its much lower signal-to-noise ratio.

2.4.3 DC Conductivity

To measure the quasi-DC conductivity (at audio frequencies) of the electron gas we measure the admittance between the top gate and ohmic contact. Fig. 2.10 shows the imaginary and real parts of the admittance versus dc gate voltage. Both traces have been normalized by ωC, the product of the angular frequency and the gate-2DES capacitance, $C = 670$ pF. At small gate voltages the conductivity of the 2DES is much greater than the conductance ωC so that the circuit looks just like a capacitor. When ωC becomes roughly equal to the conductivity of the 2DES, the imaginary and real parts of the admittance become nearly equal. Then, as the conductivity of the electron gas is lowered

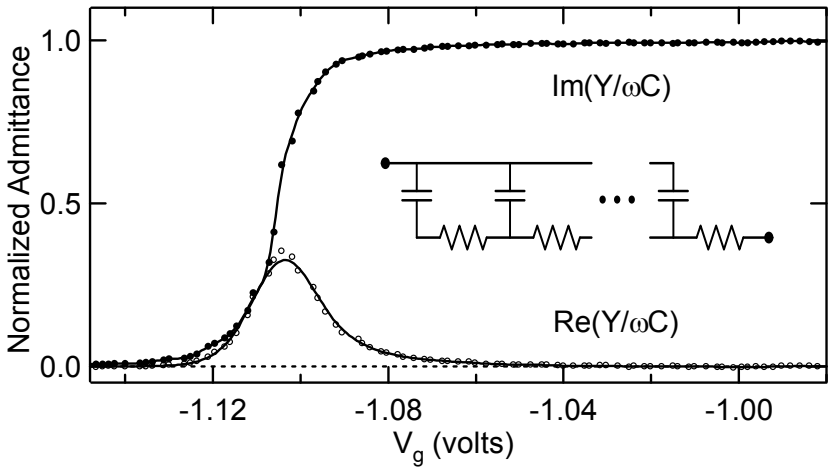

Fig. 2.10. Real and imaginary parts of the gate-2DES admittance, normalized by ωC, measured at 1.3 kHz. The inset is a schematic of the circuit model used to extract the 2DES conductivity from the admittance data.

further, the admittance drops to zero. The sample layout (see inset to Fig. 2.8) is such that the admittance is well-described by a 1-D distributed RC circuit model, which can then be used to calculate the electron gas conductivity from the admittance measurements. Measurements were made at frequencies ranging from 10 Hz – 10 kHz. Data near the peak in the real part of the admittance (where the measurement is most sensitive to the 2DES conductivity) was used to extract the 2DES conductivity using this 1-D distributed circuit model.

Figure 2.11 shows an enlarged schematic of the sample layout, where V_g is the dc gate voltage used to modify the 2DES density and V_{in} is the small ac voltage used to measure the admittance between the top gate and ohmic contact.

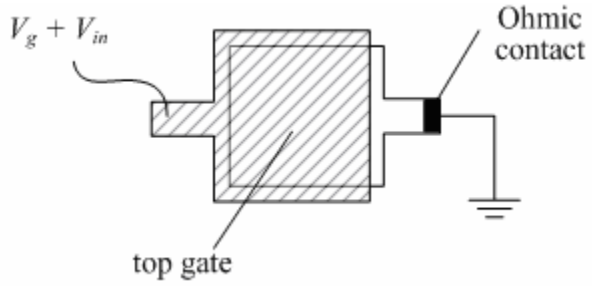

Fig. 2.11. Schematic of sample layout.

A small strip of 2DEG is left ungated on the ohmic contact side of the sample. We operate in a regime where the ungated strip has relatively high conductivity compared to the gated area. This allows us to model the gate-2DES admittance as a 1-D distributed *RC* circuit.

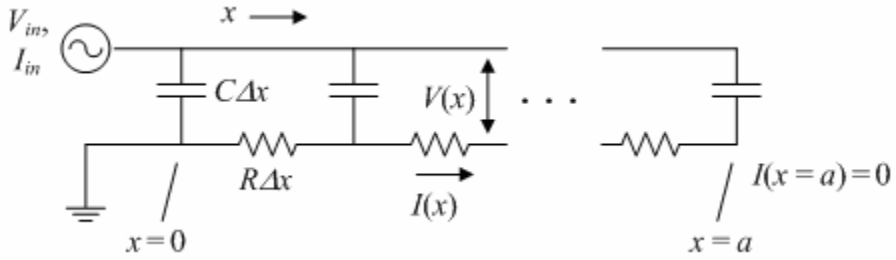

Fig. 2.12. Distributed circuit model.

Fig. 2.12 shows this circuit model, which is basically a transmission line circuit with a resistance replacing the usual inductance, where *C* is the capacitance per unit length, *R* is the resistance per unit length, and *a* is the length of the gated 2DES region. We solve for the admittance in the limit $\Delta x \to 0$. Then

$$\frac{\partial V}{\partial x} = IR,$$

and

$$\frac{\partial I}{\partial x} = -\omega C(V_{in} - V),$$

with the boundary condition requirement that $I(x=a)=0$. We wish to know the admittance $1/Z = I_{in}/V_{in}$ in terms of *R* and *C*. The result is

$$\frac{V_{in}}{I_{in}} = \frac{Z_0}{\tanh(\gamma a)}, \tag{4}$$

where

$$\gamma = \frac{1+i}{\sqrt{2}}\sqrt{R\omega C}, \tag{5}$$

$$Z_0 = \frac{1-i}{\sqrt{2}}\sqrt{\frac{R}{\omega C}}.$$

To check some limiting cases,

for $\gamma a \ll 1$,

$$Z \approx \frac{1}{i\omega C} + R$$

and for $\gamma a \gg 1$,

$$Z \approx \frac{1-i}{\sqrt{2}}\sqrt{\frac{R}{\omega C}}.$$

To obtain the 2DES conductivity, the gate-2DES admittance is measured and Eq's (4) and (5) are numerically inverted to solve for R. The admittance measurement is most sensitive to the 2DES conductivity when $R \sim 1/\omega C$, so measurements are made at several frequencies in order to obtain good resolution over a wide range of conductivities.

2.4.4 Temperature Dependence

Figure 2.13 shows the resulting low-frequency conductivity as a function of gate voltage and density. The calibration of density versus gate voltage was obtained by measuring the magnetic field dependence of the gate-2DES admittance. The minima in the imaginary part of the admittance correspond to an integer number of filled Landau levels. The density was determined in this way for several gate voltages, and a linear relation between density and gate voltage was assumed to obtain a calibration down to the lowest densities. The uncertainty in this calibration is $\approx 10^9$ cm^{-2}. The conductivity is shown in units of the conductance quantum $e^2/h \approx 3.9 \times 10^{-5}$ Ω^{-1}, on a log scale, showing that the conductivity vanishes very quickly for conductivities below e^2/h. Data is shown for three different temperatures: 50, 150, and 400 mK. For densities above 8×10^9 cm^{-2}, changing the temperature has negligible effect on the conductivity, suggesting that the 2D electron gas is in a 'metallic' phase. For densities below about 6×10^9 cm^{-2}, the conductivity falls

quickly with decreasing temperature, indicating that the sample is most likely insulating in the low temperature limit. This temperature dependence suggests that the metal-insulator transition in our sample occurs at a density of about 7×10^9 cm^{-2}, where the conductivity is roughly e^2/h.

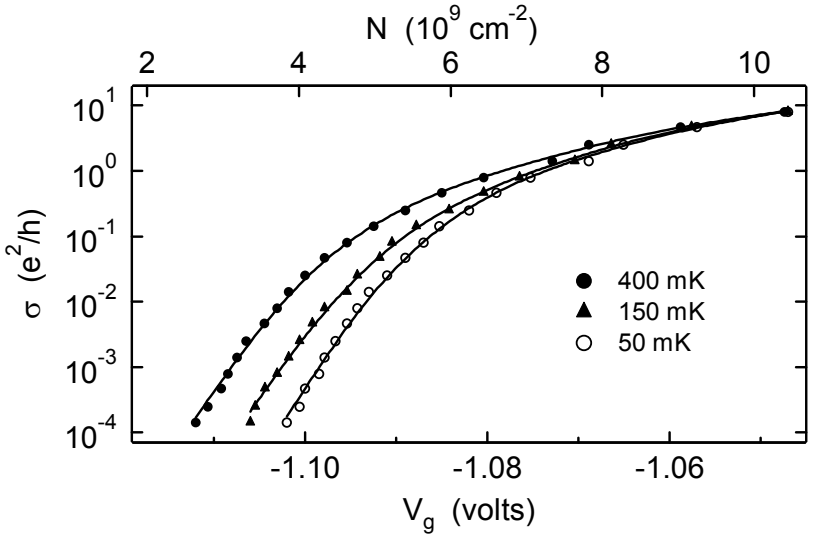

Fig. 2.13. 2DES conductivity vs. gate voltage (and density) at three temperatures. For densities below $\approx 7 \times 10^9$ cm^{-2} the 2DES appears to have an insulating ground state.

2.4.5 SAW versus DC Conductivity

At first glance, by application of Eq. (3) using conductivity values like those shown in Fig. 2.13, one should be able to predict how the SAW velocity shift will behave as a function of gate voltage as the conductivity of the electron gas passes through σ_M. Fig. 2.14 displays the result of following this procedure, along with the actual measured SAW velocity shift. The closed symbol data of Fig. 2.13 is the 2DES conductivity from admittance measurements as a function of density and gate voltage at a temperature of 300 mK. The dashed line is a prediction of the expected surface acoustic wave velocity shift from this conductivity data using Eq. (3). For the experimental conditions relevant to Fig. 2.14 (top gate with a 2DES 0.6 μm below the surface and SAW $\lambda \sim 3.4$ μm), $\sigma_M \sim 7 \times 10^{-7}\ \Omega^{-1}$. The open symbols are the measured SAW velocity shift at 856 MHz. There is a striking conflict between the measured and predicted velocity shift. The measured velocity shift begins to change at conductivities nearly two orders of magnitude above σ_M

and continues to change for conductivities about three orders of magnitude below σ_M. By contrast, the change in the predicted velocity shift occurs in a very narrow density and conductivity range.

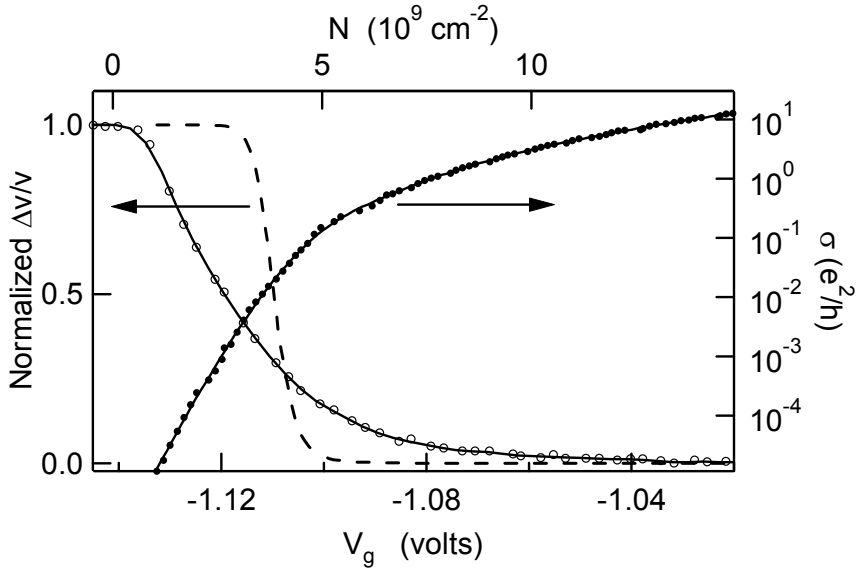

Fig. 2.14. Low-frequency conductivity σ and normalized SAW velocity shift at 856 MHz vs. gate voltage and density at $T = 300$ mK. The dashed line is the prediction of Eq. (3) using the measured σ.

One likely explanation for this conflict between the measured and predicted surface acoustic wave velocity shift is that the electron gas becomes very inhomogeneous near depletion. The model (Eq. (3)) used to calculate the expected velocity shift obviously breaks down for a strongly inhomogeneous conductor. For example, if the majority of the 2DES had a local conductivity much greater than σ_M, but contained a few isolated patches with conductivity lower than σ_M, there would be a response in the measured velocity shift even though the conductivity obtained via standard transport measurements would still be much greater than σ_M.

That the electron gas is inhomogeneous at these densities is consistent with expectations about density fluctuations caused by the Si donors, and also with magnetotransport measurements on a similar sample, which estimate density fluctuations on the order of 5×10^9 cm^2. Pikus and Efros have shown [16] that for randomly

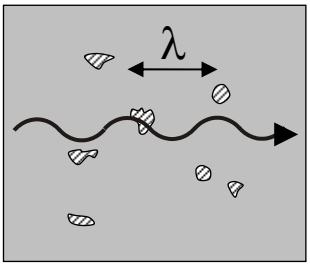

Fig. 2.15. Cartoon of SAW propagation near a 2DES with density inhomgeneities. Hatched areas represent low-density regions where the conductivity is less than σ_M. The SAW wavelength, λ, is greater than the disorder length scale.

distributed ionized donors of concentration C, located a distance d from the 2DES, that the rms 2DES density variation is

$$\delta N = \sqrt{C/8\pi d^2} \ .$$

Using the 2DES ungated density of our sample for $C = 1.4 \times 10^{11}$ cm^{-2} and the spacer distance $d = 70$ nm, this gives a density variation of $\delta N \sim 1 \times 10^{10}$ cm^{-2}. The length scale of these density fluctuations is set by the spacer distance d. Considering that our smallest experimentally accessible SAW wavelength was 2.2 μm, the lack of wavelength dependence seen in Fig. 2.9 is not surprising.

Looking at the temperature dependence of the conductivity (Fig. 2.13) we see that the onset of insulating behavior in the temperature dependence is roughly coincident with the initial rise in surface acoustic wave velocity. If our picture of an inhomogeneity-driven increase in $\Delta v/v$ is correct, this coincidence suggests that the apparent metal-insulator transition will be strongly influenced by the presence of inhomogeneities. In light of this, it seems likely that for our system, the transition is better described as a disorder-driven, percolation-type transition rather than as an exotic, interaction-driven quantum phase transition.

2.5 Conclusion

In conclusion, we have examined the conductivity of a low-density 2DES via two very different experimental techniques – low-frequency transport measurements versus surface

acoustic wave propagation. Interpreting our measurements within a model for a homogeneous conductor leads to a strong conflict in the results obtained from the two types of measurements. This conflict demonstrates the importance of the inhomogeneous nature of the 2DES near the putative metal-insulator transition.

References

[1] L.A. Tracy, J.P. Eisenstein, M.P. Lilly, L.N. Pfeiffer, K.W. West, *Solid State Comm*. **137**, 150 (2006).

[2] S.V. Kravchenko, T.M. Klapwijk, *Phys. Rev. Lett.* **84**, 2909 (2000).

[3] B.L. Altshuler, D.L. Maslov, V.M. Pudalov, *Physica E* **9**, 209 (2001).

[4] M.P. Lilly, J.L. Reno, J.A. Simmons, I.B. Spielman, J.P. Eisenstein, L.N. Pfeiffer, K.W. West, E.H. Hwang, S. Das Sarma, *Phys. Rev. Lett.* **82**, 394 (1999).

[5] E. Abrahams, S.V. Kravchenko, M.P. Sarachik, *Rev. Mod. Phys.* **73**, 251 (2001).

[6] Sypriyo Datta. *Electronic Transport in Mesoscopic Systems*. Cambridge University Press, Cambridge 1997.

[7] A. Lee and T. V. Ramakrishnan, *Rev. Mod. Phys*. **75**, 287 (1985).

[8] A. L. Efros and B. I. Shklovskii, *J. Phys. C* **8**, L49 (1975).

[9] E. Abrahams, P.W. Anderson, D.C. Licciardello, T.V. Ramakrishnan, *Phys. Rev. Lett.* **42**, 673 (1979).

[10] C. Attaccalite, S. Moroni, P. Gori-Giorgi, G. B. Bachelet, *Phys. Rev. Lett.* **88**, 256601 (2002).

[11] S. H. Simon, *Phys. Rev. B* **54**, 13878 (1996).

[12] A. Wixforth, J. Scriba, M. Wassermeier, J. P. Kotthaus, G. Weimann, W. Schlapp, *Phys. Rev. B* **40**, 7874 (1989).

[13] R. L. Willett, M. A. Paalanen, R. R. Ruel, K. W. West, L. N. Pfeiffer, and D. J. Bishop, *Phys. Rev. Lett.* **65**, 112 (1990).

[14] R.L. Willett, R.R. Ruel, K.W. West, L.N. Pfeiffer, *Phys. Rev. Lett.* **71**, 3846 (1993).

[15] J. Zhu, W. Pan, H.L. Stormer, L.N. Pfeiffer, K.W. West, *Phys. Rev. Lett.* **88**, 116803 (2002).

[16] F.G. Pikus, A.L. Efros, *Phys. Rev. B* **47**, 16395 (1993).

Chapter 3:
Two-dimensional Electrons in a Magnetic Field

This chapter reviews the transport properties of 2DES's in a magnetic field, from a low-field, classical picture to the integer and fractional quantum hall states.

3.1 Classical Magnetotransport

We start with the Drüde model for conductivity of the electron gas, which assumes a background of static, positively charged ions with a gas of classical, non-interacting electrons whose motion is damped by collisions with the background ions. These collisions reduce an electron's average momentum at a rate m*v_d /τ_m, where m^* is the electron effective mass, v_d is electron drift velocity, and τ_m is called the momentum relaxation time. The application of magnetic and electric fields modify the electron drift velocity, v_d:

$$\frac{m^*\vec{v}_d}{\tau_m} = -e\left(\vec{E} + \vec{v}_d \times \vec{B}\right),$$

The current density in terms of the drift velocity is $\vec{j} = -\vec{v}_d en$, where n is the electron number density.

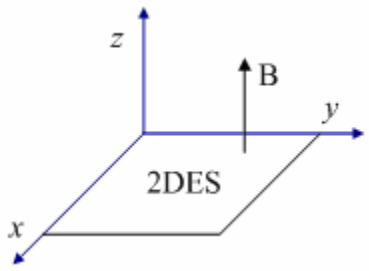

Fig. 3.1. Coordinate system for magnetotransport analysis.

The resistivity tensor ρ is defined by $\vec{E} = \rho\vec{j}$. Then, in 2D and using the coordinate system shown in Fig. 3.1,

$$\begin{pmatrix} E_x \\ E_y \end{pmatrix} = \begin{pmatrix} -m/e\tau & -B \\ B & -m/e\tau \end{pmatrix} \begin{pmatrix} v_x \\ v_y \end{pmatrix}.$$

So,

$$\rho = \begin{pmatrix} m/ne^2\tau & B/ne \\ -B/ne & m/ne^2\tau \end{pmatrix}.$$

Conventionally, $\rho_{xx} = \rho_{yy} = m/ne^2\tau$ is known as the longitudinal resistivity and $\rho_{xy} = \rho_{yx} = B/ne$ is referred to as the transverse or Hall resistivity.

3.2 Integer Quantum Hall Effect

3.2.1 Landau Levels

Next, we consider the effect of quantum mechanics on 2DES magnetotransport. In a magnetic field, the usual momentum in the Hamiltonian is replaced with $\vec{p} - q\vec{A}$, where $\vec{p}$ is the canonical momentum, $\vec{A}$ is the vector potential and q is the charge. Then, for electrons

$$H = \frac{1}{2m}\left|\vec{p} + e\vec{A}\right|^2 - eV.$$

We consider an electron confined to a sheet in the *x*-*y* plane with $V = 0$ everywhere and a magnetic field B in the *z*-direction. Using the Landau gauge for the vector potential, we can choose $\vec{A} = \hat{y}Bx$. Solving for the eigenvalues and eigenstates, we obtain

$$E_n = \left(n + \frac{1}{2}\right)\hbar\omega_c,$$

$$\psi_{nk}(x,y) = \left(\frac{1}{L}\right)^{1/2}\left(\frac{1}{2^n n! l_B\sqrt{\pi}}\right)^{1/2} H_{n-1}\left(\frac{x - x_k}{l_B}\right)\exp\left[-\frac{(x-x_k)^2}{2l_B^2}\right]\exp(iky),$$

where n is an integer, k is any wavevector satisfying the desired boundary conditions, L is the system size in the *y*-direction, $x_k = -\hbar k/eB$, H_{n-1} are Hermite polynomials,

$\omega_c = eB/m^*$ is the cyclotron frequency, and $l_B = \sqrt{\hbar/eB}$ is the magnetic length. The evenly spaced, allowed energies E_n are called Landau levels.

If we impose periodic boundary conditions in the *y*-direction such that $\psi_{nk}(x,0) = \psi_{nk}(y,L)$ for some length *L*, then the allowed *k*'s are $k = N2\pi/L$, where *N* is an integer. A given state with label *k* is localized in the *x*-direction around the position $x_k = -\hbar k/eB$ by the Gaussian factor in the wavefunction, with a decay length on the order of l_B. Then, if we count the states within an area of length and width *L*, for a given Landau level *n*, the number of available states per unit area will be $N/L^2 = eB/h$.

3.2.2 Localized States

From the above solution for an electron moving in a magnetic field, we might expect the density of states of a 2DES to consist of a series of equally spaced delta functions corresponding to the Landau levels E_n. However, in actual physical systems, disorder modifies this energy spectrum, broadening the Landau levels and also creating localized states, as shown in Fig. 3.2. Disorder due to impurities and defects in the crystalline lattice gives rise to a random, spatially varying background potential for the electron gas. For example, in doped GaAs/AlGaAs heterostructures random fluctuations in the distribution of donor ions can lead to a slowly varying (compared to l_B) background potential. This disorder then leads to spatial fluctuations in the electron density and the formation of localized states -- states which are localized in spatial extent and, in the limit of zero temperature, do not contribute to carrying current across the sample. Local valleys in the potential landscape trap and localize electrons, especially in the presence of a large perpendicular magnetic field. Due to the presence of these localized states, the Fermi energy can lie at energies between Landau levels.

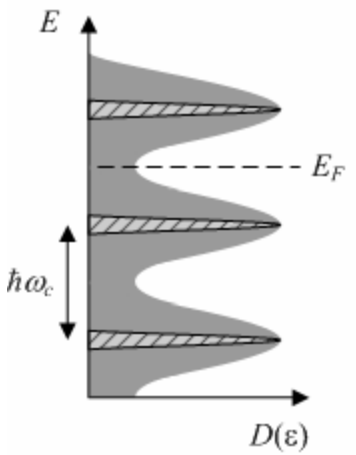

Fig. 3.2. Density of states $D(\varepsilon)$ with Landau levels (spin neglected) with extended (hatched) and localized (shaded) states. The Fermi energy E_F is indicated by the dashed line.

3.2.3 Spin

Another contribution to the density of states in a magnetic field will be the Zeeman splitting due to the electron spin degree of freedom. As shown in Fig. 3.3, this will lead to a second set of energy levels separated from the first by $E_Z = g\mu_B B$.

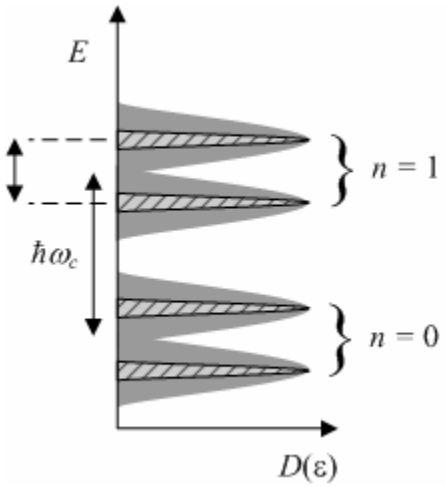

Fig. 3.3. Density of states $D(\varepsilon)$ with spin-split Landau levels with extended (hatched) and localized (shaded) states. Drawing is not to scale.

Please note that Fig. 3.3 is not to scale. For electrons in GaAs, the energy gap between spin-resolved energy levels is $E_Z = g\mu_B B = 0.29 \times B$ (K), which is much smaller than the cyclotron splitting $\hbar\omega_c = 20.1 \times B$ (K), where B is in Tesla.

3.2.4 Magnetotransport – IQHE

Below, Fig. 3.4 shows the magnetotransport of a 2DES in moderately large magnetic fields. The longitudinal resistance R_{xx} displays oscillations versus increasing magnetic field. As the magnetic field rises, the energy gap between Landau levels increases so that, at fixed 2DES carrier density, the Fermi level will drop through the ladder of Landau levels as they are depopulated, leading to oscillations in the conductivity. Instead of the linear Hall resistance R_{xy} versus B one would expect from a classical analysis, R_{xy} is actually quantized. When $R_{xx} = 0$, the Hall resistance plateaus at a value $R_{xy} = h/qe^2$, where q is an integer such that $\nu < q < \nu + 1$, and $\nu \equiv nh/eB$ is the number of filled Landau levels and is called the Landau level filling factor. Amazingly, the exact value of the quantized Hall resistance is completely independent of the sample used! In fact, the quantized Hall resistance is used as a resistance standard due to the fact that the value of R_{xy} at the plateaus does not depend on the material system containing the 2DES or disorder.

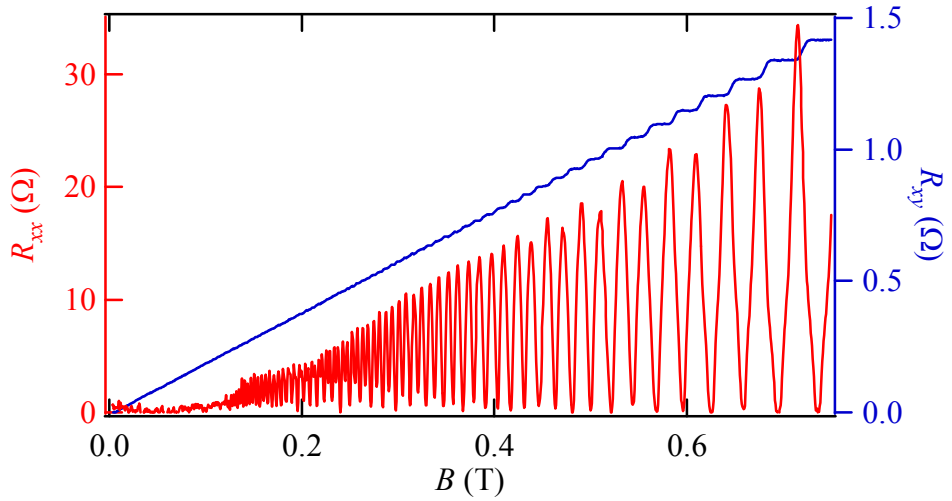

Fig. 3.4. Magnetotransport displaying longitudinal resistance R_{xx} oscillations (red trace) and quantized Hall resistance R_{xy} (blue trace) in the integer quantum Hall effect regime.

This quantization is known as the integer quantum Hall effect (IQHE). The IQHE was experimentally discovered by von Klitzing et al. in 1980 [1], who saw the quantization of the Hall resistance in a Si MOSFET. This work was awarded a Nobel prize in 1985.

The presence of localized states is necessary for observation of the IQHE. The zeroes in R_{xx} versus B correspond to magnetic fields where the Fermi level lies between Landau levels so that only localized states are occupied at the Fermi energy. As mentioned earlier, the conductivity of these localized states vanishes at low temperature. Inverting the 2D conductivity tensor we obtain $R_{xx} = \sigma_{xx}/(\sigma_{xx}^2 + \sigma_{xy}^2)$, which, since $\sigma_{xy} \neq 0$, leads to the (somewhat non-intuitive) conclusion that when $\sigma_{xx} = 0$, $R_{xx} = 0$ as well. The precise quantization of Hall resistance can be understood by an analysis of how current flows at the edges of a 2DES sample.

3.2.5 Edge States

Consider a 2DES confined in the y-direction such that $V(y) = 0$ for $|y| < L$ and $V(y)$ increases for $|y| > L$ (see Fig. 3.5). If the confining potential varies slowly, such that $\partial V / \partial y < \hbar\omega_C / l$, then we can make the approximation that the energy levels simply rise in energy near the sample edge such that $E_n = \hbar\omega_C(n + 1/2) + V(y)$. These energy levels will then cross the Fermi energy near the edge, leading to a nonzero density of states at the Fermi level.

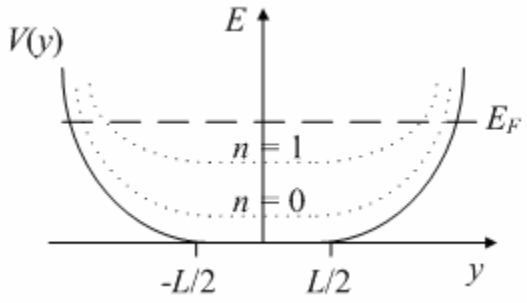

Fig. 3.5. Landau levels (dotted lines) in a confining potential $V(y)$, showing the formation of edge states.

These edge states carry current in the IQHE and are chiral, meaning that the motion of electrons in an edge state is limited to only one direction [2]. Depending on the direction

of the magnetic field, the left edge states carry current into the page and the left states carry current out of the page, or vice versa. Because the left and right edge states are spatially separated from one another, it is difficult for electrons to scatter from the states carrying current one direction into states traveling in the other direction. This leads to ballistic conduction in the edge states in the quantum Hall regime. The Landauer-Büttiker formula for the conductance of ballistic 1-D conductor can be applied to find the conductance of the edge states [3, 4]. In this formalism, the conductance of M parallel 1-D modes is given by Me^2/h.

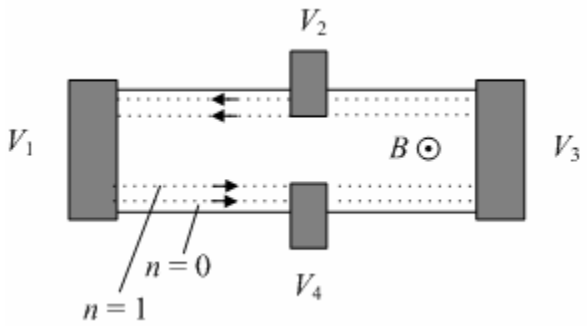

Fig. 3.6. Edge state transport in the IQHE. The central region contains a 2DES, while the shaded regions are Ohmic contacts.

Consider applying a voltage $V = V_1 - V_3$ across the sample shown in Fig. 3.6. The number of edge channels is equal to the number of filled Landau levels ν (in Fig. 3.6 $\nu =$ 2, since the $n = 0$ and $n = 1$ levels are occupied). The conductance between contacts 1 and 3 will be the conductance of two ballistic channels in parallel: $\sigma_{13} = I/V = 2 \times e^2/h$. The Hall resistance will be given by $R_{xy} = (V_4 - V_2)/I$. Now, $V_4 = V_1$ since there is no voltage drop along a ballistic edge state. Similarly, $V_2 = V_3$. Thus, $R_{xy} = V/I = h/2e^2$. In general, the quantized Hall resistance is given by

$$R_{xy} = h/\nu e^2.$$

3.3 Fractional Quantum Hall Effect

We have so far neglected the effect of electron-electron interactions. However, Coulomb interactions become increasingly important at large perpendicular magnetic fields. At

high enough perpendicular magnetic fields, such that the Landau levels do not overlap in energy, within a given Landau level the kinetic energy is the same for all electrons and becomes an irrelevant constant in the Hamiltonian. This removal of kinetic energy from the problem is referred to as "quenching of kinetic energy".

One striking consequence of Coulomb interactions in 2DES's at high magnetic fields is the fractional quantum Hall effect (FQHE), which was discovered by D. C. Tsui, H. L. Stormer, and A. C. Gossard [5], who were awarded a Nobel prize for their discovery in 1998. They observed a minimum in R_{xx} and plateau for R_{xy} in the magneotransport of a relatively high-mobility 2DES which appeared to correspond to a Landau level for a fractional filling factor, $\nu = 1/3$. Eventually, the fractional quantum Hall effect was observed at other fractional filling factors as well.

Laughlin [6] wrote the following trial wavefunction to describe the $\nu = 1/q$ FQH states:

$$\psi_q(z_1, z_2, \ldots, z_N) = \prod_{i>j=1}^{N} (z_i - z_j)^q \exp\left(-\sum_{i=1}^{N} |z_i|^2 / 4\right),$$

where q is an odd integer, N is the number of electrons, and the complex coordinate $z = (x + iy)/l_B$. This wavefunction is the exact solution for the case of 2D electrons in a perpendicular magnetic field with hard core interactions; it is a very good approximation for the Coulomb potential. The form of the wavefunction is reminiscent of the non-interacting solution; for $q = 1$ ($\nu = 1$), it is just an antisymmetric product of the single-particle wavefunctions. For general q, the polynomial product factor provides the correct symmetry (complete spin polarization is assumed) and ensures that any two electrons i and j avoid one another, since when $z_i = z_j$, the value of the wavefunction is zero.

A standard series of fractional quantum hall states [7] are allowed for all ν such that

$$\nu = \frac{p}{2pq \pm 1},$$

where p and q are integers. Particle-hole symmetry leads to another set of allowed FQH states for holes instead of electrons:

$$\nu = 2 - \frac{p}{2pq \pm 1},$$

including the spin degree of freedom (the formula is $\nu = 1 - p/(2pq \pm 1)$ for a fully polarized system). Figure 3.7 shows an example of magnetotransport displaying several FQHE states.

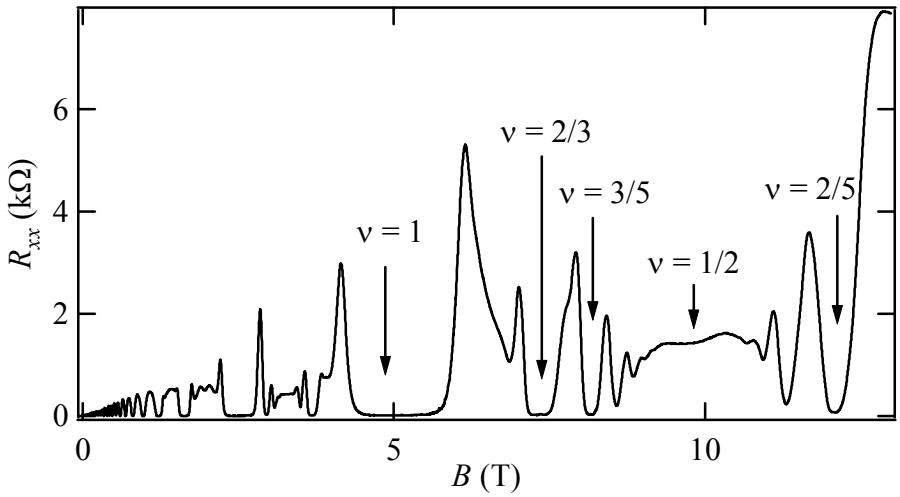

Fig. 3.7. Magnetotransport displaying the FQHE. Several fractional states, including ν = 2/3, 3/5, and 2/5 can be seen.

3.3.1 Composite Fermions

One elegant picture used to explain the FQHE, proposed initially by J. K. Jain [8], is the composite fermion model. In this picture, electrons in a perpendicular magnetic field are replaced by quasiparticles called composite fermions (CF's), where a CF is an object consisting of an even number of magnetic flux quanta rigidly attached to an electron. The hope is that strongly-interacting electrons can be replaced by more weakly-interacting CF's.

The flux attachment process is accomplished mathematically via a gauge transformation. Following the treatment in Ref. [9], consider the Schrödinger equation for the initial problem of 2D electrons in a perpendicular magnetic field:

$$\left[\frac{1}{2m}\sum_i\left(\vec{p}_i+\frac{e}{c}\vec{A}\left(\vec{r}_i\right)\right)^2+V\right]\Psi=E\Psi.$$

Then make the gauge transformation

$$\Psi=\exp\left(-i2p\sum_{j<k}\theta_{jk}\right)\Psi_{CS}=\prod_{j<k}\left(\frac{z_j-z_k}{\left|z_j-z_k\right|}\right)^{2p}\Psi_{CS},$$

where p is an integer, $z=\left(x+iy\right)/l_B$ is the complex coordinate for the position of an electron, and θ_{jk} is the angle between two particles:

$$\theta_{jk}=i\ln\left(\frac{z_j-z_k}{\left|z_j-z_k\right|}\right).$$

This is known as the composite fermion Chern-Simons transformation [10 – 11], which is why the wavefunction in the new gauge is labeled with the subscript "CS". The Schrödinger equation for the new wavefunction Ψ_{CS} is

$$\left[\frac{1}{2m}\sum_i\left(\vec{p}_i+\frac{e}{c}\vec{A}\left(\vec{r}_i\right)-\frac{e}{c}\vec{a}\left(\vec{r}_i\right)\right)^2+V\right]\Psi_{CS}=E\Psi_{CS},$$

where

$$\vec{a}\left(\vec{r}_i\right)=\frac{2p}{2\pi}\phi_0\sum_j\nabla_j\theta_{ij}$$

and $\phi_0=h/e$ is the flux quantum. The magnetic field generated by the vector potential $\vec{a}$ is

$$\vec{b}\left(\vec{r}_i\right)=\nabla\times\vec{a}\left(\vec{r}_i\right)=\hat{z}\left(2p\phi_0\right)\sum_j\delta^2\left(\vec{r}_i-\vec{r}_j\right),$$

which is the magnetic field due to attaching a "flux tube" or point flux to the electrons at positions $\vec{r}_j$. The number of flux quanta attached to each particle, $2p$, is even, so that this flux does not modify the statistics of the particles, since when two particles are exchanged the extra Aharonov-Bohm phase accumulated due to the extra flux will be $2\pi p$, giving an extra phase factor of $\exp(2\pi pi) = 1$, which is unobservable.

We next rewrite the problem once more, defining

$$\vec{A}^* + \delta\vec{A} \equiv \vec{A} - \vec{a},$$

where $\vec{A}^*$ is defined by

$$\nabla \times \vec{A}^* = \hat{z}B^* = \hat{z}\left(B - 2pn\phi_0\right),$$

where n is the electron number density and B^* is a uniform magnetic field. Then, the Schrödinger equation can be written as

$$\left[\frac{1}{2m}\sum_i\left(\vec{p}_i + \frac{e}{c}\vec{A}^*\left(\vec{r}_i\right)\right)^2 + V + V'\right]\Psi_{CS} = \left(H' + V + V'\right)\Psi_{CS} = E\Psi_{CS},$$

where $V' \sim \delta A$. Then, a mean field approximation can be used, where the problem is first solved exactly for H' and then the $V + V'$ term is treated perturbatively.

In this mean field approximation, the attached flux cancels some of the external magnetic field so that the effective magnetic field experienced by a CF is $B^* = B - 2pn\phi_0$. The effects of fluctuations of the electron density n, which will lead to fluctuations of the effective magnetic field, are treated as perturbations. It is not obvious that the perturbations will be small. However, for judicious choice of flux attachment, this approach is able to predict the locations in filling factor space of most FQH states, and has even met some success in describing compressible states near even-denominator filling factors.

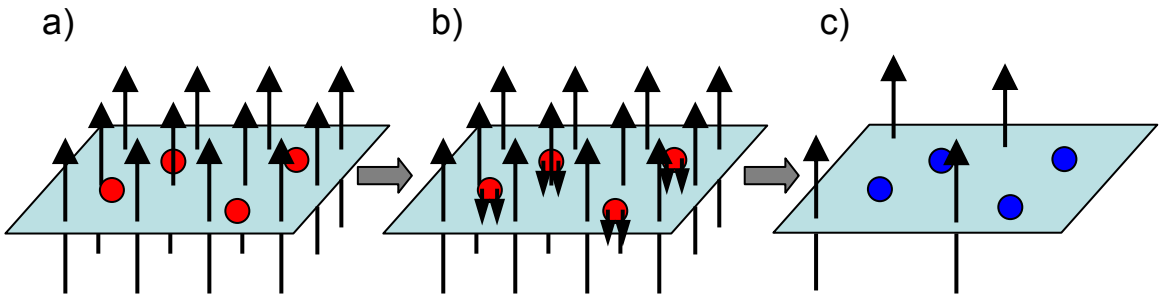

Fig. 3.8. Transformation of ordinary electrons in a magnetic field into composite fermions. a) Electrons in a magnetic field are transformed into b) composite fermions by attachment of two flux quanta, opposing the actual magnetic field. c) In a mean-field picture, the composite fermions experience a reduced magnetic field. The figure shows the case for ν = 1/3, where each electron absorbs two flux quanta and the effective magnetic field for CF's corresponds to one flux quanta per CF.

Using this effective magnetic field, the FQH states can be understood as states corresponding to the IQHE for CF's. The CF filling factor is given by $\nu_{CF} = n\phi_0 / B^*$. The electron filling factor is then $\nu = n\phi_0 / B = \nu_{CF} / (2p\nu_{CF} \pm 1)$. If we require ν_{CF} to be equal to some integer q, then

$$\nu = q / (2pq \pm 1),$$

which is just the expression given earlier for the principle series of FQH states.

The composite fermion picture can also be used to describe the compressible states between QH states. For the case of the half-filled lowest Landau level, ν = 1/2, CF's consisting of an electron bound to two flux quanta will, in a mean field approximation, experience zero effective magnetic field; at exactly ν = 1/2, B^* = 0. This suggests that the state at ν = 1/2 may be described as a Fermi sea of composite fermions. A seminal paper by Halperin, Lee, and Read [12] put this picture on firmer theoretical footing, arguing that the CF Fermi surface at ν = 1/2 survives beyond mean field theory, when the effect of fluctuations in the effective magnetic field are included. The existence of a Fermi surface at ν = 1/2 has also been demonstrated experimentally by Willett and others [13-15]. In these experiments, the motion of CF's very near ν = 1/2 appears to be described by classical cyclotron orbits of radius $R^* = \hbar k_F / eB_{eff}$.

3.4 Other 2DES States

Yet more fascinating physics has been found in high-quality 2DES's at low temperature and large magnetic fields – for example: a FQHE at even denominator filling factor (forbidden according to the expected hierarchy of FQHE wavefunctions) $\nu = 5/2$, possible charge density wave formation at high Landau levels ($\nu > 3$), and an exciton condensate in bilayer 2DES's at total filling factor $\nu_T = \nu_{layer1} + \nu_{layer2} = 1$. More physics likely awaits discovery as sample quality improves, experimentally accessible temperatures decrease, and new experimental probes are developed.

References

[1] K. von Klitzing, G. Dorda, and M. Pepper, *Phys. Rev. Lett.* **45**, 494 (1980).

[2] B. I. Halperin, *Phys. Rev. B* **25**, 2185 (1982).

[3] M. Büttiker, *IBM J. Res. Dev*. **32**, 63 (1998).

[4] S. Datta. *Electronic Transport in Mesoscopic Systems*. Cambridge University Press, Cambridge 1995.

[5] D. C. Tsui, H. L. Stormer, and A. C. Gossard, *Phys. Rev. Lett.* **48**, 1559 (1982).

[6] R. B. Laughlin, *Phys. Rev. Lett.* **50**, 1395 (1983).

[7] F. D. M. Haldane, *Phys. Rev. Lett*. **51**, 605 (1983).

[8] J. K. Jain. *Phys. Rev. Lett.* **63**, 199-202 (1989).

[9] J. K. Jain. *Composite Fermions*. Cambridge University Press, Cambridge 2007.

[10] S. C. Zhang, H. Hansson, and S. Kivelson, *Phys. Rev. Lett*. **62**, 82 (1989).

[11] A. Lopez and E. Fradkin, *Phys. Rev. B* **44**, 5246 (1991).

[12] B. I. Halperin, P. A. Lee, N. Read. *Phys. Rev. B.* **47**, 7312 (1993).

[13] R. L. Willett, R. R. Ruel, K. W. West, and L. N. Pfeiffer, *Phys. Rev. Lett*. **71**, 3846 (1993).

[14] W. Kang, H. L. Stormer, L. N. Pfeiffer, K. W. Baldwin, and K. W. West, Phys. *Rev. Lett*. **71**, 3850 (1993).

[15] V. J. Goldman, B. Su, and J. K. Jain, *Phys. Rev. Lett*. **72**, 2065 (1994).

Chapter 4:
Spin and NMR Techniques

In the overview of the basic phenomena of 2D electrons in a magnetic field given in Chapter 3 the spin degree of freedom was largely ignored. However, several chapters in this thesis will discuss examples of 2DES states where spin does play an important role. This chapter gives a basic introduction to the role of spin in 2DES's and also introduces a resistively-detected nuclear magnetic resonance technique (RDNMR) that we use to probe the electron spin at several 2DES states.

4.1 Background

In a large enough magnetic field the Zeeman energy $E_Z \propto B$ will eventually dominate the Coulomb energy $E_C \propto \sqrt{B}$, and the spin degree of freedom will be frozen. However, the g-factor in GaAs is reduced from that in vacuum: g^* = -0.44 instead of 2. This means that at intermediate magnetic fields the Coulomb interaction may play a large role in determining the behavior of the electron spin.

The spin degree of freedom leads to a variety of phenomena in 2DES's. Laughlin's wavefunction (see Chapter 3) assumes complete spin polarization. However, Halperin proposed [1] incompletely spin polarized versions of fractional quantum Hall states. Experimentally, it has been shown that transitions can occur between FQH states with ground states of differing spin polarization, but at the same filling factor, by tuning the ratio of the Zeeman to Coulomb energy. Some of the first experiments to observe this type of transition were performed by tilting the sample in a magnetic field, so that the total magnetic field, and thus the Zeeman splitting, can be varied relative to the perpendicular magnetic field, which determines the filling factor and the Coulomb energy. Using this technique, spin transitions were observed for the ν = 8/5 and 2/3 states [2, 3]. Spin excitations are also strongly affected by electron-electron interactions. For example, it is predicted that, due to Coulomb interactions, the lowest-lying charged excitations at ν = 1 are Skyrmions -- objects with multiple reversed spins and a smooth spatial variation in spin [4, 5].

4.2 Nuclear Magnetic Resonance

4.2.1 Hyperfine Interaction

We are not interested in the nuclear spin itself, but, due to the hyperfine interaction, NMR can be used to probe the electron spin. The full hyperfine Hamiltonian [6] describing the interaction between an electron and the magnetic moment due to the spin of the nucleus is

$$H_{hf} = -\frac{\mu_0}{4\pi}\left\{\frac{q}{m_e R^3}\vec{L}\cdot\vec{M}_I + \frac{1}{R^3}\left[\frac{3\left(\vec{M}_S\cdot\vec{R}\right)\left(\vec{M}_I\cdot\vec{R}\right)}{R^2} - M_S\cdot M_I\right] + \frac{8\pi}{3}M_S\cdot M_I\,\delta\left(\vec{R}\right)\right\},$$

where q is the nuclear charge, m_e is the mass of the electron, $\vec{R}$ is the relative separation between the electron and nucleus, $\vec{L}$ is the orbital angular momentum of the electron relative to the nucleus, $\vec{M}_I$ is the magnetic moment of the nucleus, $\vec{M}_I = g_n\mu_n\vec{I}/\hbar$, where g_n is the nuclear g-factor, μ_n is the nuclear Bohr magneton, $\vec{I}$ is the nuclear spin, and $\vec{M}_S = g_0\mu_B\vec{S}/\hbar$ is the magnetic moment of the electron, where g_0 is the free electron g-factor, μ_B is the electron Bohr magneton, and $\vec{S}$ is the electron spin. The first term is due to the interaction between the nuclear magnetic moment and the magnetic field created at the nucleus by the orbital angular momentum of the electron. The second and third terms stem from the dipole-dipole interaction between the nuclear and electronic spin, where the last term is the contribution from the singularity that occurs when the electronic wavefunction and nucleus spatially overlap. It turns out that this last term, named the "point contact" term, is the dominant contribution to H_{hf} for our 2DES samples.

4.2.2 Point Contact Interaction in n-Type GaAs

For electrons in the conduction band at the Γ point in GaAs, the electronic wavefunction is composed mostly of an s-type orbital. This means that the first term in H_{hf} can be neglected since for $L = 0$, this first term is zero. Because of the spherical symmetry of the s-type orbital versus the symmetry of the dipole interaction, the second term also vanishes. The third term, however, remains since the s-type orbital wavefunction is nonzero at the origin. Thus,

$$H_{hf} = -\frac{\mu_0}{4\pi}\frac{8\pi}{3} g_0 \mu_B \gamma_n \hbar \left\langle \vec{I} \right\rangle \cdot \left\langle \vec{S} \right\rangle \delta\left(\vec{R}\right),$$

where $\gamma_n = g_n \mu_n / \hbar$ is the nuclear gyromagnetic ratio. The value of the hyperfine correction to the total energy is then

$$E_{hf} = \frac{2\mu_0}{3} g_0 \mu_B \gamma_n \hbar \left\langle \vec{I} \right\rangle \cdot \left\langle \vec{S} \right\rangle \left|\psi(0)\right|^2,$$

Where $\psi(0)$ is the value of the electronic wavefunction at the position of the nucleus. Paget *et al*. have estimated the magnitude of this term for n-type GaAs [7] for each of the three nuclear species present in GaAs: ^{75}As, ^{69}Ga, and ^{71}Ga. The result is given in terms of an effective magnetic field B_N due to the nuclear polarization of the host semiconductor:

$$B_N = \sum_\alpha B_\alpha = \frac{2\mu_0}{3}\left(\frac{g_0}{g^*}\right)\hbar \sum_\alpha \gamma_\alpha x_\alpha d_\alpha \left\langle \vec{I}_\alpha \right\rangle,$$

where B_α is the contribution due to the individual nuclear species, g^* is the effective g-factor for electrons in the conduction band at the Γ point in GaAs (g^* = -0.44), x_α is the fractional concentration of each nuclear species, d_α is the electron density at the nucleus, and $\left\langle \vec{I}_\alpha \right\rangle$ is the average value of the nuclear spin. The estimated contribution from each nuclide at T = 0 is $B_{75\mathrm{As}}$ = -2.76 T, $B_{69\mathrm{Ga}}$ = -1.37 T, and $B_{71\mathrm{Ga}}$ = -1.17 T, giving rise to a maximum total contribution of $B_N \approx$ -5.3 T. These effective fields are negative, meaning they will oppose any externally applied magnetic field B_0. This leads to a total electronic Zeeman splitting given by

$$\Delta E_Z = g^* \mu_B \left(B_0 + B_N\right).$$

A decrease in the nuclear polarization will reduce the magnitude of B_N, causing an increase in the magnitude of the Zeeman splitting. Also note that B_N affects only the Zeeman energy, not the electron's orbital motion.

4.2.3 Nuclear Polarization

In the case of an externally applied magnetic field B_0, it is simple to obtain the equilibrium fractional nuclear polarization of a given nuclear species at temperature T:

$$\xi_0 = \frac{\sum_{m_z=-I}^{I} m_z \exp(-\beta m_z)}{I \sum_{m_z=-I}^{I} \exp(-\beta m_z)},$$

where $\beta = \gamma_n \hbar B_0 / kT$. When β is small we can use the approximation

$$\xi_0 = \frac{\gamma_n \hbar B_0 (I+1)}{3kT},$$

which is just the nuclear Curie law.

For reference, Fig. 4.1 shows B_α and B_N versus temperature for B_0 = 10 T. At conditions roughly similar to those of our experiments, $B_0 \sim 10$ T, $T \sim 100$ mK, we have $B_N \sim$ -0.2 T and a nuclear polarization of $\xi_0 \sim 4\%$.

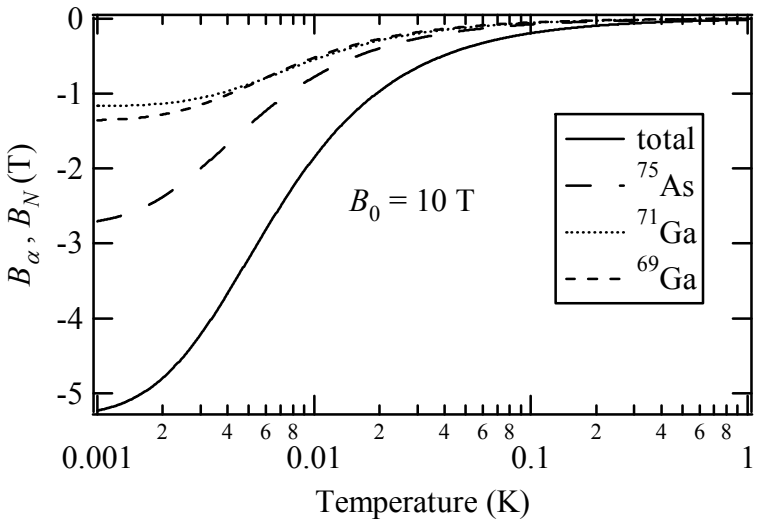

Fig. 4.1. Effective magnetic field due to thermal equilibrium polarization of host semiconductor nuclides at a static magnetic field of B_0 = 10 T. Dotted and dashed lines show the contribution from ^{75}As, ^{71}Ga, and ^{69}Ga separately, and the solid line displays the total contribution due to all three species.

4.2.4 Bloch Equations

The phenomenological equations of Bloch [8] describe the evolution of the nuclear magnetization in the presence of a static magnetic field $\vec{B}_0 = B_0\hat{z}$, and an ac magnetic field $\vec{B}_1 = B_1\hat{x}\cos(\omega_1 t)$, perpendicular to B_0. It is assumed that the nuclear magnetization reaches thermal equilibrium with relaxation times T_1 and T_2, known as the longitudinal and transverse relaxation times, respectively, such that in the absence of the ac magnetic field ($B_1 = 0$)

$$\frac{dM_x}{dt} = -\frac{M_x}{T_2},$$

$$\frac{dM_y}{dt} = -\frac{M_y}{T_2},$$

and

$$\frac{dM_z}{dt} = \frac{M_0 - M_z}{T_1},$$

where M_0 is the thermal equilibrium magnetization. With $B_1 \neq 0$, the full Bloch equations are

$$\frac{d\vec{M}}{dt} = \gamma\vec{M} \times \vec{B} - \frac{M_x\hat{x} + M_y\hat{y}}{T_2} - \frac{M_z - M_0}{T_1}\hat{z},$$

where γ is the nuclear gyromagnetic ratio and $\vec{B} = \vec{B}_0 + \vec{B}_1$. It is convenient to transform this equation into a rotating frame of reference that rotates in the *x*-*y* plane at the same frequency ω_1 as the ac magnetic field. Then

$$\frac{dM'_x}{dt} = \Delta\omega M'_y - \frac{M'_x}{T_2},$$

$$\frac{dM'_y}{dt} = -\Delta\omega M'_x - \frac{M'_y}{T_2} - \omega_r M_z$$

and

$$\frac{dM_z}{dt} = \omega_r M'_y + \frac{M_0 - M_z}{T_1},$$

where $\vec{M}'$ is the magnetization in the rotating frame, $\omega_r = \gamma B_1 / 2$ is the Rabi frequency, and the detuning $\Delta\omega = (\omega_1 - \omega_0)$, where ω_0 is the NMR resonance frequency. Under steady state conditions, $d\vec{M}'/dt = 0$, we have for the deviation of the z-component of the nuclear polarization from equilibrium:

$$M_0 - M_z = M_0 \frac{\omega_r{}^2 T_1 T_2}{1 + (\Delta\omega)^2 T_2{}^2 + \omega_r{}^2 T_1 T_2}.$$

This describes a Lorentzian NMR lineshape (NMR-induced change in polarization versus ω) with a half-width at half-max given by

$$\text{HWHM} = \frac{1}{T_2}\sqrt{1 + \omega_r{}^2 T_1 T_2}\,.$$

4.3 Resistively Detected NMR

We use NMR to study the electron spin degree of freedom via the nuclear spins of the host semiconductor. The NMR technique employed in this thesis is known as resistively-detected NMR (RDNMR) [9]. In RDNMR, instead of measuring the response of the nuclear spin system to resonant RF, the 2DES sample transport is monitored while modifying the nuclear spin polarization; this allows one to measure dR/dE_Z. This technique is especially useful for studying systems with a small number of nuclei in the region of interest (as in nanostructures), where directly-detected NMR would be too difficult. Previous applications of this technique include studying spin excitations in single layer systems near filling factor $\nu = 1$ [10-12] and the spin transitions at fractional quantum Hall states, such as the $\nu = 2/3$ state [13, 14].

4.3.1 Experimental Setup

Fig. 4.2 shows a photograph of a typical RDNMR experimental setup. The 2DES sample sits inside of a small NMR coil and has ohmic contacts for standard low-frequency transport measurements. The coil and sample are mounted on a standard 18-pin DIP header. The coil leads are wired to the central pin and ground of a semi-rigid coaxial lead (see Chapter 1, section 1.2.4).

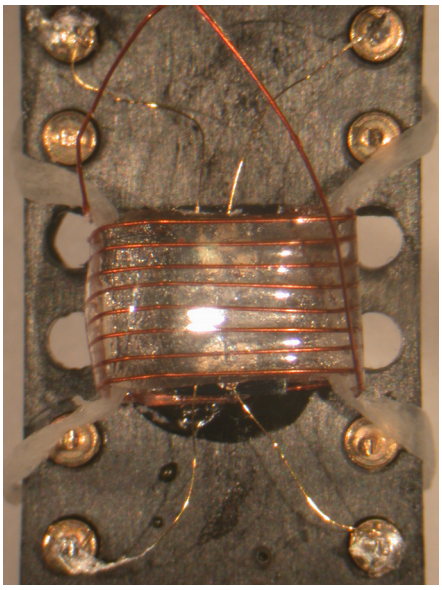

Fig. 4.2. 2DES sample mounted inside approximately 8-turn rectangular NMR coil. The sample size is ~ 5 × 3 mm^2.

The magnitude of the ac magnetic field B_1 applied via the NMR coil is typically in the ~ 0.1 - 1 μT range. We discuss the estimation of the magnitude of this RF *B*-field in the next section. Since the nuclear dipolar fields are on the order of 0.1 mT >> B_1, we work in a regime where $\omega_r << 1/T_2$.

4.3.1a Estimation of RF B-field

The coil was designed so that the magnetic field in the sample area would be somewhat uniform and so that the magnitude of the RF *B*-field would have a weak frequency dependence (convenient for experiments which are performed over a wide range of static

magnetic fields, and thus a wide range of NMR frequencies). Figure 4.3 shows a sketch of the NMR coil with relevant dimensions.

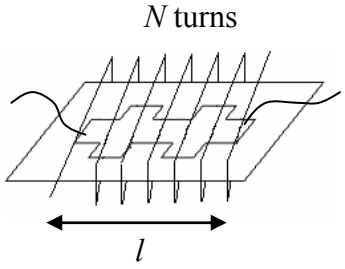

Fig. 4.3. Hall bar 2DES sample in *N*-turn NMR coil of length *l*.

As a typical example, consider a coil with 8 turns, a cross sectional area of 2 mm × 6 mm, and a length of 4 mm. The coil is connected to the RF generator by a 50 Ω impedance transmission line (we assume the fridge coax looks roughly like this).

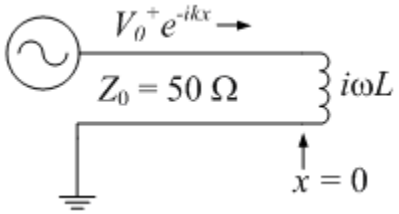

Fig. 4.4. Coil terminating 50 Ω coax.

We first find the current in the coil for a given power into the line, assuming that the coil looks like an inductance *L*. The voltage along the transmission line is

$$\begin{aligned} V(x) &= V_0^+ e^{-ikx} + V_0^- e^{ikx} \\ &= V_0^+ [e^{-ikx} + \Gamma e^{ikx}], \end{aligned}$$

where

$$\Gamma = \frac{Z_L - Z_0}{Z_L + Z_0}.$$

Let $Z_L = i\omega L$. Then

$$V(x=0) = V_0^+(1+\Gamma)$$
$$= V_0^+\left(1+\frac{i\omega L-50}{i\omega L+50}\right)$$
$$= V_0^+\left(\frac{2i\omega L}{i\omega L+50}\right)$$

and

$$I(x=0) = \frac{V(x=0)}{i\omega L}$$
$$= 2V_0^+\left(\frac{1}{i\omega L+50}\right).$$

Next, we can estimate the magnetic field in the coil as a function of current. If the *B*-field is uniform inside the coil, then $LI_{coil} = B_{coil}An$, so $B_{coil} = LI_{coil}/AN$, where A is the cross-sectional area of the coil, and N is the number of turns.

We also need to know the inductance of the coil. The inductance can be measured using a resonant *LRC* circuit and measuring reflected power versus frequency. For this 8-turn coil, the inductance measured via this method was L = 250 nH. As a check, using the coil dimensions and the formula for an infinitely long solenoid, $B = \mu_0 NI$, we obtain L = 290 nH, which is in the right ballpark.

Now we can estimate B_{coil}. At 50 MHz (a typical operation frequency), $i\omega L = 78i\ \Omega$. For -30 dBm (1 μW) of power out of the RF source, $V_0^+ = 10$ mV.

$$B_{coil} = \frac{LI}{An}$$
$$= 2V_0^+\left|\frac{1}{i\omega L+50}\right|\frac{L}{An}$$
$$= 2\times 0.01\,\text{V}\times\left(\frac{1}{\sqrt{78\,\Omega^2+50\,\Omega^2}}\right)\times\frac{250\,\text{nH}}{((2\,\text{mm}\times 6\,\text{mm})\times 8)}$$
$$= 0.5\,\mu\text{T}.$$

Figure 4.5 shows a plot of B_{coil} versus frequency for this 8-turn coil.

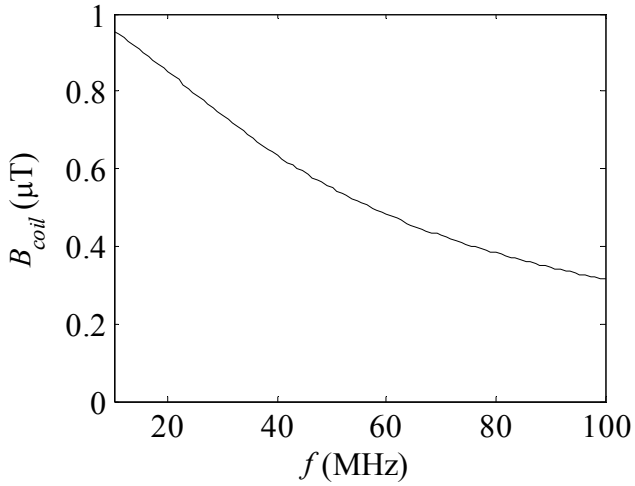

Fig. 4.5. Frequency response of NMR coil (dimensions given in text) terminating a 50 Ω transmission line. The RF source output is 1 μW.

Ohmic loss

We have ignored the resistance of the coil wire until now. The ohmic loss in the NMR coil is important to consider since it may affect the magnitude of the RF *B*-field and/or cause unwanted heating of the coil. The surface resistance of the coil wire is given by

$$R_s = \sqrt{\frac{\omega\mu}{2\sigma}}\,.$$

For for copper wire at low temperature ($T < 4$ K), $\sigma \sim 10^9/\Omega\cdot\text{m}$. Then

$$R_s = \sqrt{f(\text{MHz})} \times 6 \times 10^{-5}\,\Omega/\square.$$

For 100 mm (length of coil wire + leads) of 0.0033" diameter wire, this gives a total resistance of about $R = \sqrt{f(\text{MHz})} \times 0.02\,\Omega$, which is much less than 1 Ω for frequencies below 100 MHz. For our coil design, the reactance of the coil is about $50i$ Ω at typical operation frequencies, so the effect of the resistance of the coil in determining the RF magnetic field is negligible.

The power dissipated by ohmic heating will be given by I^2R. For -30 dBm of RF power from the generator (this is an upper bound – the RF power is usually less) and a

coil reactance of $50i\ \Omega$, the current will be $I = 0.2$ mA. Then, for $f = 50$ MHz (a typical operating frequency) we have $R \sim 0.14\ \Omega$ and the power dissipated $I^2R \sim 6$ nW.

4.3.2 RDNMR Signal

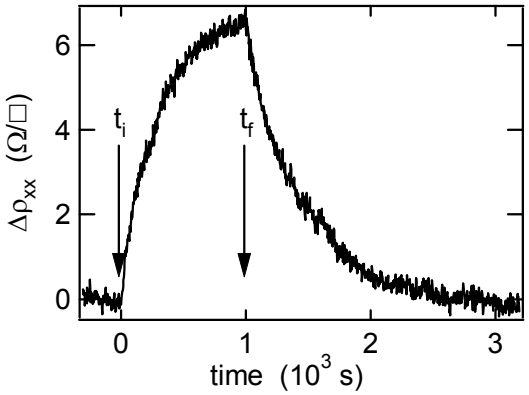

Fig. 4.6. Typical RDNMR trace ($\nu = 1/2$, $B = 4.48$ T, $T = 45$ mK) showing the response in R_{xx} to an NMR pulse and the transient signal used to measure T_1. The RF is on resonance for times between the dotted lines, and off resonance for all other times.

Fig. 4.6 shows a typical change in longitudinal resistance $\Delta\rho_{xx}$ at filling factor $\nu = 1/2$ obtained by applying resonant RF to change the nuclear spin polarization. For times earlier than t_i, the nuclear spin polarization is at thermal equilibrium and the RF magnetic field is on, but off resonance. Then, at t_i the RF is brought onto resonance and an increase in the 2DES resistance is observed. The rise time is RF power dependent. At time t_f the RF is moved off resonance and the resistance falls as the nuclear spin polarization decays back to thermal equilibrium with a time constant T_1.

From the data of Fig. 4.6, the magnitude of the ac magnetic field and the change in the nuclear polarization due to NMR can be estimated from the rise time and T_1, where τ_{rise} and T_1 are determined via an exponential fit to the data for $t_i < t < t_f$ and $t > t_f$, respectively. The fall time is T_1, and, in the limit $T_2 << T_1$ and $\omega_r T_2 << 1$, the rise time is given by

$$1/\tau_{rise} = \omega_r{}^2 T_2 + 1/T_1,$$

and the fractional change in the magnetization is approximately

$$\frac{M_0 - M_z}{M_0} = \left[\frac{\omega_r^2 T_1 T_2}{1 + \omega_r^2 T_1 T_2} \right] = 1 - \tau_{rise} / T_1 .$$

Appendix D contains a derivation of the above expressions, starting from the Bloch equations.

4.3.3 Lineshape

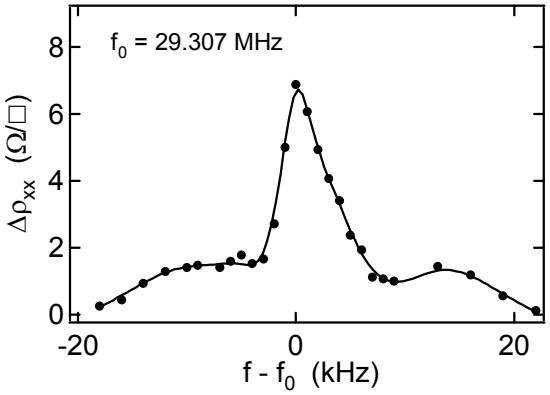

Fig. 4.7. Typical RDNMR lineshape for ^{75}As. The 2DES is at filling factor $\nu = 1/2$, B = 4 T. The center resonance frequency is f_0 = 29.307 MHz. The solid line is a guide to the eye.

Fig. 4.7 shows a typical RDNMR lineshape for ^{75}As. This plot shows the NMR-induced change in resistance $\Delta\rho_{xx}$ obtained by using the technique described by Fig. 5, versus frequency, measured relative to the center of the NMR line. The two shoulders are due to quadrupole splitting. The linewidth is ~ 5 kHz FWHM and the asymmetry of the peak is likely due to the shape of the 2DES electronic wavefunction in the confinement direction. Both the intensity of the RDNMR signal and the NMR frequency Knight shift (a negative shift) will depend on the magnitude of the wavefunction for a given in-plane slice of the 2DES region.

A sketch of how the subband wavefunction determines the lineshape is shown in Fig. 4.8. For nuclei located at a z-position near the peak of the wavefunction, the magnitude of the Knight shift (marked as $|K_{S1}|$ in Fig. 4.8) will be relatively large,

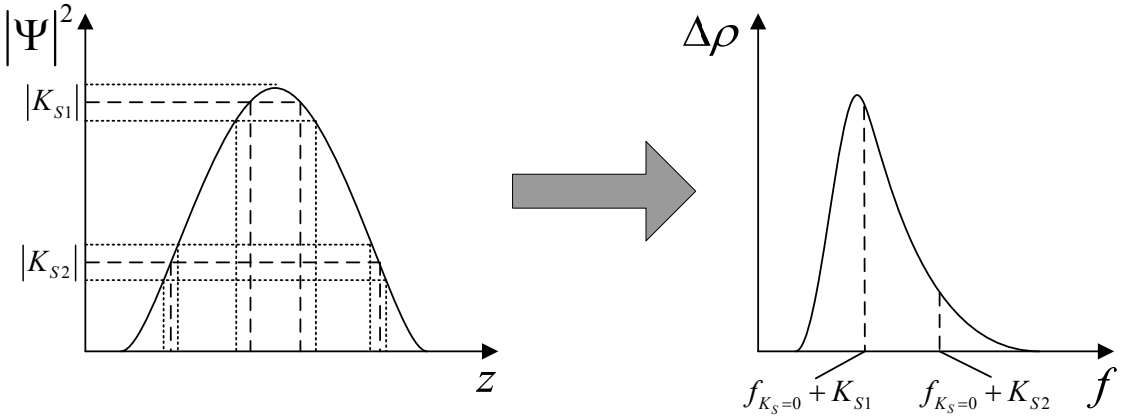

Fig. 4.8. Cartoon showing how the shape of the 2DES subband wavefunction affects the RDNMR lineshape, $\Delta\rho$ vs. f. The distance between the dotted lines in the left figure represents the NMR linewidth broadening that would be present without including the effect of finite wavefunction thickness.

whereas nuclei located near the tails of the wavefunction will have a smaller Knight shift (marked as $|K_{S2}|$ in Fig. 4.8). The width between the dotted lines in the left panel of Fig. 4.8 represents the NMR linewidth broadening that would be present before including the effects of the finite wavefunction thickness (due to, for example, nuclear dipole-dipole coupling or magnetic field inhomogeneity). At a given NMR frequency, this linewidth broadening and the shape of the wavefunction will determine the number of nuclei which will be influenced by the RF. Because coupling between the nuclei and the 2DES is greatest near the peak in the wavefunction, nuclei located near this peak will have the greatest influence on $\Delta\rho$, the NMR-induced change in resistivity. Combining all of these effects leads to a RDNMR lineshape similar to that sketched in the right-hand panel of Fig. 4.8.

4.4 Applications

Several applications of the RDNMR technique will be discussed in this thesis. The RDNMR data of Chapter 5 provide evidence of a spin transition in a correlated bilayer 2DES. Next, Chapter 6 presents detailed RDNMR measurements near a spin transition for composite fermions in the half-filled Landau level. Finally, Chapter 7 probes the electron spin near $\nu = 1$ in a single layer 2DES, where the presence of Skyrmions, charged spin-texture excitations, are expected to play a role in nuclear spin dynamics.

References

[1] B. I. Halperin, *Helv. Phys. Acta* **56**, 75 (1983).

[2] J. P. Eisenstein, H. L. Stormer, L. Pfeiffer, and K. W. West, *Phys. Rev. Lett*. **62**, 1540 (1989).

[3] J. P. Eisenstein, H. L. Stormer, L. N. Pfeiffer, and K. W. West, *Phys. Rev. B* **41**, 7910 (1990).

[4] S. L. Sondhi, A. Karlhede, S. A. Kivelson, and E. H. Rezayi, *Phys. Rev. B* **47**, 16419 (1993).

[5] S. M. Girvin, *Physics Today*, June 2000, p. 39.

[6] See, for example, C. Cohen-Tannoudji, B. Diu, and F. Laloe, *Quantum Mechanics*. Hermann, Paris 1977.

[7] D. Paget, G. Lampel, B. Sapoval, and V. I. Safarov, *Phys. Rev. B* **15**, 5780 (1977).

[8] A. Abragam. *The Principles of Nuclear Magnetism*. Oxford University Press, Oxford 1961.

[9] M. Dobers, K. v. Klitzing, J. Schneider, G. Weimann, and K. Ploog, *Phys. Rev. Lett*. **61**, 1650 (1988).

[10] W. Desrat, D. K. Maude, M. Potemski, J. C. Portal, Z. R. Wasilewski, and G. Hill. *Phys. Rev. Lett*. **88**, 256807 (2002).

[11] G. Gervais *et al*., *Phys. Rev. Lett*. **94**, 196803 (2005).

[12] L. A. Tracy, J. P. Eisenstein, L. N. Pfeiffer, and K. W. West, *Phys. Rev. B* **73**, 121306 (2006).

[13] S. Kronmuller *et al*., *Phys. Rev. Lett*. **82**, 4070 (1999).

[14] J. H. Smet, R. A. Deutschmann, W. Wegscheider, G. Abstreiter, and K. von Klitzing, *Phys. Rev. Lett*. **86**, 2412 (2001).

Chapter 5:
Spin Transition in the Half-Filled Landau Level

As discussed in Chapter 3, the fractional quantum Hall effect can be understood in an elegant way using a composite fermion (CF) picture. In this picture, a single layer 2DES at Landau level filling fraction $\nu = 1/2$ can be described as a Fermi liquid of CF's, where a CF is an electron with two magnetic flux quanta attached [1]. The CF picture has been very effective at describing a wide range of experiments, but the limit of its applicability is still an ongoing subject of interest.

Just as in the case of an ordinary Pauli paramagnet, one might expect a spin transition for CF's at $\nu = 1/2$ to occur as the magnitude of the electronic Zeeman energy is tuned relative to the Fermi energy. Starting with a partially polarized electron gas, as the ratio of Zeeman to Fermi energy is increased, the electronic spin polarization will increase and eventually there will be a transition to a completely polarized state. However, this deceptively simple picture hides some of the differences between this strongly interacting system and a simple Pauli paramagnet. For example, in the case of CF's the Fermi energy is determined by the strength of the Coulomb interaction instead of the kinetic energy. This chapter presents low-temperature resistively detected NMR measurements which examine the spin transition for CF's at $\nu = 1/2$ [2].

5.1 Composite Fermions and Spin

The notion of composite fermions was introduced in Chapter 3. However, the spin degree of freedom was neglected. Next, we introduce a simple picture that includes spin at $\nu = 1/2$.

Even though $\nu = 1/2$ occurs in the presence of a large perpendicular magnetic field, in a mean field approximation, at exactly $\nu = 1/2$ the system can be treated as a Fermi sea of CF's. The CF orbital degree of freedom behaves as if there were effectively zero magnetic field. However, the spin degree of freedom is still affected by the presence of the magnetic field. Adopting a simple picture, we assume that the effect of the magnetic field on the CF spin is to simply shift the energy of the up spins with respect to the down spins by the Zeeman energy, and that this shift is given by the electron spin g-factor g^*

such that the Zeeman gap is $E_Z = \mu_B g^* B$. We set the CF g-factor equal to the electron g-factor [3]. We also assume that the CF's have a parabolic dispersion relation E vs. k with an effective mass m_{CF} such that, using the usual relation for the density of states for free fermions in 2D, the Fermi energy of a single spin branch of CF's is $E_F = 2\pi\hbar^2 n/m_{CF}$. The relative magnitude of the Zeeman splitting and Fermi energy will determine the spin polarization of the system, as sketched in Fig. 5.1. For $E_Z < E_F$ the system is partially spin polarized, and for $E_Z > E_F$, the system is completely spin polarized.

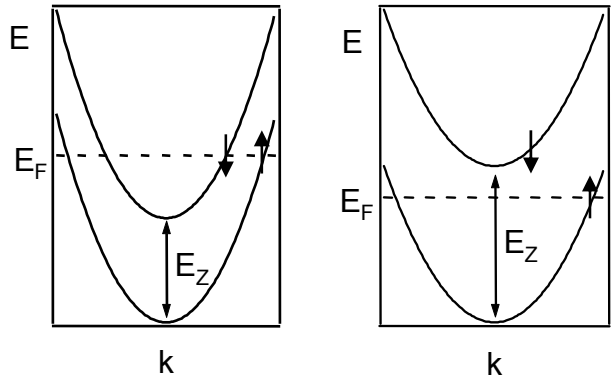

Fig. 5.1. Simple model of composite fermion spin polarization. The dashed line is the Fermi Energy. The two parabolas are the dispersion relations for up and down CF's The left and right plot show the case of a partially and completely spin polarized electron gas, respectively.

The mass m_{CF} is referred to as the "polarization mass" and is different from the effective mass commonly extracted from measurements of activation energies of FQH states via magnetotransport measurements [3]. A phenomenological, transport-derived effective mass $m_{CF\_transport}$ for CF's can be obtained by setting the activation energy Δ (measured via the temperature dependence of the resistivity) at a FQH state equal to the CF cyclotron energy. Then $\Delta = eB_{eff}/m_{CF\_transport}$, where $B_{eff} = B - B_0 = \phi_0 n\left(1/\nu - 2\right)$ is the effective magnetic field experienced by a CF at filling factor ν, $B_0 = \phi_0 2n$ for a CF comprised of an electron bound with two flux quanta, $\phi_0 = h/e$ is the quantum of magnetic flux, and n is the electron density. The activation gap at FQH states is determined by the Coulomb energy, so that $\Delta \sim \sqrt{n}$. Then, for fixed ν, $m_{CF\_transport} \sim \sqrt{n}$.

The polarization mass is not equal to the transport mass. The activation gap used to define $m_{CF\_transport}$ contains contributions from both the bare CF cyclotron energy and the

self energies of an excited CF particle and CF hole. The polarization mass will not be determined by just the bare CF cyclotron energy alone, but the contribution due to interactions should be less than for the transport activation mass. However, the Fermi energy used to define the polarization mass is proportional to the Coulomb energy so that the polarization mass at fixed $\nu = 1/2$ also scales like $m_{CF} \sim \sqrt{n} \sim \sqrt{B}$.

Within the model presented above, a spin transition between partial and complete spin polarization at $\nu = 1/2$ should occur as a function of density and magnetic field (if n is held fixed, then $n \sim B$). The situation is sketched in Fig. 5.2. At fixed $\nu = 1/2$, as a function of magnetic field, the Zeeman splitting rises more rapidly than the Fermi energy. The Fermi energy is proportional to the Coulomb energy so that $E_F \sim \sqrt{B}$, while $E_Z \sim B$. Thus, E_Z and E_F will cross at some critical magnetic field B_C. For fields below B_C, $E_Z < E_F$ so that the spin polarization is partial. As B is increased, the spin polarization will increase until $B \geq B_C$, at which point the spin polarization will be complete.

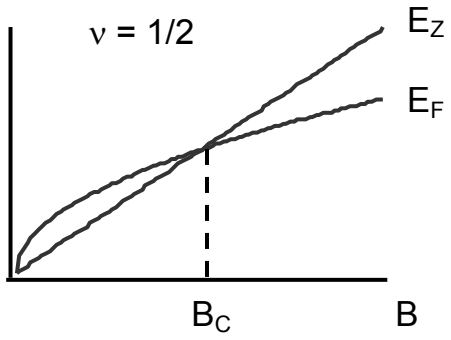

Fig. 5.2. Scaling of CF spin Zeeman and Fermi energies with magnetic field at $\nu = 1/2$, showing the critical field B_C at which the two energies are equal and the transition from partial to complete spin polarization should occur.

The value of the composite fermion effective mass m_{CF} determines the critical magnetic field and density at which the 2DES becomes completely spin polarized. The transition occurs when the Zeeman splitting is equal to the Fermi energy:

$$g\mu_B B = E_F$$
$$g\left(e\hbar/2m_e\right)B = \pi\hbar^2 n/m_{CF},$$

where m_e is the bare electron mass in vacuum and g is the g-factor for the composite fermions, which we assume is the same as that for electrons, g = -0.44. Now, at $\nu = 1/2$, $n = Be/2h$, so at the critical magnetic field we find that

$$m_{CF} / m_e = 1/|g|.$$

To start the chapter, we have presented a very simple picture of spin at $\nu = 1/2$. More sophisticated versions of this Pauli paramagetism picture that, for example, do not assume a parabolic dispersion relation for CF's, can be found in Ref.'s [3, 4]. More speculatively, there is a possibility that the spin transition at $\nu = 1/2$ is weakly first order. Ferromagnetism, driven by residual interactions between CFs, has been theoretically predicted for CF's at $\nu = 1/4$ [5]. We will return to the topic of ferromagnetism for CF's later in the Chapter. There is also theoretical evidence that the $\nu = 1/2$ state is energetically near a state in which composite fermions form spin-polarized pairs [6].

Previous experimental evidence exists for a spin transition for CF's at $\nu = 1/2$. The first observation of this transition was by Kukushkin *et al*. using polarization-resolved photoluminescence; the electron spin polarization was observed to increase and then saturate when increasing the electron density and magnetic field while maintaining fixed filling factor $\nu = 1/2$ [7]. Optically pumped NMR measurements of the Knight shift, using multiple quantum well samples (~ 100 closely spaced QW's), also suggest that a spin transition occurs when the total magnetic field is increased by rotating the sample in the magnetic field while maintaining fixed perpendicular magnetic field to remain at $\nu = 1/2$ [8, 9]. A combination of RDNMR and standard directly detected NMR has been used to measure the NMR Knight shift versus magnetic field in a variable density sample at $\nu = 1/2$; the Knight shift versus field data show a change in slope that is suggestive of a spin transition [10]. The electronic spin-flip excitations have been probed using inelastic light scattering; the spin-flip gap was shown to collapse as $\nu \rightarrow 1/2$ for a sample at relatively low magnetic field and remain finite for another sample at higher magnetic field [11].

The RDNMR measurements discussed in this chapter take a closer look at the spin transition at $\nu = 1/2$, using higher quality samples and lower temperatures than previously achieved. Our measurements more thoroughly examine the nuclear spin-lattice

relaxation time T_1 temperature and magnetic-field dependence for temperatures ranging from 35 to 200 mK over a wide magnetic field and density range. We also show the first measurements of how transport at $\nu = 1/2$ depends on the electron spin polarization.

5.2 Experiment

We probe the transition from partial to complete electron spin polarization as a function of density in a 2DES at $\nu = 1/2$ using the resistively detected NMR (RDNMR) technique outlined in Chapter 4. Both the nuclear spin lattice relaxation time T_1 of ^{75}As and the response in resistance to a change in the nuclear spin polarization reflect this transition. At low densities, where the electron spin polarization is partial, the T_1 time is relatively short, due to the presence of both electron spin states at the Fermi level. In this regime T_1 is density independent and has a Korringa-like [19] temperature dependence. At higher densities, T_1 increases and the RDNMR signal eventually vanishes, consistent with a transition to complete electron spin polarization. In the transition region we observe an unexpected enhancement of the RDNMR signal.

5.2.1 Sample

The sample used in the present experiment is a GaAs/AlGaAs heterostructure grown by molecular beam epitaxy. A high mobility 2DESs is created in these structures via modulation doping with Si. For the data presented here, the 2DES is confined in GaAs at a single interface with AlGaAs and is laterally patterned into a wide (500 μm) Hall bar geometry. An aluminum top gate was used to control the 2DES density. The as-grown density of the 2DES is $n \sim 1.3 \times 10^{11}$ cm^{-2} and its low temperature mobility ranges from $\mu \sim 5 \times 10^6$ cm^2/Vs at $n \sim 1.3 \times 10^{11}$ cm^{-2} to $\mu \sim 1 \times 10^6$ cm^2/Vs at $n \sim 0.3 \times 10^{11}$ cm^{-2}.

5.2.2 Transport

Magnetotransport for this sample is shown below in Fig. 5.3. At both low and high densities, longitudinal resistance minima are seen at several integer and fractional quantum Hall states.

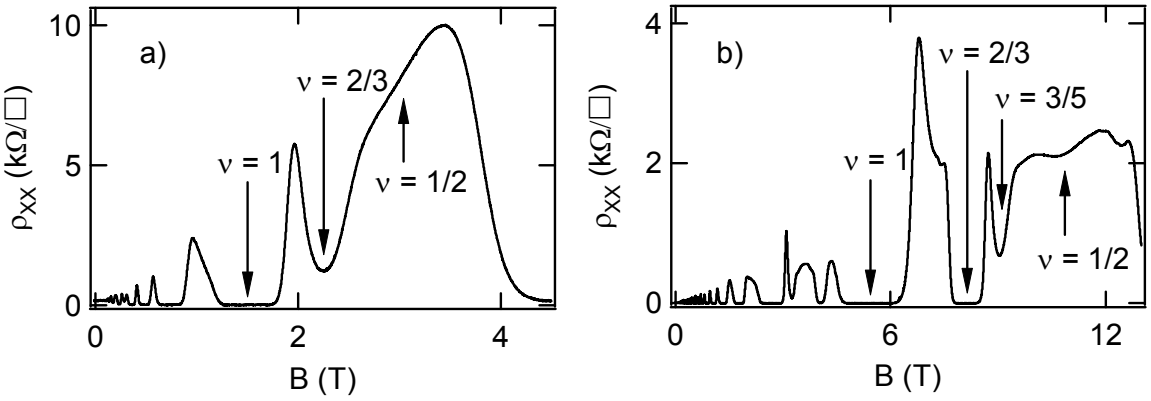

Fig. 5.3. Low temperature magnetotransport for the single layer 2DES used for the CF spin transition RDNMR data shown in this chapter, at low and high density. a) $n \sim 0.4 \times 10^{11}$ cm^{-2} ($\nu = 1/2$ occurs at $B \sim 3.0$ T). b) $n \sim 1.3 \times 10^{11}$ cm^{-2} ($\nu = 1/2$ occurs at $B \sim 10.8$ T).

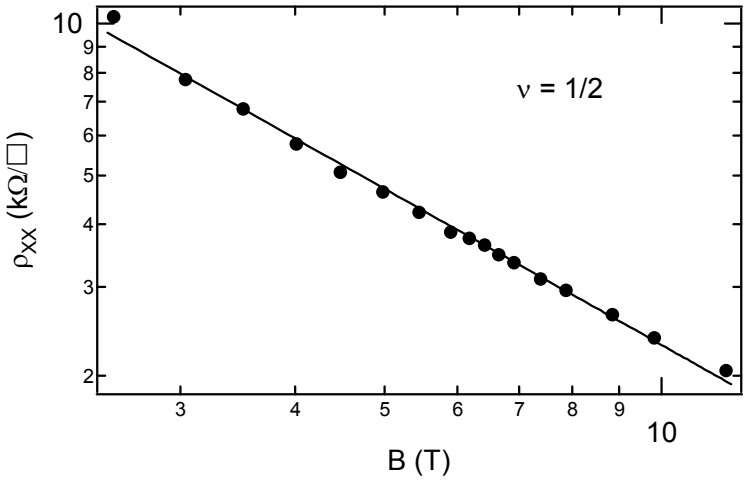

Fig. 5.4. Log-log plot of ρ_{xx} vs. B, at fixed filling factor $\nu = 1/2$, $T = 45$ mK. The solid line is a power-law fit to the data, which yields $\rho_{xx} \sim B^{-1.0}$.

Figure 5.4 shows the longitudinal resistivity right at $\nu = 1/2$ versus magnetic field, while tuning the density to maintain fixed filling factor $\nu = 1/2$. The data approximately follow a power law: $\rho_{xx} \sim B^{-1.0} \sim n^{-1.0}$. Using the Drüde formula for resistivity at zero magnetic field, $1/\rho = ne^2\tau_{tr}/m^*$, where m^* is an effective CF mass. This implies τ/m^* is independent of density. This does not agree with theoretical calculations of the resistivity at $\nu = 1/2$ by HLR [12] which predict $\tau_{tr}/m^* \sim k_F$. See section 6.3.3, "Transport at $\nu = 1/2$", later in this chapter for further description of transport at $\nu = 1/2$ as discussed in HLR. The fit of Fig. 3.4 gives $\tau_{tr}/(m^*/m_e) = 1.2 \times 10^{-11}$ s, where m_e is the electron

mass in vacuum. Experimentally, the CF effective mass obtained from transport measurements at FQH states near $\nu = 1/2$ [13] is of the same order of magnitude as m_e. Then, we have a transport lifetime for CF's $\tau_{tr} \sim 10$ ps. For comparison, at zero magnetic field, the transport lifetime of ordinary electrons for this sample is roughly $\tau \sim$ 100 ps.

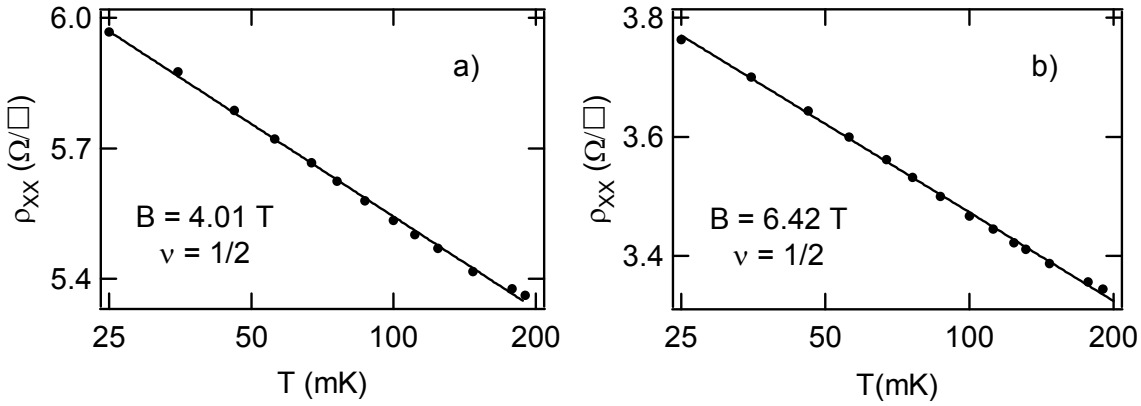

Fig. 5.5. Temperature dependence of resistivity at $\nu = 1/2$. In both graphs, solid line is a fit to the data of the form $\rho_{xx} = a + b \ln T$. a) $\rho_{xx} = 6.96 - 0.31 \ln T$ (kΩ). b) $\rho_{xx} = 4.45 - 0.21 \ln T$ (kΩ).

As seen in Fig. 5.5, the temperature dependence of the longitudinal resistivity at $\nu = 1/2$ is of the form $\rho_{xx} \sim a + b \ln T$. This logarithmic temperature dependence at $\nu = 1/2$ has been seen previously by Kang *et al*. and Rokhinson *et al*. [14], but is not theoretically well-understood [12].

5.2.3 Sample Temperature

An approximately rectangular 8-turn NMR coil is wound around the sample for applying RF magnetic fields parallel to the 2DES plane and perpendicular to the large applied dc magnetic fields. We estimate the RF magnetic fields H_1 to be in the 0.1 μT range, much less than typical nuclear dipolar fields $H_d \sim 1$ gauss (see Chapter 4, section 4.3.1a). The electron temperature with the RF magnetic field on was determined by using the 2DES resistance as an in-situ thermometer, which was calibrated with the RF power off. Figure 5.6 shows the 2DES electron temperature, as determined via the 2DES resistance, vs. cold finger temperature with the RF power on, at a fairly high power where the estimated

RF magnetic field is $H_1 \sim 0.5$ μT. At this power level, there is a noticeable rise in the electron temperature below about 100 mK, and it is not possible to reach electron temperatures below about 50 mK.

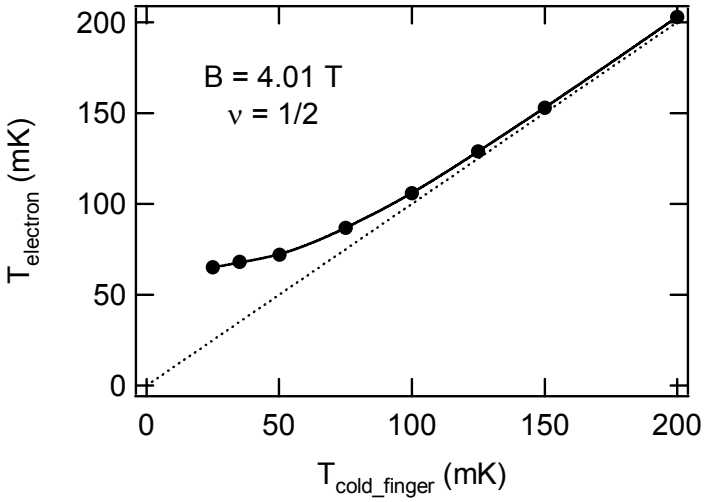

Fig. 5.6. Electron temperature, as determined from sample resistivity, vs. cold finger temperature with RF on, at B = 4.01 T, ν = 1/2, at a relatively high RF power, $H_1 \sim 0.5$ μT, $f \sim 29$ MHz. The solid line is a guide to the eye. The dotted line is the case for no RF heating (RF off), for reference.

5.2.4 RDNMR signal at $\nu = 1/2$

Below, Fig. 5.7 shows a typical change in resistance $\Delta\rho_{xx}$ at filling factor ν = 1/2 obtained by applying resonant RF to change the nuclear spin polarization. For times earlier than t_i, the nuclear spin polarization is at thermal equilibrium and the RF magnetic field is on, but off resonance. Then, at t_i the RF is brought onto resonance and an increase in the 2DES resistance is observed. As discussed in Chapter 4, the rise time is RF power dependent and is determined by $T_1/(1+\omega_R^2 T_2 T_1)$, where ω_R is the Rabi frequency (see appendix H). At time t_f the RF is moved off resonance and the resistance falls as the nuclear spin polarization decays back to thermal equilibrium with a time constant T_1.

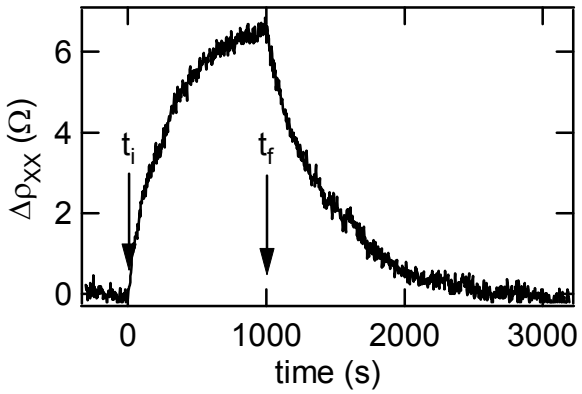

Fig. 5.7. Typical RDNMR trace (B = 4.48 T, T = 45 mK) showing the response in ρ_{xx} to an NMR pulse and the transient signal used to measure T_1. The RF is on resonance for times between the dotted lines, and off resonance for all other times.

5.2.5 RDNMR Lineshape

Figure 5.8 shows a typical RDNMR lineshape for ^{75}As. The solid markers show the change in resistance $\Delta\rho_{xx}$, obtained by using the procedure described in Fig. 4, versus frequency measured relative to the center of the NMR line. The two satellite peaks are due to quadrupole splitting. The linewidth is ~ 5 kHz FWHM and the asymmetry of the peak is likely due to the shape of the 2DES electronic wavefunction in the confinement

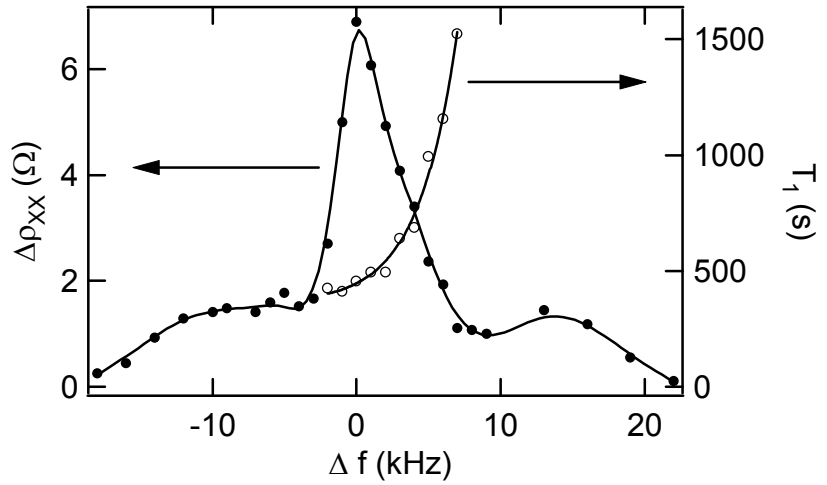

Fig. 5.8. RDNMR lineshape and nuclear T_1 time vs. frequency on the NMR line for ^{75}As at filling factor ν = 1/2, B = 4.01 T. The center of the resonance is at f_0 = 29.307 MHz.

direction. Both the intensity of the RDNMR signal and the NMR frequency Knight shift (a negative shift for electrons in GaAs) will depend on the magnitude of the wavefunction for a given in-plane slice of the 2DES region. T_1 also varies as a function of frequency through a similar argument. See Chapter 4, section 4.3.3 for a more detailed explanation of the NMR lineshape. Subsequent measurements of T_1 and $\Delta\rho_{xx}$ shown in this chapter correspond to data taken at the center frequency ($\Delta f = 0$, as shown in Fig. 5.8) of the NMR line, defined as the frequency at which the NMR-induced change in the resistivity is greatest.

5.2.6 RDNMR Signal Temperature Dependence

Figure 5.9 shows the RDNMR signal vs. temperature at $\nu = 1/2$ at fixed magnetic field and RF power. There are two contributions to this temperature dependence. The first is the temperature dependence of the thermal equilibrium nuclear polarization, which is roughly proportional to $1/T$ (nuclear Curie Law). This expected contribution is sketched

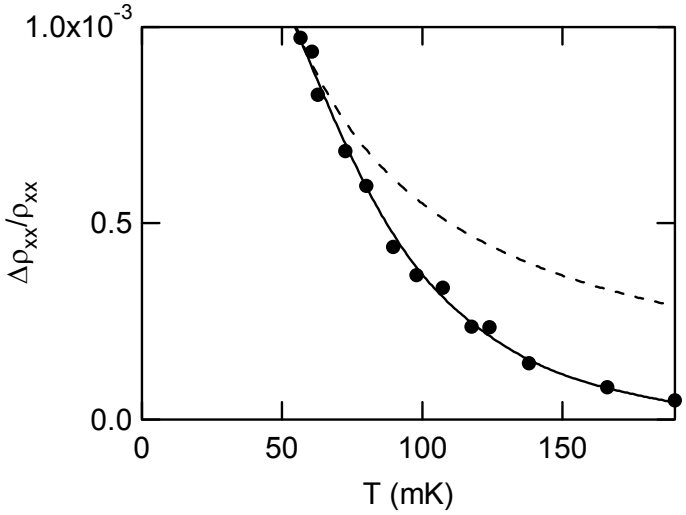

Fig. 5.9. Fractional change in longitudinal resistance due to NMR at B = 4.01 T, $\nu = 1/2$. Solid line is a guide to the eye. The dashed line shows the expected temperature dependence due to just the nuclear Curie Law, arbitrarily fitted to the lowest temperature data point.

in Fig. 5.9 by the dotted trace, which is of the form $\Delta\rho_{xx}/\rho_{xx} = \alpha T^{-1}$, where α is arbitrarily set by the lowest temperature data point. A second contribution is from the temperature dependence of the response of the 2DES resistivity to changes in the Zeeman splitting (temperature dependence of $\partial\rho_{xx}/\partial E_Z$).

5.3 RDNMR Density Dependence at $\nu = 1/2$

RDNMR measurements at $\nu = 1/2$ over a wide density and magnetic field range at two temperatures, $T = 45$ and 100 mK, are shown in Fig. 5.10, below. The spin transition is evident from both the RDNMR signal size and T_1 data. Figure 5.10a displays the RDNMR signal versus density. The quantity $S \equiv (\partial\rho_{xx}/\partial E_Z)/\rho_{xx}$ is the NMR-induced fractional change in resistance divided by the NMR-induced change in the Zeeman splitting.

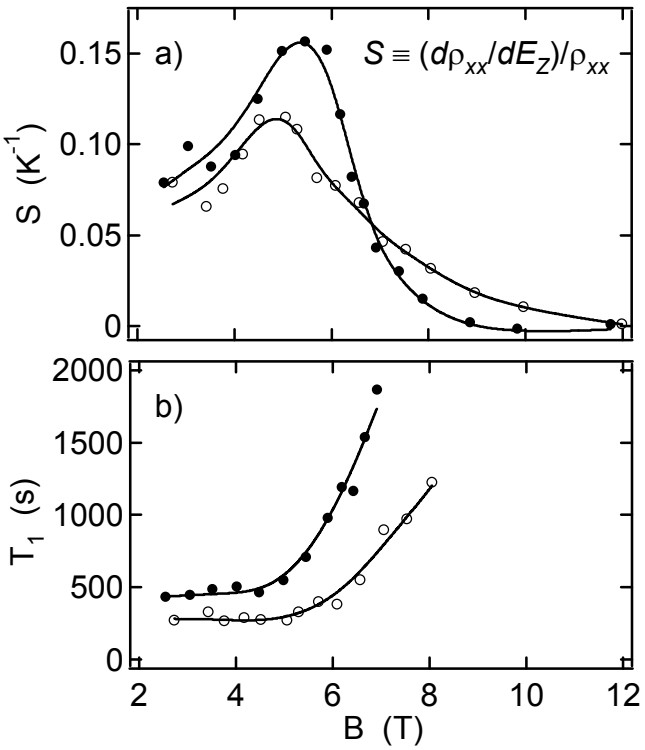

Fig. 5.10. a) RDNMR signal S and b) nuclear T_1 time and vs. magnetic field at fixed filling factor $\nu = 1/2$. Closed and open symbols correspond to a temperature of 45 and 100 mK, respectively.

5.3.1 Zeeman Energy Calibration

The change in the Zeeman energy is calculated using the known strength of the hyperfine coupling in GaAs [15] and an estimate of the NMR-induced change in the nuclear polarization. From Chapter 4, using the Bloch equations, we derived the expression

$$\Delta\xi / \xi = \left[\frac{\omega_r{}^2 T_1 T_2}{1 + \omega_r{}^2 T_1 T} \right] = 1 - \tau_{rise} / T_1, \tag{1}$$

where $\Delta\xi / \xi$ is the NMR-induced fractional change of the nuclear polarization. Thus, the NMR-induced change in the nuclear polarization can be extracted from the rise and fall time ($\tau_{fall} = T_1$) of transient data, like that shown in Fig. 5.4, or by measuring the RF power dependence (RF power ~ ω_r^2) of the RDNMR signal and fitting the data to a function of the form given by the middle term in Eq. (1).

Figure 5.11 shows the magnitude of the fractional NMR-induced change in nuclear polarization $\left|\Delta\xi / \xi\right|$ obtained using these two methods, versus magnetic field, at fixed filling factor $\nu = 1/2$. The scatter in the data is due to uncertainty in the measurement of the RDNMR rise and fall time. To calculate S in Fig. 10a we use the average of the $\left|\Delta\xi / \xi\right|$ values shown Fig. 5.11, which is $\left|\Delta\xi / \xi\right|_{avg} = 47\%$.

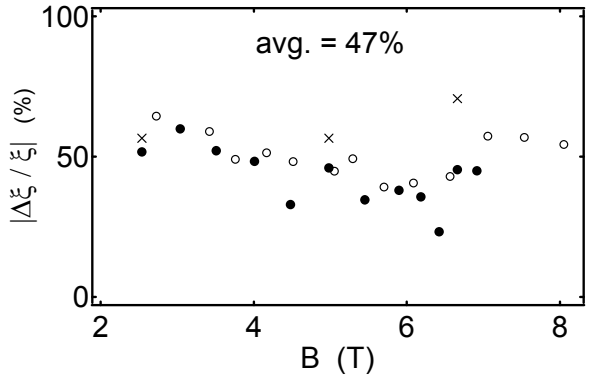

Fig. 5.11. Change in nuclear polarization of ^{75}As due to NMR. Crosses correspond to values determined from power dependence. Circles are points calculated from NMR T_1 and rise time, closed and open circles correspond to 45 mK and 100 mK data, respectively.

5.3.2 Density Dependence: $d\rho_{xx}/dE_Z$

Although the resistivity ρ_{xx} at ν =1/2 has a gradual, monotonic dependence on density/magnetic field (see Fig. 5.4), Fig. 5.10a shows that the RDNMR signal displays a dramatic change while passing through the transition. At low magnetic fields, in the partially polarized phase, there is a positive, finite response. At higher magnetic fields, when the 2DES becomes completely spin polarized, the signal vanishes; the resistance is no longer sensitive to RDNMR since increasing the Zeeman splitting only further stabilizes a fully polarized state. A peculiar enhancement of the RDNMR response is seen in the transition region, especially at T = 45 mK. A similar peak has been seen in a second sample, an undoped, gated heterojunction with a mobility ranging from $\mu \sim 1 - 2 \times 10^6$ cm^2/Vs at densities ranging from $n \sim 0.3\text{-}1.2 \times 10^{11}$ cm^{-2}. This feature is weak but present at T = 100 mK and seems to quickly sharpen with decreasing temperature.

5.3.3 Transport at $\nu = 1/2$

The origin of the RDNMR signal is not fully understood. Indeed, a theory of transport at ν = 1/2, that fully explains current experimental data, such as the value of ρ_{xx} at ν = 1/2, and its density and temperature dependence, is lacking [12, 14, 15]. HLR [12] estimates the resistance at ν = 1/2 by assuming that the transport scattering rate $1/\tau_{tr}$ is dominated by static fluctuations in the effective magnetic field for composite fermions, B_{eff}, due to density variations in the sample. These density fluctuations are assumed to be due to ionized dopants, of average density n_{imp}, distributed randomly in a modulation doped layer a distance d_s from the 2DES. Then, HLR finds

$$\frac{1}{\tau_{tr}} = \frac{4\pi\hbar n_{imp}}{m^* k_F d_s},$$

where m^* is an effective CF mass, and k_F is the Fermi wavevector. Using a Drude-like model, where the conductivity for CF's at ν = 1/2 is defined by $\sigma_{CF} \equiv 1/\rho_{xx}$,

$$\sigma_{CF} = \frac{ne^2\tau_{tr}}{m^*} = \frac{e^2 n k_F d_s}{4\pi\hbar n_{imp}}.$$

This formula is valid only for spinless electrons. If we include two spin species and assume the total conductivity σ_{CF} will be simply the sum of the individual conductivities of the two species $\sigma_{CF\uparrow}$ and $\sigma_{CF\downarrow}$, we have

$$\begin{aligned}\sigma_{CF} &= \sigma_{CF\uparrow} + \sigma_{CF\downarrow} \\ &= \frac{e^2 d_s}{4\pi\hbar n_{imp}}\left(n_\uparrow k_{F\uparrow} + n_\downarrow k_{F\downarrow}\right).\end{aligned}$$

We next hold the total electron density n constant and ask about σ_{CF} as a function of the spin polarization $\chi \equiv \left(n_\uparrow - n_\downarrow\right)/n$. The densities of the individual spin species can be written as $n_\uparrow = \left(\chi+1\right)n/2$, $n_\downarrow = \left(1-\chi\right)n/2$. Using the fact that the Fermi wavevector is proportional to the square root of the density: $k_{F\uparrow,\downarrow} \sim n_{\uparrow,\downarrow}{}^{1/2}$, the conductivity is

$$\sigma_{CF} = \alpha n^{3/2}\left[\left(\chi+1\right)^{3/2} + \left(1-\chi\right)^{3/2}\right],$$

where α is a constant determined by n_{imp}, d_s, and the electron charge. This expression predicts that the conductivity increases monotonically with increasing spin polarization. For example, if the system is unpolarized (χ = 0), $\sigma_{CF} = 2\alpha n^{3/2}$, whereas for a completely spin polarized (χ = 1), $\sigma_{CF} = 2^{3/2}\alpha n^{3/2}$. Recall that $\rho_{xx} = 1/\sigma_{CF}$. Then, we find that ρ_{xx} should decrease with increasing spin polarization. This does not agree with our experiment. The sign of $\partial\rho_{xx}/\partial E_Z$ is actually positive in the data of Fig. 5.10a, i.e. ρ_{xx} increases with increasing spin polarization

5.3.4 Dependence of RDNMR Signal on Current

Interestingly, the RDNMR response can depend on the magnitude of the measurement current. Figure 5.12 shows the RDNMR signal versus the magnitude of the current driven through the 2DES, at ν = 1/2, in the partially polarized regime, B = 3.6 T. For low currents, there is a regime where the RDNMR signal is current independent. The measurements shown in this chapter were made in this low current regime. However, as shown in Fig. 5.12, we find that large currents can change the magnitude of the RDNMR signal and even cause it to change sign. Many of the features of this non-linear response

at high current are similar to those seen at $\nu = 2/3$, where large currents have been shown to dynamically pump the nuclear polarization to magnitudes greater than at thermal equilibrium [16, 17]. That the nuclear spin system is pumped by high measurement currents is supported by the fact that, after application of a large current, subsequent application of resonant RF tends to bring the resistance back to the equilibrium, non-pumped value. See Appendix E for preliminary data demonstrating this pumping mechanism at $\nu = 1/2$.

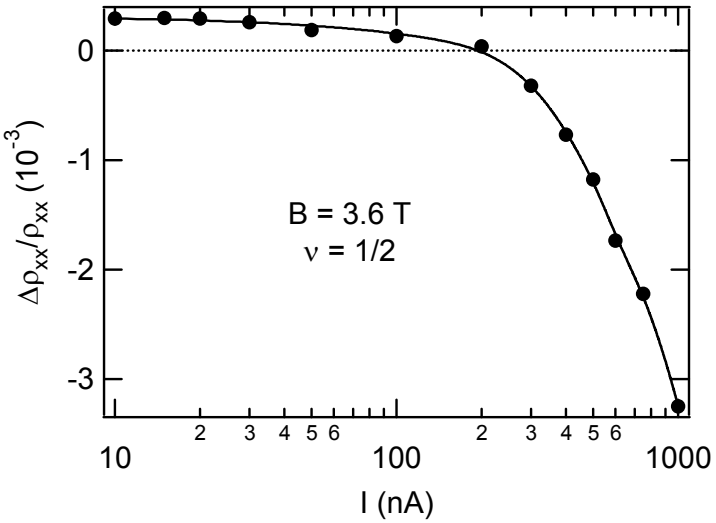

Fig. 5.12. NMR-induced fractional change in longitudinal resistivity vs. quasi-dc current driven through the 2DES.

5.3.5 Density Dependence: T_1

Figure 5.10b shows T_1 versus magnetic field. At low magnetic fields, deep in the partially polarized phase, T_1 is relatively short (the T_1 time for bulk GaAs at these temperatures can be hours or even days). Using the simple picture sketched in Fig. 1, the 2DES consists of a Fermi sea of spin up and down composite fermions, the two spin branches simply shifted in energy with respect to one another by the Zeeman splitting. In the partially polarized phase both up and down spin states are present at the Fermi level. This presence of both spin species at the Fermi level provides a route for nuclear spin relaxation. An electron and nucleus can perform a simultaneous spin flip, while conserving total energy and momentum. Since $g_N\mu_N B$, the nuclear Zeeman splitting, is

much less than kT, there must be empty and full electron states available differing in energy by $g_N\mu_N B$, allowing for energy conservation. As sketched in Fig. 5.13, the electron must experience a change in linear momentum during this process. This momentum is provided by the hyperfine point contact interaction with the nuclei (see Chapter 4). The Hamiltonian is of the form $\vec{I}\cdot\vec{S}\delta\left(\vec{R}\right)$ – proportional to a delta function in real space, and thus, couples the electron and nucleus for all values of momentum transfer. In ordinary 3D paramagnetic metals, nuclear spin relaxation occurs via a similar process and is known as Korringa relaxation. As shown in Fig. 10b, at higher magnetic fields T_1 increases dramatically. This is consistent with a transition to complete electron spin polarization, in which case the Korringa relaxation mechanism will no longer exist. Raising the electron temperature from T = 45 to 100 mK thermally smears the transition over a broadened magnetic field range.

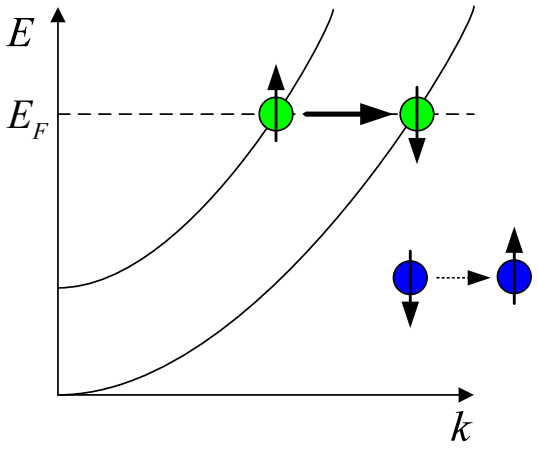

Fig. 5.13. Cartoon of Korringa nuclear relaxation process, showing a simultaneous nuclear spin flip (blue) and electron spin flip (green) at the Fermi energy. The hyperfine point contact interaction provides the momentum transfer for the electron spin flip.

5.3.6 Korringa Relaxation Rate

The Korringa nuclear relaxation rate is given by [19]

$$\frac{1}{T_1}=16\pi^3\hbar\left(\frac{K_{s1}}{n}\right)^2\int_{E_Z}^{\infty}D_\uparrow(\varepsilon)D_\downarrow(\varepsilon)f(\varepsilon,T)\left(1-f(\varepsilon,T)\right)d\varepsilon\,,$$

where the strength of the hyperfine coupling is given by the Knight shift for a fully polarized electron gas K_{s1} divided by the electron density n, the energy ε is measured from the bottom of the lowest energy spin branch, T is the temperature, $D_\uparrow(\varepsilon)$, $D_\downarrow(\varepsilon)$ are the density of states for up and down electrons, respectively, and $f(\varepsilon, \tau)$ is the Fermi function. This expression assumes that $kT >> g_N\mu_N B$, so that the nuclear Zeeman splitting can be ignored. Using the fact that the density of states is energy independent in 2D, we have

$$\begin{aligned}\frac{1}{T_1} &= 16\pi^3\hbar\left(\frac{K_{s1}}{n}\right)^2 D^2 \int_{E_Z}^{\infty} f(\varepsilon,T)\left(1-f(\varepsilon,T)\right)d\varepsilon \\ &= 16\pi^3\hbar\left(\frac{K_{s1}}{n}\right)^2 D^2 \int_{E_Z}^{\infty} \left(\frac{1}{1+e^{(\varepsilon-\mu)/kT}}\right)\left(1-\frac{1}{1+e^{(\varepsilon-\mu)/kT}}\right)d\varepsilon.\end{aligned}$$

This integral can be done analytically:

$$\frac{1}{T_1} = 16\pi^3\hbar\left(\frac{K_{s1}}{n}\right)^2 D^2 \frac{kT}{1+e^{(E_Z-\mu)/kT}}. \tag{1}$$

Next, we find the chemical potential μ as a function of temperature. Using the fact that the total density n of the 2DES remains fixed, we have

$$\begin{aligned} n &= n_\uparrow + n_\downarrow \\ &= \int_0^{\infty} D_\uparrow(\varepsilon) f(\varepsilon,T)\,d\varepsilon + \int_{E_Z}^{\infty} D_\downarrow(\varepsilon) f(\varepsilon,T)\,d\varepsilon \\ &= D_\uparrow \int_0^{\infty} \frac{1}{1+e^{(\varepsilon-\mu)/kT}} d\varepsilon + D_\downarrow \int_{E_Z}^{\infty} \frac{1}{1+e^{(\varepsilon-\mu)/kT}} d\varepsilon \\ &= D_\uparrow\left[\ln\left(1+e^{\mu/\tau}\right) + \ln\left(1+e^{(\mu-E_Z)/\tau}\right)\right].\end{aligned}$$

Solving for μ gives

$$\mu = \frac{E_Z}{2} + kT\ln\left[\sqrt{e^{n/DkT} + \sinh^2\left(E_Z/2kT\right)} - \cosh\left(E_Z/2kT\right)\right]. \tag{2}$$

Within the Korringa relaxation picture given above, the $1/T_1$ rate will be proportional to the square of the density of states at the Fermi energy, which for will be given by the effective mass m_{CF}, where $D(\varepsilon) = m_{CF}/2\pi\hbar^2$ for one CF spin branch. As mentioned earlier, this effective mass scales like $m_{CF} \sim \sqrt{B}$. Then, the expected density/magnetic field dependence for T_1 in the partially polarized phase will be $T_1 \sim 1/B$. However, Fig. 5.10b shows that T_1 is nearly density independent at low magnetic fields.

5.3.6a Finite Thickness Effects

A more careful analysis should include the variation of the 2DES subband wavefunction $\psi(z)$, whose amplitude and thickness will vary with density; this will affect both the strength of the hyperfine coupling and also the 2DES Coulomb interaction.

The hyperfine coupling constant (K_{S1}/n) will be proportional to the square of the peak magnitude of $\psi(z)$, so that $1/T_1 \sim (K_{S1}/n)^2 \sim 1/\langle z \rangle^2$, where $\langle z \rangle$ is the rms wavefunction thickness (this is only strictly true when the nuclear T_2, without linewidth broadening due to the shape of the 2DES subband wavefunction, is much longer than $1/K_S$). Using a Fang-Howard approximation for the wavefunction (see Chapter 1), $\langle z \rangle \sim n^{-1/3} \sim B^{-1/3}$ at fixed filling factor $\nu = 1/2$. This will lead to an additional variation of T_1 with density, due to the variation of the strength of the hyperfine coupling alone, of the form $T_1 \sim B^{-2/3}$.

The variation of the strength of the Coulomb interaction with wavefunction thickness will also affect T_1. The composite fermion Fermi energy is proportional to the Coulomb energy, so that that $E_c \sim E_F = (\hbar k_F)^2 / 2m_{CF}$. Then, $m_{CF} \sim 1/E_c$, so that, using $1/T_1 \sim D(\varepsilon)^2 \sim m_{CF}^2$, we have $T_1 \sim E_c^2$. The dependence of the Coulomb interaction on the 2D subband wavefunction can be estimated by calculating the Haldane pseudopotentials V_m for the Coulomb interaction in the lowest Landau level, as a function of the wavefunction thickness. The Coulomb pseudopotential V_m is the expectation value of the interaction energy for two electrons interacting via the Coulomb potential with relative angular momentum m, in the lowest Landau level [20]. The dependence of V_m on the effective wavefunction thickness parameter $1/bl$, where b is the Fang-Howard thickness parameter (see Chapter 1), and l is the magnetic length, is shown in Fig. 5.14. At fixed Landau level filling factor, the parameter $1/bl$ is proportional to the wavefunction thickness

normalized by the spacing between electrons. The psuedopotential is normalized relative to $e^2/\varepsilon l$, the Coulomb energy for the case of an infinitely-thin wavefunction. Figure 5.14 shows that V_m weakens with increasing effective thickness.

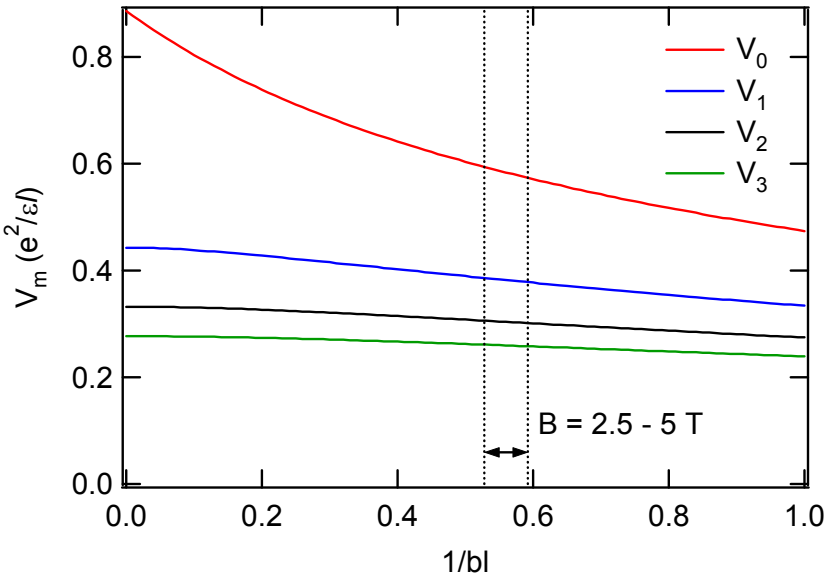

Fig. 5.14. Coulomb psuedopotentials V_m for m = 0 to 3 versus effective wavefunction thickness $1/bl$, where b is the Fang-Howard thickness parameter and l is the magnetic length. The dotted lines mark the magnetic field range, B = 2.5 – 5 T, over which the T_1 data of Fig. 5.10b is roughly magnetic field independent.

The wavefunction thickness can be estimated by using the Fang-Howard approximation for the wavefunction as a function of density, or by calculating a self-consistent solution to the Schrodinger and Poisson equations, as discussed briefly in Chapter 1. Both methods yield a fairly weak dependence of the effective thickness parameter $1/bl$ on density/magnetic field at fixed filling factor ν = 1/2. In the Fang-Howard approximation, $b \sim n^{1/3} \sim B^{1/3}$, while $l \sim B^{-1/2}$. Then, $1/bl \sim B^{1/6}$. From Fig. 5.14, we then see that the interaction energy will rise with density/magnetic field more slowly than for an ideal, infinitely-thin 2DES. Even though the actual thickness of the wavefunction is decreasing with increasing density, the spacing between electrons is decreasing even more rapidly, so that the effect of finite thickness at large densities actually becomes more important.

The relative importance of V_m for different values of m at $\nu = 1/2$ is unclear, but a rough upper bound on the effect of finite thickness on the interaction energy can be obtained from V_0, which is most sensitive to finite thickness effects. Using the above Fang-Howard approximation ($1/bl \sim B^{1/6}$), over the magnetic field range of interest, from $B \sim 2$ to 5 T at $\nu = 1/2$, there is a roughly 5% decrease in $V_0/(e^2/\varepsilon l)$. Since $T_1 \sim E_c^{\,2}$, this will lead to a ~ 10% maximum additional decrease in T_1 over this density/magnetic field range. Using self-consistent solutions to the Schrodinger-Poisson equation for the wavefunction yields similar results.

In short, the two above mentioned finite-thickness effects due to the variation of the strength of the hyperfine coupling and the Coulomb interaction with wavefunction thickness should cause T_1 to fall even faster with magnetic field than $1/B$, worsening the comparison between experiment and composite fermion theory.

5.3.7 Korringa Relaxation – Comparison to Data

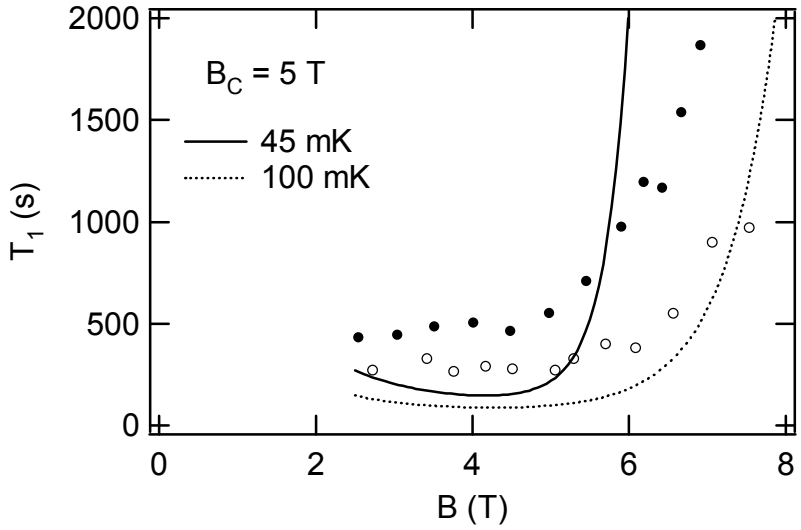

Fig. 5.15. T_1 vs. magnetic field/density at $\nu = 1/2$ calcuated using a simple 2D Korringa relaxation theory for a critical magnetic field for the spin transition of B_C = 5 T . Solid and dotted line: calculated T_1 at 45 and 100 mK, respectively. Solid and open circles: RDNMR measured T_1 at 45 and 100 mK, respectively.

Figure 5.15 shows T_1 vs magnetic field/density at $\nu = 1/2$ using the simple 2D Korringa theory of Eq.'s (1) and (2). The effect of the density dependence of the width of the 2D subband wavefunction on the hyperfine coupling strength has been included, but the smaller effect of the variation in the Coulomb energy due to the changing thickness has been ignored. We estimate the hyperfine coupling constant (K_{S1}/n) for ^{75}As by using measurements of the NMR Knight shift for ^{71}Ga in 2DES quantum wells at $\nu = 1/3$ published by Khandelwal *et al*. [21]. For ^{71}Ga (K_{S1}/n) = 4.5 $\times 10^{-19}/w$ m^2/s, where w is the 2DES width measured in meters . We then scale this value by the magnitude of the electronic wavefunction at a nucleus for ^{75}As versus ^{71}Ga, as calculated by Paget [15], and also scale by the gryomagnetic ratio of these two atoms. This gives $K_S / n = \left(4.3 \times 10^{-19}\right)/ w$ Hz m^2, where w is the rms width of the 2DES subband wavefunction, which we estimate via the Fang-Howard approximation.

Unlike the experimental T_1 vs. magnetic field/density data, the calculated T_1's in Fig. 5.15 at low magnetic fields show the simple Korringa theory prediction of a decreasing T_1 with increasing magnetic field/density deep in the partially polarized phase. Another qualitative difference between data and theory is the sharpness of the rise in T_1 at the transition to complete spin polarization. Possibly, disorder may broaden this transition in the experimental T_1 data. A recent calculation by Murthy and Shankar including a disorder-induced broadening of all momentum states predicts a broadened transition and is able to provide a better match to the experimental data than the simple calculations of Fig. 5.15 [22].

5.3.8 Effective Mass

A theoretical estimate of the mass $m_{CF} / m_e = 0.6\sqrt{B}$ is given by Park and Jain [3]. Using this relation, the critical magnetic field for the transition is given by

$$m_{CF} / m_e = 1/|g| \sim 2.3 = 0.6\sqrt{B_C}$$
$$\rightarrow B_C = 14.7 \text{ T}.$$

This value is for an ideal 2DES; the calculation does not take finite thickness or disorder effects into account. A rough estimate of the B_C can be obtained from our T_1 vs. magnetic field data (the temperature dependence of T_1 also allows an estimate of B_C as

will be explained below). Because at 45 mK T_1 begins to rise at above about B = 5 T, it seems reasonable that $B_C \sim 5$ T, although disorder/finite temperature effects may affect the validity of this estimate. Using polarization resolved photoluminescence, Kukushkin *et al*. have measured a critical field of B_C = 9.3 T for a 2DES in a GaAs/AlGaAs heterojunction [7]. However, this number was obtained by observing the apparent saturation of the spin polarization as a function of magnetic field/density at a temperature of $T \sim 0.3$ K. Possibly, finite temperature effects may cause the polarization to drop below full polarization even at magnetic fields above B_C.

5.4 T_1 Temperature Dependence

Figure 5.16 shows the temperature dependence of $1/T_1$ for several magnetic fields spanning the transition ($B \approx 3.0$, 4.0, 5.0, and 6.4 T, corresponding to densities of n = 0.36, 0.48, 0.60, and 0.78 $\times 10^{11}$ cm^{-2}). In the partially polarized phase, at magnetic fields below about B = 5 T, T_1 is density independent over a wide range of temperatures and $1/T_1 \sim aT + b$. However, at B = 6.4 T, $1/T_1$ has a very steep, nonlinear temperature dependence, indicating that the Zeeman splitting now exceeds the Fermi energy. At T =

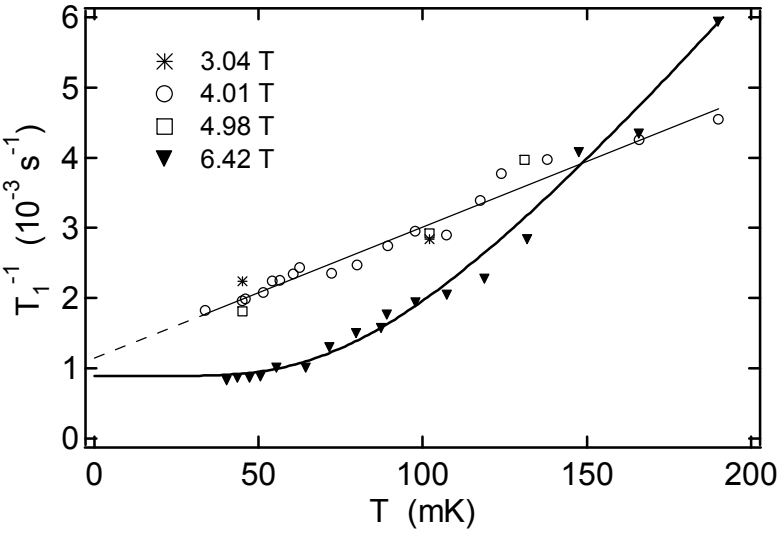

Fig. 5.16. Temperature dependence of T_1. The solid line passing through the data for B = 3.04, 4.01, and 4.98 T is a least squares linear fit. The dashed line is an extrapolation to T = 0. The solid line passing through the B = 6.42 T data is a fit using Eq.'s (1) and (2) (see text).

0 the 2DES would be fully spin polarized. The solid line passing through the B = 6.4 T data of Fig.5.16 is a fit to the data using the simple 2D Korringa theory of Eq.'s (1) and (2), plus an offset due to non-electronic nuclear spin relaxation mechanisms that will be discussed below.

5.4.1 Korringa Temperature Dependence

Figure 5.16 shows the prediction of Eq.'s (1) and (2) for the temperature dependence of T_1 at several magnetic fields/densities for a critical field B_C = 5 T. The curves in Fig. 5.12 look fairly similar to the data of Fig. 11. In fact, as mentioned above, the solid line passing through the data at B = 6.4 T in Fig. 15 is a best fit to the data using our simple Korringa model. The data of Fig. 5.15 at $B \approx 5$ T, showing a $1/T_1$ that is roughly linear in T, can also be described by this model if B = 5 T is relatively near the critical field B_C. For the temperature range $|n/D - E_Z| \ll T \ll |n/D|$, where n is the total density and D is the density of states for a single spin branch, we have that $1/T_1 \sim a + bT$. The left side of the inequality keeps the exponential in the denominator of Eq. (1) small, while the right side keeps finite temperature corrections to the chemical potential relatively small.

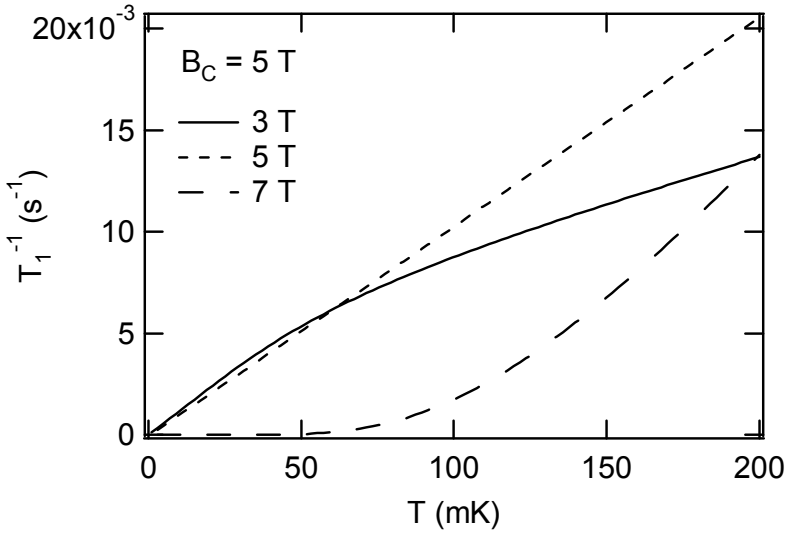

Fig. 5.17. $1/T_1$ vs. temperature for several magnetic fields (B = 3 – 7 T) for a critical magnetic field B_C = 5 T, calculated from the simple 2D Korringa formula of Eq.'s (1) and (2).

5.4.2 Critical Magnetic Field

The temperature dependence of T_1 allows for an estimate of B_C. Although it is difficult to pinpoint the exact field which satisfies this condition from our data, we can still say that the transition occurs below B = 6.4 T. The fit to the B = 6.4 T data of Fig. 5.11 yields a Fermi energy of roughly $E_F \approx E_Z - 260$ mK. If we assume $E_F \sim \sqrt{B}$, and using $E_Z \sim B$,

$$E_F\left(B = 6.4\text{ T}\right)\sqrt{\frac{B_C}{6.4\text{ T}}} = E_Z\left(B = 6.4\text{ T}\right)\frac{B_C}{6.4\text{ T}}$$

$$\rightarrow B_C = \left(6.4\text{ T}\right)\left(\frac{E_F\left(B = 6.4\text{ T}\right)}{E_Z\left(B = 6.4\text{ T}\right)}\right)^2 = 4.8\text{ T},$$

which is fairly close to our previous estimate of $B_C \approx 5$ T from the magnetic field/density dependence of T_1.

5.4.3 Nuclear Spin Diffusion

The extrapolations of $1/T_1$ to zero temperature shown in Fig. 5.15 show an offset in T_1 on the order of 1,000 s that is not predicted by the simple Korringa model. The most likely explanation for this relaxation is that nuclear spins diffuse from the 2DES region into the bulk of the substrate. Remember that the NMR frequency corresponding to nuclei in the region of the sample containing the 2DES is Knight shifted. The RDNMR data is taken at this Knight shifted frequency, which is different from the resonant frequency of the nuclei in the bulk of the sample. Only a thin slice of nuclei near the 2DES are affected by the RF, while the rest of the sample remains in thermal equilibrium. Then, one way for nuclear spins located in this thin slice to relax back to thermal equilibrium is to diffuse outward into the bulk of the sample [19]. Nuclear relaxation rates of similar magnitude have been seen in previous $1/T_1$ measurements in 2DES's in GaAs where the 2DES is completely depleted during the time that the nuclei are allowed to relax [23].

5.5 Discussion

The origin of the peak in $d\rho_{xx}/dE_Z$ near the transition is not explained by the simple CF theory we have presented so far. Indeed, as previously mentioned, even the sign of the NMR-induced change in the resistivity is not understood and is actually the opposite of what is expected [12].

5.5.1 Screening and Spin Polarization

Due to the lack of a realistic theory of transport at $\nu = 1/2$, we turn to 2D electrons at zero magnetic field. Figure 5.17 shows the resistivity of a 2DEG as a function of parallel magnetic field $B_{\|}$, with no perpendicular magnetic field ($B_{\perp} = 0$), as calculated by Das Sarma and Hwang under the assumption that the resistivity is dominated by screened impurity scattering [24]. The parallel magnetic field is assumed to simply create a Zeeman spin splitting $E_Z = g\mu_B B$, but have no effect on the orbital motion of the 2DES electrons (this will be strictly true only for an infinitely-thin 2DES). As $B_{\|}$ is increased,

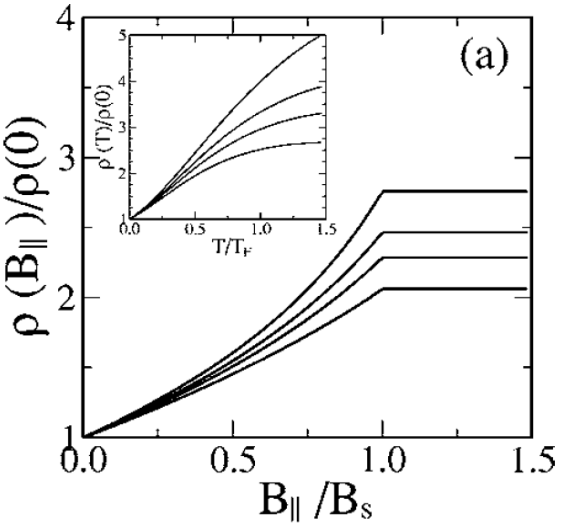

Fig. 5.17. Main plot: Resistivity of a 2DEG in a parallel magnetic field $B_{\|}$ ($B_{\perp} = 0$). As the magnetic field increases, the spin polarization increases continuously until $B_{\|} = B_S$, at which point the 2DEG is completely spin polarized. Spin-dependent screening causes the resistivity to increase with $B_{\|}$. The four curves correspond to electron densities n = 0.4, 0.8, 1.2, and 2.0_10^{10} cm^{-2}. Taken from Das Sarma and Hwang [24]. (Reprinted with permission).

the spin polarization gradually increases, until the 2DEG becomes completely spin polarized for $B_{\|} \geq B_S$, where B_S is the magnetic field at which $E_F = E_Z$. Spin polarization dependent screening leads to the variation in the resistivity as a function of $B_{\|}$.

The dependence of the conductivity on spin polarization can be roughly understood from the dependence of the Fermi wavevector k_F and screening wavevector q_{TF} on spin polarization. The impurity scattering rate depends on the relative magnitude of k_F and q_{TF}. Screening is more effective at reducing scattering for q_{TF} large compared to k_F, so that the conductivity is an increasing function of $\left(q_{TF}/k_F\right)$. How does $\left(q_{TF}/k_F\right)$ depend on spin polarization? In the Thomas-Fermi screening approximation, $q_{TF} \sim D\left(E_F\right)$, the density of states at the Fermi level. The density of states contains a degeneracy factor for spin; $D_{unpol}\left(E_F\right) = 2D_{pol}\left(E_F\right)$, where $D_{unpol}\left(E_F\right)$ is the density of states for an unpolarized 2DES (χ = 0) and $D_{pol}\left(E_F\right)$ is the density of states for a completely polarized 2DES (χ = 1). Thus, the screening wavevector for an unpolarized system is twice as large as for a polarized 2DES: $q_{TF\,unpol} = 2q_{TF\,pol}$. The Fermi wavevector scales with density like $k_F \sim \sqrt{n}$. Then, for a given 2DES density, the Fermi wavevector for a completely polarized system is larger than that of an unpolarized system: $k_{F\,pol} = \sqrt{2}k_{F\,unpol}$. Combining our results, $\left(q_{TF}/k_F\right)_{unpol} = 2^{3/2}\left(q_{TF}/k_F\right)_{pol}$. Thus, screening is more effective for an unpolarized 2DES, which explains the increasing resistivity with increasing spin polarization seen in Fig. 5.17.

Assuming that CF's at ν = 1/2 behave like 2D electrons at zero perpendicular magnetic field, our RDNMR signal $\partial\rho_{xx}/\partial E_Z$ at ν = 1/2 as a function of magnetic field/density should look like the derivative of the curves in the main plot of Fig. 5.17. This derivative will have a peak near the transition magnetic field B_S and vanish for $B_{\|} > B_S$, similar to what is seen in the RDNMR data at ν = 1/2.

5.5.2 Bloch Ferromagnetism

Another, perhaps more speculative, scenario to describe the transition is that two phases of differing electronic spin polarization coexist near the transition region. As mentioned earlier, theoretical calculations of the energy of FQH states near ν = 1/4 as a function of spin polarization suggest that the ν = 1/4 state should exhibit interaction-driven ferromagnetism, even in the absence of Zeeman splitting [5]. The type of spin transition

that occurs at $\nu = 1/2$ will also be determined by the character of any residual interactions between CF's at $\nu = 1/2$.

In 2D systems at zero magnetic field it is hypothesized that a ferromagnetic phase may exist at low enough densities due to exchange interactions. As the 2DES density is lowered the Coulomb interaction becomes increasingly important relative to the kinetic energy. The Coulomb energy scales like $E_C \sim n^{1/2}$, while the Fermi energy scales linearly with density, $E_F \sim n$. The dimensionless parameter $r_s = E_C / E_F \sim n^{-1/2}$ is frequently used to characterize the relative importance of these two energy scales.

In a Hartree-Fock approximation, the total energy per particle, in units of Rydbergs (e^2/a_B, where a_B is the Bohr radius), for a 2DES at zero magnetic field is the sum of the kinetic and exchange energy [25]

$$E_{tot} = \frac{0.5}{r_s^2}\left(1+\chi^2\right) - \frac{0.3}{r_s}\left[\left(1+\chi\right)^{3/2} + \left(1-\chi\right)^{3/2}\right],$$

where χ is the fractional spin polarization. At a critical value $r_s \approx 2$, the system develops a ferromagnetic instability where the two lowest energy configurations correspond to unpolarized (χ = 0) or completely polarized (χ = 1) and are equally energetically favorable. As a function of r_s, there is a first-order transition from an unpolarized to completely polarized state. This type of ferromagnetism is referred to as "Bloch ferromagnetism". As a side note, the actual value of r_s at which ferromagnetism occurs is larger than that predicted by Hartree-Fock. Experiments do not see a transition at r_s = 2 and, although more realistic calculations also predict a ferromagnetic transition, they estimate a higher transition value of $r_s \sim 26$ [26].

For composite fermions, we can write the total energy per particle as a sum of the effective kinetic energy for composite fermions, using the CF effective mass, and the Zeeman energy:

$$E_{tot} = \frac{\pi\hbar^2 n}{2m_{CF}}\left(1+\chi^2\right) - \frac{1}{2}E_Z\chi\,.$$

Writing this in terms of the Coulomb energy and the parameter $\eta \equiv E_Z / E_C$, we have

$$E_{tot} = 0.0056\left(1+\chi^2\right) - 0.5\eta\chi \,, \tag{1}$$

where we use $m_{CF}/m_e = 0.6\sqrt{B}$ at $\nu = 1/2$, based on the calculations of Ref. [3]. This expression describes CF paramagnetism. A plot of Eq. (1) for two values of η is shown in Fig. 5.18. The dotted line corresponds to η = 0.1, where a minimum in the energy occurs at a polarization of $\chi \sim 0.45$, as marked by the arrow. As η is increased, the value of χ at which the energy is minimized increases. There is a continuous transition from partial to complete polarization as a function of η. When η = 0.22 (dashed line in Fig. 5.18), the energy is minimized at χ = 1, i.e., the polarization is complete. This corresponds to $E_F = E_Z$, so that $E_{tot} = E_F/2 - E_Z/2 = 0$ at $\chi = 1$.

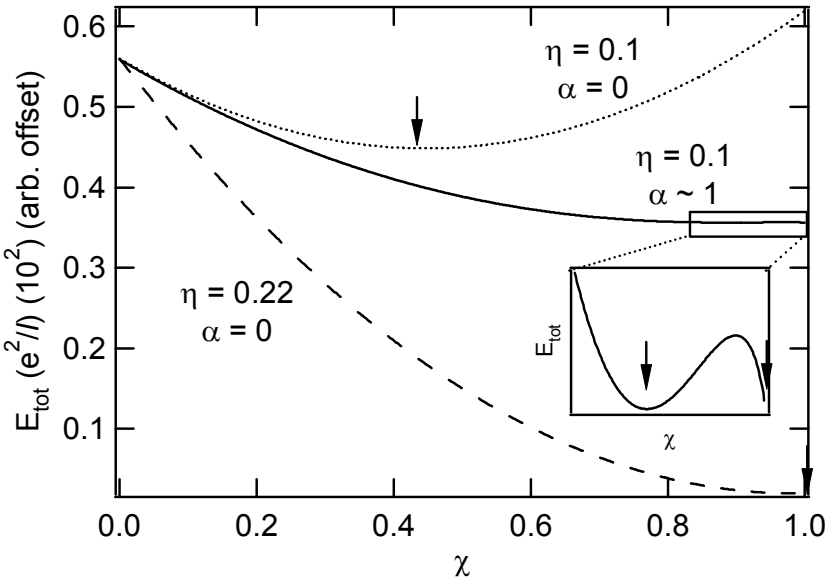

Fig. 5.18. Total energy per particle as a function of spin polarization χ for composite fermions in a simple model, with and without an exchange-like term, proportional to α. The parameter $\eta \equiv E_Z/E_C$. Dotted line: The system is partially polarized (minimum energy configuration at χ = 0.45, as marked by the arrow) with η = 0.1, no exchange energy. Dashed line: The system is completely polarized when η = 0.22, with no exchange energy. Solid line: The system develops a ferromagnetic instability at η = 0.1 if an exchange-like term is included, for α = 1, where $\alpha \equiv E_{ex}/E_F$ at χ = 0. The inset shows the development of two minima, marked by arrows, for $\chi \sim 0.9$ and $\chi \sim 1$.

Making an analogy to Bloch ferromagnetism at $B = 0$, we next add an exchange-like term to the energy per particle:

$$E_{tot} = 0.0056\left(1+\chi^2\right) - 0.5\eta\chi - 0.0028\alpha\left[\left(1+\chi\right)^{3/2} + \left(1-\chi\right)^{3/2}\right],$$

where $\alpha \equiv E_{ex} / K.E.$, the ratio of this exchange-like energy to CF effective kinetic energy, at $\chi = 0$. Although we have no way of knowing the actual form of this hypothetical exchange-like term, as an example, we assume that its dependence on spin polarization is like that of like that of the exchange term in the $B = 0$ Hartree-Fock expression for the total energy. For nonzero α, a first-order spin transition is possible. The solid trace in Fig. 5.18 shows the energy versus spin polarization when $\alpha \sim 1$, $\eta = 0.1$. In this case, a ferromagnetic instability occurs, where the energy as a function of χ develops two distinct minima with nearly equal energy at $\chi \sim 0.9$ and $\chi = 1$. For this value of α, for $\eta < 0.1$, the system will prefer $\chi < 0.9$, while for $\eta > 0.1$, the system will prefer $\chi = 1$.

How might this ferromagnetic transition affect the RDNMR signal? Assume that the resistivity depends on the spin polarization in a smooth way such that $\rho_{xx}(\chi)$ is a continuous, increasing function of χ. The RDNMR signal is proportional to $\partial\rho_{xx} / \partial E_Z \sim \partial\rho_{xx} / \partial\eta = (\partial\rho_{xx} / \partial\chi)(\partial\chi / \partial\eta)$. Even though $\partial\rho_{xx} / \partial\chi$ may be well-behaved, near the ferromagnetic instability $\partial\chi / \partial\eta$ will diverge. This could explain the peak in $\partial\rho_{xx} / \partial E_Z$ near the transition to complete spin polarization seen in the data of Fig. 5.10a.

5.6 Conclusion

In summary, our RDNMR measurements show that at $\nu = 1/2$, the nuclear spin-lattice relaxation time T_1 has temperature dependence that is roughly described by a simple 2D version of Korringa nuclear spin relaxation. However, the density dependence of T_1 fails to agree with a simple free CF picture. We also show the first measurements of the Zeeman energy dependence of transport at $\nu = 1/2$. The sign of the NMR-induced change in the resistivity as well as the peak in $d\rho_{xx}/dE_Z$ near the spin transition that develops at low temperatures are not explained by a conventional CF theory of transport at $\nu = 1/2$.

References

[1] J. K. Jain. *Phys. Rev. Lett*. **63**, 199 (1989).

[2] L. A. Tracy, J. P. Eisenstein, L. N. Pfeiffer, and K. W. West. *Phys. Rev. Lett.* **98**, 086801 (2007).

[3] K. Park and J. K. Jain, *Phys. Rev. Lett*. **80**, 4237 (1998).

[4] G. Murthy and R. Shankar, *Rev. Mod. Phys*. **75**, 1101 (2003).

[5] K. Park and J. K. Jain, *Phys. Rev. Lett*. **83**, 5543 (1999).

[6] K. Park, V. Melik-Alaverdian, N. E. Bonesteel, and J. K. Jain. *Phys. Rev. B*. **58**, 10167 (1998).

[7] I. V. Kukushkin *et al*., *Phys. Rev. Lett*. **82**, 3665 (1999).

[8] S. Melinte *et al*., *Phys. Rev. Lett*. **84**, 354 (2000).

[9] N. Freytag *et al*., *Phys. Rev. Lett*. **89**, 246804 (2002).

[10] O. Stern *et al*., *Phys Rev. B*. **70**, 075318 (2004).

[11] I. Dujovne, et al., Phys. Rev. Lett. 95, 056808 (2005).

[12] B. I. Halperin, P. A. Lee, and N. Read, *Phys. Rev. B* **47**, 7312 (1993).

[13] R. R. Du *et al*. *Phys. Rev. Lett*. **70**, 2944 (1993) and *Phys. Rev. Lett*. **73**, 3274 (1994); D. R. Leadley *et al*. *Phys. Rev. Lett*. **72**, 1906 (1994); P. T. Coleridge *et al*., *Phys. Rev. B* **52**, R11603 (1995).

[14] W. Kang, Song He, H. L. Stormer, L. N. Pfeiffer, K. W. Baldwin, and K. W. West, *Phys. Rev. Lett*. **75**, 4106 (1995); L. P. Rokhinson, B. Su, and V. J. Goldman, *Phys. Rev. B* **52**, R11588 (1995); L. P. Rokhinson and V. J. Goldman, *Phys. Rev. B* **56**, R1672 (1997).

[15] D. Paget, G. Lampel, B. Sapoval, and V. I. Safarov, *Phys. Rev. B* **15**, 5780 (1977).

[16] C-T Liang, M. Y. Simmons, D. A. Ritchie, and M. Pepper, *J. Phys. Cond. Matt*. **16**, 1095 (2004).

[17] S. Kronmüller *et al*. Phys. Rev. Lett. **81**, 2526 (1998); S. Kronmuller, *et al*., *Phys. Rev. Lett*. **82**, 4070 (1999).

[18] J. H. Smet, *et al*., Phys. Rev. Lett. **86**, 2412 (2001).

[19] A. Abragam. *The Principles of Nuclear Magnetism*. Oxford University Press, Oxford 1961.

[20] R. E. Prange and S. M. Girvin. *The Quantum Hall Effect*. Springer-Verlag, New York 1987.

[21] P. Khandelwal *et al*., *Phys. Rev. Lett*. **81**, 673 (1998).

[22] G. Murthy and R. Shankar, arXiv: 0704.3210v1.

[23] K. Hashimoto, *et al*., *Phys. Rev. Lett*. **88**, 176601 (2002).

[24] S. Das Sarma and E. H. Hwang, *Phys. Rev. B* **72** 035311 (2005).

[25] A. K. Rajagopal, *Solid State Comm*. **21** 483 (1977); A. K. Rajagopal *et al*., *Surf. Sci*. **73** 365 (1978).

[26] B. Tanatar and D. M. Ceperley, *Phys. Rev. B* **39**, 5005 (1989); C. Attaccalite, S. Moroni, P. Gori-Giorgi, G. B. Bachelet, *Phys. Rev. Lett.* **88**, 256601 (2002).

Chapter 6:
Spin Transition in a Correlated Bilayer 2DES

In Chapter 5 we observed that a spin transition occurs in a single-layer 2DES at $\nu = 1/2$ and that at low magnetic fields, below this transition, this system is partially spin polarized. We next consider a bilayer 2DES consisting of two closely spaced single-layer 2DES's, each at filling factor $\nu = 1/2$. If the layers are far enough apart so that interactions between the two layers can be neglected and if they are separated by a tall enough energy barrier such that tunneling between the layers can be ignored, then the individual layers behave like two independent 2DES's. However, the addition of interlayer interactions can create new many-body states in bilayers that have no single-layer 2DES analog. An example of one such state occurs at total filling factor $\nu_T = 1$, where $\nu_T = \nu_1 + \nu_2$ is the sum of the filling factors of the individual layers. At $\nu_T = 1$ and small effective interlayer spacing a remarkable state emerges that can be viewed as a Bose condensate of excitons. There is a phase transition from a compressible state, where the layers are weakly coupled, to an incompressible excitonic state when the effective interlayer spacing is reduced below a critical value. This chapter discusses experiments which investigate the role of spin in this phase transition, performed by Ian Spielman and myself [1].

6.1 Bilayer 2DES

Figure 6.1 shows a sketch of the conduction band energy and ground and first excited state subband wavefunctions for a typical bilayer 2DES. As shown in Fig. 6.1, the ground state wavefunction is symmetric with respect to the two wells while the first excited state wavefunction is antisymmetric. One important parameter for bilayer samples is Δ_{SAS}; the symmetric-antisymmetric splitting; Δ_{SAS} is the energy difference between the ground and first excited state. This parameter is determined by the strength of the tunneling between the two layers. One can estimate Δ_{SAS} by solving for the 2DES eigenstates and their energies (see Chapter 1 for a discussion of calculations of eigenstates using a Schrodinger-Poisson solver). If the splitting is large enough Δ_{SAS} can be resolved

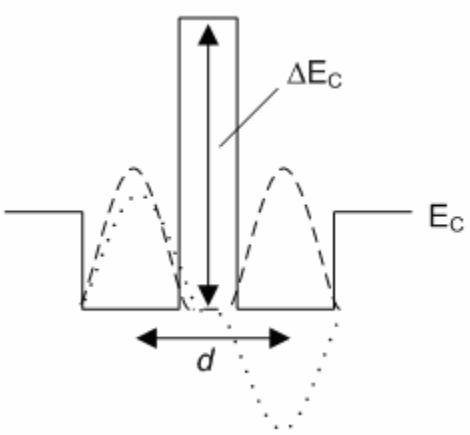

Fig. 6.1. Cartoon of conduction band profile and subband wavefunctions for a typical bilayer sample. Solid line: conduction band energy E_C. Dashed line: ground state electron wavefunction. Dotted line: first excited state wavefunction. The center-to-center spacing between the two wells is labeled "*d*". The height of the barrier between the wells is labeled "ΔE_C".

experimentally via Shubnikov-de Haas oscillations in magnetotransport. However, this is difficult to observe in weakly-tunneling samples (small Δ_{SAS}).

6.1.1 Tunneling at $B = 0$

Figure 6.2 shows a schematic of energies relevant for 2D-2D tunneling at zero magnetic field. Momentum and energy conservation during the tunneling process requires alignment of the left and right well's subband energies ($\Delta E_0 = 0$); a tunneling current can be observed when the interlayer bias V is adjusted to meet this condition. The inset to Fig. 6.3 shows an example of the enhanced differential tunneling conductance dI/dV seen when this condition is met, for the case of equal layer densities, where $\Delta E_0 = 0$ when $V = 0$.

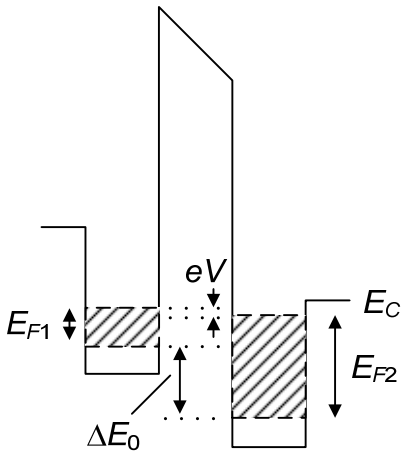

Fig. 6.2. Band diagram for 2D-2D tunneling. The solid line is the conduction band energy E_C. Hatched regions correspond to occupied states with 2D Fermi energies E_{F1}, E_{F2}. The difference between the ground state 1D subband energies of the two individual layers is ΔE_0, and V is the interlayer bias.

6.1.2 Tunneling in a Magnetic Field

Figure 6.3 contrasts 2D-2D tunneling at zero magnetic field to tunneling in the presence of a large perpendicular magnetic field. The main plot of Fig. 6.3 shows dI/dV at zero interlayer bias versus magnetic field for a bilayer 2DES with equal layer densities. At low magnetic fields there is a finite zero bias tunneling conductance which oscillates with Landau level filling fraction, showing behavior reminiscent of the low-field oscillations of longitudinal resistivity versus magnetic field. In this regime the tunneling conductance is at a minimum near integer ν, where ν is the filling factor of the individual layers, and at a maximum when the Fermi level lies in the middle of a Landau level. At higher magnetic fields dI/dV at zero interlayer bias is suppressed for a wide range of filling factors. The explanation for this is that interactions lead to a gap in the tunneling density of states; the width of the region in interlayer bias for which the differential tunneling conductance is suppressed is on the order of the Coulomb energy. At large perpendicular magnetic fields, a single-layer 2DES tends to form a highly correlated state (for example, a Wigner crystal is predicted to form in the limit of small disorder and strong interactions). It is believed that the suppression of tunneling near zero interlayer bias is due to the energetic penalty of tunneling an electron between two such correlated layers,

which temporarily creates a vacancy in the originating layer and an interstitial in the destination layer [3].

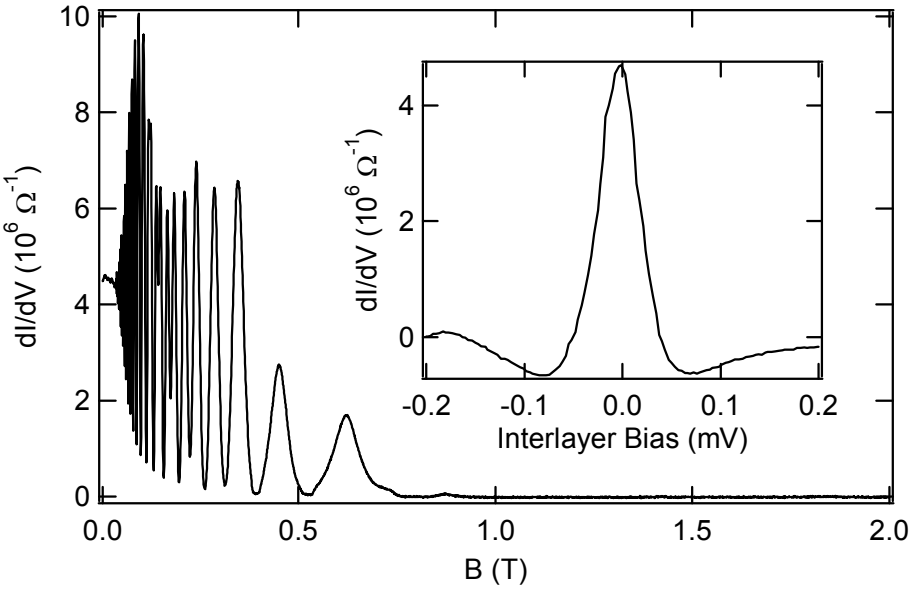

Fig. 6.3. Main plot: Differential tunneling conductance dI/dV at zero interlayer bias vs. perpendicular magnetic field at $T \sim 35$ mK. Inset: dI/dV vs. interlayer bias at $B = 0$. For both plots, the two layer densities are equal, with $n = 0.37 \times 10^{11}$ cm^{-2} per layer.

6.2 $\nu_T = 1$ State

6.2.1 Bilayer QHE

When interactions between the individual layers (interlayer interactions) of a bilayer 2DES become comparable to interactions between electrons within an individual layer (intralayer interactions), new many-body states can emerge. At $\nu_T = 1$, the effective interlayer spacing parameter d/l, which is the physical distance d between the individual 2DEG layers (see Fig. 6.1) normalized by the magnetic length l, determines the ratio of the strength of interlayer to intralayer Coulomb interactions. The Coulomb energy due to interlayer interactions is proportional to $1/d$, while the Coulomb energy due to intralayer interactions is proportional to $\sqrt{n} \sim 1/l$ when at fixed filling factor. In a bilayer 2DES at total filling factor $\nu_T = 1$ the value of d/l determines whether the system displays a bilayer

quantum Hall effect or simply behaves like two single-layer 2DES's, each in the compressible $\nu = 1/2$ state [4-9].

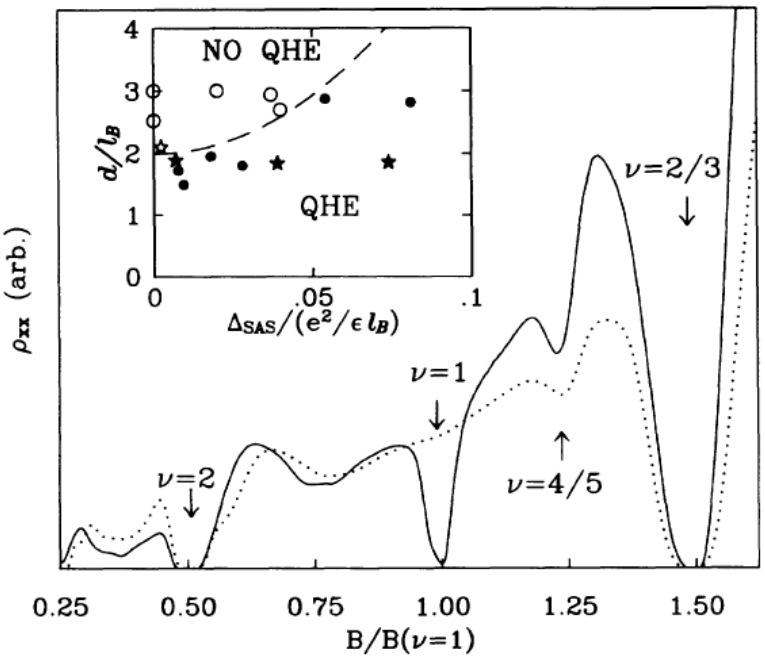

Fig. 6.4. Longitudinal resistivity ρ_{xx} vs. magnetic field for two bilayer samples with different densities. For ease of comparison, the magnetic field is normalized by $B(\nu = 1)$, the value of the magnetic field at $\nu_T = 1$. Dotted line: $d/l = 2.10$ at $\nu_T = 1$. Solid line: $d/l = 1.87$ at $\nu_T = 1$. Inset: phase diagram for bilayer quantum Hall effect at $\nu_T = 1$. Closed symbols correspond to samples which do show a QHE while open symbols correspond to samples which do not show a QHE. Figure from S. Q. Murphy *et al*. [9]. (Reprinted with permission).

Figure 6.4, which shows the data of Murphy *et al*. [9], displays the dramatic transition that occurs as a function of d/l. The main figure displays the longitudinal resistivity ρ_{xx} of a bilayer 2DES while driving the current through both layers in parallel. The dotted trace corresponds to a sample with $d/l = 2.10$ at $\nu_T = 1$ ($B / B(\nu = 1) = 1$). At magnetic fields near $\nu_T = 1$ the magnetotransport looks identical to that of a single-layer 2DES at $\nu = 1/2$. In contrast, the solid trace, corresponding to a slightly lower $d/l = 1.87$ at $\nu_T = 1$, displays a quantum Hall effect near $\nu_T = 1$. The inset of Fig. 6.4 shows the phase diagram for the $\nu_T = 1$ bilayer quantum Hall effect for finite tunneling strength ($\Delta_{SAS} \neq 0$), obtained by measuring magnetotransport in many samples with different

values of d/l and tunneling strength. The intersection of the phase boundary (dashed line) with the $\Delta_{SAS} = 0$ axis at finite $d/l \sim 2$ suggests that the incompressible state persists even in the absence of interlayer tunneling.

6.2.2 Exciton Condensate

The $\nu_T = 1$ incompressible state can actually be viewed as a Bose condensate of excitons [10, 11]. This can be seen by making a particle-hole transformation on one of the layers, as sketched in Fig. 6.5.

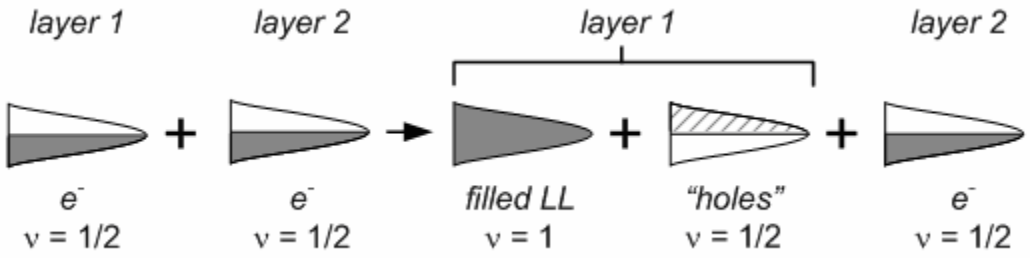

Fig. 6.5. Cartoon picture of particle-hole transformation applied to a half-filled Landau level in a bilayer system at $\nu_T = 1$.

As an example, we can view the half filled Landau level in layer number 1 as a completely filled Landau level plus a Landau level half filled with holes. The completely filled Landau level can be ignored, similar to way that the completely-filled non-valence levels in an atom are ignored. Once the particle-hole transformation is made, it can be seen that when d/l is reduced such that the interlayer and intralayer Coulomb interactions are comparable, holes in one layer will tend to pair with electrons in the other layer, forming interlayer excitons. These excitons can then Bose condense and may actually form a superfluid [12-14, 17].

An extension of Laughlin's QHE trial wavefunction to systems with an additional two-state degree of freedom was proposed by Halperin [15]. Initially, this wavefunction was intended to describe a single layer 2DES including the electron spin degree of freedom. However, the wavefunction can also be used to describe a 2DES with a layer degree of freedom, replacing up and down spin with layer 1 and layer 2. For the case of the bilayer $\nu_T = 1$ state, this trial wavefunction is

$$\psi_{111} = \prod_{i>j=1}^{N1}(z_i - z_j)\prod_{i>j=1}^{N2}(w_i - w_j)\prod_{i>j=1}^{N1,N2}(z_i - w_j)\exp\left(-\sum_{i=1}^{N1}|z_i|^2/4\right)\exp\left(-\sum_{i=1}^{N2}|w_i|^2/4\right),$$

where the complex coordinates z_i and w_j correspond to electrons in layers 1 and 2, respectively. Looking at the symmetry of the wavefunction, interlayer and intralayer correlations are equally important; the wavefunction vanishes equally rapidly for $z_i \rightarrow z_j$ as for $z_i \rightarrow z_j$ or $w_i \rightarrow w_j$. Numerical studies show good overlap between the ψ_{111} state and the exact ground state for 10 particles and small $d/l < 1$ [16].

This wavefunction can be mapped to a BCS wavefunction [10, 11]. In fact, it is predicted that the $\nu_T = 1$ state for d/l below the phase boundary will form a superfluid of excitons [12-14]. This neutral superfluid can be probed via counterflow measurements, where currents of equal magnitude but opposite sign are driven through the two individual layers. Counterflow experiments by Kellogg *et al*. [17] provide evidence for this neutral superfluid. The data of Ref. [17] show a relatively large counterflow conductivity that continues to improve with decreasing temperature down to 35 mK.

The $\nu_T = 1$ state has been studied via a variety of experimental techniques including magnetotransport, interlayer tunneling, Coulomb drag, and counterflow conductivity measurements [6-9, 17-19]. The rest of this chapter focuses on resistivity and tunneling as probes of the $\nu_T = 1$ state.

6.2.3 Tunneling at $\nu_T = 1$

Another signature of the transition to the excitonic state can be seen in interlayer tunneling. Figure 6.6 shows the interlayer differential tunneling conductance as a function of interlayer bias. For large d/l, the zero bias conductance is suppressed due to the aforementioned Coulomb gap effect. However, as shown by I. B. Spielman *et al*. [18], if d/l is brought below the critical point there is a dramatic enhancement of the zero bias tunneling conductance. Interlayer correlations cause the Coulomb gap to be replaced by a sharp tunneling peak. Roughly speaking, when interlayer interactions become significant, an electron in one layer will be positioned near a hole in the adjacent layer into which the electron can easily tunnel.

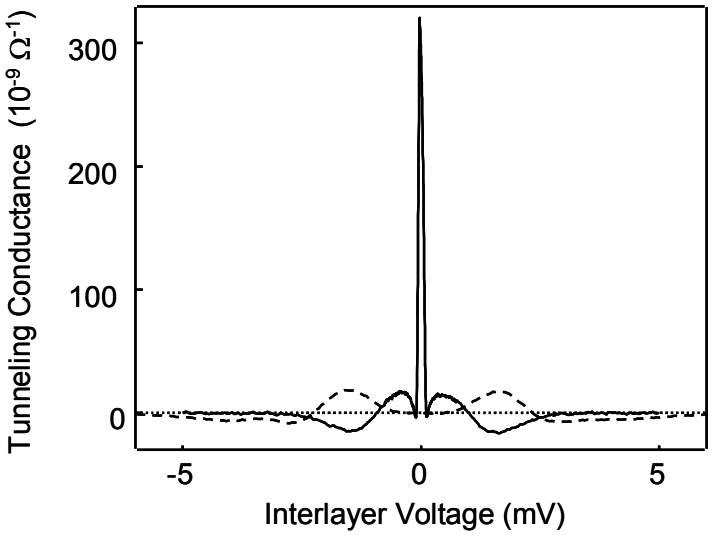

Fig. 6.6. Zero bias differential tunneling conductance peak at $\nu_T = 1$. Dashed trace: d/l above the phase boundary. Solid trace: below the phase boundary. Data courtesy of I. B. Spielman.

6.2.4 Spin at $\nu_T = 1$

As discussed in Chapter 5, a single-layer 2DES at $\nu = 1/2$ is partially spin polarized. However, the spin polarization of a bilayer 2DES at $\nu_T = 1$ when the layers are strongly coupled is not known. This raises the question of what role spin might play in the transition from the compressible to incompressible state as a function of d/l. The NMR experiments discussed next [1] show that the spin degree of freedom is actually active during this transition.

6.3 Data

6.3.1 Sample

The 2DES sample used in this experiment consists of two closely spaced GaAs quantum wells, 18 nm wide, separated by a 10 nm $Al_{0.9}Ga_{0.1}As$ barrier. The as-grown electron density in each quantum well is 4.4×10^{10} cm^{-2} and the low-temperature mobility is about

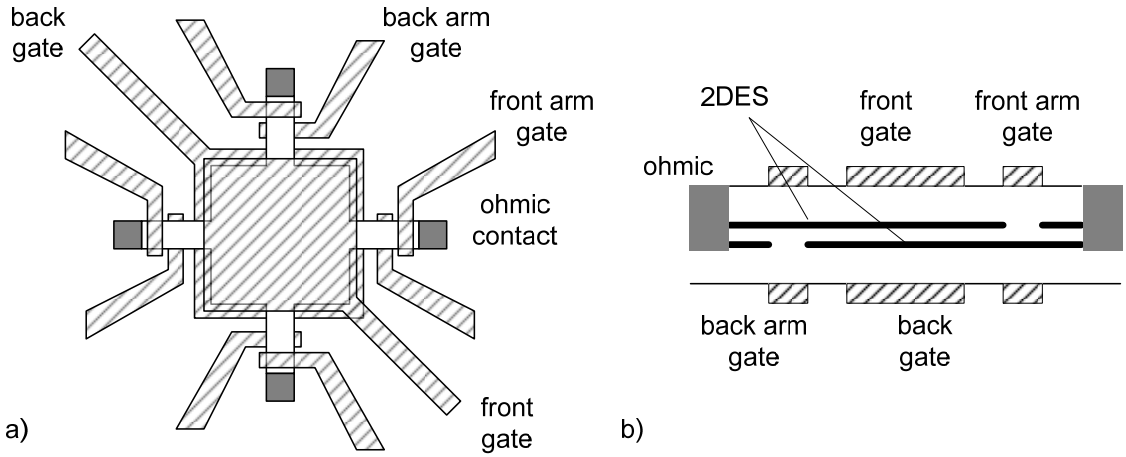

Fig. 6.7. Schematic of typical bilayer device consisting of a central mesa with arms leading to ohmic contacts, density-tuning front and back gates covering the central mesa region, and arm depletion gates. a) Top view. b) Side view (not to scale) with depletion arm gates biased in a tunneling measurement configuration.

9×10^5 cm^2/Vs. The device consists of a square mesa region, 250 μm on a side, with arms extending to ohmic contacts. Aluminum top and bottom gates covering the central mesa region allow control over the 2DES densities. Gates covering the mesa arms are used to make electrical contact to the individual layers [20]. The entire sample is thinned to a thickness of ~ 50 μm using a chemical-mechanical etch [2], in order to be able to place the back gates near enough to the 2DES so that a substantial density change can be obtained using moderate gate voltages (of magnitude less than 100 V). Figure 6.7a shows a diagram of the sample layout with ohmic contacts and front and back gates. Figure 6.7b shows a sketch of the sample in a tunneling configuration, where the left back arm gate is biased to cut off conduction between the back layer and the left ohmic and the right front arm gate is biased to cut off conduction between the top layer and right ohmic.

Measurements are made at temperatures down to $T \sim 25$ mK in a dilution refrigerator. The sample is suspended in vacuum by Au wires connected to the ohmic contacts, which provide thermal contact to the cryostat cold finger. The thermal relaxation time of the 2DES is a few seconds at 50 mK. Magnetotransport for this sample displaying the $\nu_T = 1$ quantum Hall state is shown in Fig. 6.8.

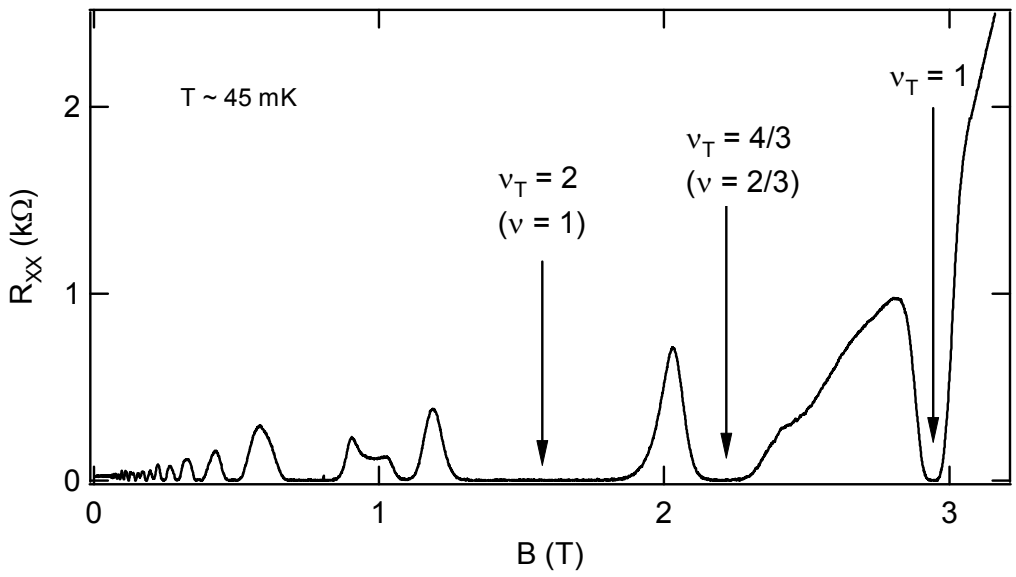

Fig. 6.8. Longitudinal resistivity versus magnetic field for $d/l = 1.87$ at $\nu_T = 1$, below the phase boundary. At this density, the sample displays a minimum in R_{xx} at $\nu_T = 1$. Minima corresponding to several single-layer QH states are also observed. Current is driven through both layers simultaneously and voltage is measured across top layer.

6.3.2 NMR Techniques

We use the resistively detected NMR (RDNMR) techniques described in Chapter 4. The 2DES sample is mounted inside a rectangular eight-turn NMR coil for applying RF

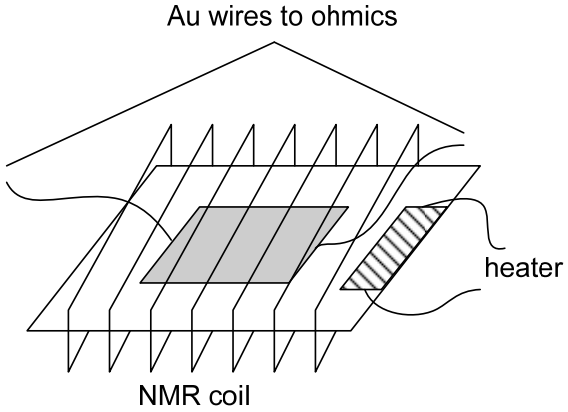

Fig. 6.9. Schematic of 2DES sample suspended in NMR coil by Au wires leading to ohmic contacts. The shaded area represents the mesa region containing the 2DES. A small resistive heater is epoxied directly onto the chip.

magnetic fields parallel to the plane of the 2DES. Additionally, a small resistive heater is attached directly to the 50 μm thick sample (5 kΩ surface mount thin-film resistor attached via Stycast 1266 epoxy) for heat pulse experiments (see Fig. 6.9).

6.3.3 RDNMR Frequency Sweep

Figure 6.10 shows a RDNMR resonance at $\nu_T = 1$, just inside the excitonic phase, at d/l = 1.90, a density at which the $\nu_T = 1$ quantum Hall state is not very strong, so that R_{xx} at ν_T = 1 is not zero. The plot displays longitudinal resistance versus frequency, while sweeping the frequency upward at + 0.33 kHz/s through the ^{71}Ga Larmor resonance, at constant RF power. The ^{71}Ga resonance occurs at $\Delta f = 0$, where the RF frequency is $f = f_0 + \Delta f$ and f_0 = 39.952 MHz is the ^{71}Ga Larmor frequency. The magnitude of the RF magnetic field is small enough such that $\omega_r \ll 1/T_2$, where ω_r is the Rabi frequency and T_2 is the nuclear spin dephasing time. Thus, sweeping through the NMR line simply reduces the magnitude of the nuclear spin polarization.

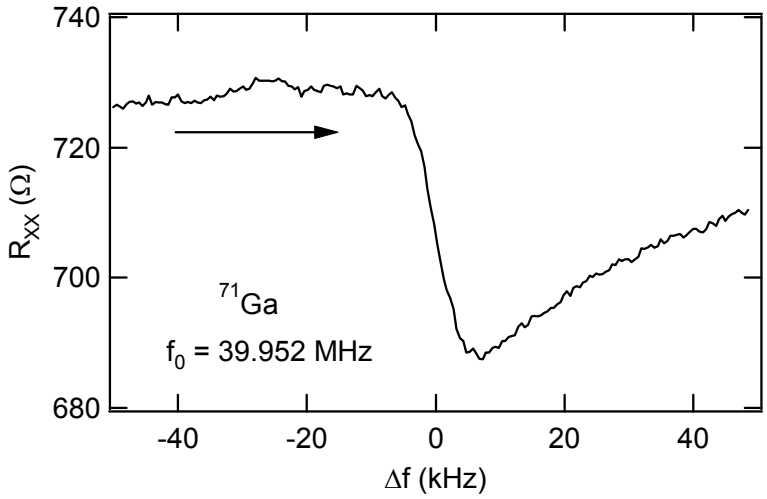

Fig. 6.10. RDNMR frequency sweep showing the resonant response of the 2DES at the ^{71}Ga resonance frequency (Larmor frequency f_0 = 39.952 MHz) at $\nu_T = 1$, just below the phase boundary (d/l = 1.90). The 2DES longitudinal resistance is monitored while the RF B-field frequency is swept at a rate of +0.33 kHz/s. The RF frequency is $f = f_0 + \Delta f$.

At the start of the sweep, the nuclear polarization is at thermal equilibrium and the longitudinal resistance is at some finite value. When the ^{71}Ga Larmor resonance is reached, the ^{71}Ga spin polarization is reduced. The data of Fig. 6.10 does not represent the equilibrium RDNMR lineshape; after passing through the NMR line, the resistance slowly decays back to the equilibrium value in a time T_1, the nuclear spin-lattice relaxation time. Depolarizing the nuclear spins leads to an increase in the electronic Zeeman splitting (see Chapter 4, section 4.2.2). Thus, the dip in resistance at the ^{71}Ga resonance seen in Fig. 6.10 implies that the quantum Hall state at $\nu_T = 1$ is strengthened by an increase in the Zeeman splitting. The NMR-induced increase in the Zeeman splitting causes the strongly-coupled incompressible phase to be energetically favored over the weakly-coupled compressible phase. This suggests that the incompressible phase has greater electronic spin polarization than the compressible phase.

6.3.4 RDNMR Transients

Figure 6.11 shows the response of the longitudinal resistivity to NMR pulses at $\nu_T = 1$ for d/l just below the phase boundary ($d/l = 1.91$), corresponding to a density at which the minimum in R_{xx} versus B at $\nu_T = 1$ has just begun to form and the resistance at $\nu_T = 1$ is

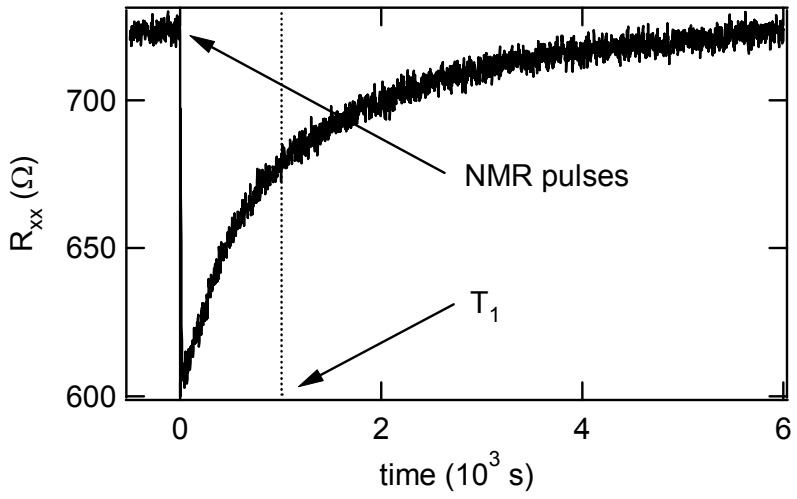

Fig. 6.11. Longitudinal resistivity versus time, near the phase boundary ($d/l = 1.91$) at $T = 35$ mK. A burst of RF pulses (50 μS in length) applied at $t = 0$ is used to completely depolarize the ^{71}Ga nuclei. The dotted line indicates the time at which the NMR-induced change in resistance has decayed by 1/e.

non-zero. Then, at time t = 0 a burst of RF pulses (50 μS in length) are applied to completely depolarize the ^{71}Ga nuclei and the resistance rapidly decreases. The effect of the NMR pulses is to depolarize the nuclei only temporarily. The resistance then decays back to the equilibrium value with a characteristic time T_1, which we can obtain from this trace. The relaxation of the resistance is not precisely described by a single exponential. This is most likely due to the fact that T_1 varies with frequency across the NMR line due to the finite width of the 2D subband wavefunction (for further discussion see Chapter 4, Section 4.3.3 and Chapter 5, Section 5.2.5). The 50 μS RF pulses correspond to a 20 kHz frequency width, which is larger than the width of the NMR line. Thus, the NMR pulses depolarize all nuclear spins in the quantum well region. This will give rise to a RDNMR transient signal which decays at a rate determined by a range of T_1 times. Therefore, instead of using a single exponential fit, we define T_1 as the time required for the NMR-induced change in resistance to decay by 1/e of its initial value.

6.3.5 Effective Interlayer Spacing Dependence

Next we examine the RDNMR signal and nuclear T_1 time over a range of d/l values near the phase boundary at ν_T = 1, as shown in Fig. 6.12. Figure 6.12a shows the longitudinal resistance and RDNMR signal versus d/l at ν_T = 1. As expected, the sample resistance (open circles) is finite in the compressible phase at large d/l and vanishes as d/l is reduced, signaling the development of the ν_T = 1 QHE. The RDNMR signal (solid markers) is the fractional change in the longitudinal resistance $\Delta R_{xx}/R_{xx}$ due to depolarizing the ^{71}Ga nuclei. This RDNMR signal is small and positive in the compressible, weakly-coupled phase (see Chapter 5 for further discussion of RDNMR signals at ν = 1/2 in a single-layer 2DES). The RDNMR signal becomes negative as d/l is reduced below the phase boundary, just as the longitudinal resistivity begins to drop. This negative RDNMR signal is consistent with the earlier data of Fig.'s 6.10 and 6.11. The NMR-induced increase in Zeeman splitting causes the quantum Hall effect to strengthen, implying that the incompressible phase has greater electronic spin polarization than the compressible phase.

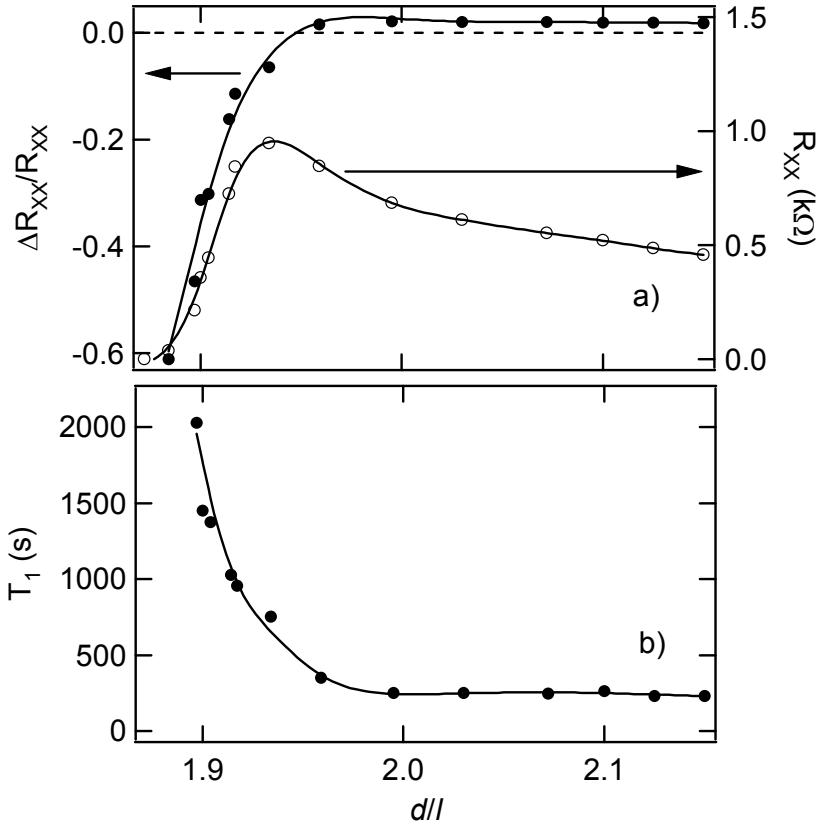

Fig. 6.12. RDNMR signal and T_1 versus d/l at $\nu_T = 1$. a) Solid markers are the RDNMR induced fractional change in the resistivity $\Delta R_{xx}/R_{xx}$ (left axis). Open circles are the longitudinal resistivity R_{xx} (right axis). b) Nuclear T_1 time. Solid lines are guides to the eye.

The nuclear spin-lattice relaxation rate T_1 is strongly affected by the nature of the electronic spin excitations. Nuclear spin relaxation in bulk GaAs at low temperatures with no electron gas present is extremely slow – the T_1 times can be hours or days. Figure 6.12b shows that for large d/l, when the system is in the compressible phase, T_1 is relatively short. This reflects the presence of low energy electron spin flip excitations in the compressible phase which lead to enhanced nuclear spin relaxation (A more detailed discussion of nuclear spin relaxation in a single-layer 2DES at $\nu = 1/2$ can be found in Chapter 5). The T_1 times rapidly increase as d/l is reduced and the 2DES enters the incompressible phase. In a 2DES with a large energy gap for spin excitations, where the nuclei cannot efficiently relax via the electron gas, the T_1 time in the 2DES region is most likely limited by the rate of nuclear spin diffusion out of the 2DES region into the bulk of the sample (see Chapter 5, section 5.4.3 for a discussion of nuclear spin diffusion). This

diffusion time is roughly 1,000 – 2,000 s [21] and sets an upper bound for the measured T_1 time.

6.3.6 RDNMR and Tunneling

Next, we look at the effect of NMR on interlayer tunneling at $\nu_T = 1$. The solid trace in Fig. 6.13 shows the response of the zero bias tunneling conductance G_0 to NMR at $\nu_T = 1$ for d/l just below the phase boundary, where there is a small zero bias peak in the tunneling conductance. For times before $t = 0$, the RF B-field is off, the nuclear polarization is in thermal equilibrium and the conductance is at some finite value. Then, at time $t = 0$ a burst of RF pulses (50 μS in length) are applied to completely depolarize the ^{71}Ga nuclei and the tunneling conductance rapidly increases. The effect of the NMR pulse is to depolarize the nuclei only temporarily. The conductance then decays back to the equilibrium value at a rate determined by the nuclear T_1.

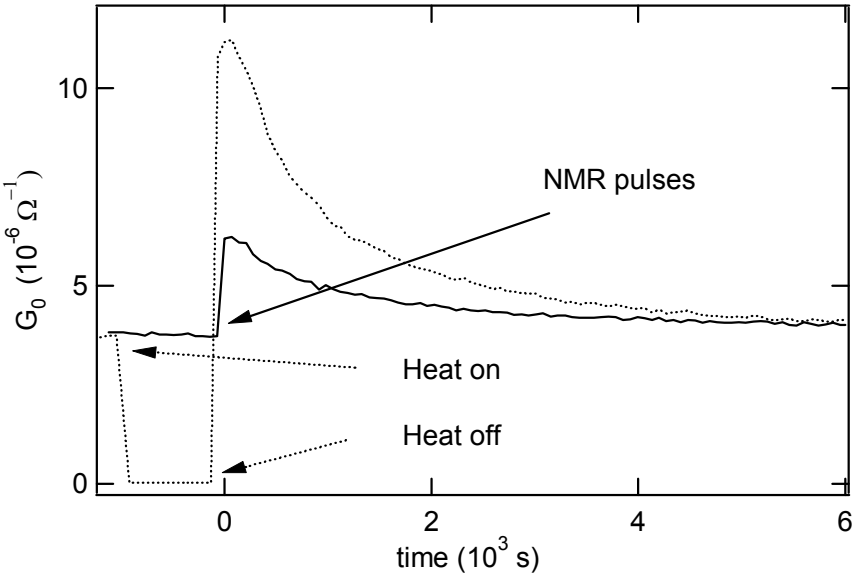

Fig. 6.13. Zero bias differential tunneling conductance G_0 at $\nu_T = 1$ versus time, near the phase boundary (d/l = 1.92) at T = 35 mK. For the solid trace a burst of RF pulses applied at $t = 0$ is used to completely depolarize the ^{71}Ga nuclei. For the dotted trace a heat pulse is applied for ~ 900 sec. prior to $t = 0$. The heat pulse depolarizes all nuclear species.

The nuclear polarization can also be modified by applying a voltage pulse to the resistive heater sketched in Fig. 6.9. The dotted trace in Fig. 6.13 shows the result of applying a 900 sec. heat pulse, which raises the sample temperature to roughly $T = 350$ mK, depolarizing all nuclear species (^{71}Ga, ^{69}Ga, and ^{75}As). Initially, the nuclear polarization is at thermal equilibrium. During the heat pulse, G_0 vanishes since the incompressible $\nu_T = 1$ state is destroyed due to the elevated sample temperature. At $t = 0$, the heat is turned off, and the 2DES quickly cools back to the fridge cold finger temperature ($T = 35$ mK) with a thermal time constant of a few seconds. However, the nuclei will slowly return to thermal equilibrium, at a rate determined by the nuclear T_1 times of the three nuclear species. The zero-bias tunneling conductance after the 2DES has cooled, just after the end of the heat pulse ($t = 0$), is enhanced over the equilibrium value. This enhancement is larger than that seen for the ^{71}Ga NMR pulse, since all three nuclear species have been depolarized.

The increase in G_0 due to depolarizing the nuclei seen in Fig. 6.13 is consistent with the NMR-induced decrease in the longitudinal resistivity seen in Fig.'s 6.10, 6.11, and 6.12. Again, increasing the Zeeman splitting strengthens the strongly-coupled excitonic phase, implying that this phase has greater spin polarization than the competing weakly-coupled phase.

Figure 6.14 shows the dramatic response of the tunneling conductance to changes in the nuclear polarization seen in the compressible phase, just above the phase boundary at $\nu_T = 1$, $d/l = 1.98$. Both Fig. 6.14a and b show the differential interlayer tunneling conductance versus interlayer bias. As shown in Fig. 6.14a, for nuclear spins in thermal equilibrium there is no measurable zero-bias tunneling conductance. However, as shown in Fig. 6.14b, if a heat pulse is applied to depolarize the nuclei, a small zero-bias tunneling conductance appears. We are able to just enter the excitonic condensate phase by decreasing the nuclear polarization.

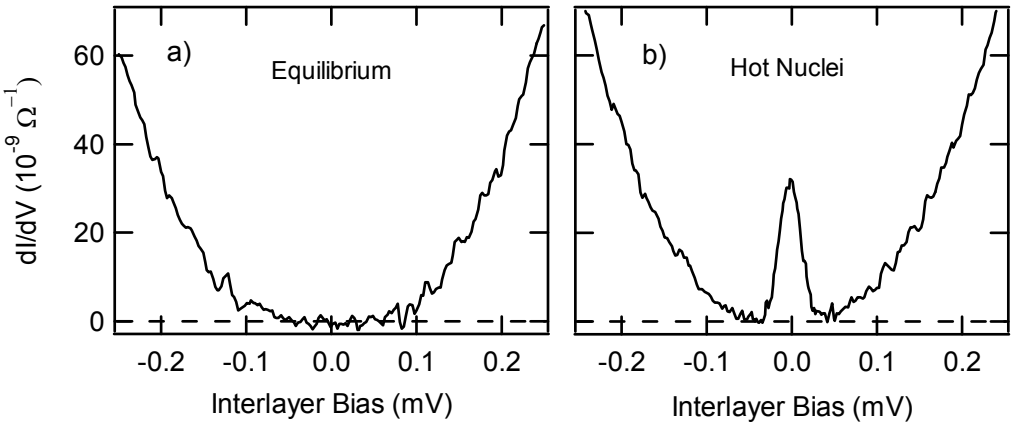

Fig. 6.14. Differential tunneling conductance vs. interlayer bias just above the phase boundary, $d/l = 1.98$, $\nu_T = 1$ at $T = 35$ mK. a) The nuclei are in thermal equilibrium. b) A heat pulse has been applied immediately prior to the conductance measurement to depolarize all nuclei.

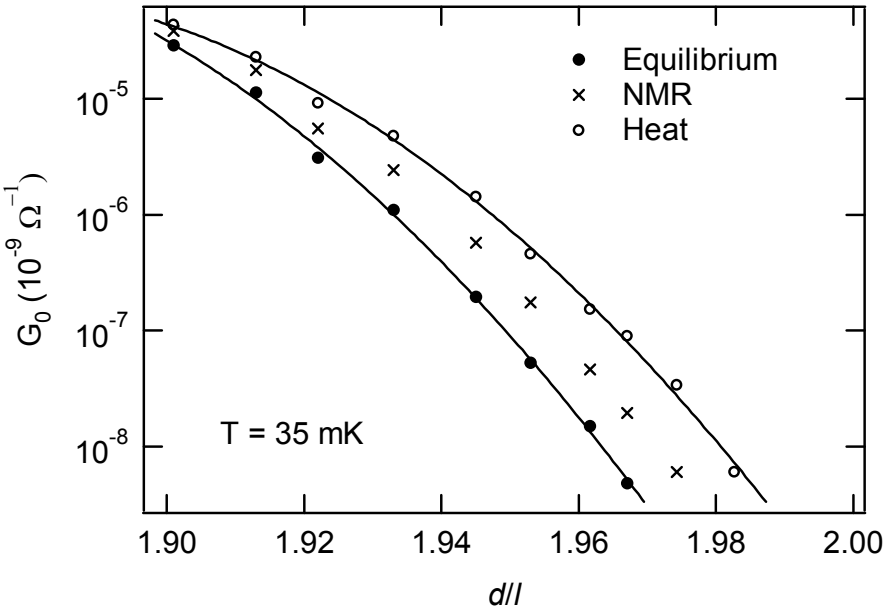

Fig 6.15. Evolution of zero-bias interlayer tunneling conductance, at equilibrium (solid dots), with ^{71}Ga nuclei depolarized via NMR (crosses), and with all nuclei depolarized via a heat pulse (open circles). The solid lines are guides to the eye.

The experiment of Fig. 6.14 can be repeated for several d/l values near phase boundary, using both NMR and heat pulse techniques. The result is shown in Fig. 6.15, which plots the zero-bias tunneling conductance G_0 versus d/l, at equilibrium, just after

an NMR pulse at the ^{71}Ga resonance, and just after a heat pulse used to depolarize all the nuclei. At all d/l near the phase boundary, the effect of depolarizing the nuclei is to enhance the G_0, the effect becoming proportionally more pronounced near the critical d/l (vanishing G_0).

In conclusion, we find that increasing the Zeeman splitting via NMR leads to an enhancement of G_0 for all d/l near the phase boundary between the weakly-coupled and strongly-coupled phase. The NMR tunneling data are consistent with the RDNMR R_{xx} data and provide additional confirmation that the strongly-coupled phase has greater spin polarization than the competing weakly-coupled phase.

6.3.7 Simple Model

To make the explanation of our observations more concrete, consider a simple model where the bilayer 2DES at $\nu_T = 1$ near the phase boundary contains two competing phases with differing spin polarization, where the two phases are the weakly-coupled compressible phase and the incompressible exciton condensate phase. The phase separation can be driven by static fluctuations in the electron density or variations in the tunnel barrier width, both of which are present in our bilayer sample.

From the RDNMR measurements shown above we know that increasing the Zeeman splitting via application of NMR or heat pulses causes the excitonic phase to be

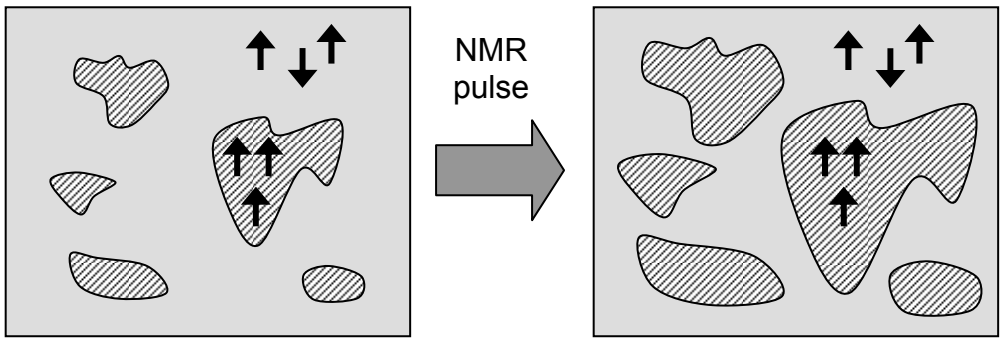

Fig. 6.16. Cartoon showing phase separation near the phase boundary where the excitonic phase (hatched) has greater spin polarization than the compressible phase (shaded). The application of an NMR pulse temporarily increases the fraction of the sample occupied by the excitonic phase.

favored, suggesting a picture where the excitonic phase has greater spin polarization than the competing compressible phase.

Consider the situation sketched in Fig. 6.16 where the system is at $\nu_T = 1$ near the phase boundary and the two coexisting phases are present. The hatched regions are in the incompressible, excitonic phase and have greater spin polarization than the shaded regions, which are in the compressible phase. Application of an NMR pulse will temporarily increase the Zeeman splitting, causing the state with greater spin polarization, the excitonic state, to be energetically favored. The fraction of the sample area occupied by the excitonic state will increase, which will lead to an enhanced zero-bias tunneling conductance and a decrease in the longitudinal resistivity.

6.3.8 Filling Factor Dependence

Figure 6.17 shows the dependence of the RDNMR signal and T_1 on total filling factor, varying the magnetic field while holding the 2DES density fixed such that $d/l = 1.90$ at $\nu_T = 1$. Figure 6.17a shows the NMR-induced fractional change in longitudinal resistance $\Delta R_{xx}/R_{xx}$ versus ν_T^{-1}. For reference, the longitudinal resistivity is also displayed, showing the dip in R_{xx} versus ν_T^{-1} that forms at $\nu_T = 1$. The magnitude of $\Delta R_{xx}/R_{xx}$ falls rapidly as the filling factor is raised or lowered above or below $\nu_T = 1$. In the compressible phase at filling factors outside of the range where the dip in R_{xx} occurs, $\Delta R_{xx}/R_{xx}$ is positive. Figure 6.17b shows the dramatic dependence of T_1 on ν_T^{-1}, showing a very long $T_1 \sim$ 2,000 s right at $\nu_T = 1$. T_1 decreases sharply when the filling factor deviates slightly from $\nu_T = 1$.

The data of Fig. 6.17 can be understood if we assume that moving away in filling factor from $\nu_T = 1$ drives the system out of the incompressible, excitonic phase and into a compressible phase that is similar to the weakly-coupled phase seen at $\nu_T = 1$ for larger d/l. Then, the decrease of $\left|\Delta R_{xx} / R_{xx}\right|$ and T_1 with increasing $\left|\nu_T - 1\right|$ is analogous to the behavior observed upon increasing d/l as shown in Fig. 6.12.

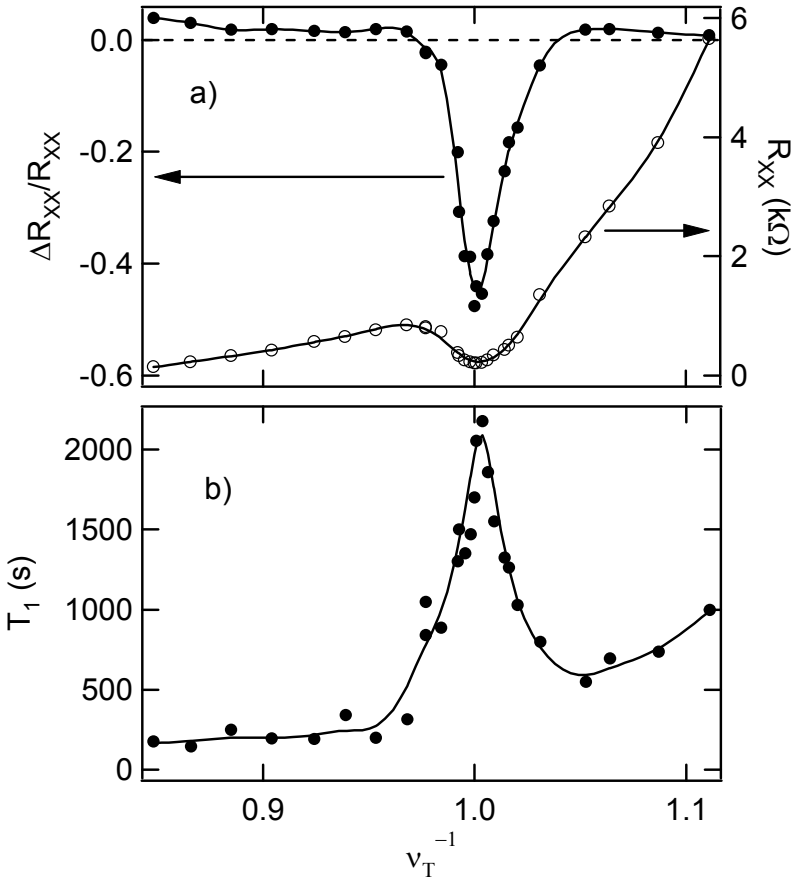

Fig. 6.17. RDNMR signal and T_1 versus ν_T^{-1}, varying the magnetic field while maintaining a fixed density, such that $d/l = 1.90$ at $\nu_T = 1$. a) Solid markers are the NMR-induced fractional change in the resistivity $\Delta R_{xx}/R_{xx}$. Open circles are the longitudinal resistivity R_{xx}. b) Nuclear T_1 time. Solid lines are guides to the eye.

We also note that the data of Fig. 6.17b looks similar to what is seen in single layer 2DES's at $\nu = 1$, where a similar peak in T_1 near $\nu = 1$ is expected due to the presence of skyrmions (see Chapter 7 for further discussion). Theoretically, it is speculated that the excitations of the bilayer system at $\nu_T = 1$ may have a similar structure, where the excitations are a type of skyrmion that involves both the pseduospin (layer index) and spin degree of freedom [22].

6.4 Conclusions

We have shown that, contrary to the usual assumption, that the spin degree of freedom is active during the transition between the compressible and incompressible state at $\nu_T = 1$.

The strengthening of the incompressible, excitonic phase that occurs when increasing the electronic Zeeman splitting via NMR shows that the compressible phase is partially polarized and that the excitonic phase has greater spin polarization than the competing compressible phase.

References

[1] I. B. Spielman, L. A. Tracy, J. P. Eisenstein, L. N. Pfeiffer, and K. W. West, *Phys. Rev. Lett*. **94**, 076803 (2005).

[2] I. B. Spielman. PhD Dissertation, California Institute of Technology (2004).

[3] J. P. Eisenstein, L. N. Pfeiffer, and K. W. West, *Phys. Rev. Lett*. **69**, 3804 (1992).

[4] T. Chakraborty and P. Pietiläinen, *Phys. Rev. Lett*. **59**, 2784 (1987).

[5] D. Yoshioka, A.H. MacDonald and S.M. Girvin, *Phys. Rev. B* **39**, 1932 (1989).

[6] G.S. Boebinger, H.W. Jiang, L.N. Pfeiffer and K.W. West, *Phys. Rev. Lett*. **64**, 1793 (1990).

[7] J. P. Eisenstein, G. S. Boebinger, L. N. Pfeiffer, K. W. West, and S. He, *Phys. Rev. Lett*. **68**, 1383 (1992).

[8] Y.W. Suen, L.W. Engel, M.B. Santos, M. Shayegan and D.C. Tsui, *Phys. Rev. Lett*. **68**, 1379 (1992).

[9] S. Q. Murphy, J. P. Eisenstein, G. S. Boebinger, L. N. Pfeiffer, and K. W. West, *Phys. Rev. Lett*. **72**, 728 (1994).

[10] H. A. Fertig, *Phys. Rev. B* **40**, 1087 (1989).

[11] A. H. MacDonald and E. H. Rezayi, *Phys. Rev. B* **42**, 3224 (1990).

[12] X.G. Wen and A. Zee, *Phys. Rev. Lett*. **69**, 1811 (1992) .

[13] Z.F. Ezawa and A. Iwazaki, *Phys. Rev. B* **47**, 7295 (1993).

[14] K. Moon, et al., *Phys. Rev. B* **51**, 5138 (1995).

[15] B. I. Halperin, *Helv. Phys. Acta* **56**, 75 (1983).

[16] D. Yoshioka, A.H. MacDonald and S.M. Girvin, *Phys. Rev. B* **39**, 1932 (1989).

[17] M. Kellogg, J. P. Eisenstein, L. N. Pfeiffer, and K. W. West, *Phys. Rev. Lett*. **93**, 036801 (2004).

[18] I. B. Spielman, J. P. Eisenstein, L. N. Pfeiffer, and K. W. West, *Phys. Rev. Lett*. **84**, 5808 (2000).

[19] M. Kellogg, I. B. Spielman, J. P. Eisenstein, L. N. Pfeiffer, and K. W. West, *Phys. Rev. Lett*. **88**, 126804 (2002).

[20] J. P. Eisenstein, L. N. Pfeiffer, and K. W. West, *Appl. Phys. Lett*. **57**, 2324 (1990).

[21] K. Hashimoto *et al.*, *Phys. Rev. Lett*. **88**, 176601 (2002).

[22] J. Bourassa, *et al*., *Phys. Rev. B* **74**, 195320 (2006).

Chapter 7:
$\nu = 1$ Quantum Hall Ferromagnet

The $\nu = 1$ quantum Hall state in a single layer 2DES might at first glance appear to be readily explained via a simple non-interacting picture invoking the single-particle Landau levels described in Chapter 3. However, upon greater scrutiny, one finds that Coulomb interactions actually play a large role in determining the behavior of this state. For example, the activation energy of the $\nu = 1$ state is much larger than the bare Zeeman gap that one would predict from a single-particle picture, due to the exchange interaction. Exchange also plays a role in determining the spin and charge excitations of this quantum hall state. The lowest energy charged excitations at filling factors at and nearby $\nu = 1$ are actually predicted to be skyrmions [1], excitations with a smooth spatial variation in spin which carry spin and charge. This chapter discusses resistively-detected NMR (RDNMR) measurements that probe the electron spin near $\nu = 1$ [2]. The presence of skyrmions is expected to have a large impact on nuclear spin dynamics at this state. Experimentally, RDNMR near $\nu = 1$ is quite different when compared to the data of earlier chapters. Near $\nu = 1$, the RDNMR lineshape is "anomalous", having a derivative-like lineshape rather than the simple unipolar lineshape seen at $\nu = 1/2$ (Chapter 5) and in the bilayer 2DES at $\nu_T = 1$ (Chapter 6). The nuclear $1/T_1$ relaxation rates near $\nu = 1$ can also be more than an order of magnitude faster than those seen in the partially polarized, compressible phase at $\nu = 1/2$ or $\nu_T = 1$.

7.1 Background

7.1.1 Skyrmions

A 2DEG at $\nu = 1$ is a two-dimensional ferromagnet. Even in the absence of spin Zeeman energy (i.e., $g = 0$), the ground state will be completely spin polarized due to Coulomb interactions. In a single-particle picture, with nonzero g-factor, one would expect the activation energy of this state to be equal to the bare Zeeman splitting, corresponding to a single spin flip obtained by moving one electron up in energy to the next spin-resolved Landau level. However, in reality, the energy gap at $\nu = 1$ is greatly enhanced by exchange interactions in typical 2DEG's in GaAs/AlGaAs heterostructures.

Magnetotransport measurements show that the activation energy is nearly 20 times greater than the bare Zeeman splitting [3, 6].

As was mentioned in the introduction, the lowest-lying charged excitations near $\nu = 1$ are strongly affected by the exchange interaction and are theoretically predicted to be objects called skyrmions [1]. The skyrmions at and near $\nu = 1$ carry charge $\pm e$ and multiple reversed spins. When the exchange energy penalty due to a single spin flip is larger than the Zeeman energy, in order to make a spin excitation, instead of reversing a single spin it is favorable to flip multiple spins in order to attempt to align neighboring spins. The spatial configuration of the spin and charge of a skyrmion is sketched in Fig. 7.1. A skyrmion has a single reversed spin located at the center and the surrounding spins gradually rotate back to the ground state spin alignment with increasing radius.

Fig. 7.1. Sketch of a single skyrmion showing the electron spin configuration (arrows) versus position in the 2D plane.

The size of the skyrmion and number of reversed spins K is determined by the relative magnitude of the exchange and Zeeman energies. For vanishing Zeeman energy K and the size of the skyrmion diverges. As the Zeeman splitting is increased the

energetic cost of creating multiple flipped spins increases and K and the skyrmion size are reduced. Above a critical ratio of the Zeeman splitting to the Coulomb energy, the lowest energy quasiparticle will be a single spin flip, rather than a skyrmion. A lower bound for this critical ratio $E_Z/E_C > 0.054$ is given in Ref. [1]. For 2DES's in GaAs/AlGaAs heterostructures, where g = -0.44, this critical ratio implies that for perpendicular magnetic fields less than B = 25 T, skyrmions will be the lowest energy charged excitations at $\nu = 1$.

Skyrmions with charge -e or antiskyrmions with charge +e are added to the ground state as the filling factor ν of the 2DEG is raised or lowered above or below $\nu = 1$, respectively. Since skyrmions (and antiskyrmions) carry reversed spins, this leads to a drop in the electron spin polarization as ν deviates from $\nu = 1$, as was predicted by Fertig *et. al* [4]. In fact, this rapid decrease in the spin polarization has been observed experimentally. Optically pumped NMR Knight shift measurements performed by Barrett *et al*. [5], show that right at $\nu = 1$, the spin polarization is maximal, and then drops rapidly with increasing $|\nu - 1|$. The rate at which the spin polarization decreases with respect to filling factor provides an estimate of the number of reversed spins per skyrmion. From a fit of the Knight shift versus ν data, Barrett *et al*. find that $K = 3.6$ for the case where the ratio $E_Z/E_C = 0.016$ at $\nu = 1$. Schmeller *et al*. [6] also make an experimental estimate of K via transport activation energy measurements versus Zeeman energy at $\nu = 1$. Small changes in the Zeeman energy were made via applying an in-plane magnetic field. The slope of the transport gap versus Zeeman splitting gave $K \approx 3.5$ for $E_Z/E_C \sim 0.01$ at $\nu = 1$.

7.1.2 Skyrmion Solid

Away from $\nu = 1$, where the ground state of the system contains a finite density of skyrmions, it is expected that interactions between skyrmions will lead to the formation of a skrymion solid. Brey *et al*. predict the formation of skyrme crystal for $|1-\nu| < 0.2$ [7]. Square or triangular lattice formation is predicted where the type of lattice depends on both ν and the ratio of the Zeeman to Coulomb energy [8].

The prediction of a skyrme crystal near $\nu = 1$ remains somewhat controversial. An unpolarized liquid state has also been predicted for filling factors near $\nu = 1$ [9]. Also, in most of the theoretical work to date the effect of disorder has not been well established.

7.1.3 Collective Modes

The skyrme crystal has magnetic modes that correspond to the orientational and positional degrees of freedom for the skrymions [8]. These are the spin-wave and phonon modes of the skyrme crystal. Fig. 7.2 sketches the dispersion at low energies for both modes.

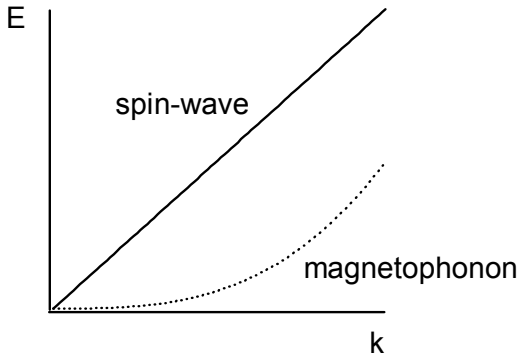

Fig. 7.2. Collective mode dispersions for skyrme crystal for low energies, showing the spin-wave (solid line) and magnetophonon (dotted line) modes.

The magnetophonon mode corresponds to fluctuations in the position of the skyrmions, while the spin-wave mode corresponds to fluctuations in the in-plane (x-y) component of the spin. Ideally, these modes are gapless – they have zero energy at zero wavevector.

These low-energy modes are expected to influence nuclear spin relaxation in the vicinity of the 2DES. Both modes give rise to local fluctuations in the z-component of the electron spin. These modes should lead to a Korringa-like temperature dependence for the nuclear spin relaxation rate $1/T_1$ (see Chapter 5, section 5.3.6 for a discussion of Korringa relaxation). In the presence of disorder, pinning of the skyrme crystal to charged impurities may occur, which will lead to a gapped phonon mode (nonzero energy at zero wavevector). However, the spin-wave mode will remain gapless. In this case, the

T_1 time will be determined by the thermal occupation of the spin-wave modes and will be given by [8]:

$$1/T_1 \sim \frac{k_B T}{UJ}\left|\nu - 1\right|, \tag{1}$$

where the constant UJ determines the stiffness of the spin-wave mode: $E \sim \sqrt{UJ}k$.

Alternate temperature dependences for T_1 are predicted by Green [10], who considers the importance of quantum fluctuations. Green predicts a relaxation rate that can either increase or *decrease* with increasing temperature, depending on the relative magnitude of the spin-wave stiffness, skyrmion size, and Zeeman energy.

7.1.4 Previous Experiments

Some of the earliest experiments probing the electron spin degree of freedom near $\nu = 1$ have already been mentioned – the optically-pumped NMR Knight shift measurements of the electron spin polarization versus filling factor by Barrett *et al*. [5] and the dependence of the activation energy on Zeeman energy measured by Schmeller *et al*. [6]. Both works suggest the presence of finite-size skyrmions near $\nu = 1$. The nuclear T_1 time near $\nu = 1$ has also been measured via NMR. Tycko *et al.*, using optically pumped NMR, find a rapidly decreasing T_1 as the filling factor deviates from $\nu = 1$, suggesting the presence of low-lying electronic spin-flip excitations near $\nu = 1$ [11]. Bayot *et al*. find a giant enhancement of the heat capacity of a 2DES near $\nu = 1$ at low temperatures, which can be explained by a nuclear spin contribution to the heat capacity, suggesting a strong coupling between the electrons and the nuclear spins in the 2DES region [12].

Using a RDNMR technique, Hashimoto *et al.* observe a nuclear relaxation rate which increases dramatically as ν is raised above or lowered below $\nu = 1$ [13]. Smet *et al*. [14] and Desrat *et al*. [15] also observe a relatively short T_1 time as ν deviates slightly away from $\nu = 1$ using RDNMR. Desrat *et al*. were also the first authors to report an "anomalous" derivative-like RDNMR lineshape, very similar to the lineshape we observe under comparable conditions, as shown in Fig. 7.6b [15].

RDNMR measurements of Gervais *et al*. also yield a fairly short T_1 time [16]. However, the RDNMR lineshape of Gervais *et al*. looks very different from that observed

by Desrat *et al*., having a unipolar rather than a derivative-like lineshape. Gervais *et al*. also perform a systematic study of the temperature dependence of T_1 and find an *increasing* T_1 with increasing temperature, which the authors interpret as evidence for formation of a skyrme crystal at low temperatures. This interpretation is consistent with the theory of the T_1 temperature dependence of Green, as mentioned above (see section 7.1.3), for some values of the skyrme spin-wave stiffness, skyrmion size, and Zeeman splitting [10].

7.2 Experiment

We use RDNMR (see Chapter 4 for a general introduction to RDNMR) to examine the spin degree of freedom near $\nu = 1$ in a single layer 2DES, with the aim of further investigating the "anomalous", derivative-like RDNMR lineshape seen in Ref. [15] and the peculiar temperature dependence of T_1 (T_1 increasing with rising temperature) found in Ref. [16].

7.2.1 Samples

We studied two different single-layer 2DES samples, labeled "A" and "B". The sample structure, mobility and density of these two samples is shown in Table 7.1.

Sample	**Structure**	**Mobility** (cm^2/Vs)	**Density** (cm^{-2})
A	heterojunction	8×10^6	1.6×10^{11}
B	quantum well (300 Å)	14×10^6	1.6×10^{11}

Table 7.1. Sample structure, mobility, and density for single-layer 2DES samples used in RDNMR experiment near $\nu = 1$.

Figure 7.3 shows magnetotransport for both of these samples, displaying minima in R_{xx} versus B corresponding to several fractional and integer quantum Hall states.

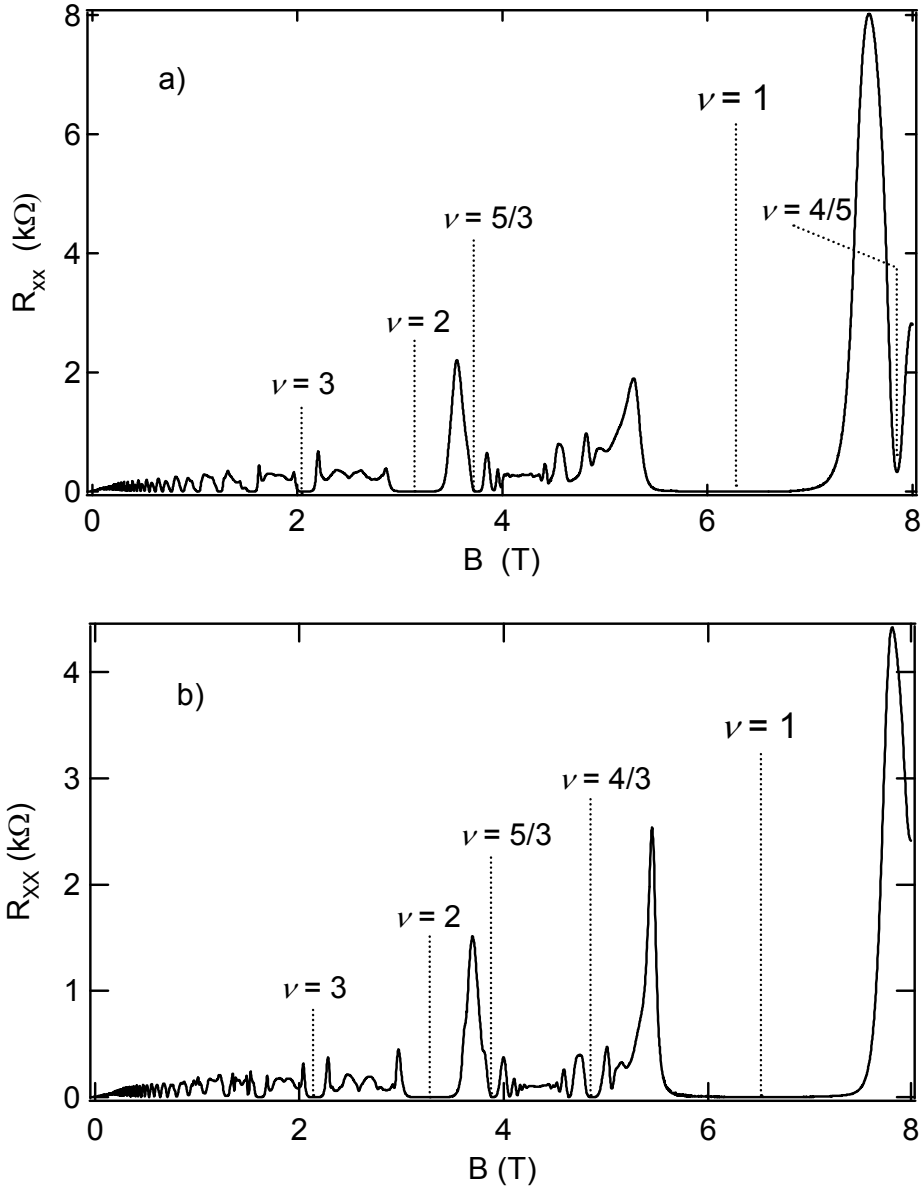

Fig. 7.3. Magnetotransport R_{xx} vs. B at $T \sim 50$ mK for a) sample "A" and b) sample "B".

7.2.2 Setup

The 2DES sample is placed in an approximately rectangular 8-turn NMR coil for application of an RF magnetic field H_1 parallel to the 2DES and perpendicular to the magnetic field. The magnitude of H_1 ranges from roughly 0.1 – 0.5 μT, as determined via an analysis of our coax/coil circuit (see Chapter 4, section 4.3.1a). These RF fields are much less than the nuclear dipolar field, $H_d \sim 0.1$ mT.

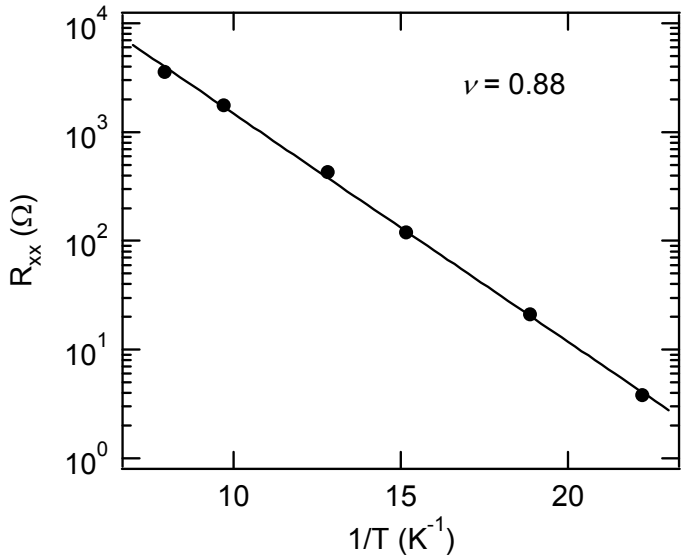

Fig. 7.4. Temperature dependence of the longitudinal resistivity R_{xx} at $\nu = 0.88$. The solid line is an Arrhenius fit: $R_{xx} = R_0 e^{-\alpha/T}$. The fit gives $\alpha = 0.48$ K.

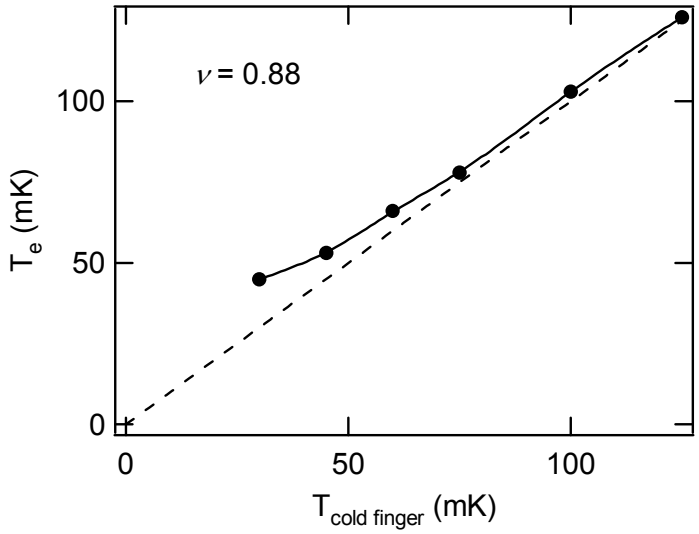

Fig. 7.5. Electron temperature T_e, as determined from sample resistivity, vs. cold finger temperature with RF on, at $\nu = 0.88$, where $H_1 \sim 0.5$ μT, $f \sim 52$ MHz. The solid line is a guide to the eye. The dashed line is the case for no RF heating (RF off), for reference.

Non-resonant RF heating of the sample raises the 2DES temperature above that of the cryostat cold-finger. The electron temperature with the RF power on is determined by using the longitudinal resistivity as an in-situ thermometer. As an example, Fig. 7.4

shows the temperature dependence of R_{xx} near $\nu = 1$ (at $\nu = 0.88$), which displays an Arrhenius behavior. Figure 7.5 shows the magnitude of the RF heating at $\nu = 0.88$ with $H_1 \sim 0.5$ μT, in which case the lowest reachable electron temperature is roughly 45 mK.

The 2DES is thermally connected to the cold finger via the ohmic contacts and leads. The thermal time constant for cooling of the 2DES is short. The 2DES can be temporarily be heated (due to ohmic heating) by application of a current pulse through the sample. For filling factors near $\nu = 1$, this ohmic heating can be detected via a rise in the longitudinal resistivity. The time required for the 2DES resistance to relax back to the thermal equilibrium value yields the thermal time constant for cooling of the 2DES electrons. For the experiments in this chapter, this thermal time constant is less than 0.1 s.

7.2.3 RDNMR lineshape

Figure 7.6a shows R_{xx} versus B near $\nu = 1$ at a temperature of $T = 70$ mK for sample A. Figure 7.6b shows the RDNMR lineshape – the NMR-induced change in resistance ΔR_{xx} versus frequency, while sweeping the frequency upward at 0.13 kHz/s. The arrow in Fig.

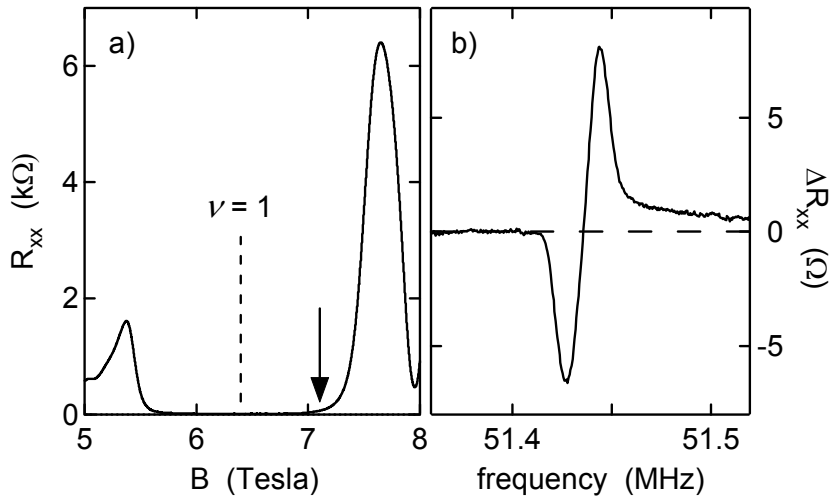

Fig. 7.6. Anomalous RDNMR lineshape near $\nu = 1$ as seen in sample A. a) R_{xx} vs. B near $\nu = 1$. The arrow marks the magnetic field at which the RDNMR lineshape shown in b) was acquired. b) RDNMR lineshape ΔR_{xx} vs. frequency for ^{75}As. The frequency is swept up at 0.13 kHz/s.

7.6a marks the magnetic field at which the lineshape of Fig. 7.6b was taken. We observe the same "anomalous" derivative-shaped RDNMR lineshape for filling factors near $\nu = 1$ as seen previously by Desrat *et al*. [15].

Figure 7.7 shows a typical RDNMR transient ΔR_{xx} versus time, where the RF power is held constant in order to keep the non-resonant RF heating of the 2DES constant. For times earlier than t_i, the frequency is off of the ^{75}As resonance and the resistance is at the thermal equilibrium value. At t_i the frequency is brought onto resonance and the resistance falls. Finally, at t_f the frequency is brought off resonance and the resistance decays back to the equilibrium value. The inset to Fig. 7.7 shows the ^{75}As RDNMR lineshape, where the open circle marks the "off resonance" frequency and the closed circle marks the "on resonance" frequency.

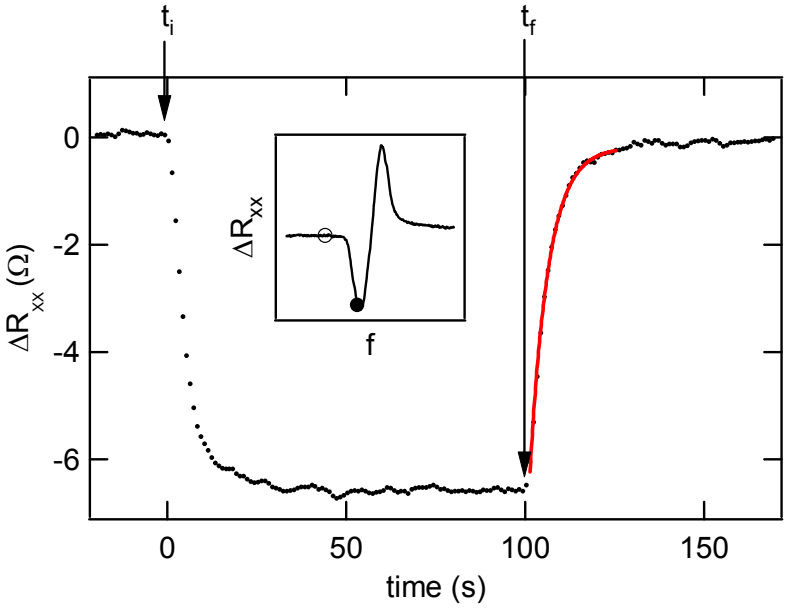

Fig. 7.7. RDNMR transient ΔR_{xx} vs. time, showing the fall and rise of the resistivity with application of resonant RF at the ^{75}As resonance frequency. At time t_i the frequency is brought onto resonance and at t_f the RF is brought off resonance. The data is taken at B = 7.1 T ($\nu = 0.89$), at a temperature T = 70 mK. The solid red line for times greater than t_f is an exponential fit to the data. Inset: RDNMR lineshape obtained by sweeping the frequency upward at 0.13 kHz/s. The solid circle marks the "on resonance" frequency (f = 51.425 MHz), while the open circle corresponds to "off resonance" (f = 51.42 MHz).

The time required for the relaxation of the longitudinal resistivity back to equilibrium is the nuclear T_1 time. The red line in Fig. 7.7 is an exponential fit to the data during this relaxation period, yielding $T_1 = 5.2$ s.

7.2.4 Power Dependence

Figure 7.8 shows the power dependence of the RDNMR line. The derivative-like lineshape is preserved for all RF power levels. The maximum power in Fig. 7.8 corresponds to $H_1 \sim 0.5$ μT, and for the minimum power $H_1 \sim 0.1$ μT.

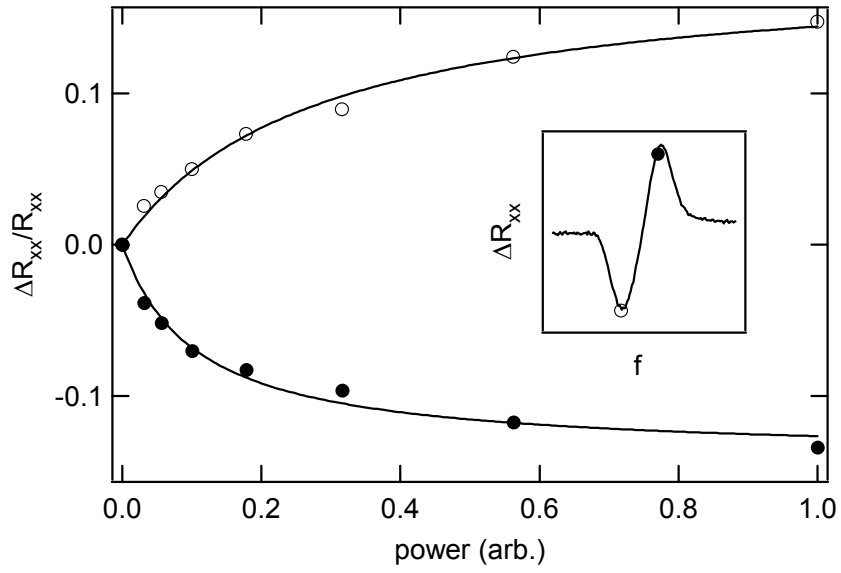

Fig. 7.8. RF power dependence of RDNMR lineshape amplitude $\Delta R_{xx}/R_{xx}$ at $\nu = 0.89$ for $f = 51.425$ MHz (open circles) and $f = 51.441$ MHz (filled circles). Solid lines are a fit to the data of the expected form of the power dependence from the Bloch equations (see text). Inset: RDNMR lineshape showing the location of $f = 51.425$ MHz (open circle) and 51.441 MHz (filled circle).

From the Bloch equations we expect the fractional change in the nuclear polarization due to NMR to be given by (see Chapter 4)

$$\Delta\xi / \xi = \left[\frac{\omega_r{}^2 T_1 T_2}{1 + \omega_r{}^2 T_1 T_2} \right] = 1 - \tau_{rise} / T_1 , \qquad (2)$$

where ξ is the nuclear polarization, ω_r is the Rabi frequency, T_2 and T_1 are the nuclear spin-spin and spin-lattice relaxation times, respectively, and τ_{rise} is the initial rise time of the change in the nuclear polarization, just after the RF is brought onto the NMR resonance. We next assume that the RDNMR signal $\Delta R_{xx}/R_{xx}$ is proportional to the NMR-induced change in Zeeman energy, which is proportional to the change in the nuclear polarization. Then, since RF power ~ ω_r^2, we fit the data of Fig. 7.8 to a function of the form

$$\frac{\Delta R_{xx}}{R_{xx}} = \alpha \frac{\beta P}{1+\beta P},$$

where P is the RF power (measured in the arbitrary units shown in Fig. 10), and α and β are fitting parameters. The resulting fits are the solid lines shown in Fig. 7.8. The parameter β will be determined by T_1T_2 and the calibration between RF power and H_1^2. For the data taken at f = 51.425 MHz (at the dip in the RDNMR line) we obtain β = 9.5. For the data at f = 51.441 MHz (at the peak in the RDNMR line) we find β = 3.6. In both cases, the fact that $\beta > 1$ suggests that for the higher RF power levels shown in Fig. 7.8 the NMR line is near saturation, i.e. the nuclear polarization has been reduced to nearly zero.

We can also calculate $\Delta\xi/\xi$ using our rough estimate for H_1 from an analysis of the coil/coax circuit. In GaAs the intrinsic nuclear T_2 time is on the order of 1 ms. Using our estimate of H_1 and the nuclear gyromagnetic ratio, $\omega_r \sim 2\pi \times 0.5\ \mu\text{T} \times 7.29$ MHz/T ~ 23 Hz. Then, $\omega_r^2 T_1 T_2 \sim 3$, which is in the same ballpark as the above estimate, using the power dependence of the RDNMR signal.

From Eq. (2) we find that we should also be able obtain $\Delta\xi/\xi$ from T_1 and τ_{rise}, which are the rise and fall times in the RDNMR transient shown in Fig. 7.7. An exponential fit to the data of Fig. 7.7 for times immediately after t_i yields τ_{rise} = 4.3 s. As mentioned previously, a fit to the relaxation of ΔR_{xx} after t_f in Fig. 7.7 gives T_1 = 5.2 s. Then, $\Delta\xi/\xi = 1 - \tau_{rise}/T_1 = 0.17$, which is much smaller than the value obtained by the power dependence fits of Fig. 7.8. It appears that the Bloch equations fail to adequately describe the RF power dependence of RDNMR near ν = 1.

7.2.5 Nuclear T_1 Time

As previously observed, [11, 15] the data of Fig. 11a show that the nuclear relaxation rate $1/T_1$ grows with increasing $|1-\nu|$, near $\nu = 1$. This filling factor dependence is consistent with Eq. (1) from the theory of Cote *et al*., where nuclear spin relaxation via the skyrmion spin-wave modes is enhanced since raising $|1-\nu|$ leads to an increase the density of skyrmions [8].

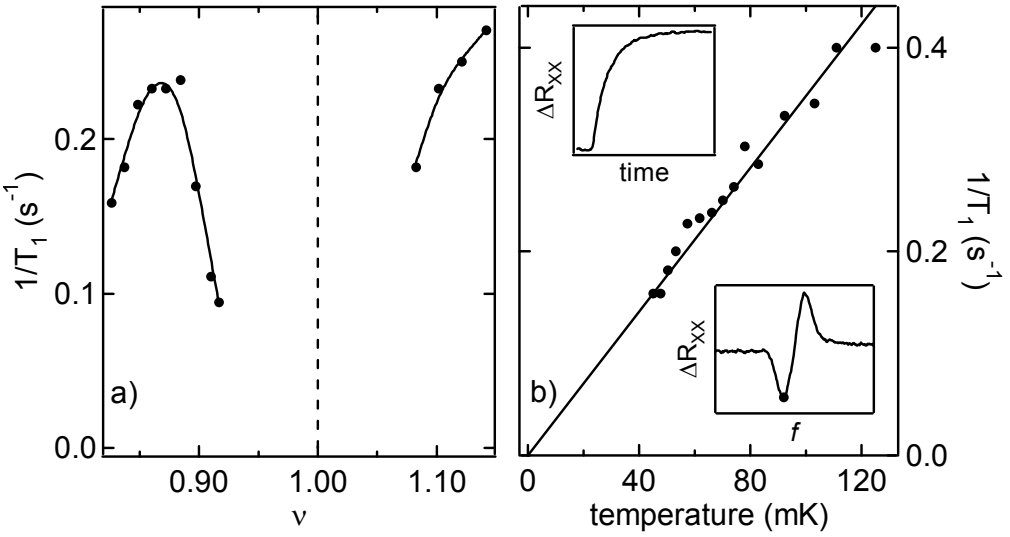

Fig. 7.9. Nuclear spin relaxation rate T_1 for ^{75}As near $\nu = 1$ for sample A. a) $1/T_1$ vs. filling factor at $T = 70$ mK. Solid lines are a guide for the eyes b) $1/T_1$ vs. temperature at $\nu = 0.88$. Solid line is a Korringa law fit: $T_1T = 0.28$ s K. Top inset: RDNMR transient ΔR_{xx} vs. time showing the relaxation of the resistivity after the frequency is brought off the NMR resonance. Bottom inset: RDNMR lineshape, ΔR_{xx} vs. frequency. The solid circle marks the resonant frequency at which the T_1 time data was acquired.

Figure 7.9b shows $1/T_1$ versus temperature at $\nu = 0.88$. The upper inset to Fig. 7.9b shows a representative transient RDNMR signal used to obtain the T_1 time via an exponential fit. The lower inset shows the frequency on the NMR line at which the T_1 data was taken. The data show a Korringa-like temperature dependence, $1/T_1 \sim \alpha T$, consistent with the prediction of Cote *et al.* in Eq. (1). As mentioned previously, the theory of Green [10] predicts an increasing or decreasing T_1 with respect to increasing

temperature, depending on the relative values of the skyrme spin-wave stiffness, skyrmion size, and Zeeman splitting. However, comparison between our experiment and the theory of Green is difficult since we have no reliable way of estimating the spin-wave stiffness.

As discussed earlier, the RDNMR data of Gervais *et al*. show a *decreasing* $1/T_1$ with increasing temperature, at the same filling factor and over a similar temperature range as our data [16]. One difference between the two experiments is the sample structure and mobility. The sample of Gervais *et al*. is a 40 nm wide quantum well with a mobility of 17×10^6 cm^2/Vs, while the data of Fig. 11b was taken using sample A, which is a heterojunction with a mobility of 8×10^6 cm^2/Vs (see Table 7.1). In light of this, we decided to perform RDNMR near $\nu = 1$ on a different sample (sample B), with a higher mobility ($\mu = 14 \times 10^6$ cm^2/Vs) and a quantum well structure (30 nm wide). The data of Fig. 7.10 show a similar temperature dependence for T_1 as seen in sample B, for which we also find a derivative-like RDNMR lineshape.

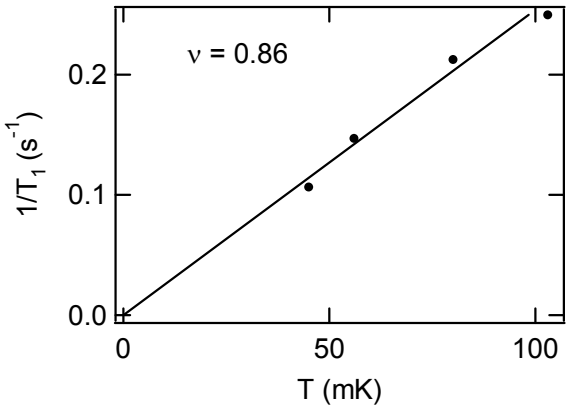

Fig. 7.10. $1/T_1$ temperature dependence at $\nu = 0.86$ for sample B. The solid line is a Korringa fit to the data: $T_1T = 0.27$ s K.

7.2.6 Lineshape and *dR/dT*

As seen in Fig. 7.11, the RDNMR lineshape can actually invert from a resonance with dip at low frequencies and peak at higher frequencies to the opposite shape, with a peak on

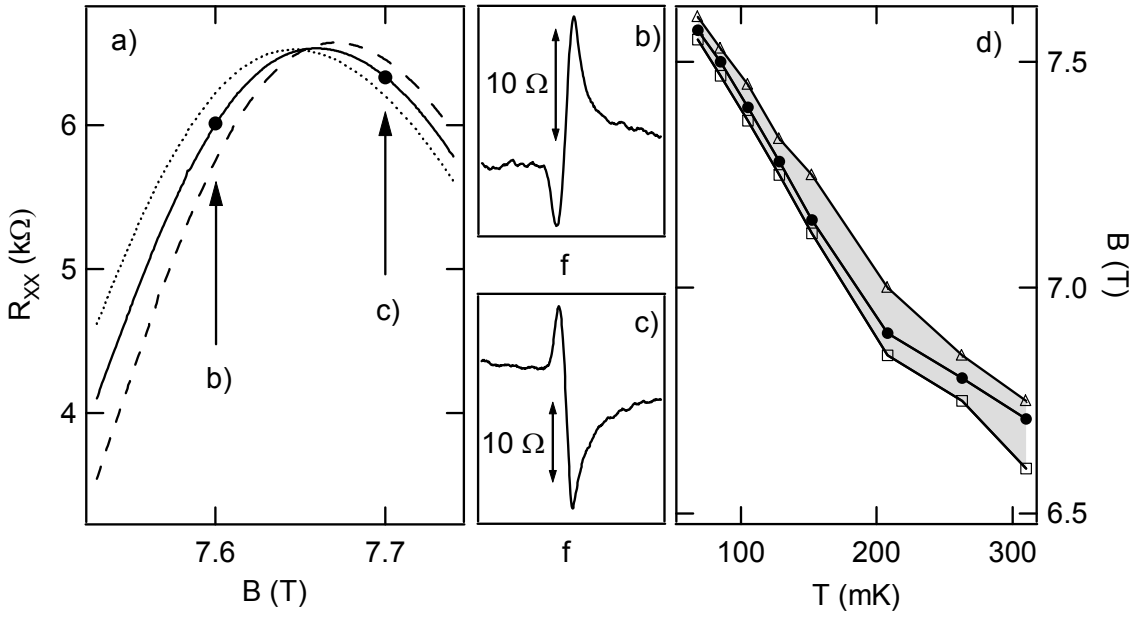

Fig. 7.11. Inversion of RDNMR lineshape with temperature dependence of R_{xx}. a) R_{xx} vs. B for three temperatures: 62 mK (dashed), 65 mK (solid), and 70 mK (dotted). The arrows mark the magnetic fields at which the RDNMR lineshapes shown in b) and c) were obtained. b) RDNMR lineshape at B = 7.6 T, T = 70 mK. c) RDNMR lineshape at B = 7.7 T, T = 70 mK. d) Magnetic field – temperature coordinates at which the lineshape and temperature dependence invert. Solid circles: points at which dR_{xx}/dT changes sign. Open squares: points at which the lineshape has a dip at low frequencies and a peak at higher frequencies, as shown in b). Open triangles: points at which the lineshape has a peak at low frequencies and a dip at higher frequencies, as shown in c). The shaded region corresponds to the range in which the RDNMR lineshape must invert. Note that the data shown in d) is taken from a different cool-down than that of a) – c). This produced a small density shift, and thus a shift in the B-fields at which dR_{xx}/dT changes sign.

the low-frequency side and a dip on the high-frequency side. The data also show that this inversion occurs roughly when the temperature dependence of the longitudinal resistivity changes sign, i.e. where $dR_{xx}/dT \sim 0$.

Fig. 7.11b shows the RDNMR lineshape at B = 7.6 T, T = 70 mK, where the resonance consists of a dip in R_{xx} at low frequencies and a peak at higher frequencies. Fig 7.11c shows the resonance at B = 7.7 T, T = 70 mK, with a lineshape that is inverted from that seen in Fig. 7.11b, i.e., a peak on the low-frequency side of the resonance and dip on the high-frequency side. Fig. 7.11a shows R_{xx} versus magnetic field at three

temperatures with arrows marking the magnetic fields (B = 7.6 and 7.7 T) at which the lineshapes of Fig. 7.11b and c were taken. Note that the crossing of these three curves (where dR_{xx}/dT changes sign), at $B \sim 7.65$ T, occurs between these two markers. The solid circles in Fig. 7.11d show the points at which $dR_{xx}/dT = 0$, while the shaded region indicates the magnetic field-temperature range over which the lineshape must invert. The data of Fig. 7.11d show that the inversion of the lineshape and change of the sign of dR_{xx}/dT coincide over a large range of magnetic field and temperature. Note that the data of Fig. 7.11d corresponds to a different cool-down than that of Fig. 7.11a – b. This produced a small difference in density between the two data sets, and thus a difference in the magnetic fields at which dR_{xx}/dT changes sign.

In the usual picture of RDNMR, the application of resonant RF reduces the nuclear polarization, which increases the electronic Zeeman splitting through the hyperfine interaction. Right at $\nu = 1$, one would expect that $R_{xx} \sim \exp(-E_Z/T)$. Then, an increase in E_Z would lead to a decrease in R_{xx}. In this picture, NMR should lead to a simple dip in the resistivity at resonance, inconsistent with a derivative-like lineshape. However, we note that the data is not taken at exactly $\nu = 1$ and that it is not known if the Zeeman energy dependence of the resistivity follows this simple form at filling factors away from $\nu = 1$. If we assume that the resistivity near $\nu = 1$ is of the general form $R_{xx} \sim f(E_Z/T)$, where f is a function of E_Z/T, then an increase in the Zeeman splitting will have roughly the same effect as a decrease in temperature. This may explain the apparent connection between the lineshape and the temperature dependence of the resistivity.

One explanation for the derivative-like lineshape could be a combination of Zeeman and thermal effects. If we assume f is a decreasing function of E_Z/T, an NMR-induced increase in the Zeeman energy could lead to a dip in R_{xx}, while a heat load from the nuclear spin system could raise the 2DES temperature, causing an increase in R_{xx}. Reduction of the nuclear polarization via resonant RF corresponds to an increase in the temperature of the nuclear spin system. The relaxation of the nuclear spins back to thermal equilibrium via the 2DES requires a heat flow from the nuclear spin system to the 2DES. Thus, one might expect a small increase in the 2DES temperature due to NMR. Therefore, a combination of the NMR-induced change in Zeeman energy and 2DES temperature might explain the presence of both a peak and dip in R_{xx} vs. frequency.

However, why the Zeeman effect would dominate on the low-frequency side of the resonance and the thermal effect on the high-frequency side is unclear.

7.3 Discussion

Fig. 7.12 shows the striking difference between the RDNMR lineshape seen at a) $\nu = 1/2$ (see Chapter 5) versus b) near $\nu = 1$ ($\nu = 0.89$). The most noticeable difference between the RDNMR linehsapes of Fig. 14a and 14b is the general shape. The data of Fig. 7.12a show a simple peak in R_{xx} vs. frequency, while that of Fig. 7.12b show a derivative-like lineshape.

Another prominent difference is the width of the resonance. The FWHM for the lineshape of Fig. 7.12a (ignoring the satellite peaks due to quadrupole splitting) is ~ 5 kHz, while the spacing between the dip and peak (corresponding to the FWHM of the integral of the lineshape) in R_{xx} in Fig. 7.12b is roughly 17 kHz, over three times the linewidth seen at $\nu = 1/2$. However, this linewidth variation is roughly consistent with broadening of the line due to the finite with of the 2DES subband wavefunction (see Chapter 4, sec. 4.3.2). The maximum Knight shift is determined by the electron density and the shape of the subband wavefunction: $K_{S1} \sim n/w$, where w is the subband wavefunction width. Using the Fang-Howard approximation (see Chapter 1, section

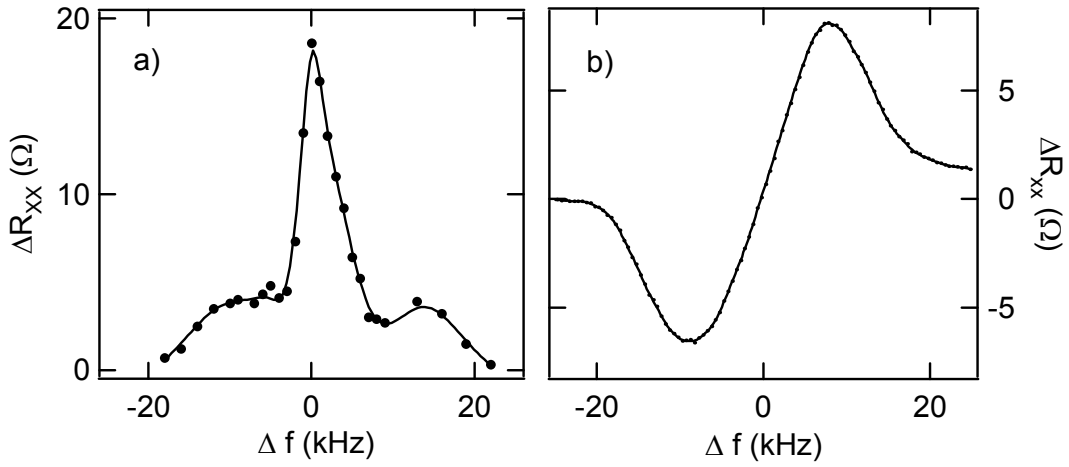

Fig. 7.12. Comparison between ^{75}As RDNMR lineshape at a) $\nu = 1/2$, $B = 4.01$ T and at b) $\nu = 0.89$, $B = 7.1$ T.

1.1.5) to estimate w, we find that $K_{S1} \sim n^{4/3}$. The density is over three times larger for the data of Fig. 7.12b than in 14a. Thus, assuming that the electron spin polarization is not too different for the case of Fig. 7.12a and b, the extra broadening seen at $\nu = 0.89$ is consistent with finite-thickness effects giving rise to variation in the NMR resonance frequency due to the Knight shift and shape of the 2DES subband wavefunction.

Derivative-like RDNMR lineshapes have been seen near other quantum Hall states. Stern *et al*. observe derivative-like lineshapes near $\nu = 1/3$ and 2/3 [17] and Gervais *et al*. find this type of lineshape near $\nu = 2/9$ and 1/5 [18]. The formation of skyrmions is not expected at these FQH states under typical experimental conditions for 2DES's in GaAs/AlGaAs heterostructures [19, 20]. The observation of this anomalous lineshape near these states suggests that the lineshape is not related to the presence of skyrmions, but rather some common feature of quantum Hall states, such as the presence of localized states.

7.4 Conclusion

In summary, we have observed a derivative-like RDNMR lineshape near $\nu = 1$, as seen previously by Desrat *et al*. [15]. Our data show that the lineshape inverts when dR_{xx}/dT changes sign. This inversion of the RDNMR lineshape may be a clue to the origin of this "anomalous" derivative-like lineshape. We also observe a fast $1/T_1$ nuclear relaxation rate, relative to that seen at other filling factors, which suggests interesting spin physics unique to filling factors near $\nu = 1$, possibly due to skrymions. However, we find a different RDNMR lineshape and opposite T_1 temperature dependence to that seen in Gervais *et al*. [16]. A complete picture of RDNMR near $\nu = 1$ and the origin of this conflict remains unclear.

References

[1] S. L. Sondhi, A. Karlhede, S. A. Kivelson and E. H. Rezayi. *Phys. Rev. B* **47**, 16419 (1993).

[2] L. A. Tracy, J. P. Eisenstein, L. N. Pfeiffer, and K. W. West, *Phys. Rev. B* **73**, 121306 (2006).

[3] A. Usher, R.J. Nicholas, J.J. Harris, and C.T. Foxon, *Phys. Rev. B* **41**, 1129 (1990).

[4] H. A. Fertig, L. Brey, R. Cote, and A. H. MacDonald, *Phys. Rev. B* **50**, 11018 (1994).

[5] S. E. Barrett, G. Dabbagh, L. N. Pfeiffer, K. W. West, and R. Tycko, *Phys. Rev. Lett*. **74**, 5112 (1995).

[6] A. Schmeller, J.P. Eisenstein, L.N. Pfeiffer, and K.W. West, *Phys. Rev. Lett.* **75**, 4290 (1995).

[7] L. Brey, H. A. Fertig, R. Côté, and A. H. MacDonald, *Phys Rev. Lett*. **75**, 2562 (1995).

[8] R. Côté, A. H. MacDonald, L. Brey, H. A. Fertig, S. M. Girvin, and H. T. C. Stoof, *Phys. Rev. Lett*. **78**, 4825 (1997).

[9] B. Paredes and J. J. Palacios, *Phys. Rev. B* **60**, 15570 (1999).

[10] A. G. Green, *Phys. Rev. B* **61**, R16299 (2000).

[11] R. Tycko, S. E. Barrett, G. Dabbagh, L. N. Pfeiffer, and K. W. West, *Science* **268**, 1460 (1995).

[12] V. Bayot, E. Grivei, S. Melinte, M. B. Santos, and M. Shayegan, *Phys. Rev. Lett*. **76**, 4584 (1996).

[13] K. Hashimoto, K. Muraki, T. Saku, and Y. Hirayama, *Phys. Rev. Lett*. **88**, 176601 (2002).

[14] J. H. Smet *et al*. *Nature* **415**, 281 (2002).

[15] W. Desrat, D. K. Maude, M. Potemski, J. C. Portal, Z. R. Wasilewski, and G. Hill, *Phys. Rev. Lett*. **88**, 256807 (2002).

[16] G. Gervais, H. L. Stormer, D. C. Tsui, P. L. Kuhns, W. G. Moulton, A. P. Reyes, L. N. Pfeiffer, K. W. Baldwin, and K. W. West, *Phys. Rev. Lett*. **94**, 196803 (2005).

[17] O. Stern, N. Freytag, A. Fay, W. Dietsche, J. H. Smet, K. von Klitzing, D. Schuh, and W. Wegscheider, *Phys. Rev. B* **70**, 075318 (2004).

[18] G. Gervais, H. L. Stormer, D. C. Tsui, L. W. Engel, P. L. Kuhns, W. G. Moulton, A. P. Reyes, L. N. Pfeiffer, K. W. Baldwin, and K. W. West, *Phys. Rev.* B **72**, 041310R (2005).

[19] A. Wójs and J. J. Quinn, *Phys. Rev. B* **66**, 045323 (2002).

[20] D. R. Leadley, R. J. Nicholas, D. K. Maude, A. N. Utjuzh, J. C. Portal, J. J. Harris, and C. T. Foxon, *Phys. Rev. Lett*. **79**, 4246 (1997).

Conclusions and Future Directions

In summary, we have examined the role of spin in several 2DES states, using RDNMR techniques to examine a spin transition for composite fermions at $\nu = 1/2$, a phase transition in the correlated $\nu_T = 1$ state in a bilayer 2DES, and spin excitations near $\nu = 1$ in a single layer 2DES. We have also probed the low density 2DES via SAW measurements under conditions where the putative metal-insulator transition should occur. In all of these experiments, puzzles remain for further investigation. In conclusion, we briefly discuss a few possible directions for future related experiments.

Composite Fermions at $\nu = 1/2$

A fairly high mobility 2DES (~ 1 – 5 × 10^6 cm^2/Vs) was used for the RDNMR measurements at $\nu = 1/2$ described in this thesis (Chapter 5). It would be interesting to see how the RDNMR signal and nuclear T_1 time near the spin transition evolve as a function of mobility. Higher mobility samples exist, although it is somewhat challenging to fabricate a high mobility sample with tunable density. An undoped FET structure [1] might be a possible candidate.

Our data shows a peak in the RDNMR signal as a function of density near the spin transition (Chapter 5, Fig. 10a) that continues to sharpen as the temperature is lowered. However, we were unable to reach temperatures below roughly 45 mK due to non-resonant RF heating of the 2DES. It may be feasible to reduce this non-resonant heating and see if the RDNMR signal versus density feature near the transition continues to sharpen as the temperature reduced.

The RDNMR signal at $\nu = 1/2$ is a nonlinear function of dc measurement current for large currents. Appendix C presents very preliminary data which seems to show that this nonlinearity is due to pumping of the nuclear spin population out of equilibrium. Further investigation of this nonlinear RDNMR signal as a function of magnetic field, temperature, etc. is needed in order to understand the origin of this nonlinearity.

RDNMR could also be used to examine spin transitions for composite fermions at other compressible states, such as at $\nu = 3/2$ or $\nu = 1/4$. Interactions between CF's could

be different at these filling factors, which, in turn, could change the nature of any spin transition that occurs for these states [2].

Bilayer 2DES's

RDNMR could be used to probe bilayer states other than $\nu_T = 1$. For example, the bilayer state at total filling factor $\nu_T = 2$ is predicted to possess interesting spin configurations, including a canted antiferromagnetic state [3], due to the interplay between the tunneling gap Δ_{SAS}, the Zeeman energy, and the strength of intralayer versus intralayer interactions (d/l). Although Kumada *et al*. have recently published a RDNMR study of this state [4], they use a somewhat different experimental technique [5]. Further experiments could be performed using our bilayer samples and variant of RDNMR technique.

Surface Acoustic Waves

The surface acoustic wave (SAW) experiments of Chapter 2 suggest that density inhomogneities are important at the densities where the metal-insulator transition should occur in our sample. The density inhomogeneities in our 2DES are most likely due to ionized donor in the doping layer. It would be interesting to see if the same results hold for a cleaner 2DES, such as an undoped FET structure, in which the issue of density fluctuations due to the ionized dopants has been removed.

References

[1] B. E. Kane, L. N. Pfeiffer, and K. W. West, *Appl. Phys. Lett*. **67**, 1262 (1995).

[2] K. Park and J. K. Jain, *Phys. Rev. Lett*. **83**, 5543 (1999).

[3] L. Zheng, R. J. Radtke, and S. Das Sarma, *Phys. Rev. Lett*. **78**, 2453 (1997).

[4] N. Kumada, K. Muraki, and Y. Hirayama, *Science* **313**, 329 (2006).

[5] K. Hashimoto, K. Muraki, T. Saku, Y. Hirayama, *Phys. Rev. Lett*. **88**, 176601 (2002).

Appendix A
Sample Processing

The following is a description of the processes used to fabricate the samples described in this thesis. Other recipes and guidelines can be found in Ref [1], which is a good general reference for GaAs processing.

A.1 Dicing

The first step in preparing a sample usually consists of separating a small chip from the parent wafer. To cleave (or "dice") a chip from the parent wafer (usually 4 × 4 or 5 mm × 5 mm), place the wafer on a pad of clean paper and gently score along the top of the edge of the wafer at the spot where you wish to cleave using a scribe tool. Flip the wafer over (shiny side down -- avoid placing the wafer on GaAs particles, as this may scratch the surface) and roll the round end of the scribe across the score. A (100) oriented GaAs wafer will cleave nicely along the [110] and $[1\,\bar{1}0]$ directions.

A.2 Photolithography

Patterning of the 2DES sample can be done via standard photolithography. The sample surface is coated with a UV light-sensitive organic polymer and the area of the sample that one desires to pattern is then selectively exposed to UV light through a mask. After development, selected areas of the resist will be removed, defining a pattern of resist that can then be used to selectively etch or metallize the sample.

The following is a recipe for defining features > 1 μm using the Karl Suss MJB3 mask aligner with a Hg vapor lamp UV light source and the Clariant AZ5214E i-line resist. The AZ5214E resist is a positive resist, meaning that the exposed areas of resist will be removed (it can also be used as a negative resist by performing a post exposure bake and flood exposure before development).

1. Clean the sample surface. At a minimum, the sample should be allowed to soak in acetone for a few minutes, followed immediately by a rinse in methanol and then

in DI water. Blow dry immediately with dry nitrogen. The purpose of the methanol rinse is to avoid residues that can be left by allowing acetone to dry on the sample surface. Stubborn surface contamination can be removed by sonicating in a solvent, such as acetone.

2. Dry the sample before applying the resist. Baking the sample in an oven at 150º C for a half hour greatly improves the adhesion of the resist and is helpful for patterning of long, thin (< 10 μm) features.

3. (Optional) To improve resist adhesion apply a drop of HMDS and spin the sample at 3000 rpm for 30 sec.

4. Apply a drop of AZ5214E resist and spin at 5000 rpm for 30 sec. This gives a ~1.5 μm thick resist layer.

5. Soft bake for 45 sec. at 100º C on a hot plate.

6. Place the sample at the center of the mask aligner vacuum chuck and align the mask and sample. Raise the sample until the resist edge bead is barely touching the mask (look for the appearance of Newton's rings at at least three of the four corners of the sample). Expose for 15 sec. at an intensity of 15 mW/cm^2. The intensity at the sample position should be regularly measured using the stand-alone intensity meter.

7. For lift-off of fine metal features (< 10 μm), soak the sample in chlorobenzene for 10 min [2]. This changes the resist profile by hardening the top of the resist layer to make more of an undercut, which then prevents tearing during lift-off.

8. Develop in AZ400K developer:H20, 1:4. Start with about 45 sec. of development time, followed by rinsing in DI water. View the results using the mask aligner microscope, and repeat if necessary.

9. For subsequent etching, hard bake the resist by placing the sample on a hot plate for 60 sec. at 130º C.

10. After the subsequent etch or metallization is done, the resist can be removed by soaking in butyl acetate (do not use acetone to remove AZ5214E resist) for 15 min at 60º C.

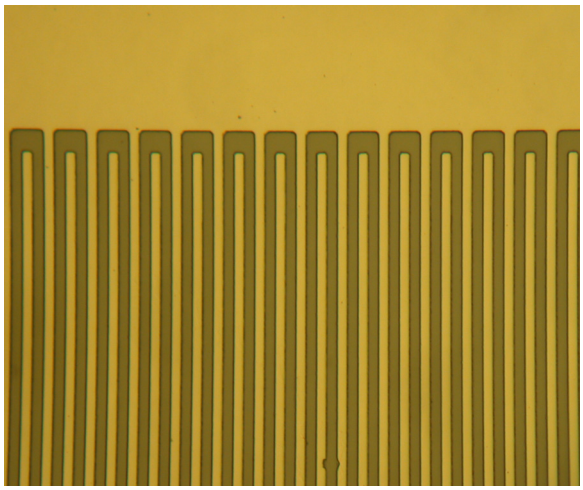

Fig. A.1. Surface acoustic wave transducer (see Chapter 2) with 6 μm wide aluminum fingers patterned via optical lithography.

Figure A.1 shows an example of an aluminum surface acoustic wave transducer on the surface of a 2DES sample patterned via photolithography.

A.2.1 Masks for Photolithography

There are three methods of creating masks for photolithography:

1. Order a mask from Berkeley Microlab. UC Berkeley offers a relatively cheap mask making service. The lab has a software package called "LinkCAD" that will convert an AutoCAD file into the GDSII file format that Berkeley will accept.

2. Transparency. For features > 30 μm, high-resolution film transparencies can be used to make a mask. A trip to a printshop may be necessary since it is best to use a 3000 dpi

printer[1]. Tape the transparency to a soda-lime glass plate of appropriate size for the mask aligner chuck. The exposure time may need to be increased to compensate for the poor transmission of the transparency film.

3. A mask can be written onto a metallized plate or glass cover slip using e-beam lithography.

A.3 Wet Etch

An isolated region of 2DES can be patterned using lithography and a GaAs etch, to remove the 2DES everywhere except in a select "mesa" region. One convenient recipe for a GaAs mesa etch uses a dilute phosphoric acid, hydrogen peroxide solution. For a ~ 0.1 μm/min. etch rate use H_2O:H_3PO_4:H_2O_2, 50:5:1. Remaining etch solution can be successfully stored for later use in an airtight bottle if kept in a refrigerator.

A.4 Metallization

We typically use aluminum gates and deposit the aluminum using a thermal evaporator. A thickness of 1000 – 2000 Å is good for achieving a continuous film with decent step coverage for depositing a continuous trace over the edge of a ~ 0.5 μm tall mesa. Problems can occur with the continuity of the metal at the mesa edge for taller mesas or thinner aluminum films.

1. Firmly clamp a tungsten basket into the center terminals of the evaporator.

2. Place two Al pellets (4 – 8 mm pellets, 99.999% pure) into the basket.

3. Pump down with the diffusion pump for ~ 1 hr. The bell jar pressure should reach ~10^{-7} Torr.

4. Use a power level of 30 – 35% and evaporate at a rate of ~ 20 Å/s.

---

[1] The printshop Mika Color (6000 Monterey Rd., Los Angeles, CA 90042, Ph: (323) 254-4116) has a high resolution printer and has experience making transparency masks both for our group and others at Caltech.

Patterning of the metal can be done either by a metal etch or a "lift-off" process. In the lift-off process, the chip is first coated with resist. Then, resist is removed via lithography in the regions where metal is desired. Next, metal is deposited. Finally, the remaining resist is removed with a resist stripping solvent. In regions where the metal is on top of resist, the metal will "lift-off", while regions without resist (bare GaAs) will remain metallized.

A.5 Ohmic Contacts

An ohmic contact is defined as an electrical contact that obeys Ohm's Law – the contact resistance is independent of bias. The two types of ohmic contacts employed in the devices described in this thesis are diffused NiAuGe and indium contacts.

In the case of NiAuGe contacts, the idea is to dope heavily enough with Ge (an *n*-type dopant) so that the metal/*n*-GaAs Schottky barrier becomes thin enough for electrons to tunnel [3]. The NiAuGe recipe typically gives lower contact resistances than the indium method. First evaporate 150 Å of Ni at ~6 Å/s; use a small tungsten boat. Then evaporate 1700 Å of AuGe (88:12 % by weight) eutectic at ~25 Å/s using a tungsten boat with an oxide barrier to prevent alloying of the boat with the AuGe. Empty the AuGe boat fully before re-using it, since the process of evaporating may change the ratio of Au:Ge. Anneal in forming gas, at 440 ºC for 15 min. Figure A.2 shows typical NiAuGe ohmics after thermal annealing. The roughness is due to balling up of the metal during the anneal.

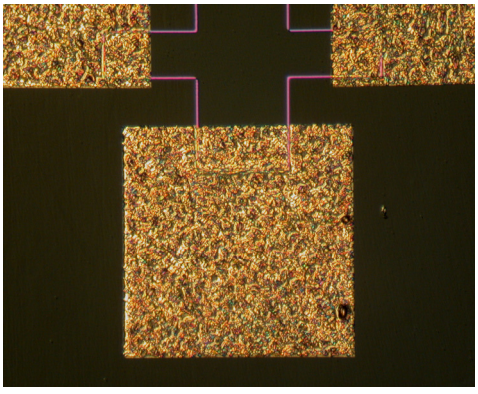

Fig. A.2. Annealed NiAuGe alloy making ohmic contact to a hall bar (2DES mesa boundary indicated by purple outline).

Indium is not an *n*-type dopant for GaAs. The indium contact is referred to as a "graded heterojunction type" contact. In this case, an InGaAs alloy is formed. InAs is a smaller band-gap semiconductor in which the Fermi level is pinned in the conduction band at the surface. The InAs surface makes contact to the *n*-GaAs through a graded heterojunction formed by a gradual change in Ga versus In content of the InGaAs alloy [4]. Indium contacts can be formed by diffusing In down to the 2DEG layer. Indium contacts are very convenient because they are simple to make. Place dots of In on the sample using a low-temp soldering iron (In melts at 157º C). Use a dedicated soldering tip used for In ohmic contacts only. Anneal the In contacts in the rapid thermal annealer (strip heater) in forming gas (to prevent oxidation) for 5 min. at 425º C. Flow forming gas for 5 min. before turning on the heater and leave the flow on until the strip has cooled to < 100º C. Set the forming gas flow to ~ 3 L/min. Figure A.3 shows a sample with annealed indium dots making ohmic contact to a hall bar-shaped 2DES.

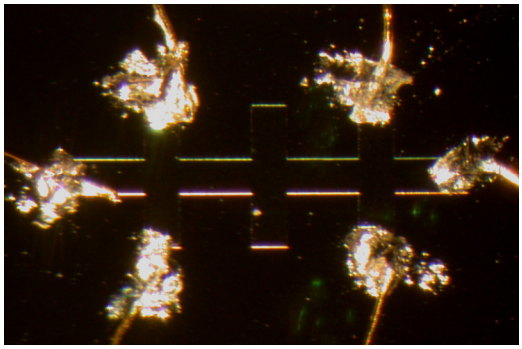

Fig. A.3. Annealed indium dots (also attached to gold wires), making ohmic contact to a 2DES hall bar mesa.

A.6 E-Beam Lithography

The lab has a JEOL 840A SEM for both imaging and e-beam writing of features down to ~ 50 nm. This procedure uses a bilayer of PMMA resists of differing molecular weights. A bilayer recipe is used rather than a single layer in order to achieve better lift-off.

1. Clean the sample as described in the optical lithography section.

2. Spin 6% 495k PMMA in chlorobenzene at 3000 rpm.
3. Bake on a hotplate at 180º C for 1 hr.
4. Spin 1.5% 950k PMMA in chlorobenzene at 7000 rpm.
5. Bake on a hotplate at 180º C for 1 hr.
6. Store sample in 70º C oven.
7. Load the sample into the SEM and pump down for ~ 30 min. Turn on the accelerating voltage and filament current and set probe current to desired value. Adjust the focus and astigmatism and let settle for ~ 30 min. Check probe current, focus, and astigmatism again. If stable, perform the e-beam exposure.
8. Develop 70 sec. in 3:1, isopropanol (IPA): methyl isobutyl ketone (MIBK). Rinse 10 sec. in IPA and blow dry with nitrogen.
9. After the subsequent etch or metallization is done, the resist can be removed by soaking in acetone at 60º C.

Write the e-beam pattern in DesignCAD and use the NPGS (Nabity Pattern Generation System) software to write the pattern. Work at an SEM acceleration voltage of 35 kV for the finest features.

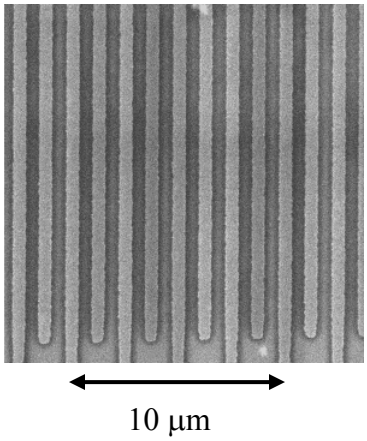

Fig. A.4. SEM image of SAW transducer with 0.6 μm wide aluminum fingers patterned using e-beam lithography. The entire transducer (not shown) is ~ 1 mm long.

E-beam writing takes some practice. The exposure dose has to be tweaked for each individual pattern due to exposure of nearby areas of the pattern due to secondary electrons (proximity effect). First read the online Nabity tutorial, which is very helpful, and try writing the pinwheel practice pattern, which will show if the focus and astigmatism have been correctly adjusted.

A.7 Packaging

For dc resistance measurements, the sample is mounted on a standard 18-pin DIP (dual inline package) plastic header. The chip is typically attached to the header surface using vacuum grease or thermal paste. As shown in Fig. A.5, gold wires, 0.001 – 0.002" in diameter, are used to connect the header pins to the sample gates and ohmics. The wires are attached to the sample via indium solder joints, wire bonding, or conducting epoxy. It is strongly suggested that conducting epoxy be used only for gates. Epoxy connections can sometimes become very resistive over time, creating problems when used for connections to ohmic contacts.

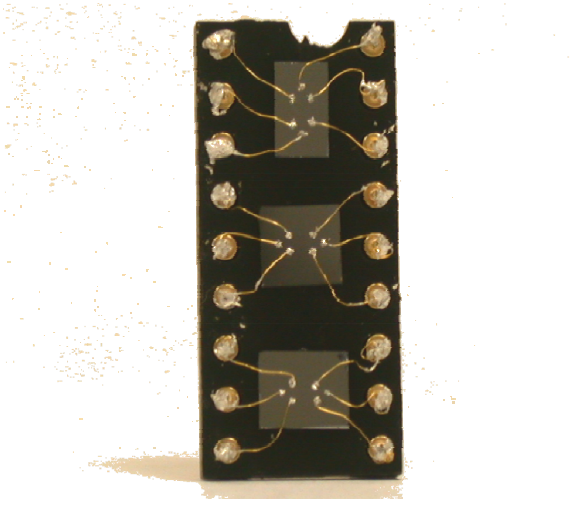

Fig. A.5. 2DES samples attached and wired to 18-pin DIP header with gold wires.

References

[1] Ralph Williams. *Modern GaAs Processing Methods*. Artech House, Boston 1990.

[2] M. Hatzakis *et al*. IBM J. Res. Develop. **24**, 452 (1980).

[3] N. Braslau, J.B. Gunn and J.L. Staples, *Solid State Electron*. **10**, 381 (1967).

[4] J.M. Woodall, J.L. Freeouf, G.D. Pettit, T. Jackson and P. Kirchner, *J. Vac. Sci. Technol.* **19**, 626 & 794 (1981); A.A. Lakhani, *J. Appl. Phys*. **56**, 1888 (1984).

Appendix B
Heat Sinking of RF Leads

B.1 Overview

The following is an overview of the RF leads installed in the lab cryostats.

B.1.1 ^{3}He Cryostat

In one of the inserts for the ^{3}He immersion cryostat ("stick B"), there are two CuBe UT-34 (Ag-plated inner conductor) semi-rigid coax from room temperature to the sample stage. There is an OFHC copper clamp which thermally sinks the coax to the insert 1 K cone (which mates with the 1 K pot).

B.1.2 Dilution Unit

The 200TL and Kelvinox 25 dilution refrigerators also have two RF leads, but with multiple heat sinks and thermal lags, as shown in Fig. B.1. RF connections are made with SMA connectors (ideally good up to 26 GHz). Connectors for UT-34 cable (a somewhat unusual size) can be purchased from Huber-Suhner. The 4 K clamp heat sink is simply two plates of OFHC copper with grooves which firmly sandwich the coax. A detailed discussion of the performance of the microstrip heat sinks and various coaxial segments follows. Some of the choices for the type of coax used for different segments were not necessarily driven by performance, but instead by what coax and connectors were on hand in lab or what was previously installed.

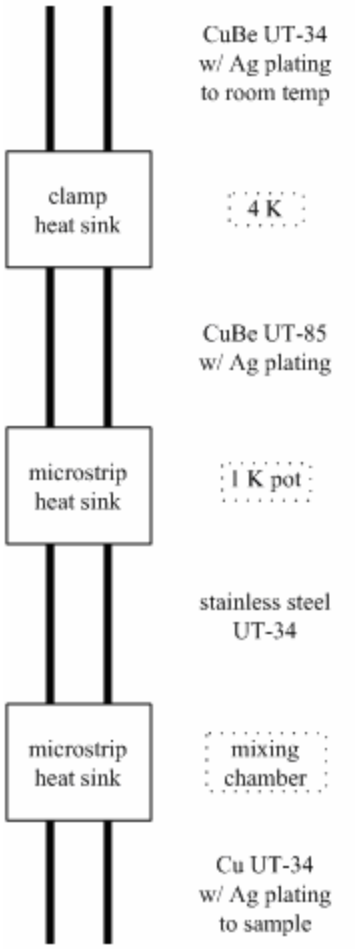

Fig B.1. RF connections and heat sinking in 200TL dilution refrigerator (not to scale). (Kelvinox 25 dilution unit installation is similar)

B.2 Semi-Rigid Cryogenic Coax

Many material choices for coax are available, including Cu, CuBe alloy, stainless steel, and Nb superconducting. The inner conductor is frequently silver-plated for lower loss at high frequencies. Common cable sizes for low-temperature application are UT-34 and UT-85. For each material and size choice, there is a trade-off between good signal transmission and low thermal conductivity.

CuBe UT-34 w/ Ag plating was used for most leads except in cases where the thermal conductivity had to be very low, in which case stainless steel UT-34 without Ag plating was used. Figure B.2 indicates the dimensions for UT-34 coax.

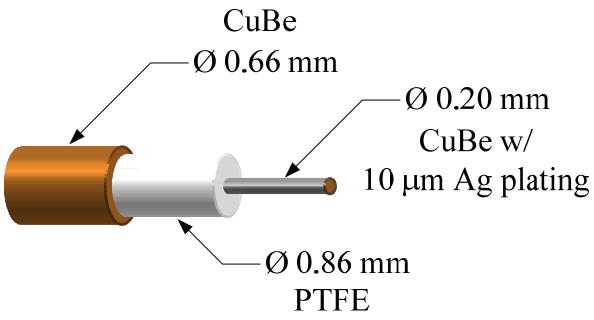

Fig. B.2. CuBe semi-rigid cable with silver-plated inner conductor. UT-34 coax is 0.034" (0.86 mm) in outer diameter.

B.2.1 RF Transmission

The role of the silver plating becomes important for RF transmission at frequencies above ~ 1 MHz. For good conductors ($\sigma >> \varepsilon\omega$) the RF skin depth is

$$\delta = \sqrt{\frac{2}{\omega\mu\sigma}}.$$

For Ag with a conductivity of 10^{10} /Ω·m at $T = 4$ K, $\delta \approx 10\,\mu\text{m}/\sqrt{f(\text{MHz})}$. The measured RF insertion loss at $T = 4$ K is 2 dB/GHz·m for CuBe UT-34 w/ Ag-plated inner conductor, and 9 dB/GHz·m for 304 stainless UT-34.

B.2.2 Thermal Performance

Heat load

It is useful to first calculate roughly what the heat load will be assuming the heat sinking is successful. The thermal conductivity of metals at low temperature (T < 10 K) is typically dominated by conduction electrons rather than phonons. This leads to a thermal conductivity which is proportional to kT, so that $\kappa = \kappa_0 T$, which results in a heat load given by

$$\dot{Q} = \frac{A\kappa_0}{2L}(T_2^2 - T_1^2),$$

where A is the cross-sectional area, L is the length, and T_1 and T_2 are the temperatures at the conductor endpoints.

1 K Pot Heat Sink

The segment of coax from 4 K to ~ 1 K is CuBe UT-85 (0.086" outer diameter) coax with Ag-plating on the inner conductor. The heat load at the 1 K pot heat sink will be

$$\dot{Q} = \frac{(A_{CuBe}\kappa_{0\_CuBe} + A_{Ag}\kappa_{0\_Ag})}{2L}(T_2^2 - T_1^2),$$

where the diameter of the inner conductor is 0.51 mm, κ_{0_CuBe} = 0.6 W/K·m, the thickness of the silver plating is ~ 10 μm, κ_{0_Ag} = 10 W/K·m, and L ~ 10 cm. Then, $\dot{Q} = 100\ \mu$W. This should be fine for the 1 K pot stage.

Mixing chamber

Stainless steel UT-34 coax without silver plating was used for the link from 1 K to the mixing chamber because CuBe UT-34 w/ Ag-plating would have created a heat load of several μW. The dimensions of this segment of coax are the same as for the CuBe UT-34 depicted in Fig. B.2. For the stainless steel coax,

$$\dot{Q} = \frac{(A_{SS}\kappa_{0\_SS})}{2L}(T_2^2 - T_1^2),$$

where κ_{0_SS} = 0.1 W/K·m, and L ~ 10 cm. Then $\dot{Q} = 0.2\ \mu$W.

Heat sinking of the inner conductor

The coaxial PTFE insulator should provide a thermal link between the inner and outer conductor. However, there is a possibility that the thermal connection between the PTFE and outer conductor is poor at low temperature due to the mismatched thermal contraction of PTFE versus CuBe or stainless steel. As discussed next, better heat sinking of the inner conductor was done using microstrip heat sink units.

B.3 Microstrip Heat Sinks

Heat sinking of the inner conductor at temperatures below 1 K was done with microstrip transmission line heat sinks. The heat sink unit consists of an OFHC copper box containing a microstrip line fabricated from Sheldahl copper-laminated Kapton (Kapton is a polyimide film made by DuPont). The microstrip copper ground plane is lead-tin soldered to the bottom of the box. In hindsight, the thermal connection between the copper backing and bottom of the box should probably have been done differently due to the fact that PbSn goes superconducting at low temperatures, and thus has poor thermal conductivity. Figure B.3 shows the typical dimensions of one of these heat sink units.

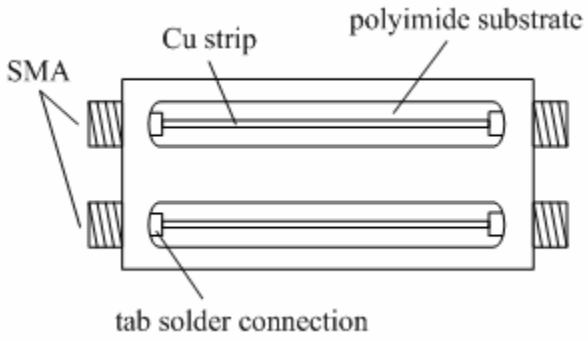

Fig B.3. Microstrip heat sink unit (lid not shown). Box dimensions: 2 cm × 4 cm. Stripline: 0.04 mm thick, ~ 0.6 mm wide copper strip on 0.16 mm thick polyimide.

Thermal Performance

Figure B.4 shows a sketch of the coordinates and variables used to calculate the heat flow through the Cu-polyimide-Cu laminate.

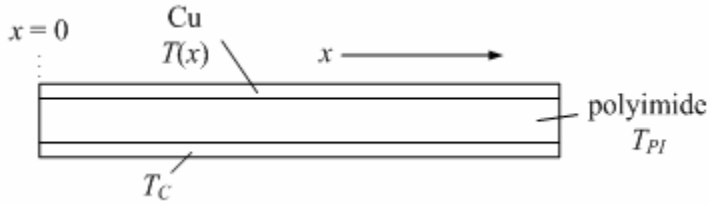

Fig. B.4. Cu-polyimide-Cu laminate. $T(x)$ is the temperature of the top copper strip, as a function of position x, T_{PI} is the temperature of the polyimide, and T_C is the temperature of the copper back plane.

The heat flow from the top copper strip through the polyimide to the back plane is given by

$$d\dot{Q} = \kappa_{PI} \frac{w}{t_{PI}} (T_C - T(x)) dx ,$$

where κ_{PI} is the thermal conductivity of the polyimide, w is the width of the strip, and t_{PI} is the polyimide thickness. The heat flow down the top copper strip is given by

$$\dot{Q} = (w t_{Cu}) \kappa_{Cu} \frac{dT(x)}{dx} ,$$

where κ_{Cu} is the thermal conductivity of the copper and t_{Cu} is the copper thickness.

1 K pot heat sink

We assume that the outer body of the heat sink, which is soldered to the laminate back plane, is at T_C = 1 K. For a worst case scenario, we use the 1 K value for κ_{PI} ~ 7 mW/K·m [2] and the 4 K value for κ_{Cu} ~ 200 W/K·m (RRR ~ 40). Then,

$$\kappa_{PI} \frac{w}{t_{PI}} (1\,\mathrm{K} - T(x)) = (w t_{Cu}) \kappa_{Cu} \frac{d^2 T(x)}{dx^2} .$$

The solution for $T(x)$ will decay exponentially with a characteristic length

$$\lambda = \sqrt{t_{Cu} t_{PI} \frac{\kappa_{Cu}}{\kappa_{PI}}} \sim 0.7 \text{ cm.}$$

So, for the inner conductor to reach T ~ 1 K, a heat sink length greater than about a centimeter should be sufficient.

Mixing chamber heat sink

Assume that the outer body of the heat sink is at T_C = 25 mK. For a worst case scenario, we use the 25 mK value for κ_{PI} ~ 160 μW/K·m [2] and the 1 K value for κ_{Cu} ~ 50 W/K·m. Then, λ ~ 2.2 cm. In actuality, κ_{Cu} and κ_{PI} are proportional to temperature, so the performance will be better than this simple estimate.

As a final note, the experiments described in this thesis (surface acoustic wave and NMR measurements) do not require a direct connection between the RF leads and the 2DES. In these experiments, the RF is applied to the 2DES via a transducer or coil situated near the 2DES. It is not actually experimentally known whether the 2DES would reach the lowest cryostat temperatures if the RF leads were directly connected to the 2DES via ohmic contacts.

RF Transmission

Next, we estimate the performance of the microstrip transmission line width dimensions shown in Fig. B.5.

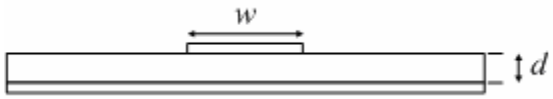

Fig. B.5. Microstrip transmission line of width *w* and dielectric thickness *d*.

For a lossless microstrip line with $W/d \geq 1$ the characteristic impedance is given by [3]

$$Z_0 = \frac{120\pi}{\sqrt{\varepsilon_e}\left[W/d + 1.393 + 0.667\ln(W/d + 1.444)\right]},$$

where

$$\varepsilon_e = \frac{\varepsilon_r + 1}{2} + \frac{\varepsilon_r - 1}{2}\frac{1}{\sqrt{1 + 12d/W}}$$

is the effective dielectric constant (ε_r is the relative dielectric constant of the substrate).

For $W/d \sim 3$, $Z_0 \sim 50$ and is approximately matched to the rest of the lines. However, for fabrication ease, the strip was made slightly wider, but still less than 1 mm ($W/d \sim 6$). Figure B.6 shows that for a 3 cm long heat sink, the loss due to the wider strip is less than 1 dB for frequencies below 1 GHz.

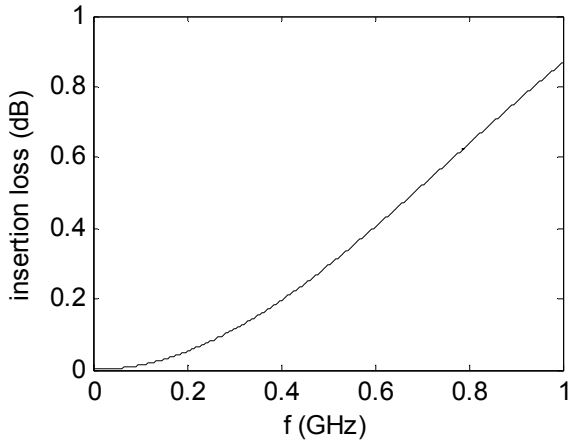

Fig. B.6. Calculated insertion loss due to a 3 cm long microstrip with 1 mm wide metalization on 0.16 mm thick polyimide substrate.

The copper metallization thickness should not be an issue for loss at frequencies above 1 MHz. For a Cu strip with a low temperature conductivity of $\sim 10^9$ /Ω·m, the skin depth is $\delta \sim 10\ \mu\text{m}/\sqrt{f(\text{MHz})}$, which is comparable to the 40 μm laminate thickness at MHz frequencies. Measurements of the insertion loss of a typical microstrip heat sink unit yield 0.16 dB/GHz, which corresponds to a strip width of ~ 0.6 mm, which is in reasonable agreement with the actual strip dimensions.

References

[1] Pobell, F. *Matter and Methods at Low Temperatures*, *2nd ed*. Springer, 1996.

[2] Barucci M., Gottardi E., Peroni I., Ventura G. *Cryogenics* **40**, 145 (2000).

[3] Pozar, D. *Microwave Engineering*, *2nd ed*. Wiley, 1998.

Appendix C
SAW's in GaAs

C.1 SAW's in GaAs

We first present an overview of SAW's in GaAs and their coupling to a 2DES. The experiments described in this thesis used SAW's propagating in the [110] or [$1\bar{1}0$] crystalline direction on the surface of devices grown on (100) oriented wafers.

C.1.1 Piezoelectricity in GaAs

GaAs is a piezoelectric material, meaning that applying an electric field to the material will create strain and application of stress will change the electric polarization. The crystalline structure of GaAs is shown in Fig C.1.

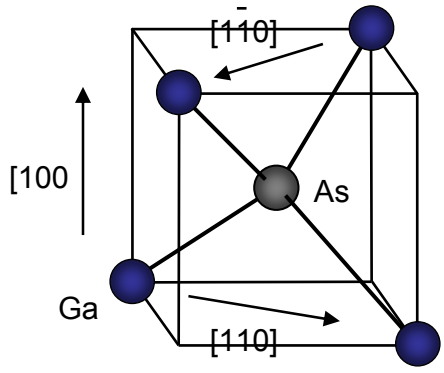

Fig. C.1. GaAs unit cell (zinc-blende structure).

The electric polarization generated in response to strain is described by the piezoelectric tensor e_{ij}, defined by $D_i = e_{ij}S_j + \varepsilon E_i$, where D_i is the electrical displacement ($D_i = 0$ for the case of no free charge), ε is the dielectric constant, S_j is the strain, and E_i is the electric field. The stress generated by application of an electric field is given by $T_i = c_{ij}S_j - e_{ji}E_j$, where T_i is the stress and c_{ij} is the elastic stiffness tensor. For GaAs the piezoelectric tensor is

$$e_{ij} = \begin{pmatrix} 0 & 0 & 0 & e_{14} & 0 & 0 \\ 0 & 0 & 0 & 0 & e_{14} & 0 \\ 0 & 0 & 0 & 0 & 0 & e_{14} \end{pmatrix},$$

where i = 1 to 3 with $1 \equiv x_1, 2 \equiv x_2$, and $3 \equiv x_3$, and j = 1 to 6 with $1 \equiv x_1x_1$, $2 \equiv x_2x_2$, $3 \equiv x_3x_3$, $4 \equiv x_2x_3$, $5 \equiv x_3x_1$, $6 \equiv x_1x_2$, where $x_1 \equiv [100]$, $x_2 \equiv [010]$, $x_3 \equiv [001]$. The value of e_{14} is approximately 0.16 C/m^2. For example, for a pure shear strain of only S_6 nonzero (elongation along the [110] direction and contraction along $[1\,\bar{1}0]$) will give rise to an electric polarization in the $[00\,\bar{1}]$ direction, where a strain of ~ 10^{-3} produces a polarization of ~ ε × 10^4 V/cm.

C.1.2 Surface Acoustic Waves

Surface acoustic waves (SAW's) are elastic waves which propagate at the surface of an elastic body, where most of the energy density of the wave is confined to a depth of about one wavelength below the surface. From Newton's and Gauss's Laws, the equations describing SAW propagation in a piezoelectric material are

$$\rho \frac{\partial^2 u_j}{\partial t^2} = c_{ijkl} \frac{\partial^2 u_k}{\partial x_l \partial x_i} + e_{kij} \frac{\partial^2 \phi}{\partial x_k \partial x_i}, \tag{1}$$

and

$$\varepsilon \nabla^2 \phi = e_{ijk} \frac{\partial^2 u_j}{\partial x_i \partial x_k}, \tag{2}$$

where $u_i(\vec{x})$ is the displacement of the solid from equilibrium at position $\vec{x}$, ρ is the density, c_{ijk} is the elastic stiffness tensor, and ϕ is the electric potential. For convenience, we have temporarily switched to a notation which uses the full 3×3×3 tensor for the elastic and piezoelectric constants (three indices), rather than the abbreviated 3×6 matrix form used in section C.1.1. For GaAs, because the piezoelectric coupling is weak ($e_{ijk}^2/\varepsilon << c_{ijk}$), the last term in Eq. (1) can be ignored when solving for the motion of the elastic wave. Then

$$\rho \frac{\partial^2 u_j}{\partial t^2} = c_{ijkl} \frac{\partial^2 u_k}{\partial x_l \partial x_i}. \tag{3}$$

For a cubic crystal this gives

$$\rho\frac{\partial^2 u_i}{\partial t^2} = c_{11}\frac{\partial^2 u_i}{\partial^2 x_i} + c_{44}\sum_{j\neq i}\frac{\partial^2 u_i}{\partial^2 x_j} + (c_{12}+c_{44})\sum_{j\neq i}\frac{\partial^2 u_j}{\partial x_i \partial x_j}. \tag{4}$$

Consider an infinitely large slab of GaAs occupying all space for $x_3 < 0$, and vacuum for $x_3 > 0$. We look for solutions that describe a surface wave propagating in the [110] direction:

$$\vec{u} = \left(\frac{1}{\sqrt{2}}(\vec{u}_1 + \vec{u}_2)A + \vec{u}_3 B\right)\exp\left[ik_{[110]}\frac{1}{\sqrt{2}}(x_1+x_2) + k_3 x_3 - iv_s t\right], \tag{5}$$

where v_s is the SAW velocity and $\vec{u}_i$ are unit vectors. We also require $k_{[110]}$ real and $\mathrm{Re}[k_3] > 0$ so that the wave amplitude decays in the bulk.

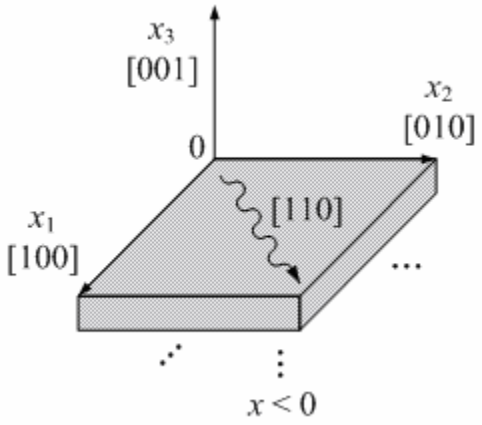

Fig. C.2. SAW propagation in [110] direction on GaAs (001) surface.

After substitution we find that

$$\begin{aligned} A\left(\rho v_s^{\,2} - c'_{11} + c_{44}q^2\right) - iBq\left(c_{12}+c_{44}\right) &= 0, \\ -iAq\left(c_{44}+c_{12}\right) + B\left(\rho v_s^2 - c_{44} + q^2 c_{11}\right) &= 0, \end{aligned} \tag{6}$$

where $q \equiv k_3 / k_{[110]}$ and $c'_{11} \equiv (c_{11}+c_{12}+2c_{44})/2$. The full solution will be a linear combination of solutions of the form of Eq. (5) that satisfy our boundary conditions. The boundary conditions are that the GaAs surface at $x_3 = 0$ is stress free:

$$c_{3jkl}\frac{\partial u_k}{\partial x_l}=0 \text{ at } x_3=0. \tag{7}$$

After substitution and some algebra,

$$\begin{aligned} ic_{12}\sum A_n - c_{11}\sum q_n B_n &= 0, \\ -\sum A_n q_n + i\sum B_n &= 0, \end{aligned} \tag{8}$$

where the subscript n = 1,2 indicates the two linearly independent solutions to Eq. (4). For GaAs the elastic moduli are

$$\begin{Bmatrix} c_{11}=11.877 \\ c_{12}=5.372 \\ c_{44}=5.944 \\ c'_{11}=14.569 \end{Bmatrix}\times 10^{10} \text{ Pa},$$

and ρ = 5316.9 kg/m^3. This gives a SAW velocity of v_s = 2860 m/s. The solution for the elastic displacement is

$$\begin{aligned} \vec{u} = U\left[\left(\frac{1}{\sqrt{2}}(\vec{u}_1+\vec{u}_2)+\vec{u}_3\lambda_+\right)\exp\left(k_{[110]}q_+x_3\right)+R\left(\frac{1}{\sqrt{2}}(\vec{u}_1+\vec{u}_2)+\vec{u}_3\lambda_-\right)\exp\left(k_{[110]}q_-x_3\right)\right] \\ \times\exp\left(ik_{[110]}\frac{1}{\sqrt{2}}(x_1+x_2)-iv_st\right), \end{aligned} \tag{9}$$

where $q_\pm = 0.50013 \pm 0.47991i$, $\lambda_\pm = \pm 1.15414 + 0.67737i$, $R = -0.50617 + 0.86243i$, $\vec{u}_i$ are unit vectors, sand U is the wave amplitude.

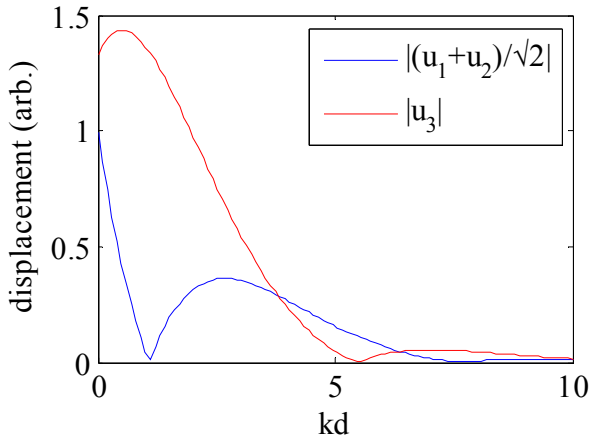

Fig. C.3. Depth dependence of magnitude of elastic displacement, where d is the distance below the GaAs surface and $k = k_{[110]}$.

Next, we can substitute into Eq. (2) to find the piezoelectric potential created by the elastic wave:

$$\begin{aligned}\varepsilon\nabla^2\phi &= e_{14}\sum_{i\neq j\neq k}\frac{\partial^2 u_i}{\partial x_j \partial x_k} \\ &= e_{14}k^2U\left[a_+\exp\left(kq_+x_3\right)+Ra_-\exp\left(kq_-x_3\right)\right]\exp\left(ik(x_1+x_2)/\sqrt{2}\right),\end{aligned} \tag{10}$$

where $a_\pm \equiv i(2q_\pm - \lambda_\pm)$. We try a solution of the form

$$\phi = \left[\phi_0\exp(kx_3)+\phi_+\exp(kq_+x_3)+\phi_-\exp(kq_-x_3)\right]\exp\left(ik(x_1+x_2)/\sqrt{2}\right).$$

Upon substitution into Eq. (10) we find that $\phi_+ \equiv (e_{14}/\varepsilon)Ua_+/(q_+^2-1)$ and $\phi_- \equiv (e_{14}/\varepsilon)URa_-/(q_-^2-1)$. Next, we use the boundary conditions that the normal component of the electric displacement and the electric potential are continuous at $x_3 = 0$. For $x_3 > 0$, the potential will be of the form $\phi = \phi_a\exp(-kx_3)$. Then, at $x_3 = 0$

$$\begin{aligned}D_3 &= \varepsilon\frac{\partial\phi}{\partial x_3}+e_{14}\left(\frac{\partial u_1}{\partial x_2}+\frac{\partial u_2}{\partial x_1}\right) \\ &= -k_{[110]}\varepsilon_0\phi_a\exp\left(ik(x_1+x_2)/\sqrt{2}\right) \\ &= \left[\varepsilon\left(\phi_0+q_+\phi_++q_-\phi_-\right)+ie_{14}(1+R)\right]k_{[110]}\exp\left(ik(x_1+x_2)/\sqrt{2}\right)\end{aligned}$$

and

$$\phi_a = \phi_0 + \phi_+ + \phi_- .$$

So

$$\phi_0 = -\frac{\phi_+(\varepsilon_0 + q_+\varepsilon) + \phi_-(\varepsilon_0 + q_-\varepsilon) + ie_{14}(1+R)}{(\varepsilon + \varepsilon_0)}.$$

The resulting form of the potential is shown below in Fig. C.4.

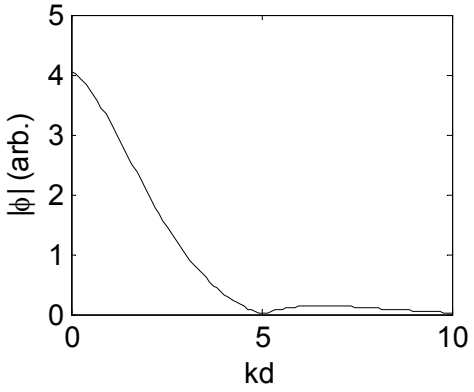

Fig. C.4. Depth dependence of the magnitude of the piezoelectric potential.

C.1.3 SAW interaction with a 2DES

The electric potential created by the SAW will be screened by a 2DES located near the GaAs surface. This screening will affect both the velocity and amplitude of the SAW. The resulting attenuation and velocity shift are given by [1]

$$\Gamma = k_{[110]} \frac{K_{eff}^2}{2} \frac{\sigma/\sigma_M}{1+(\sigma/\sigma_M)^2}, \tag{11}$$

$$\frac{\Delta v_s}{v_s} = \frac{K_{eff}^2}{2} \frac{1}{1+(\sigma/\sigma_M)^2}, \tag{12}$$

where Γ is the attenuation per unit length, K_{eff}^2 is a piezoelectric coupling coefficient, σ is the electron gas conductivity, and σ_M is a characteristic conductivity ~ 3.3×10^{-7} Ω^{-1}.

The velocity change $\Delta v_s \equiv v_s(\sigma) - (\sigma \gg \sigma_M)$ is referenced to the SAW velocity in the presence of a perfect conductor ($\Delta v_s \to 0$ as $\sigma \to \infty$).

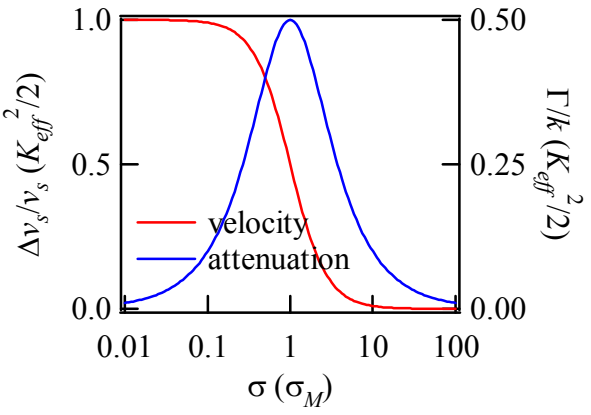

Fig. C.5. Dependence of SAW attenuation and velocity shift on 2DES conductivity from Eq. (11) and (12).

For conductivities below σ_M, the amplitude and velocity of the SAW are unaffected by the 2DES and propagate as in bulk GaAs. As shown in Fig. C.5, for conductivities comparable to or greater than σ_M, the screening of the piezoelectric potential causes attenuation and a decrease in the SAW velocity. The value of σ_M can be crudely understood by considering the capacitive charging of the 2DES. Consider a square patch of 2DES of area λ^2, where λ is the SAW wavelength. To screen the piezoelectric potential, the charge on this patch must be rearranged to match the SAW potential. If we set the RC time constant for this charging equal to the SAW period, λ/v_s, we find that $R \sim 1/\varepsilon v_s \sim 1/\sigma_M$.

The form of the σ dependence of $\Delta v/v$ given by Eq. (12) can be roughly understood using a similar RC-circuit argument. The SAW fractional velocity shift is equal to the electrostatic energy required to charge the 2DES divided by the elastic energy of the SAW. When a SAW enters a region containing a 2DES, some of the elastic energy of the wave is given up in order to charge the 2DES. This results in a reduction of the wave velocity. As in the previous paragraph, consider a square patch of 2DES of area λ^2, where the charge on this patch will be rearranged to try to screen the SAW potential. The charging energy will be proportional to V^2, where V is the capacitive charging voltage. This charging voltage will depend on the conductivity of the 2DES, where

$V = V_{SAW}\left(1/i\omega C\right)/\left(\left(1/i\omega C\right)+R\right)$ and R and C are an effective resistance and capacitance and V_{SAW} is the SAW potential. This gives $\left(V/V_{SAW}\right)^2 \sim 1/\left(1+\left(R\omega C\right)^2\right)$. Now, in Eq. (12) the velocity shift is referenced so that $\Delta v/v = 0$ for a perfect conductor ($R = 0$). Thus, we set $\Delta v/v \sim 1-\left(V/V_{SAW}\right)^2 = 1/\left(1+1/\left(R\omega C\right)^2\right)$. As argued in the previous paragraph, $1/R\omega C = \sigma/\sigma_M$, so that we have $\Delta v/v \sim 1/\left(1+\left(\sigma/\sigma_M\right)^2\right)$.

The precise value of K_{eff}^2 and σ_M depend on kd, due to the kd dependence of ϕ and the effective dielectric constant ε_{eff}. Simon [2] has analyzed the 2DES – SAW interaction and shown that

$$\frac{K_{eff}^2}{2} = \frac{\varepsilon_{eff}}{4\pi H}\left|\frac{\phi}{C}\right|^2, \tag{13}$$

where C is the amplitude of the SAW, H is a material dependent constant, and

$$\frac{1}{\varepsilon_{eff}} = \frac{1}{\varepsilon}\left[1+\left(\frac{\varepsilon-\varepsilon_0}{\varepsilon+\varepsilon_0}\right)e^{-2kd}\right].$$

The value of σ_M is proportional to ε_{eff} and is shown in Fig. C.6.

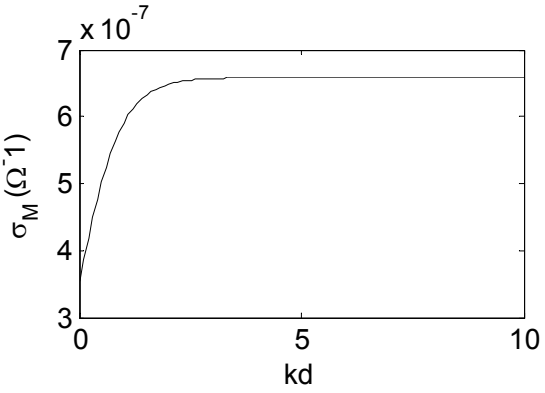

Fig. C.6. Variation of σ_M with kd.

$K_{eff}^2/2$ is basically the ratio of the capacitive charging energy of the 2DES, when its conductivity is infinite so that the piezoelectric potential is completely screened, to the elastic energy of the SAW. The kd dependence of $K_{eff}^2/2$ is shown below in Fig. C.7. The value of $H = 3.624 \times 10^{11}$ J/m^3 in Eq. (13) was obtained by calculating the SAW elastic energy per unit area. This gives a piezoelectric coupling constant of $K_{eff}^2/2 = 2.2 \times 10^{-4}$ at $kd = 0$. This is a reasonable value, considering that the experimental value for

$K_{eff}^2/2$ in GaAs/AlGaAs heterostructures is ~ 3.2 × 10^{-4} [1, 2], where the piezoelectric constant $e_{14} \sim 0.26$ C/m^2 for AlAs is slightly larger than for GaAs.

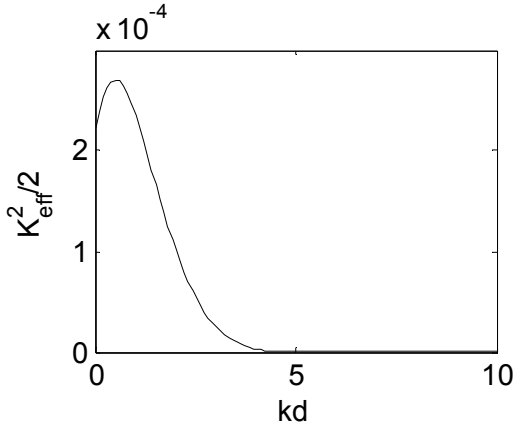

Fig. C.7. Variation of K_{eff}^2 with *kd*.

C.1.4 Interaction in the Presence of a Gate

The presence of a top gate on the GaAs surface, above the 2DES in the region of SAW propagation can have a strong effect on the 2DES-SAW interaction. The value of both ε_{eff} and K_{eff}^2 will be modified.

The modified effective dielectric constant leads to a different σ_M dependence on *kd*:

$$\sigma_M = 2v\varepsilon_{eff}$$

where

$$\frac{1}{\varepsilon_{eff}} = \frac{1}{\varepsilon}\left[1 - e^{-2kd}\right].$$

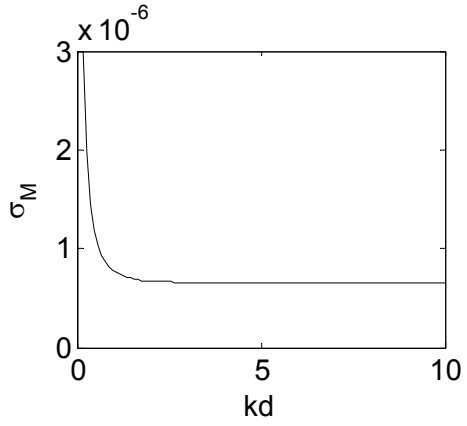

Fig. C.8. σ_M vs *kd* in the presence of a highly conductive top gate.

And, solving for the SAW piezoelectric potential with the new boundary conditions gives the *kd* dependence shown in Fig. C.9.

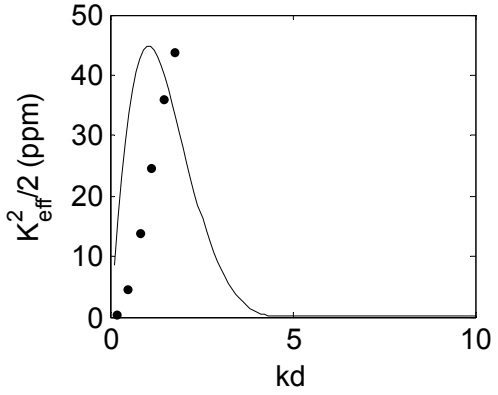

Fig. C.9. $K_{eff}^2/2$ vs. *kd* in the presence of a highly conductive top gate. The solid line is the calculated coupling and the points are experimental SAW velocity shift data (see text).

The solid data points in Fig. C.9 correspond to experimental SAW velocity shift data from SAW propagation in a GaAs/AlGaAs heterostructure with a 2DEG 0.6 μm below a top gate. $K_{eff}^2/2$ was experimentally determined by measuring the SAW velocity difference for a highly conducting 2DEG versus a completely depleted 2DEG (zero conductivity), at several wavevectors corresponding to the harmonics of the SAW transducers. It is unclear why there is a mismatch between experiment and theory, but we note that one source of the discrepancy may be due to the fact that the calculated curve is for a SAW in bulk GaAs, not a GaAs/AlGaAs heterostructure.

C.2 Transducer design

The surface acoustic wave experiments performed in this thesis used aluminum interdigitated SAW transducers created either via optical or e-beam lithography (see appendix A for fabrication information). A sketch of a generic interdigitated transducer is shown in Fig. C.10. An RF voltage is applied between the two sets of fingers and the normal component of the electric field causes a strain that generates a SAW of wavelength $\lambda = 2(a+b)$ (see Fig. C.10).

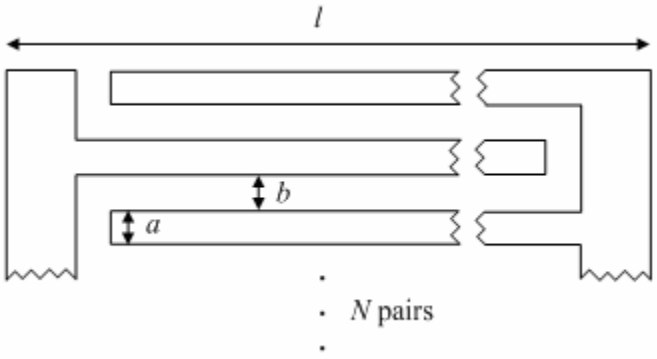

Fig. C.10. Interdigitated SAW transducer of length *l*, finger width *a*, finger spacing *b*, and *N* finger pairs.

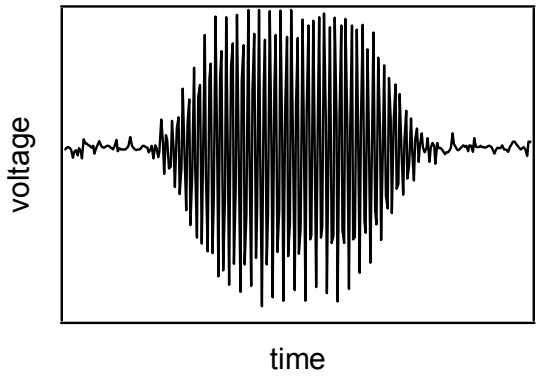

Fig. C.11. Output transducer voltage vs. time for a ~300 ns pulse at 72 MHz.

Fig. C.11 shows a typical SAW pulse after detection by the output transducer and amplification. The pulse shape is determined by the transducer width in the direction of SAW propagation $2(a+b)N$ and the SAW velocity. The duration of the triangular

envelope at the start and end of the pulse is given by the time required for a SAW to propagate across the transducer width.

C.2.1 Frequency response

The frequency response of an interdigitated SAW transducer is roughly given by the Fourier transform of the normal electric field E_3 at the GaAs surface. As a first approximation, consider infinitely thin fingers so that we take the Fourier transform of a periodic array of delta functions separated by a distance b. Then

$$E_3 \propto \sum_{n=1}^{2N} \delta(x - bn)(-1)^n .$$

The wavevector response (transfer function) is then

$$H(k) \propto \sum_{n=1}^{2N} e^{-ikbn} .$$

For large N and near resonance ($k = \pi/2b$), the frequency response is a sinc function:

$$H(f) \propto \left| \frac{\sin\left[N\pi(f - f_0)/f_0\right]}{N\pi(f - f_0)/f_0} \right| .$$

Thus, the transducer resonance width $\propto 1/N$. We can see how well this model works for the frequency response of a pair of transducers (a transmitting and receiving transducer) shown in Fig. C.12. Because there are two transducers, we use the square the frequency response for a single transducer. From the above expression we then expect the FWHM to be about 6.4 MHz. The value extracted from Fig. C.12 is about 7.9 MHz, which is reasonably close to our calculated estimate.

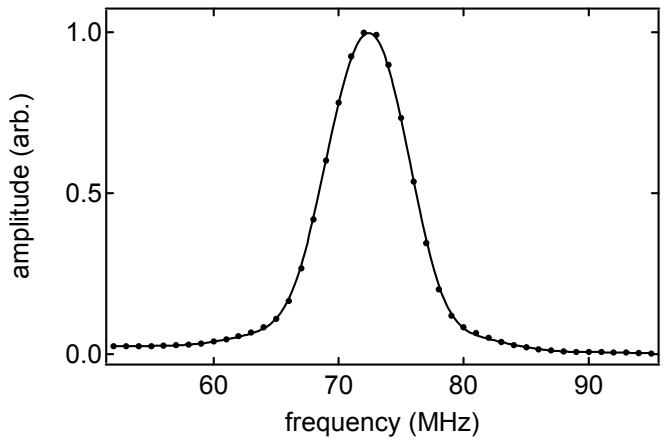

Fig. C.12. Measured frequency response for a pair of input and output transducers with 10 finger pairs with finger width and spacing $a \sim b = 10$ μm. Solid line is guide to the eye.

Although this simple delta function modeling gives a basic understanding, it fails to predict important features of transducers with finite finger width, such as the transducer harmonic response. The relative amplitudes of the various harmonics for an actual transducer have been calculated in Ref. [3]. For example, for equal finger width and spacing, $a = b$, the 1st, 5th, and 9th harmonics have relative amplitudes of 1, 0.5, and 0.4 respectively (the 3rd and 7th harmonics have zero amplitude).

C.2.2 Transducer impedance

The impedance of a typical SAW transducer was calculated using an EM solver (Sonnet). In the 0.1 – 1 GHz frequency range, the transducer basically looks like a capacitor. For example, a 1 mm long transducer with 5 μm wide fingers and 20 finger pairs looks like a 2 pF capacitor. It is useful to compare the reactance of the transducer to the input transmission line impedance (50 ohms) in order to find the voltage that is actually across the transducer fingers. Fig. C.13 shows the voltage at the transducer for an input voltage out of the RF source of 1 V. For this transducer, above about 1 GHz (where $1/\omega C \sim 50$ ohms), the transducer impedance begins to matter.

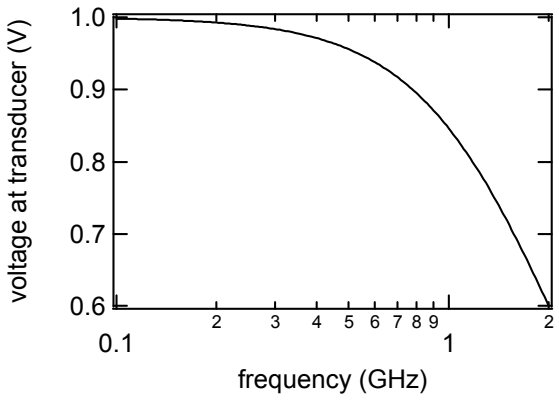

Fig. C.13. Voltage across SAW transducer (1 mm long, 5 μm wide fingers, 20 finger pairs) for a frequency generator output of 1 V.

C.2.3 Transducer efficiency

It is possible to estimate the expected efficiency of a pair of input and output SAW transducers using the dimensions of the transducer and the value for K_{eff}^2:

$$\text{total insertion loss} \approx -20\log_{10}\left[8\times(100\Omega)N^2K_{eff}^2C_pf_0\right],$$

where the total insertion loss is the difference between the power into the input transducer and out of the output transducer in dB, N is the number of finger pairs in each transducer, C_p is the capacitance per finger pair, and f_0 is the resonant frequency of the transducers [3]. To test the quality of our transducers, an input and output transducer pair with 20 finger pairs, 1.4 mm long, operating at a fundamental frequency of 144 MHz was fabricated on semi-insulating GaAs. The measured total insertion loss was about 45 dB. Using the above formula with $N = 20$, $K_{eff}^2 \sim 7.4 \times 10^{-4}$ at $kd = 0$, $C_p = 0.14$ pF/pair, and $f_0 = 144$ MHz gives a calculated loss of 46 dB, which is similar to the experimental value. The slight discrepancy is probably due to uncertainty in the value of C_p and K_{eff}^2 for GaAs.

References

[1] A. Wixforth *et al*., *Phys. Rev. B* **40**, 7874 (1989); A. R. Hutson and D. L. White *J. Appl. Phys*. **33**, 40 (1962).

[2] S. H. Simon, *Phys. Rev. B* **54**, 13878 (1996).

[3] Colin K. Campbell. *Surface Acoustic Wave Devices for Mobile and Wireless Communications*. Academic Press, New York 1998.

Appendix D
Solution to Bloch's Equations for cw NMR

D.1 Overview

Bloch's equations [1] are a set of simple equations derived from phenomenological arguments that describe the evolution of nuclear spins in external magnetic fields. The following solution to Bloch's equations allow for better understanding of the RDNMR data described in this thesis.

D.2 Solution

Consider a collection of nuclear spins in a static magnetic field $\vec{B}_0 = B_0\hat{z}$, and ac magnetic field $\vec{B}_1 = B_1\hat{x}\cos(\omega_1 t)$, perpendicular to B_0. It is convenient to work in a rotating frame of reference that rotates in the *x*-*y* plane at the same frequency ω_1 as the ac magnetic field. The Bloch equations in this rotating frame are

$$\frac{dM_x}{dt} = -\frac{M_x}{T_2} + \Delta\omega M_y$$
$$\frac{dM_y}{dt} = -\frac{M_y}{T_2} - \omega_r M_z - \Delta\omega M_y$$
$$\frac{dM_z}{dt} = -\left(\frac{M_z - M_0}{T_1}\right) + \omega_r M_y,$$

where M_x, M_y, M_z are the components of the nuclear magnetization in the rotating frame, M_0 is the thermal equilibrium value of the magnetization, $\Delta\omega = \omega - \omega_0$ is the detuning of the frequency of the transverse ac *B*-field, B_1, from the Larmor resonance frequency ω_0, and $\omega_r = \gamma B_1$ is the Rabi frequency.

Consider a situation where initially $B_1 = 0$ and the nuclear magnetization is in thermal equilibrium ($M_z = M_0$). Then, at time $t = 0$, the ac *B*-field is turned on ($B_1 > 0$) suddenly at the center NMR resonance frequency ($\Delta\omega = 0$). We want to solve for M_z as a function of time. It is only necessary to solve the equations for M_y and M_z:

$$\frac{d}{dt}\begin{pmatrix} M_y \\ M_z \end{pmatrix} = \begin{pmatrix} -1/T_2 & -\omega_r \\ \omega_r & -1/T_1 \end{pmatrix}\begin{pmatrix} M_y \\ M_z \end{pmatrix} + \begin{pmatrix} 0 \\ M_0/T_1 \end{pmatrix}$$

The solution to the above equation will be a sum of the homogeneous and particular solutions, we denote as y, z, and y_p, z_p, respectively, so that $M_y = y + y_p$, $M_z = z + z_p$. We first solve the homogeneous form of the above equation:

$$\frac{d}{dt}\begin{pmatrix} y \\ z \end{pmatrix} = \begin{pmatrix} -1/T_2 & -\omega_r \\ \omega_r & -1/T_1 \end{pmatrix}\begin{pmatrix} y \\ z \end{pmatrix}.$$

There will be two linearly independent solutions. Let the solutions be of the form

$$\begin{pmatrix} y \\ z \end{pmatrix} = \vec{A}e^{\lambda t}.$$

Then,

$$\begin{pmatrix} -1/T_2 - \lambda & -\omega_r \\ \omega_r & -1/T_1 - \lambda \end{pmatrix}\begin{pmatrix} y \\ z \end{pmatrix} = \begin{pmatrix} 0 \\ 0 \end{pmatrix}.$$

This requires

$$\begin{vmatrix} -1/T_2 - \lambda & -\omega_r \\ \omega_r & -1/T_1 - \lambda \end{vmatrix} = 0.$$

Then,

$$\left(\frac{1}{T_2} + \lambda\right)\left(\frac{1}{T_1} + \lambda\right) + \omega_r^2 = 0.$$

Thus,

$$\lambda = \frac{1}{2}\left[-\left(\frac{1}{T_1}+\frac{1}{T_2}\right) \pm \sqrt{\left(\frac{1}{T_1}+\frac{1}{T_2}\right)^2 - \left(\omega_r^2 + \frac{1}{T_1 T_2}\right)} \right]$$

$$= \frac{1}{2}\left(\frac{1}{T_1}+\frac{1}{T_2}\right)\left[-1 \pm \sqrt{1 + 4\frac{\omega_r^2 T_1 T_2 + 1}{T_1 T_2 \left(\frac{1}{T_1}+\frac{1}{T_2}\right)^2}} \right].$$

Next, we make the simplifying assumption that $T_2 / T_1 \ll 1$. This is generally a good assumption for nuclear relaxation in 2DES's in GaAs where $T_2 \sim 1$ ms and T_1 is typically much longer than 1 s. Then,

$$\lambda = \frac{1}{2T_2}\left[-1 \pm \sqrt{1 + 4\left(\omega_r^2 T_2^2 + T_2 / T_1\right)} \right].$$

If we also assume that $\omega_r T_2 \ll 1,$ expanding the square root gives

$$\lambda \approx \frac{1}{2T_2}\left(-1 \pm \left[1 + 2\left(\omega_r^2 T_2^2 + T_2 / T_1\right) \right] \right).$$

So, the two decay constants are

$$\lambda_+ = -\omega_r^2 T_2 - 1/T_1,$$
$$\lambda_- = -1/T_2 - \omega_r^2 T_2 - 1/T_1.$$

The particular solutions y_p, z_p will be constants such that

$$\begin{pmatrix} 0 \\ 0 \end{pmatrix} = \begin{pmatrix} -1/T_2 & -\omega_r \\ \omega_r & -1/T_1 \end{pmatrix}\begin{pmatrix} y_p \\ z_p \end{pmatrix} + \begin{pmatrix} 0 \\ M_0 \end{pmatrix}.$$

This gives

$$y_p = \frac{-\omega_r^2 T_2 M_0}{1 + \omega_r^2 T_1 T_2}$$
$$z_p = \frac{M_0}{1 + \omega_r^2 T_1 T_2}.$$

Next, we solve for the amplitudes of the two homogenous solutions, $\vec{A}_+$ and $\vec{A}_-$. The complete solution will be

$$\begin{pmatrix} M_y \\ M_z \end{pmatrix} = \vec{A}_+ e^{\lambda_+ t} + \vec{A}_- e^{\lambda_- t} + \begin{pmatrix} y_p \\ z_p \end{pmatrix}.$$

We use the initial conditions

$$M_z = M_0$$
$$\frac{dM_z}{dt} = 0$$

At $t = 0$. Then,

$$\vec{A}_+ + \vec{A}_- + \begin{pmatrix} y_p \\ z_p \end{pmatrix} = \begin{pmatrix} 0 \\ M_0 \end{pmatrix}$$

and

$$\lambda_+ \vec{A}_+ + \lambda_- \vec{A}_- = \begin{pmatrix} -\omega_r M_0 \\ 0 \end{pmatrix}.$$

Looking at the z-component,

$$A_{+z} + A_{-z} = M_0 \frac{\omega_r^2 T_1 T_2}{1 + \omega_r^2 T_1 T_2}$$

and

$$\lambda_+ A_{+z} + \lambda_- A_{-z} = 0.$$

Then,

$$M_z = M_0 \left[\frac{1}{1 + \omega_r^2 T_1 T_2} \right] \left[\frac{1}{1 - \lambda_+ / \lambda_-} \right] \left[\omega_r^2 T_1 T_2 \left(e^{\lambda_+ t} - \left(\lambda_+ / \lambda_- \right) e^{\lambda_- t} \right) + 1 \right].$$

Because $T_2 / T_1 \ll 1$ and $\omega_r T_2 \ll 1$, we have $\lambda_+ / \lambda_- \ll 1$. Then, we can make the approximation

$$M_z \approx M_0 \left[\frac{1}{1+\omega_r^2 T_1 T_2} \right] \left[1+\omega_r^2 T_1 T_2 e^{\lambda_+ t} \right].$$

From this expression we see that the rise time for the RDNMR signal is given by $\lambda_+ = -\omega_r^2 T_2 - 1/T_1$.

References

[1] See, for example, Abragam, A. *The Principles of Nuclear Magnetism*. Oxford University Press, London 1961.

Appendix E
Nuclear Spin Pumping at $\nu = 1/2$

This appendix describes preliminary experiments that investigate the possibility of pumping of the nuclear spins at $\nu = 1/2$ by driving large currents through the 2DES.

E.1 Phenomenology

We look at two single-layer 2DES samples, both lithographically patterned into a hall bar shape. Sample A is an undoped FET structure patterned into a 50 μm wide hall bar. Sample B is a Si modulation-doped heterojunction with a 500 μm wide hall bar.

Figure E.1 shows the effect of driving a large current (I_{rms} = 100 nA at 13 Hz) through sample A, while at $\nu = 1/2$, B = 3.3 T. There is a gradual rise in the longitudinal resistivity on a time scale of 1000's of seconds.

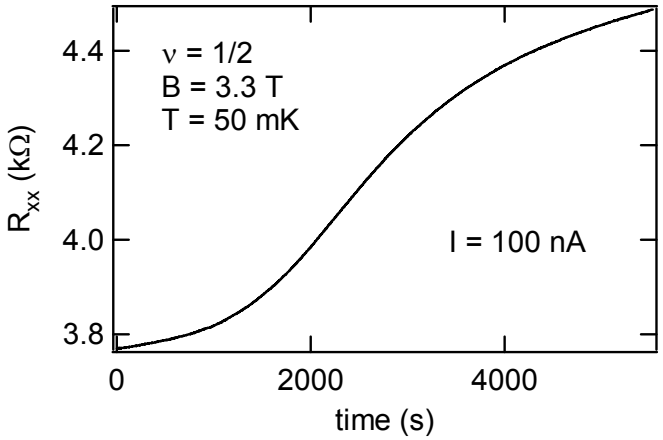

Fig. E.1. Longitudinal resistance R_{xx} vs. time at $\nu = 1/2$, B = 3.3 T, for sample A (50 μm hall bar) with application of large current. The current is I = 10 nA for times $t < 0$.

Figure E.2 shows an RDNMR frequency sweep, passing through the ^{75}As resonance while applying I = 100 nA. The sample resistance is allowed to reach equilibrium with I = 100 nA before starting the sweep. Recall from Chapter 6 that the RDNMR signal is positive for small currents. The signal in Fig. E.2 is negative – application of large currents actually reverses the sign of the RDNMR signal!

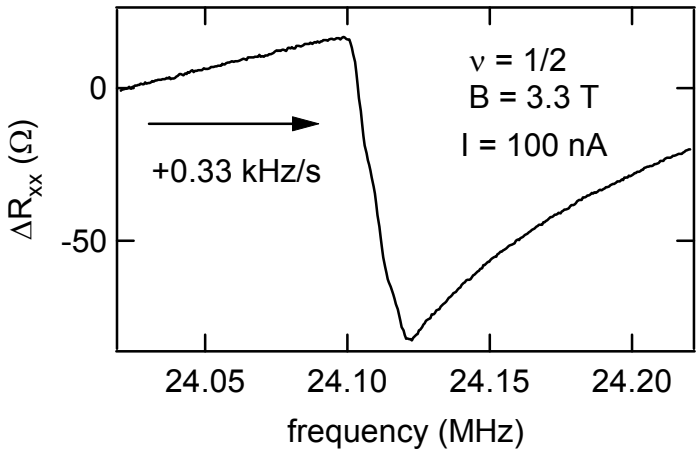

Fig. E.2. R_{xx} vs. frequency at $\nu = 1/2$, $B = 3.3$ T, for sample A with application of large current. The frequency of the RF magnetic field is swept through the ^{75}As NMR resonance ($f_{75As} = 24.110$ MHz).

Figure E.3 shows the fractional change in resistivity due to an NMR pulse at the ^{75}As resonant frequency, versus current through the 2DES. The resistance is allowed to reach equilibrium while applying the pumping current. Then, the RF ac magnetic field is always on at fixed amplitude ($B_{ac} \sim 1$ μT), but the frequency is moved onto the ^{75}As resonance, depolarizing the nuclei.

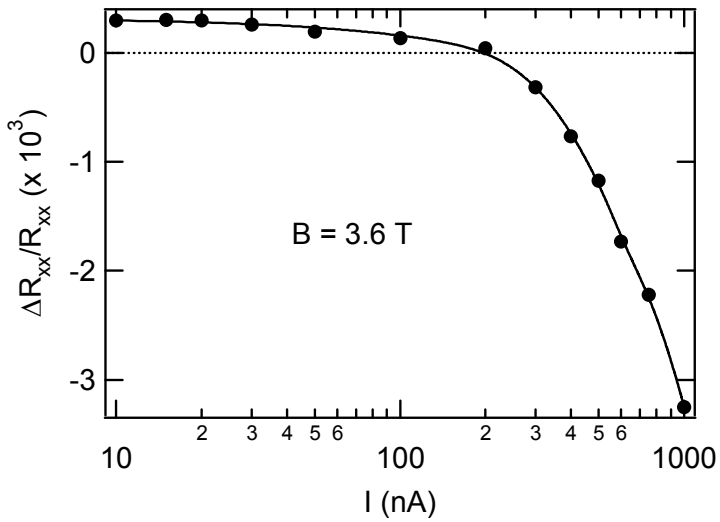

Fig. E.3. Fractional change in longitudinal resistivity $\Delta R_{xx}/R_{xx}$ due to an NMR pulse versus the current driven through the 2DES sample for sample B (500 μm hall bar) at $\nu = 1/2$, $B = 3.6$ T.

At low currents, as in Chapter 6, the RDNMR change in resistance is positive, while at large currents (I > 100 nA), the RDNMR signal decreases, changing sign, and then becomes negative and relatively large in magnitude.

E.2 Conclusions

One interpretation for the above data is that sourcing large currents through the 2DES at ν = 1/2 alters the nuclear polarization of the host substrate. Similar phenomenology involving pumping of the nuclear spin can be seen at the ν = 2/3 and other FQH states near transitions between states of differing spin polarization [1-3].

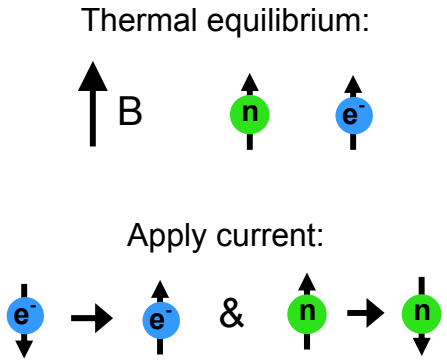

Figure E.4. Cartoon of electron and nuclear spin (small black arrows) and putative nuclear pumping mechanism at ν = 1/2.

The change in the sign of the RDNMR signal at high currents suggests that the sign of the nuclear polarization can even be reversed from thermal equilibrium. A sketch of the equilibrium electron and nuclear spin configuration and the current-driven nuclear pumping process is shown in Fig. E.4. In thermal equilibrium, the nuclear and electron spins should prefer to align with the static magnetic field (the electron spin aligns with the B-field due to the negative g-factor of electrons in GaAs). How the current induces electronic spin flips of the correct sign to pump the nuclear spin towards the direction opposite from the configuration in thermal equilibrium is unclear.

References

[1] S. Kronmüller *et al*. Phys. Rev. Lett. **81**, 2526 (1998); S. Kronmüller *et al*., *Phys. Rev. Lett*. **82**, 4070 (1999).

[2] J.H. Smet, *et al*., *Phys. Rev. Lett*. **86**, 2412 (2001).

[3] J. Eom *et al*., *Science* **289**, 2320 (2000).